

An International  
Forum For  
The AE Science  
and Technology

# JOURNAL OF ACOUSTIC EMISSION

Vol.36/January-December 2019

Editors: M.A. Hamstad (AEWG) and G. Manthei (EWGAE)

- 36-001 Receiving Sensitivities of Acoustic Emission Sensors: A data  
Compilation Kanji Ono
- 36-001EX Data File for 36-001
- 36-009 Use of Acoustic Emission for Studying Ratcheting Behavior of 304LN Stainless  
Steel Elbows C.K. Mukhopadhyay, T.K. Haneef, Suneel K. Gupta,  
Vivek Bhasin, S. Vishnuvardhan, G. Raghava and P. Gandhi
- 36-039 Far-field wave propagation signals from pencil lead breaks on the open end  
of a thick-walled layered cylinder: Part 1 Amplitudes and frequency content  
M. A. Hamstad
- 36-051 Far-field Wave Propagation Signals from Pencil Lead Breaks on the Open End  
of a Thick-walled Layered Cylinder: Part 2 Modes of wave propagation  
M. A. Hamstad
- 36-071 Detection of Defects in Spur Gears by Acoustic Emission Monitoring  
Swati Gautam and Naresh Tandon

Proceedings of International Conference on Acoustic Emission - 9  
Part I and II

Endorsed by  
AEWG  
and  
EWGAE

Published by  
Acoustic Emission Group  
Encino, CA USA  
©2019 Acoustic Emission Group

# Monitoring Fracture Formation in Additively Manufactured Anisotropic Rocks

Liyang Jiang<sup>1</sup>, Hongkyu Yoon<sup>2</sup>, Antonio Bobet<sup>3</sup>, Laura J. Pyrak-Nolte<sup>1,3</sup>

<sup>1</sup> Department of Physics and Astronomy, Purdue University, West Lafayette, IN;

<sup>2</sup> Geomechanics Department, Sandia National Laboratories, Albuquerque, NM;

<sup>3</sup> Lyles School of Civil Engineering, Purdue University, West Lafayette, IN

## ABSTRACT

This work explores the effects of oriented layers and texture (oriented minerals) on fracture evolution in 3D printed gypsum samples. During 3D printing, bassanite (calcium sulfate hemihydrate) was chemically transformed into gypsum layer by layer, giving rise to anisotropic texture. Unconfined compressive strength (UCS) tests monitored with six broadband acoustic emission (AE) transducers were performed with cylindrical specimens: casted gypsum (CG) samples, and 3D printed (3DP) samples with five different orientations of bassanite layer and gypsum texture relative to the loading direction. UCS varied by 150% among the samples, primarily due to anisotropy in the 3DP samples. The bonds of gypsum crystals between sequential bassanite layers were stronger than those of gypsum-bassanite, resulting in anisotropic material properties. Unlike the CG samples, no axial splitting was observed from the 3DP samples, and a single inclined (relative to loading direction) major crack was observed instead. The fracture location estimated by AE localization technique was comparable to that observed from reconstructed X-ray computed tomography images. CG samples failed immediately after reaching a peak load, while 3DP samples exhibited ductile post-peak behavior. Examination of the AE signal amplitude from post-peak loading revealed that more ductile behavior was associated with more AE events that occurred over a longer period of time, and the resultant fracture surfaces were rougher than for narrow distributions. Monitoring of AE signals during failure of rock has the potential to predict fracture roughness and the mineral and layering patterns.

**Keywords:** 3D printing, AE, X-ray computed tomography, fracture roughness, UCS

## 1. INTRODUCTION

Understanding the mechanical behavior of layered rock is vital in fields such as hydraulic fracturing for the exploitation of shale gas and oil reservoirs. The complex response of shale is, in part, due to its anisotropy, which is attributed to the preferred orientation of its mineral grains, pores, cracks, and bedding planes (e.g. Wenk et al., 2007). To determine the effect of anisotropic layering on rock properties, deformation and failure requires samples that enable repeatable results. This is challenging when working with natural rock because even rock samples acquired from the same rock mass can vary in mineralogy, texture and structural features (Johnson & Greenkorn, 1963; Sone & Zoback, 2013). The effect of oriented layers and oriented textural

features on the unconfined compressive strength (UCS) of an anisotropic rock is studied using 3D printed analog rock-material to overcome the challenges of working on natural samples.

## 2. SAMPLE FABRICATION

3D printing was used to create analog rock samples. 100  $\mu\text{m}$  thick layers of calcium sulfate hemihydrate (bassanite) powder were bonded with a proprietary water-based binder, which chemically transformed the bassanite into gypsum (Singh & Middendorf, 2007). The gypsum texture contained in a layer was controlled by selecting the direction of binder application and layering. The gypsum crystals formed bonds between sequential bassanite layers that were stronger than the gypsum-bassanite bonds, resulting in anisotropic material properties. UCS tests were conducted on printed cylindrical specimens (50.8 mm in height, 25.4 mm in diameter) with different orientations of bassanite layers and gypsum texture relative to the loading direction (Figure 1).

Non-layered reference samples with no preferred mineral orientation were fabricated by casting gypsum in a mold. A silicone rubber mold was created from a solid resin sample (3D printed on a FormLabs 2) with the same dimensions as the 3D printed (3DP) samples. The mold was filled with mixed gypsum and water, then vibrated to minimize the amount of trapped air, and then cured. The resulting casted gypsum (CG) samples were cylindrical in shape and had the same heights and diameters as the 3DP samples.

## 3. EXPERIMENTAL SETUP AND PROCEDURE

All samples were loaded parallel to the long axis of the cylinder with an ELE International Soil Testing load frame with an S-shaped load cell (2000 lbs capacity). A steel ball and a steel spacer were placed on top of the samples to function as a spherical seat.

AE measurements were recorded with Mistras Express II station together with loading and displacement data synced by parametric channels. Broadband transducers (F15 $\alpha$  sensors from Physical Acoustics) were attached to the side of the cylinder samples at 6 different locations. 20-1200 kHz preamplifiers were used with a 60 dB gain and 27 dB threshold setting for recording. During monitoring, acoustic sensor transmission tests were also performed to provide velocities across the samples.

A 3D X-Ray Microscope (Zeiss Xradia 510 Versa) was used to image each sample after the test if coalescence did not lead to complete failure. The induced fractures were visualized in 3D using Dragonfly Pro software. If failure resulted in a sample breaking into two pieces, then laser profilometry was performed to determine the fracture surface roughness.

An aluminum piece was also tested to determine the background noise levels. Data were analyzed by Noesis software only for signals with peak frequencies between 200-400 kHz since lower frequency signals were identified as noise.

## 4. RESULTS

The largest values of UCS were observed in samples where both the layering and gypsum texture were oriented parallel to the loading direction. The lowest UCS was found for samples with bedding layers oriented 45° to the applied load (Figure 1). Unlike the CG samples, no axial splitting was observed among the 3DP samples. Samples with bedding oriented 45° to the load failed along the bedding planes, breaking into two pieces with smooth failure surfaces as determined from laser profilometry. Irrespective of the orientation of the layers and texture, all samples exhibited a single major crack that spanned the entire length of the sample, inclined to the direction of loading.

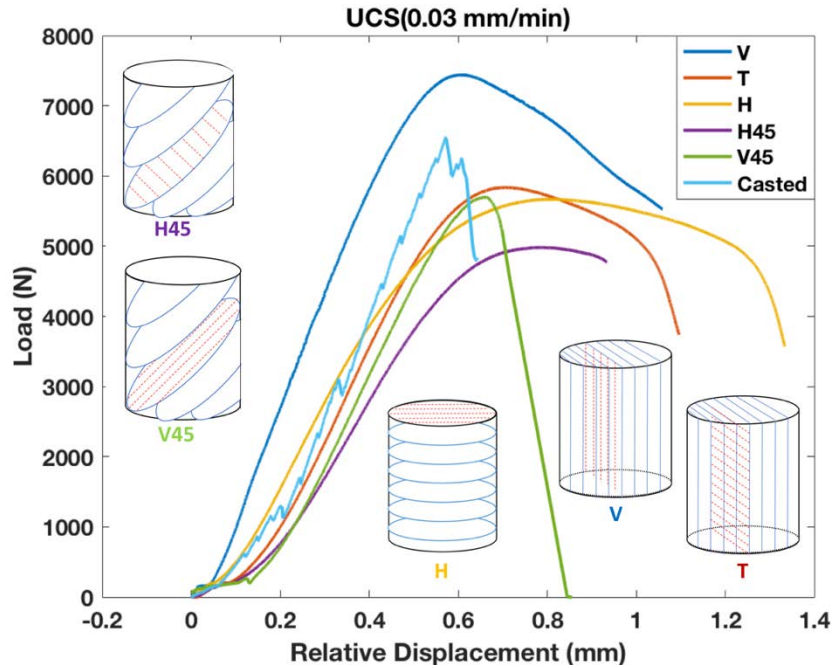


Figure 1. Sketch of 3D printed samples showing orientation of the bassanite layers (blue lines) and oriented mineral feature (red dashed lines) and the load displacement curves of each type.

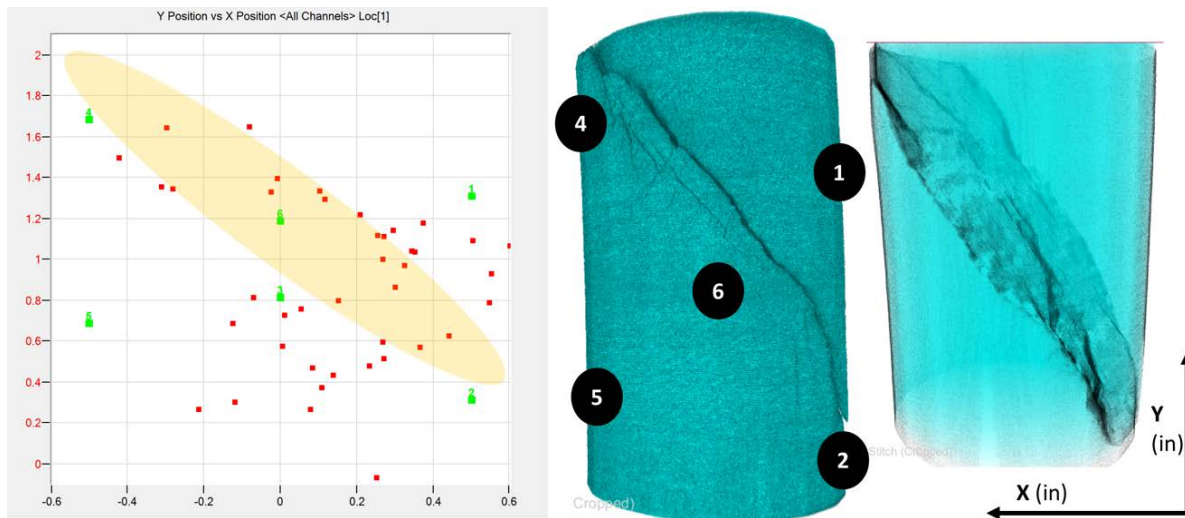


Figure 2. Estimated fracture location from AE and the reconstructed X-ray computed tomography images.

The fracture location estimated by AE localization technique was compared to that observed from reconstructed X-ray computed tomography images (Figure 2). Improved location methods are needed to include the velocity anisotropy of the sample.

CG samples failed immediately after reaching a peak load with narrow period of AE signals. 3DP samples exhibited ductile post-peak behavior. Examination of the AE signal amplitude distribution in time for post-peak loading revealed that a longer period of AE events correlated with more ductile behaviors and the resultant fracture surfaces were rougher than for narrow AE distributions (Figure 3).

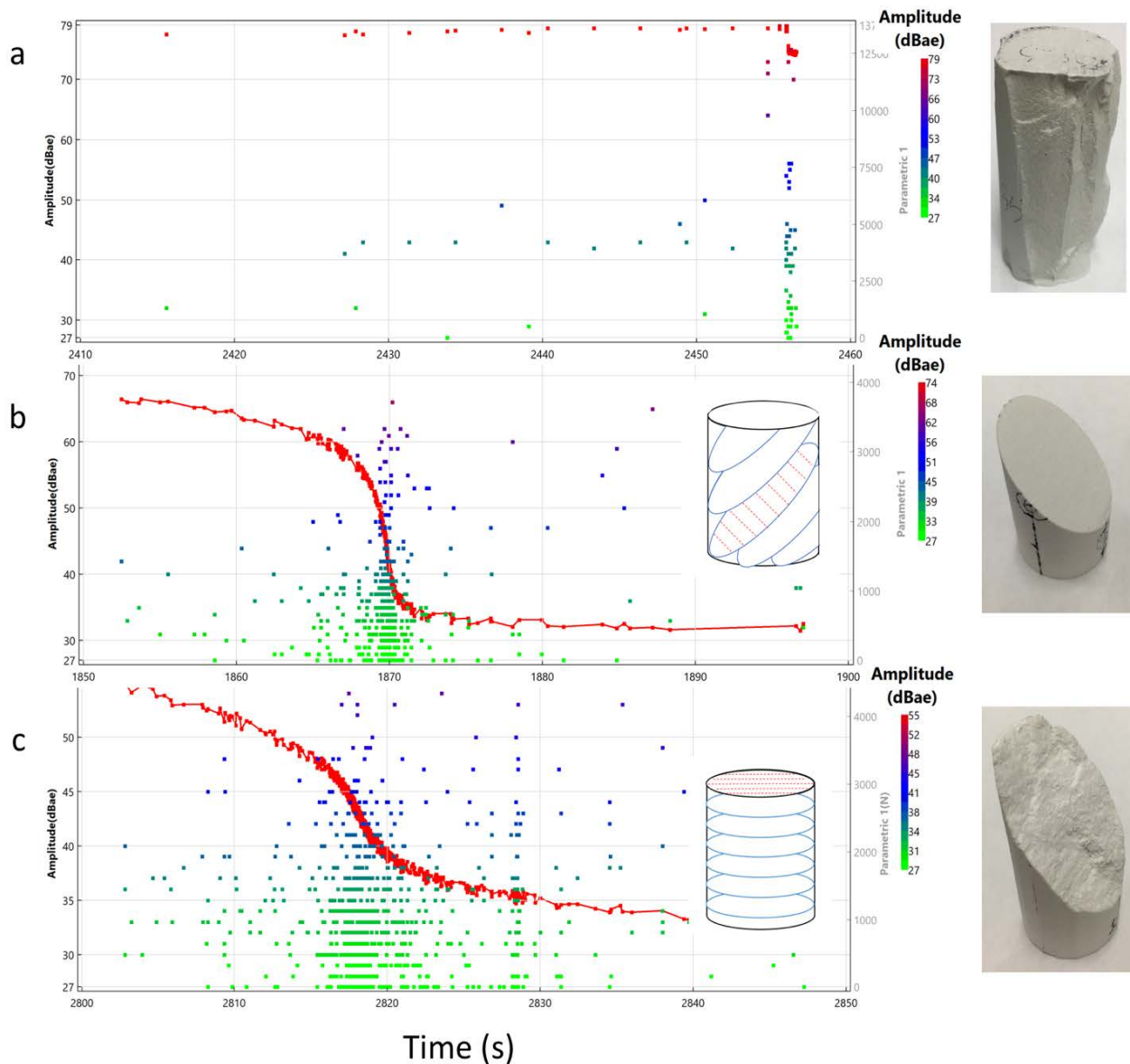


Figure 3. (a) The CG sample failed almost instantly and had the narrowest AE amplitude distribution in time; (b) The H45 sample had smoother fracture surfaces and a relatively narrower AE amplitude distribution compared to other 3DP samples; (c) The H sample exhibited the most significant ductile post-peak behavior, produced relatively rougher surfaces and a longer period of AE events.

The results have the potential to be used as an effective tool to study the influence of texture and layering on sample strength and cracking patterns and monitoring AE signals during failure of rock may have the potential to predict fracture roughness and the mineral and layering patterns.

## **5. ACKNOWLEDGMENT**

Sandia National Laboratories is a multi-mission laboratory managed and operated by National Technology & Engineering Solutions of Sandia, LLC, a wholly owned subsidiary of Honeywell International, Inc., for the U.S. Department of Energy's National Nuclear Security Administration under contract DE-NA0003525.

## **6. REFERENCE LINKING**

Johnson, C.R. and R.A. Greenkorn, Description of gross reservoir heterogeneity by correlation of lithologic and fluid properties from core samples, *Hydrological Sciences Journal*, 8:3, 52-63, 1963.

Sing, N.B. and B. Middendorf, Calcium sulphate hemihydrate hydration leading to gypsum crystallization, *Progress in Crystal Growth and Characterization of Materials*, v. 53, p57-77, 2007.

Sone, H. and M.D. Zoback, Mechanical properties of shale-gas reservoir rocks – Part 1: Static and dynamic elastic properties and anisotropy, *Geophysics*, vol. 78, No. 5, September – October 2013, PD381-D392, 2013.

Wenk, H-R., Lonardelli, I,m Franz, H., Nihei, K. and S. Nakagawa, Preferred orientation and elastic anisotropy of illite-rich shale, *Geophysics*, vol. 72, no. 2, March-April 2007, p E69-E75, 10.1190/1.2432263.

# Tensile test of 3D printed specimens for demonstrating the performance of acoustic emission measurement systems

Hironobu Yuki and Tomona Murata

The University of Electro-Communications, Chofu, Japan

## ABSTRACT

Quantitative discussion on the performance of measurement systems including both of the characteristics of the instruments and the operational skill based on the reference is necessary for establishing the traceability of measurement. In this study, an approach to provide the standard specimen as the reference for acoustic emission (AE) measurement, in which behavior of AE occurrence could be controlled, was examined. Specimens containing regions of different stress concentration resulted from different size holes were made by a stereolithography type 3D printer and those were subjected to tensile load. It was shown that the AE event in the intended position could occur for the specimen with different size rhombic holes to change the degree of stress concentration. It was also found that drop-like holes for changing the degree of stress concentration rapidly are useful to generate AE in the intended position at the intermittently time. As a consequence, the feasibility of providing the standard specimen for the AE method was demonstrated.

**Keywords:** Standard Specimen, Stereolithography, Hole, Stress Concentration, Crack Extension

## 1. INTRODUCTION

Artificial acoustic emission (AE) sources such as pencil lead breaks and the pulse generator are widely used to check the condition of the instruments and perform calibration [1] so that the frequency characteristics and the sensitivity of the system are ensured for successful monitoring. Those sources, however, cannot sufficiently simulate the dynamic characteristics such as the interval of generation and movement of the source position which are often employed as parameters to discuss the phenomenon causing AE. Hence, inappropriate settings for the instruments which lead to miss-recording of AE signals, e.g. high threshold level, low sampling rate and long dead time, are sometimes allowed in operation. Therefore, quantitative discussion on the performance of measurement systems including both of the characteristics of the instruments and the operational skill based on real AE signals which are regarded as the reference is desirable in order to avoid such situation and establish the traceability. Development of the standard specimen occurring intended real AE events is expected for this reason. In the case of AE measurement associated with fracture, such specimen is required to generate AE intermittently same as AE characteristics due to the generation and extension of the crack. AE measurement during the tensile test for the 3D printed specimen with intended defects was attempted since 3D printers could easily make the object containing defects of arbitrary geometry in the arbitrary position, and the AE signal associated with final fracture was only measured[2]. In this study, AE measurement for the specimens containing different holes made by a 3D printer was conducted by subjecting tensile load and the feasibility of providing the standard specimen for AE measurement was examined.

## 2. EXPERIMENTAL PROCEDURE

Strip specimens with the single V-shaped notch containing regions of different stress concentration resulted from different size holes, which were aligned on the extensional line of the notch tip, were made by a stereolithography type 3D printer (3D Systems, ProJet 3500 HD Max; resolution: 375×375×790 dpi, lamination pitch: 29  $\mu\text{m}$ ) using acrylic ultraviolet curing resin (3D Systems, Visi-Jet Crystal). AE signals were measured while the specimens were subjected to tensile load toward the longitudinal direction with a testing machine (Instron, 4505). Four 140 kHz resonant type AE sensors (Fuji Ceramics, AE144A) were attached to the specimen in surrounding the whole holes for source location and detected signals were recorded on a digital oscilloscope after amplification of 40 dB with the external preamplifier (NF Corporation, 9913). A wideband type AE sensor (NF Corporation, AE-900S-WB) was also attached to the opposite side of the specimen for acquiring all AE events during the test with a general AE measuring device (Physical Acoustics Corporation, USB AE Node; built-in preamplifier of 40 dB). In this study, the specimens were laminated toward the thickness direction in order to prevent the occurrence of delamination due to tensile loading. Therefore, the generation of AE caused by delamination can be negligible.

## 3. RESULTS AND DISCUSSION

### 3.1 Rhombic holes specimen

The specimen with rhombic holes of 3 mm in each side length and the opening angle along the long axis becomes larger as the distance from the notch increases for changing the degree of stress concentration as shown in Figure 1 was first used for the experiment. Figure 2(a) demonstrates the load-displacement diagram during the test obtained by the testing machine. It was shown that the specimen was broken down at the time immediately after recording the AE signal on the oscilloscope and no loss in load was observed until the final fracture. The difference of the stress concentration factor around each hole seems small to take place the intermittently crack extension. The time of AE occurrence is also indicated in this figure. While the oscilloscope only recorded a single AE event, the AE measuring device acquired several events having a different amplitude before the final fracture because of the low background noise level. However, these events are not related to the growth of the main crack since the load-displacement curve continues to increase monotonically. Further discussion should be done by obtaining the data which are capable of source location for these events. Figure 2(b) shows the results of source location for the data recorded on the oscilloscope for three same geometry specimens. It was demonstrated that AE occurred in the region between the notch and the first hole where the maximum stress appears.

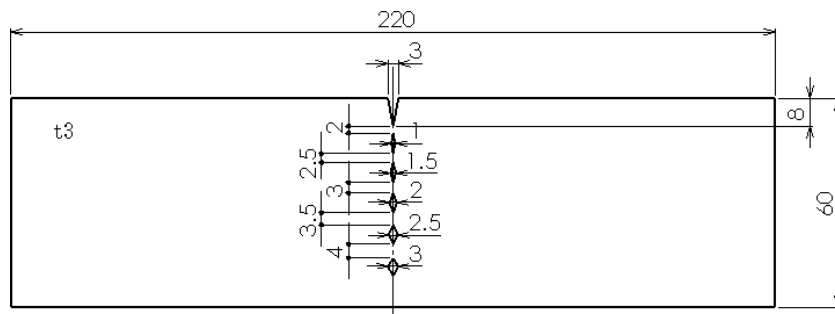


Figure 1: Geometry of the specimen with rhombic holes.

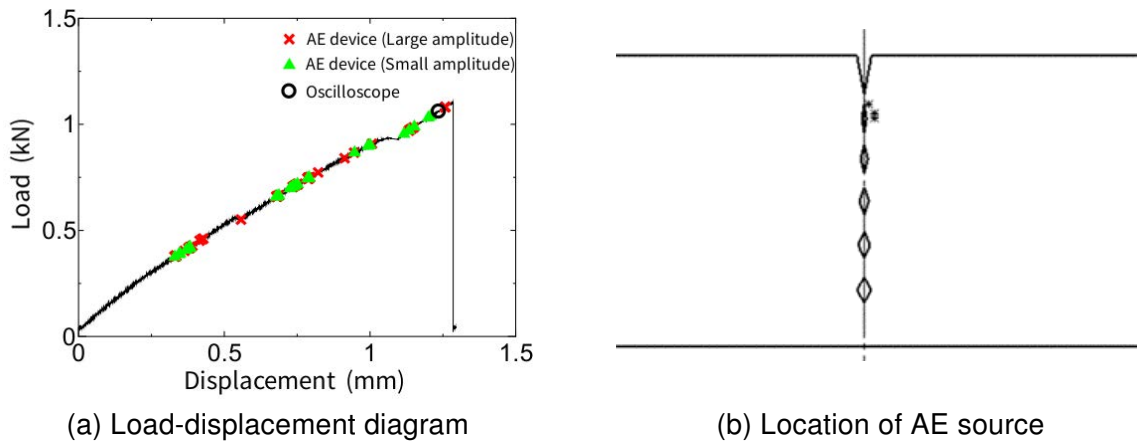


Figure 2: Results of the specimen with rhombic holes.

Therefore, it was found that although significant AE could be generated in the intended position by changing the size of the hole, intermittently measurement corresponding to the crack extension is difficult.

### 3.2 Drop-like holes specimen

Experiments using two kinds of specimens with drop-like holes, in which the stress concentration factor around the sharp tip of the hole rapidly changes depending on the distance from the notch, were next carried out. One, called "type A" as shown in Figure 3(a), has the geometry that the

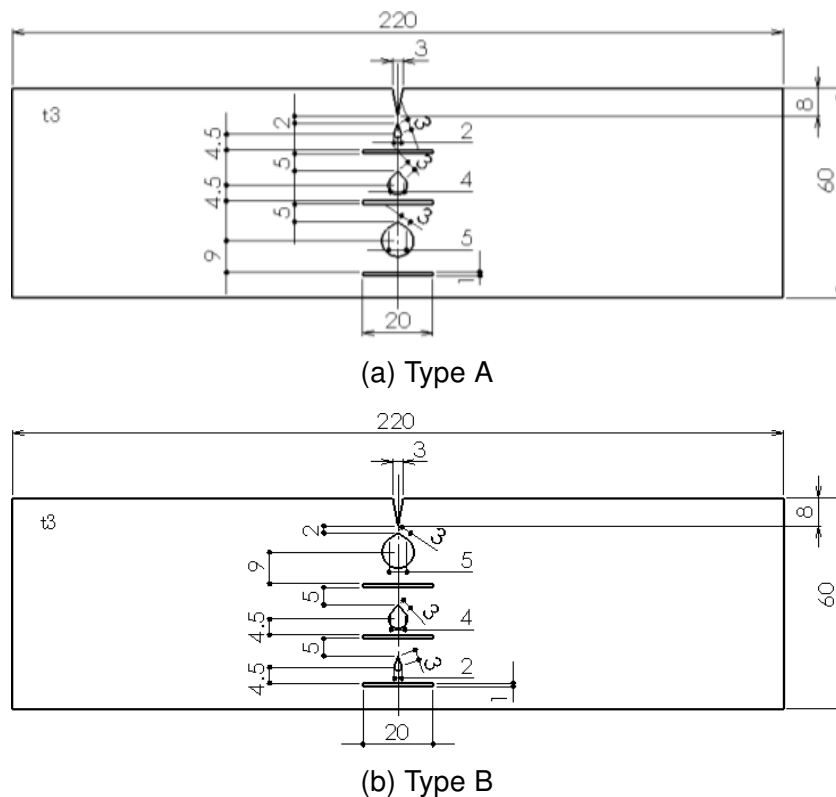


Figure 3: Geometry of the specimen with drop-like holes.

opening angle of the sharp tip increases as the distance from the notch increases, and the other called “type B” has the geometry that the angle decreases with increasing the distance as shown in Figure 3(b).

Figure 4(a) illustrates the time of AE occurrence during the test for the type A specimen by plotting marks on the load-displacement diagram. It was shown that AE signals were generated when a loss in load occurred during subjecting tensile load before the breakdown of the specimen so that it was found that starting and stopping of the crack was repeated. Figure 4(b) shows the results of source location determined by the AE signals recorded on the oscilloscope. The order of crack generation confirmed by visual observation during the test was also indicated in this figure, and it was shown that the positions of AE sources were not aligned straightforward one direction. On the other hand, the results of the type B specimen were shown in Figure 5. Several losses in the load were observed and the positions of AE sources were aligned in the order of reasonableness. These results show that AE events occur in the intended position at the intermittently time by changing the degree of stress concentration rapidly. Therefore, the performance of AE measurement can be demonstrated whether the specified events are appropriately recorded.

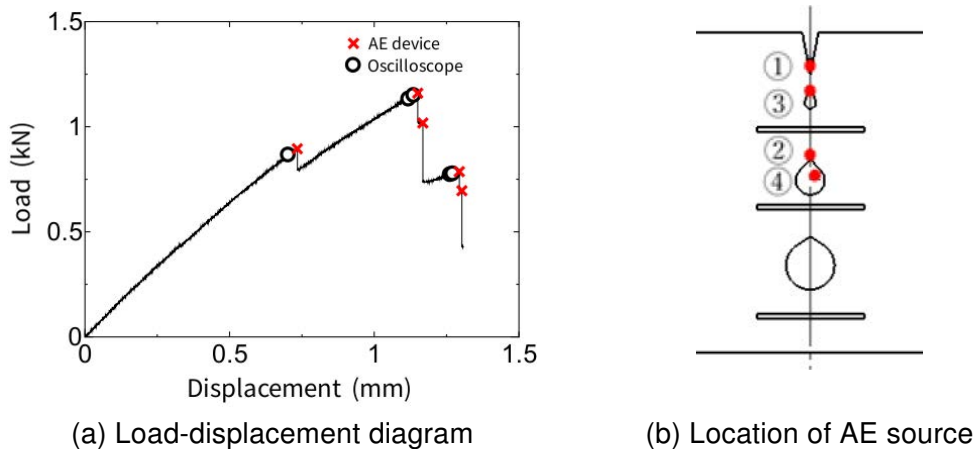


Figure 4: Results of the specimen with drop-like holes (type A).

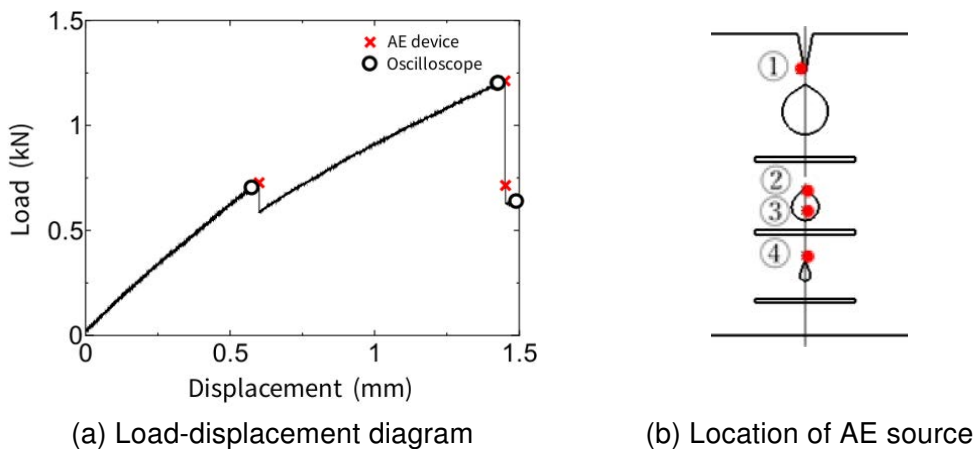


Figure 5: Results of the specimen with drop-like holes (type B).

#### 4. CONCLUSION

AE measurement of the specimens made by the stereolithography type 3D printer during the tensile test was conducted. It was shown that the AE event in the intended position could occur for the specimen with different size rhombic holes to change the degree of stress concentration. It was also found that drop-like holes for changing the degree of stress concentration rapidly are useful to generate AE in the intended position at the intermittently time. From these results, the feasibility of providing the standard specimen for the AE method by aligning the arbitrary size holes in the arbitrary positions using the 3D printer was demonstrated.

#### REFERENCES

- [1] The Japanese Society for Non-Destructive Inspection (ed.), *Practical Acoustic Emission Testing*, Springer Japan, (2016).
- [2] Obata, Y., "Prototype tensile specimen with defects by 3D printer for AE measurements", *Meeting Materials of the Research & Technical Committee on Acoustic Emission, the Japanese Society for Non-Destructive Inspection*, AE-00033, (2014), pp.35–36, (in Japanese).

# Evaluation of Damage Depth Inside Concrete Using Surface Wave Tomography

Norihiko Ogura<sup>a</sup>, Yuji Konishi<sup>a</sup> and Tomoki Shiotani<sup>b</sup>

<sup>a</sup>CORE Institute of Technology Corp. Osaka, Japan; <sup>b</sup>Kyoto University

## ABSTRACT

Surface wave tomography using an elastic wave is one of the nondestructive testing methods used for evaluating internal soundness of concrete structures. This study experimentally investigated the depth of a defect detectable by the surface wave tomography, generating elastic waves with varied frequencies. The detectable damage depth was successfully determined for each frequency level of the elastic wave based on the obtained results. It was also found that internal damage evaluation layered in the depth direction was possible even with a single elastic wave by applying the wavelet transform and sorting the data by target frequency.

**Keywords:** surface wave tomography, elastic wave, nondestructive testing, Rayleigh wave, wavelet transform

## 1. INTRODUCTION

Surface wave tomography is an applied elastic wave method which is drawing increasing attention as a means of nondestructive testing for soundness evaluation of concrete structures. Since this technique does not require the sensors to be placed on the opposing sides of the object, internal concrete soundness can be evaluated with the sensors arrayed on a single plane. This makes the surface wave tomography useful, especially in cases where the subject structure is accessible only from one side. However, the relationship between the frequency of a generated elastic wave and the detectable depth of a defect has not been identified. In the current study, elastic waves in different frequency bands were generated by using several types of steel balls to determine the relationship with the detectable damage depth. It was also investigated if it was possible to determine the depth of a defect with an elastic wave made by a single type of steel ball, by applying wavelet transform to the received waveforms and examining the tomographic images obtained for the surface wave propagation velocity at the target frequency.

## 2. SURFACE WAVE TOMOGRAPHY

### 2.1 Characteristics of the surface wave

The surface wave tomography is a type of elastic wave tomography and focuses on the Rayleigh wave which is a component of the elastic wave that propagates along the surface. The Rayleigh wave is a mixed wave consisting of the P-wave which moves in the direction of wave propagation and the S-wave which moves in the direction perpendicular to wave propagation. It is known that the vibration of particles propagates in an elliptical motion at a right angle to the plane along which the wave travels. Although the depth of an influence on the Rayleigh wave corresponds to the wavelength, one half the wavelength is used as the influence depth in this study to take into account the attenuation with depth. Figure 1 schematically shows the propagation of the Rayleigh wave.

## 2.2 Tomographic analysis

A single array measurement of the elastic wave propagation time only provides an average propagation velocity on a scan line (from the impact point to the receiving point) for soundness evaluation based on the calculated velocity. It is therefore impossible to know the location of the defect when the result indicates damage in the object. With multiple arrays of sensors, in contrast, an estimated distribution of soundness can be obtained by applying matrix operations to the propagation times measured on multiple scan lines in different directions, and determining the elastic wave propagation velocity in each cell of an arbitrarily-divided analysis model of a structure by back analysis. For the surface wave tomography in this study, an analysis model of the subject area arbitrarily divided into cells was created, and slowness (or reciprocal velocity) was given as the value for soundness evaluation. Correction of slowness was made by back analysis so that the theoretical propagation time obtained from slowness in each cell and ray path length on each scan line would be equal to the measured propagation time. The simultaneous iterative reconstructive technique (SIRT)<sup>1)</sup> was used for the back analysis.

## 3. OUTLINE OF THE EXPERIMENT

### 3.1 Specimen

An unreinforced concrete specimen with an artificial crack simulating a real structure was prepared. Figure 2 shows the external dimensions of the specimen. The artificial crack in the specimen was made by embedding a cloth tape at a depth of 50 mm from the concrete surface.

### 3.2 Layout of the sensors

Nine (9) receiving sensors were placed in three lines and three rows (500×500 mm) across the crack, and impact-side sensors were placed at 16 arbitrary points. Figure 3 shows the layout of the sensors. In this study, 60 kHz resonant acoustic emission sensors were used.

### 3.3 Calculation of the surface wave propagation velocity

Surface wave propagation velocity is used for the parameter in the surface wave tomography. Surface wave is known to be characterized by extremely large energy. In this study, the surface wave arrival time was determined by the maximum or minimum value of the received wave. The impact time was calculated by using Akaike's Information Criterion (AIC)<sup>2)</sup>.

### 3.4 Frequency of the generated elastic wave and the influence range

Steel balls were used to apply an impact and generate an elastic wave in this study. The contact time of a steel ball at the impact can be given by Equation (1) from a previous study<sup>3)</sup>. Based on the contact time, the centroid frequency and influence range of the surface wave were calculated on the assumption that a generated surface wave propagation velocity was 2,400 m/s and that one period of the surface wave was equal to two times the contact time of the steel ball. The diameters of the steel balls used were 5 mm (D5), 10 mm (D10) and 20 mm (D20). Table 1 shows the contact time of each steel ball and the frequency and influence range of the surface wave.

$$TC=0.0043D \quad (1)$$

where, TC: contact time (s), and D: steel ball diameter (m)

## **4. EXPERIMENT RESULTS**

### **4.1 Investigation on the impact frequency and the influence range of the surface wave**

The influence range of the surface wave was investigated using the elastic wave generated by an impact of a steel ball. Figures 4 to 6 show the results of tomographic analysis on the crack in the concrete specimen, using the D5, D10 and D20 steel balls. The crack was expressed almost correctly by the velocity distribution in the tomographic image with the D5 steel ball, but not in those with the D10 and D20 steel balls. These results suggest the presence of an area subject to such phenomena as diffraction and reflection in the surface wave influence range in the depth direction. The influence range determined using the D5, D10 and D20 steel balls was 51.60, 103.2 and 206.4 mm, respectively, from the concrete surface as shown in Table 1, and it was likely difficult to detect the defect when the ratio of the influence range to the crack depth (50 mm) was about 200% or over.

### **4.2 Tomography using the wavelet transform**

In the tomography performed in Section 4.1, the detectable layer (depth) was limited in relation to the steel ball diameter. In order to detect the location of a defect or a defect at an unknown depth, it is necessary to perform measurement using multiple steel balls with different diameters. For simplification of the measurement, frequency analysis was made by applying the wavelet transform to the received waveforms. The wavelet transform leaves the time domain information which is otherwise lost during the process of Fourier transform to obtain the frequency response. This enables calculating the arrival time of the maximum amplitude at a target frequency. Figure 4 shows an example of the wavelet transform results on a received waveform and the surface wave arrival time reading. If the tomography using the propagation velocity calculated by this method is valid in damage evaluation, it will be possible to obtain internal damage evaluation layered in the depth direction, using a single waveform.

The wavelet transform was performed using the received waveforms generated by an impact of the D10 steel ball. The target frequencies were 23.2 kHz respectively corresponding to the theoretical peak frequencies for the elastic waves generated by using the D5 steel ball. Figures 8 show the tomographic analysis results. The tomography at a target frequency of 23.2 kHz (corresponding to the D5 steel ball) almost correctly expressed the crack.

Consequently, the tomography using the wavelet transform is capable of providing layered evaluation of a concrete structure.

## **5. SUMMARY**

The findings of this study are summarized as follows:

- (1) The larger a defect accounting for the influence range of the surface wave, the larger its influence on the surface wave propagation velocity is, leading to more accurate expression of the velocity distribution by the surface wave tomography.
- (2) With the use of the wavelet transform, the tomography using a single waveform can provide layered evaluation of a concrete structure.

## **6. REFERENCES**

- [1] Gilbert, P.: Iterative methods for the three-dimensional reconstruction of an object from projections, *J Theor Biol* 36, pp.105-117, 1972.

- [2] H. Akaike: Markovian representation of stochastic processes and its application to the analysis of autoregressive moving average processes, Annals of the Institute of Statistical Mathematics, Vol.26, No.1, pp.363-387, 1974.
- [3] Sansalone, M. and Streett, W. B.: Impact Echo, Bullbrier Press, Ithaca, N.Y., pp.30-34, 1997.

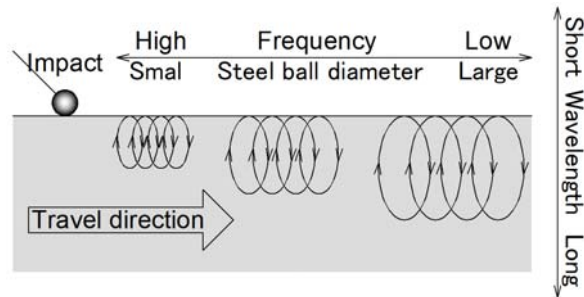


Figure 1 Schematic of the propagation of the Rayleigh wave

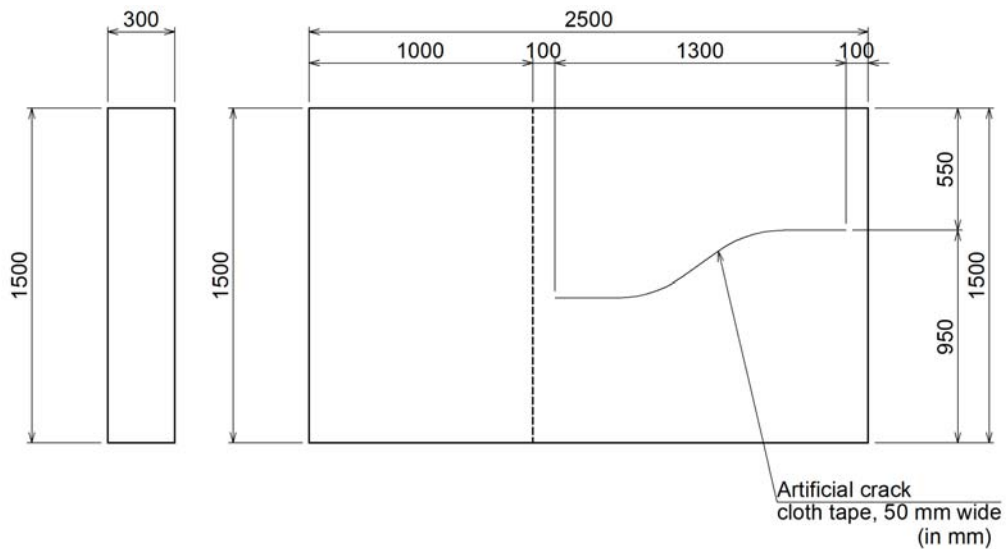


Figure 2 Specimen

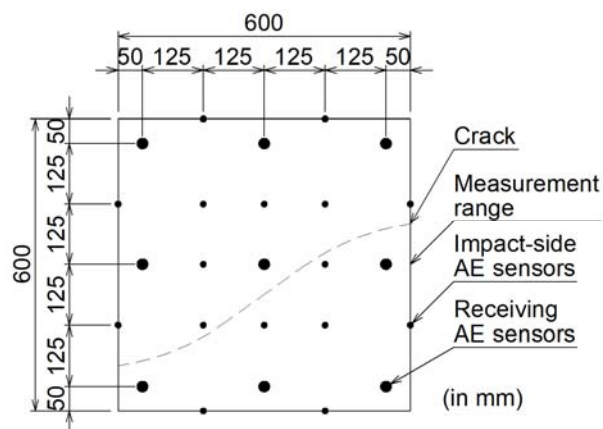


Figure 3 Layout of the sensors and location of the defect

Table 1 Steel ball diameters and surface wave influence ranges

Steel ball diameter D (mm)	Contact time TC ( $\mu$ s)	Frequency (kHz)	Influence range (mm)
0.005	21.5	23.3	51.60
0.010	43.0	11.6	103.2
0.020	86.0	5.81	206.4

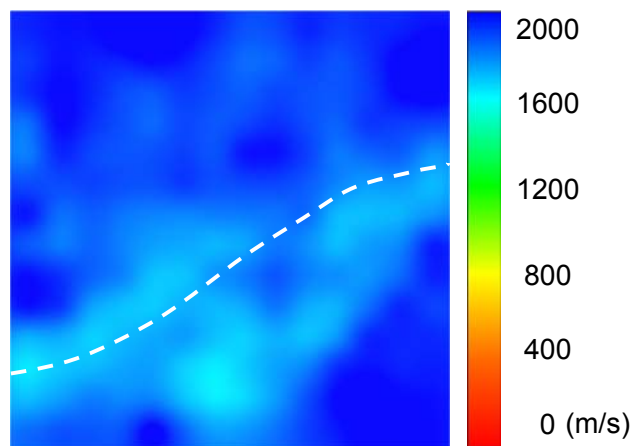


Figure 4 Tomography on the crack, with the D5 steel ball

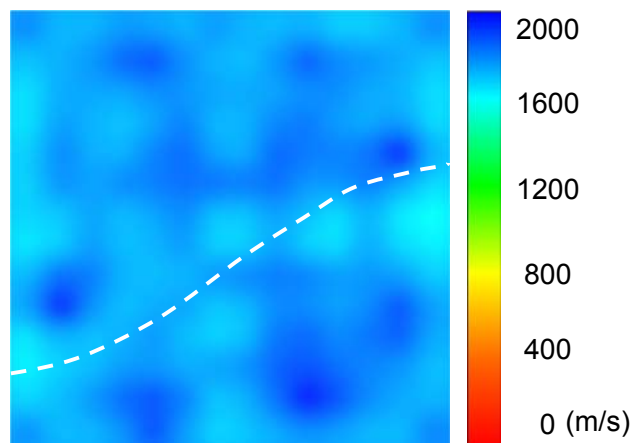


Figure 5 Tomography on the crack, with the D10 steel ball

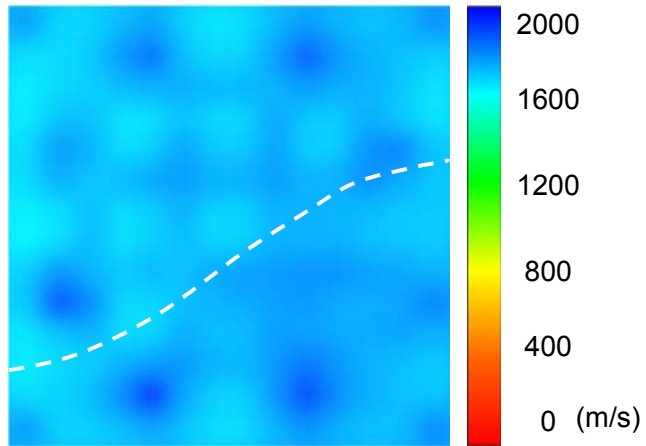


Figure 6 Tomography on the crack, with the D20 steel ball

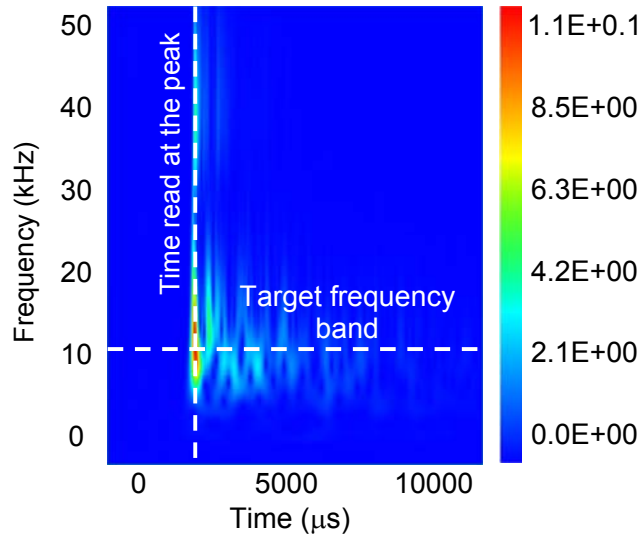


Figure 7 Arrival time reading by the wavelet transform

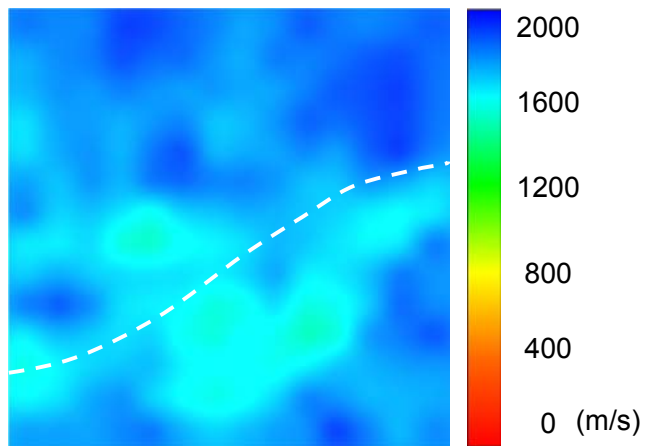


Figure 8 Tomography on the crack, with the D10 steel ball, at 23.2 kHz

# Internal Damage Detection of RC Bridge Decks with Uniformly Distributed Elastic Wave Sources

Hidefumi Takamine<sup>1,2</sup>, Yuki Ueda<sup>1,2</sup>, Kazuo Watabe<sup>1,2</sup>, Katsufumi Hashimoto<sup>3</sup>,  
and Tomoki Shiotani<sup>3</sup>

<sup>1</sup>Research & Development Center, Toshiba Corp., Kawasaki, 212-8582, Japan;

<sup>2</sup>NMEMS Technology Research Organization, Chiyoda-ku, Tokyo, 101-0026, Japan;

<sup>3</sup>Dept. Civil & Earth Resources Engineering, Kyoto University, Kyoto, 615-8540, Japan

## ABSTRACT

In order to inspect the large number of bridges, easy and efficient methods of inspection are needed. We have developed a new and efficient technique to inspect the RC bridge decks with Acoustic Emission (AE) monitoring system. As a unique point of our method, we utilized rain-induced elastic waves, which had been generally considered as noise. We installed AE sensors on the undersurface of the bridge decks and monitored the rain-induced elastic waves propagate through the decks. Usually, the rain-induced elastic wave sources are distributed uniformly on the upper surface of the decks. However, the cracks inside the decks disturb the propagation of the elastic waves and the distribution observed by the sensors on the undersurface is distorted. Therefore, analyzing the change in uniformity of the distribution of the sources can reveal the existence of the damage inside the bridge deck. Through a test at an in-service highway bridge, we have successfully verified the effectiveness of this advanced technique. The recognized cracks in the test had been hard to recognize with conventional passive Non-Destructive Testing (NDT). Besides, our method is quite efficient that the measurement is completed in a very short period of time.

In this paper, the results obtained from both test piece experiments and in-service highway bridge monitoring are shown. Furthermore, the effect of difference in the types of sources to induce the elastic waves and the sensor position to detect the elastic waves are discussed.

**Keywords:** acoustic emission, bridge deck, concrete, crack, inspection

## 1. INTRODUCTION

The maintenance of deteriorating social infrastructures is a serious issue [1]. In order to maintain the large number of social infrastructures, the inspections should be executed efficiently. As efficient inspection methods, we have been developing a monitoring system and diagnostic methods utilizing acoustic emission (AE) sensors [2]. Our system inspects concrete bridge decks by watching the AE activities, which are caused by the fracturing of materials [3]. In a previous work, we monitored highway bridge decks for about a week. From an analysis of the AE activities, we successfully diagnosed the deterioration of the RC bridge decks [4-6].

On the other hand, we have developed another novel method to detect internal cracks of the bridge decks [7, 8]. We focused on the rain-induced signals. Those signals are not generated by the fracturing at the cracks. Therefore, they should be removed as noise for accurate analysis. However, we discovered that those rain-induced signals contain the information of propagation path of the elastic waves. Figure 1 shows the schematic diagram of the propagation of rain-

induced elastic waves in a bridge deck. The raindrops hit the surface of the road and generate elastic waves. The elastic waves propagate through the deck and reach the AE sensors on the undersurface of the deck. Usually, it is assumed that raindrops fall uniformly over the entire road surface. Therefore, if the rain-induced elastic wave source locations are calculated from the sensor data, the distribution of the sources should be uniform. However, if a large crack exists in the deck, the propagation is disturbed and the source density of the damaged area would be lower. Consequently, from the calculated distribution of the rain-induced sources, we can detect the cracks inside the deck. We applied this technique to a test piece with artificial defect inside and confirmed the ability to detect internal cracks. The results of an actual bridge deck are also shown and compared with the test piece results.

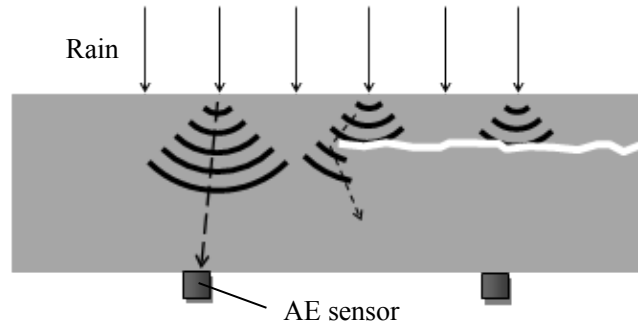


**Figure 1 Propagation of rain-induced elastic waves**

## 2. EXPERIMENTAL SETUP

We carried out experiments on a test piece of RC slab. Figure 2 shows the test piece. The test piece contains a styrene board simulating a horizontal crack. The styrene board is 600 x 600 mm and 5 mm thick. The board is placed alongside the upper rebar and it is about 140 mm deep from the undersurface of the slab. Figure 3 shows the sensor arrangement. Nine sensors are attached to the undersurface of the slab. The distance between sensors is 500 mm. The frequency range of the sensors is 25 - 70 kHz. In order to simulate the rain, we applied impacts on the upper surface of the test piece by hammer or water drops. The impacts were applied uniformly around the styrene area. The hammering was continued for about 2 minutes. The water drops were scattered from 2 or 3 m high for about 2 minutes. Estimated volume of each water drop was less than 5 ml.

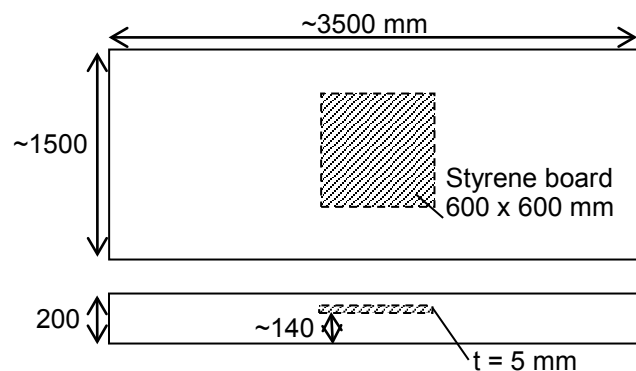


**Figure 2 Test piece of RC slab**

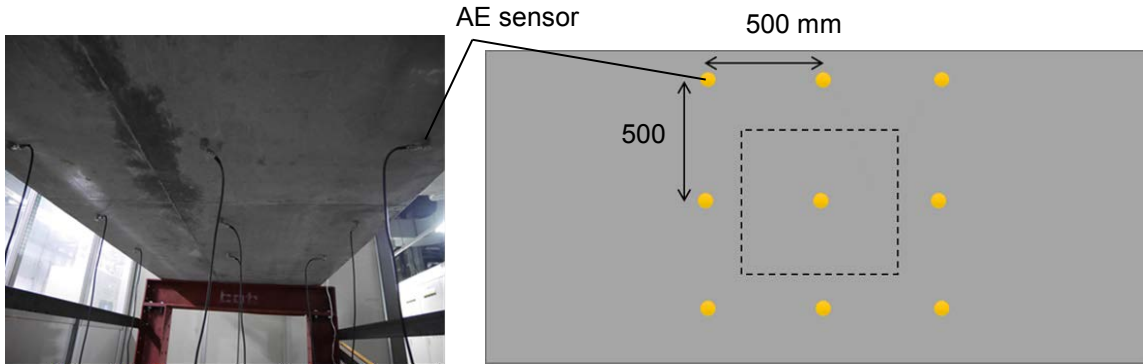


Figure 3 Sensor arrangement of test piece

### 3. RESULTS AND DISCUSSION

#### 3.1 Results of different source types

Figure 4 shows the results of the test piece experiments. The calculated source locations and the source density distributions are shown. In both hammering results and water drops results, less wave sources are located inside the square area in the center, which contain styrene board simulating the internal crack. The results shows that the hammering detected the styrene board clearer than the water scattering. Since the impacts of the hammer were stronger and more controllable than the water drops, the elastic waves generated by the hammering were larger in amplitude, more separated each other in timing, and more uniformly distributed than the waves generated by water scattering. The results indicate that well controlled and strong impacts would make this method more accurate.

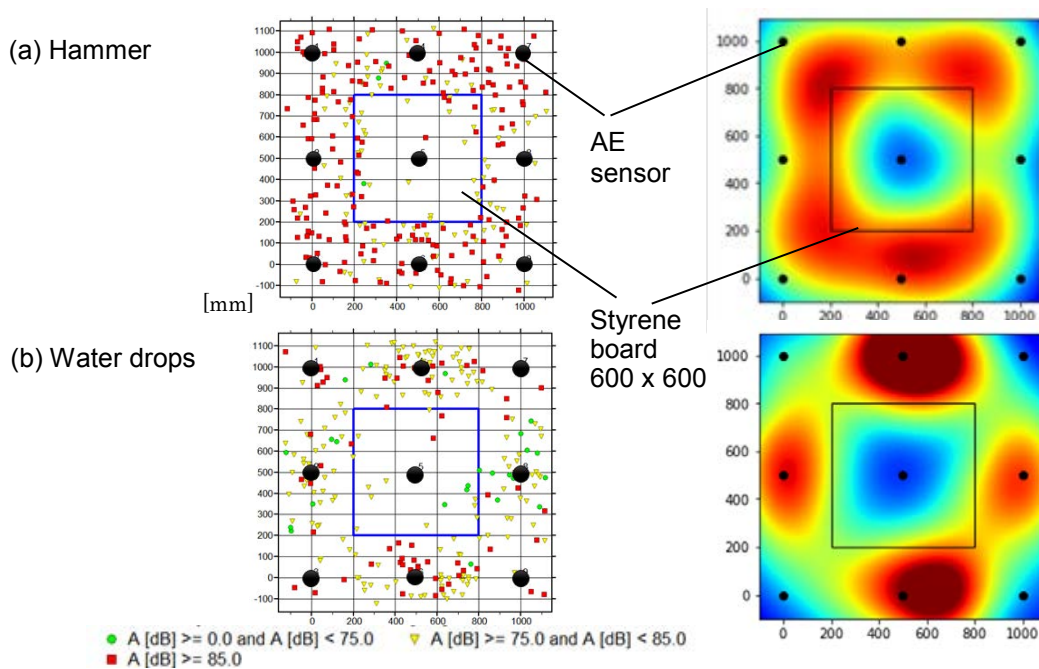


Figure 4 Results of different wave sources

### 3.2 Results of different sensor arrangements

Figure 5 shows the location analysis results in different sensor arrangements. In both arrangements, the distance between a sensor and the nearest sensor is about 700 mm. In both case, the area with defect shows the lower density and the internal crack is recognizable. However, the clarity of the results is quite different owing to the difference in the sensor positions. A notable point is the presence of the sensor just under the defect. In the case (a), many of the elastic waves were disturbed to reach the sensor in the center by the defect. On the other hand in the case (b), less waves were disturbed to reach the sensors and their source positions were able to be located by the calculation. It made the difference in the source density between the defective area and the sound area smaller. Since the crack position is not apparent before the inspection, the influence of the sensor arrangement has to be taken into account at the diagnostics.

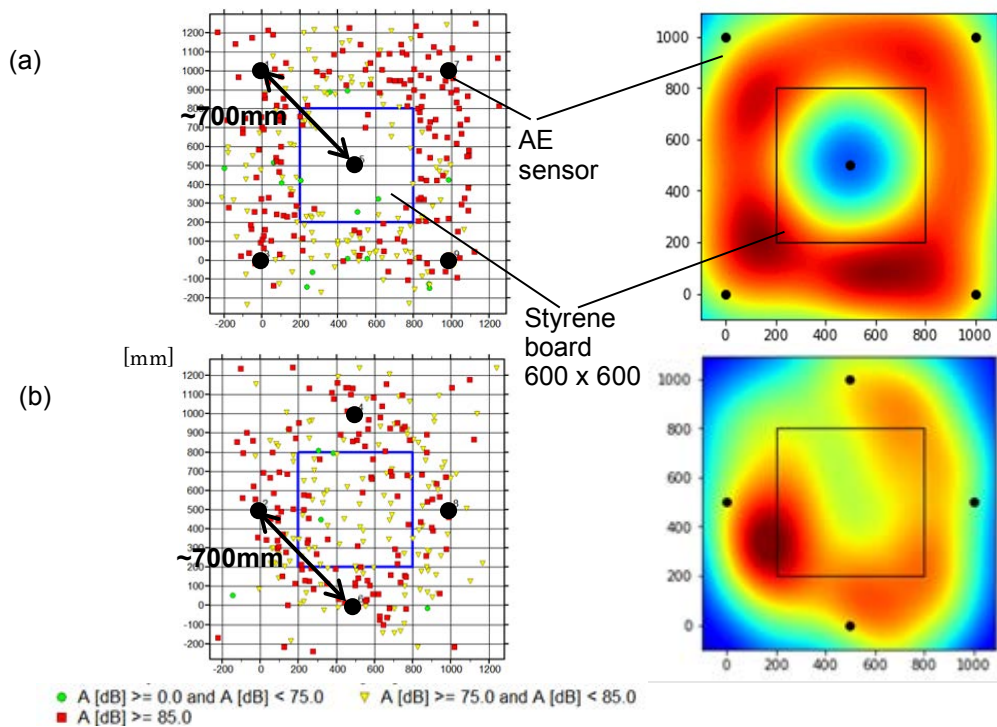
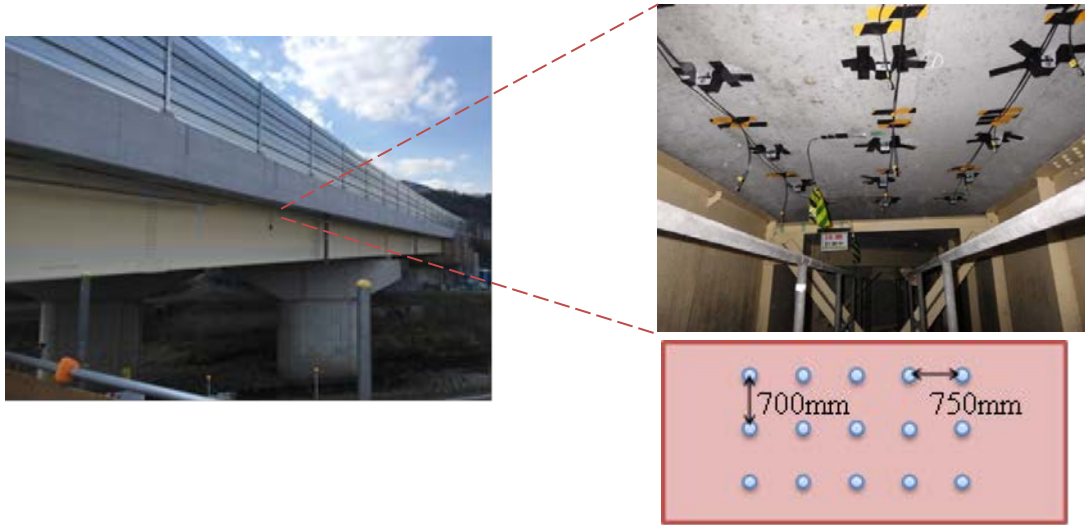


Figure 5 Results of different sensor arrangements

## 4. RESULT OF ACTUAL BRIDGE

We applied our method to an RC deck of an in-service highway bridge. Figure 6 shows the photos of the measured bridge and the sensor arrangement. Sensors were attached in a  $3 \times 5$  configuration on the undersurface of the deck. The frequency range of the sensors is 25 – 80 kHz. The distances between adjacent sensors were 700 or 750 mm. Although small cracks were found on the undersurface of the deck, no serious large crack was visible. During the measurement, we found a sudden increase in AE activities due to heavy rain lasting for about 700 seconds. Since the rain lasted for very short period of time, the traffic-induced signals were negligible compared with the large amount of rain-induced signals. We extracted those data and analyzed in detail. After the measurement, the analysis results were verified by the coring.

Figure 7 shows the location analysis result of the rain-induced signals and the coring results. The coring positions are marked with the source distribution. Some of the cores were found to be cracked and the cracked cores are represented by the cross marks. In the analysis, the center area of the deck shows lower density, which indicates the existence of the internal crack. And we discovered that the cracked cores corresponded to the low source density area. Thus, the ability of our technique to detect internal cracks was confirmed. In this case, the cracked area was so large that the some sensors were located just under the crack. Therefore, the internal crack was clearly detected. In the case that the cracks were smaller than the distance between sensors, the result could be less clear and should be diagnosed more carefully.



**Figure 6 Sensor arrangement in highway bridge deck**

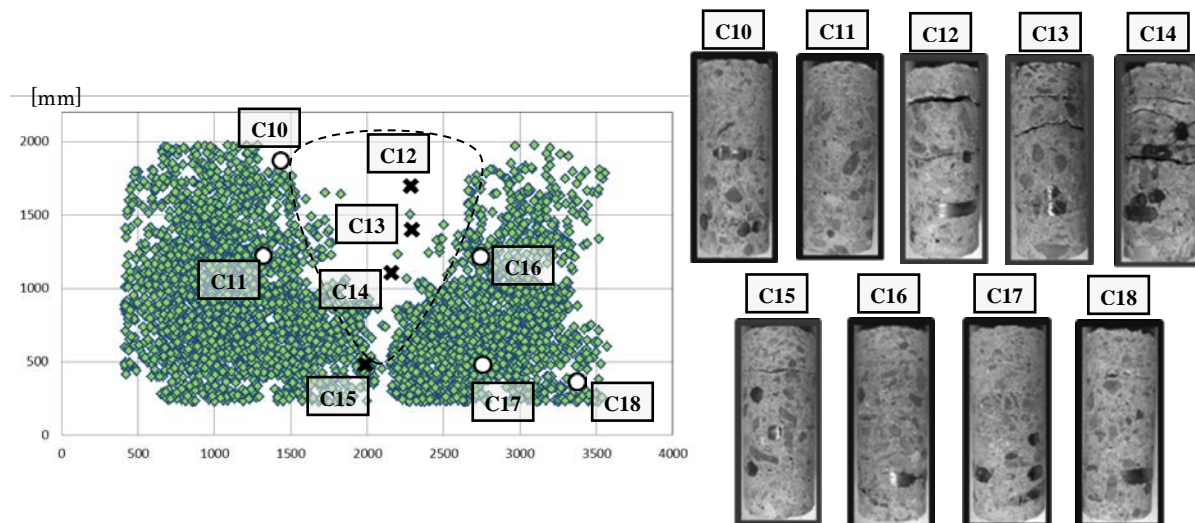


**Figure 7 Analysis and coring results of highway bridge deck**

## 5. CONCLUSION

We proposed a novel inspection method to detect the internal cracks of the bridge decks. We attached the AE sensors on the undersurface of the decks and analyzed the elastic waves propagated from the uniformly distributed sources on the upper surface of the decks. Our method successfully detected the internal cracks efficiently in the few minutes of measurement. It is also discovered that the sensor position relative to the crack position affect the source distribution and the sensor arrangement have to be considered at the diagnostics.

## ACKNOWLEDGEMENT

This work was supported by the New Energy and Industrial Technology Development Organization (NEDO) of Japan.

## REFERENCES

- [1] "WHITE PAPER ON LAND, INFRASTRUCTURE, TRANSPORT AND TOURISM IN JAPAN, 2014", Part 2, Chapter 2, <http://www.mlit.go.jp/common/001113562.pdf>
- [2] T. Shiotani, D. G. Aggelis, O. Makishima : "Global monitoring of large concrete structures using acoustic emission and ultrasonic techniques: case study", *Journal of Bridge Engineering*, Vol. 14, No.3, 188-192, (2009)
- [3] Y. Ueda, T. Usui, T. Omori, H. Takamine, K. Watabe, T. Shiotani, *Proceedings of Conference on Information, Intelligence, and Precision Equipment (IIP2018)*, the Japan Society of Mechanical Engineers, (in Japanese)
- [4] K. Watabe, H. Takamine, T. Nishida, T. Shiotani, "Novel Non-destructive Technique of Internal Deterioration in Concrete Deck with Elastic Wave Approaches", *Asset Intelligence through Integration and Contemporary Vibration Engineering Technologies*, 665, (2017).
- [5] H. Asaue, T. Shiotani, T. Nishida, K. Watabe, H. Miyata, "Applicability of AE Tomography for Accurate Damage Evaluation in Actual RC Bridge Deck", *Structural Faults & Repair-2016 Conference*
- [6] C. Granier, T. Shiotani, K. Hashimoto, T. Nishida, "Visualization of internal damage in RC slab with single side access attenuation tomography", *Journal of AE*, vol. 34, pS54-S58, (2017)
- [7] H. Takamine, K. Watabe, H. Miyata, H. Asaue, T. Nishida, T. Shiotani, "Efficient damage inspection of deteriorated RC bridge deck with rain-induced elastic wave", *Construction and Building Materials* 162, 908-913, (2018).
- [8] K. Hahimoto, T. Shiotani, N Okude, C. Glanier, K. Watabe, H. Takamine, "Simulation Investigation Of Elastic Wave Velocity and Attenuation Tomography Using Rain-Induced Excitations", *Proc. of Structural Faults + Repair 2018*

# Monitoring Geochemically-induced Fractures in Synthetic Rocks

Chven A. Mitchell<sup>a</sup>, Laura J. Pyrak-Nolte<sup>b</sup>

<sup>a</sup>Purdue University – Department of Earth, Atmospheric and Planetary Sciences

<sup>b</sup>Purdue University – Dept of Physics & Astronomy, West Lafayette, IN

## ABSTRACT

Volumetric changes in clay have the potential to produce geochemical-geomechanical interactions in rock that can lead to induced microfractures. Acoustic emission (AE) monitoring coupled with micro X-ray Computed Tomography was used to investigate microstructural alterations of synthetic rock caused by volumetric changes in clays during drying. Synthetic rock samples with and without clays were fabricated from cement and sand using protocols to produce repeatable behavior. For clay-rich samples, the type and percentage of clay were varied to identify the effect on micro-crack generation during drying. Curing methods and water content were also controlled, both of which affect host rock strength. During drying, acoustic emissions (AE) were monitored. All samples were imaged with a 3D X-Ray Microscope to examine microstructural changes. Synthetic rock samples with high clay content produced more AE events than samples with lower clay or no clay content. If the water content was increased, less AE was observed during the monitoring period and 3D XRM analysis of the samples showed that less damage occurred during drying. If clays were localized within the body of the synthetic core, fractures were observed only in these areas. X-Ray Powder Diffraction was performed on untreated and treated Montmorillonite clay particles to understand the chemo- mechanical behavior of the clays. This analysis revealed changes in the inter-atomic spacing of the clay minerals, which are indications of changes in the lattice volume of the minerals. The results suggest that hydration or dehydration of clay-rich rock during the withdrawal or injection of fluids into the subsurface has the potential to induce microstructural damage from geochemical-geomechanical coupling.

**Keywords:** AE, chemo-mechanical coupling, induced fractures, synthetic rocks, clay

## 1. INTRODUCTION

The capacity of a subsurface reservoir to securely store and retain captured fluids over long periods of time is an extremely important aspect of nuclear waste disposal, Carbon Capture and Storage, and CO<sub>2</sub> Sequestration. This means that the caprock, which overlies any subsurface reservoir selected for storage, must be a capable unyielding impermeable barrier against fluid flow or fluid migration. Two vital macro-scale characteristics of good caprock (seal) layers are continuity and ductility (Downey, 1984). Another important characteristic of a good caprock is some resistance to in-situ chemo-mechanical interactions in rocks between pore fluids and the mineralogical composition that can alter fracture geometry and degenerate the integrity of caprock systems.

For selected subsurface storage reservoir systems the caprock is expected to possess ideal physical and chemical characteristics to be a barrier to flow. Commonly identified caprocks for CO<sub>2</sub> storage (Song and Zhang, 2013; Griffith, 2011), are evaporites (salts and anhydrite) and argillaceous rocks (mudstones, clays, and shales). Shale rocks for the most part are comprised of feldspathic minerals, carbonates, and a varied amount/type of clay (kaolinite, montmorillonite-smectite, illite or chlorite). An important aspect of shale mineralogy is the type and amount of clay minerals embedded in the matrix. Clay minerals are phyllosilicates that crystalize into small-size platy grains, typically less than 10 $\mu$ m (Espinoza and Santamarina, 2012; Mitchell and Soga, 2005; Sposito, 1989). Clay and clay-bearing rocks like shale are extremely water sensitive (Sone and Zoback, 2014). Clays are known to shrink or swell upon interaction with fluids (Wagner, 2013) and clay swelling or shrinkage depends mainly on the type and mineral structure of the clay. A clay-rich mineralogy can greatly influence the subsequent hydro-chemo-mechanical behaviors of shaly caprocks, which in turn affects the mechanical moduli, microstructure, and geophysical properties of rocks (especially in cases where geochemical-geomechanical interactions are externalized as discontinuities). The detection of such geochemically induced alterations and evolutions in the microstructure of rocks in the subsurface is a challenge in geosciences. With this in mind and also because shale is considered an ideal barrier for geological storage systems, we fabricated synthetic clay-rich rocks in an attempt to replicate (with much simplification) the mineralogy and microstructure of this interesting rock. These clay-rich geoarchitected rocks were then used to examine the role of induced volumetric changes in clays (from chemo-mechanical coupling) on the integrity and fracture generation in synthetic rock during drying.

## **2. METHODS AND PROCEDURES**

### **Scanning Electron Microscopy (SEM) for Clay Analysis and Characterization**

Scanning Electron Microscopy (SEM) was performed to analyze and characterize the materials used in the experiments. An FEI NOVA nanoSEM Field Emission System with an Everhart Thornley Detector (ETD) was used at high vacuum to obtain high-magnification and high-resolution images of clay, sand and ordinary Portland cement.

### **X-Ray Powder Diffraction (XRPD) for Clay Analysis and Characterization**

Clays were examined in an untreated state and treated states using X-Ray Powder Diffraction to quantify the changes in the inter-atomic distance (d-spacing). Treated clays were prepared by first decanting them to separate the clay particles from silt particles. Then the clay particles were pipetted onto a glass slide and allowed to sediment and dry out overnight in an oven at 30°C. XRPD was then performed on the treated samples after which all samples were glycolated which is a process whereby the samples are placed in a desiccating chamber above a 2cm layer of ethylene glycol to induce swelling of the clay structure. The desiccator was then placed in the oven overnight to enable the ethylene glycol to steam into the clay structure and induce swelling.

## Fabricating Samples

Clay minerals and raw materials used for the fabrication of geo-architected rock are listed below.

- |   |   |
|---|---|
| 1. Montmorillonite(Bentonite): <b>BIM</b> | IMERYS Bentonite distributors   |
| 2. Montmorillonite: <b>SAK-10</b>         | Sigma Aldrich (SA) – K10  |
| 3. Ordinary Portland Cement: <b>OPC</b>   | LAFARGE – Alpena Plant  |
| 4. Ottawa Sand: <b>SCS250</b>             | US Silica - product SIL-CO-SIL Ground Silica - sand particle tosize @250 um |

The same proportions by weight, of the material used to create an archetypal rock (sample 1 in Table 1) was used with the addition of 20% clay, for clay-rich rocks, and samples with 25% water content (Table 1) and 30% water content (Table 2) were fabricated. All clays were hydrated before adding to the archetypal mix. All mixtures were deposited into cylindrical silicone molds with an average diameter of ~38 mm and an average length ~76 mm. The mold was then placed in a room temperature storage container for a period of 24 hours, after which the hardened samples were removed from the mold, and subjected to curing at 30°C for 7 days (unless noted otherwise).

Table 1: Material composition of fabricated samples at 25% water content

Sample 1	Sample 2	Sample 3	Sample 4
Cement	Cement	Cement	Cement
Sand	Sand	Sand	Sand
	20% SAK-10	20g (g or %) Localized K10	20% SAK-10 (No curing)

Table 2: Material composition of fabricated samples at 30% water content

Sample A	Sample B	Sample C	Sample D
Cement	Cement	Cement	Cement
	Sand	Sand	Sand
		20 % BIM	20% SAK-10

## 3D MicroCT imaging

A Zeiss Xradia 510 Versa - 3D X-Ray Microscope (3D XRM) was used to image each sample after the AE monitoring period. The Versa system maintains an in situ temperature of ~28°C.

Object Research Systems (ORS) Dragonfly Pro software was used to visualize and quantify the porosity and fracture network generated in the samples.

### **AE Monitoring**

Acoustic-emission (AE) measurements were made to monitor time-dependent crack formation in all samples. The samples were monitored using an array of six (6) Physical Acoustics Corporation transducers - F15 $\alpha$  sensors (with flat frequency response between 20-400kHz).

The sensors were connected via preamplifiers to a Mistra/Physical Acoustics AE measurement system with a 10MHz sampling frequency. The threshold amplitude was set at 27dB. To account for background noise, AE on an aluminum sample of similar dimensions was monitored alongside the geo-architected sample for the sample experimental time window. All transducers were secured to samples using hot Gorilla Glue. During monitoring, acoustic sensor transmission tests (AST) were also performed before and after active monitoring to determine the effect of drying and crack formation on compressional wave speeds. AST is a process by which the system allows the transducers to act as both a source and a receiver. The AST data provides velocities across the sample and between transducers, which are calculated from the respective arrival times.

## **3. RESULTS**

XRPD patterns revealed a shift in the inter-atomic distance of the clay structure. From a dried state to a swollen state, BIM clay exhibited an increase of  $7.62 \times 10^4$   $\mu\text{m}$  in the inter-atomic distance (d-spacing). Conversely, no significant change in the d-spacing was observed for the Sigma Aldrich – Montmorillonite K10 (SAK10) sample. The SAK10 clay under glycolated and oriented conditions had approximately the same d-spacing ( $9.73 \times 10^4 \mu\text{m}$ ) as the d-spacing for the SAK10 clay particles in the untreated state ( $10.12 \times 10^4 \mu\text{m}$ ). From SEM imaging, the structure of the Kaolinite (non-swelling) clays was stacked and platelet-like, while the structure of the Montmorillonite clays consisted of stacked undulating surfaces. Conversely the structure of the sand and the Ordinary Portland cement was prismatic and not stacked.

The microstructures of the synthetic rocks imaged after AE monitoring show that the porosity and fracture network increased with the addition of swelling clays. No microfractures are observed for the cement only or cement mortar samples. When the clay was localized, fractures are observed only within the clay region and the sample porosity increased because of debonding of the localized clay volume from the cement mortar host matrix. When 20% montmorillonite clay is added to a cement mortar mix, a large volume of microfractures are observed, with the SAK10 montmorillonite clay having a larger increase in porosity and a fracture network that expands towards the center of the core.

In Figure 1, the AE recorded for samples 1,2,3 and samples B, C, D (Tables 1 & 2) are shown. Geoarchitected rocks with 20% distributed clay (Figure 1.c) with a weaker host matrix generated

a large number of AE that spanned a frequency range of 50-300kHz, the events cluster into two groups. When the clay is localized, the same clustering behavior of AE is observed but fewer AE are detected (Figure 1.b). Fewer AE are recorded for a synthetic rock with the same sample mineralogy as sample 2 but 30% water content (Figure 1.f), and the clustering of AE is not as distinct. In Figure 1.e, for a synthetic rock of 20% unprocessed BIM and 30% water content, fewer AE are recorded than that of sample D (Figure 1.f). Lastly, for a synthetic rock with the same mineralogy as sample 1 (Figure 1.a) but a water content of 30% (Figure 1d), more AE are recorded with a broader frequency range.

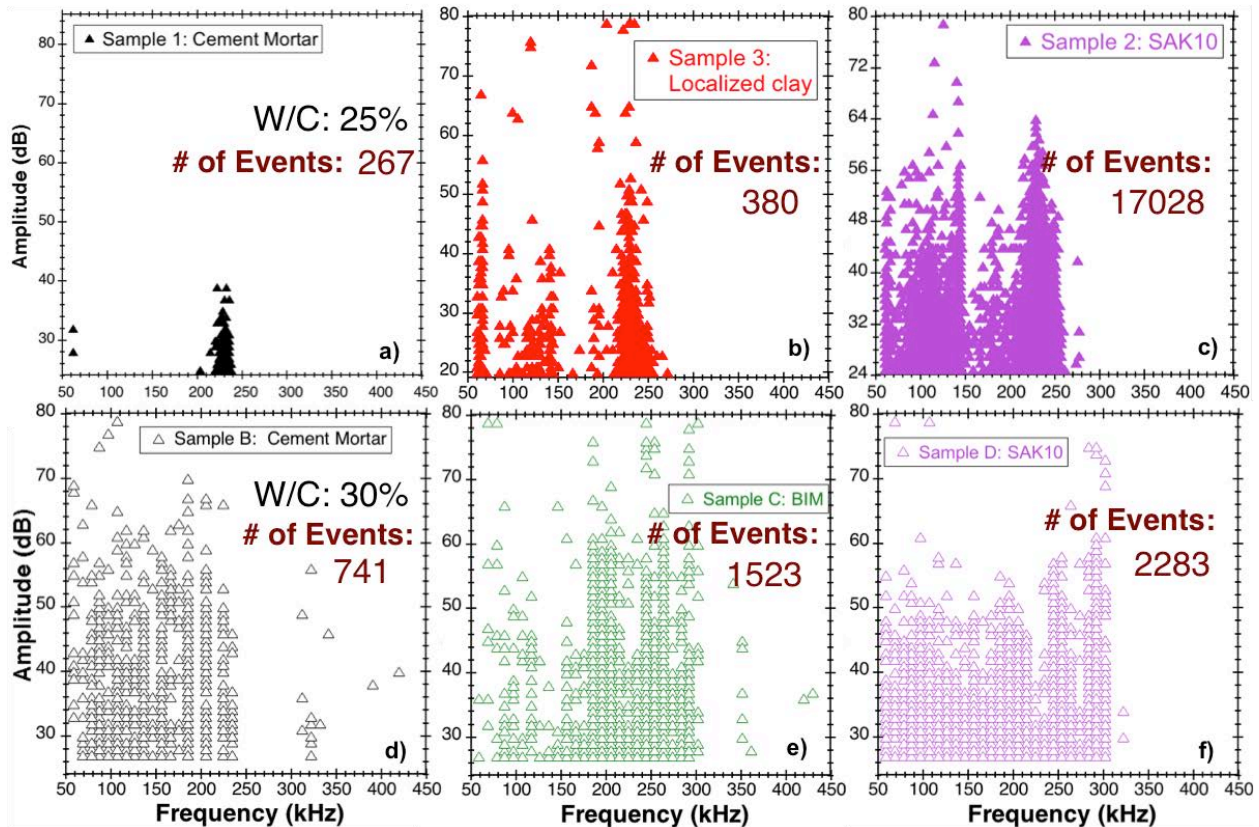


Figure 1: Peak Frequency (kHz.) vs. Amplitude for the recorded AE of samples (a)-(f)

#### 4. CONCLUSIONS

SEM of the materials used in this study, indicate that the Montmorillonite clay minerals have a much different structure from that of ordinary Portland cement, Sand, and Kaolinite. XRPD patterns revealed changes in the inter-atomic spacing of the Montmorillonite clays under different conditions. These geochemically induced local volumetric changes in swelling clays in synthetic rocks induced fractures and promoted fracture network growth during drying of a host matrix in an unpressurized system. The volumetric changes and the drying of the host-rock generated acoustic emissions that had distinct clustering by signal frequency that depended on the fabrication procedure or mineralogy. The presence of swelling clays in a rock promotes micro-cracking of the host matrix which were observed via 3D MicroCT of the structure after drying, and reflected by an uptick in number of recorded AE events which increased with

increasing clay content. When the clay was localized, the measured AE was also attributed to the de-bonding of the clay from the host rock matrix. AE observed in the samples with no clay are attributed to the movement of the drying front. Geo-architecting clay-rich rocks provide a unique opportunity to monitor the changes induced by the chemo-mechanical behavior of clays and analyze the effect on the microstructure. The chemo-mechanical behavior of clays has the potential to negatively impact the containment integrity of geological storage systems.

## 5. REFERENCES

- Downey, M.W. 1984. Evaluating seals for hydrocarbon accumulations. AAPG, Vol. 68. No. 11: 1752-1763.
- Espinoza, D.N. and J.C. Santamarina, 2012. Clay interaction with liquid and supercritical CO<sub>2</sub>: The relevance of electrical and capillary forces. *International Journal of Greenhouse Gas Control*, 10: 351-362.
- Griffith, C.A, D.A. Dzombak, and G.V. Lowry. 2011. Physical and chemical characteristics of potential seal strata in regions considered for demonstrating geological saline sequestration. *Environ Earth Sci.*, 64: 4,925 - 4,948.
- Mitchell, J.K. and K. Soga. 2005. *Fundamentals of Soil Behavior*, 3rd ed. Wiley.
- Sone, H. and M. D. Zoback. 2013. Mechanical properties of shale-gas reservoir rocks - Part 2: Ductile creep, brittle strength, and their relation to the elastic modulus. *Geophysics* 78: 5,393-402
- Sone H. and M.D. Zoback. 2014. Time-dependent deformation of shale gas reservoir rocks and its long term effect on the in situ state of stress. *International Journal of Rock Mechanics & Mining Sciences* 69: 120-132. Song J. and D. Zhang. 2013. Comprehensive Review of caprock-sealing mechanisms for geologic carbon sequestration, *Environ. Sci. Technol.*, 47: 9-22.
- Song J. and D. Zhang. 2013. Comprehensive Review of caprock-sealing mechanisms for geologic carbon sequestration, *Environ. Sci. Technol.*, 47: 9-22.
- Sposito, G. 1989. *The Chemistry of Soils*, Oxford University Press, New York. Espinoza, D.N. and J.C. Santamarina, 2012. Clay interaction with liquid and supercritical CO<sub>2</sub>: The relevance of electrical and capillary forces. *International Journal of Greenhouse Gas Control*, 10: 351-362.
- Wagner, J.F. 2013. Mechanical Properties of Clays and Clay Minerals, Ch. 9: pp. 347-381. *Developments in Clay Science*, vol. 5A

# Omnidirectional Horizontal Shear Wave Sensor for Enhanced Acoustic Emission Data Collection and Analysis

Jason Philtron<sup>a</sup>, Cody Borigo<sup>a</sup>, Steven Owens<sup>a</sup>, Ronnie K. Miller<sup>b</sup>, and Joseph L. Rose<sup>a</sup>

<sup>a</sup>Guidedwave, 450 Rolling Ridge Dr., Bellefonte, PA 16823;

<sup>b</sup>Independent AE Consultant

## ABSTRACT

A new, patent-pending, omnidirectional shear wave acoustic emission (AE) sensor has been developed. This sensor provides several advantages over conventional AE sensors, such as improved and simplified location analysis, reduced sensitivity to environmental noise, and increased options for source type identification and characterization. Additionally, the active piezoelectric element is also designed as an ultrasonic source, allowing use in emerging hybrid AE-guided wave passive/active test applications. Source localization is improved because threshold-based triggering can occur off of a single mode, the fundamental shear horizontal (SH) mode, with a single velocity: the shear wave velocity. The fundamental SH mode wave velocity is independent of test structure thickness or frequency, simplifying user input velocity during localization analysis and removing the need for user calibration. This is in contrast to conventional sensors, which detect multiple Lamb-type modes (e.g., S0 and A0) with different velocities that depend on frequency and test structure thickness, and where multimode content or inaccurate input velocity can generate significant error during location analysis. Reduced sensitivity to environmental noise is achieved because sources such as rain primarily excite Lamb-type modes with out-of-plane displacement content, and not SH-type waves. The shear sensor can be used alone or in tandem with conventional Lamb-type AE sensors for mode content identification. Identifying relative mode content of AE signals can be advantageous for source type identification, system development for new applications, and research purposes. Additionally, the shear sensors show promise for use during structural health monitoring applications where source characterization is desired in addition to accurate source location.

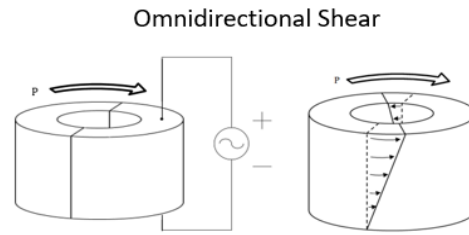
**Keywords:** shear, localization, characterization, sensors, environmental noise

## 1. INTRODUCTION

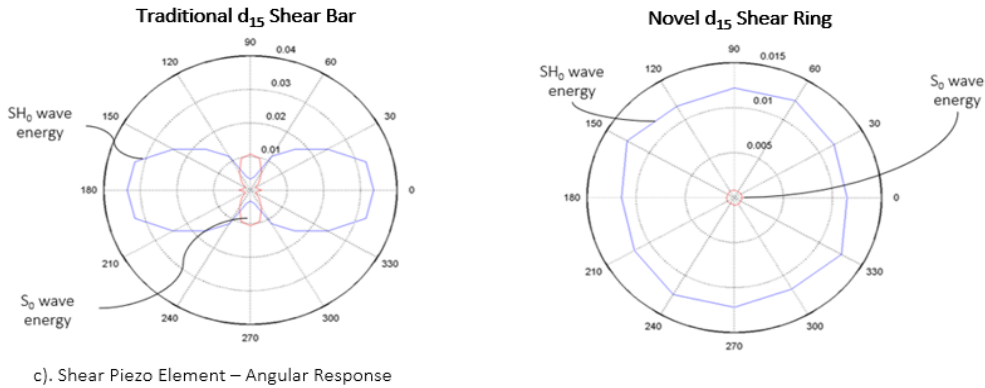
As the stress wave generated by an acoustic emission (AE) source travels to a receiver it travels as a guided wave (GW). For conventional AE sensors, a piezoelectric disk is often used which readily detects Lamb-type GWs. Historically it has been more challenging to fabricate shear-type guided waves sensors than Lamb-type guided wave sensors, and this is certainly true if omnidirectional sensing is desired. Previously, some shear sensors have been devised using wedges to convert wave types. Alternatively, highly-directional shear bars have been used to create shear sensitive sensors. Although these directional shear sensors can be used effectively for 1-D AE problems, such as along a single bar with transducers at each end, generally AE solutions require omnidirectional transducers. This omnidirectional characteristic is important for AE's adaptability for different structures and geometries, a key advantage that AE has over other nondestructive evaluation techniques. See Figure 1.



a.) An Omnidirectional Shear AE Sensor



b.) Piezoelectric Element Response



c). Shear Piezo Element – Angular Response

Figure 1. The Omnidirectional Shear Wave AE sensor characteristics

A new shear sensor has been developed that allows omnidirectional sensing of shear horizontal (SH) guided waves. The fundamental SH GW mode is non-dispersive, meaning that the wave velocity does not change with frequency or structure thickness. Additionally, the wave velocity of this mode is equal to the bulk shear wave velocity, so a look-up table can be used to assign the velocity for location calculations and pencil-lead break calibrations are not necessary.

This paper describes fundamental guided wave mode displacement characteristics and gives several examples showing the increase in location accuracy, precision, and ease of use with the shear sensors. An experiment with simulated rain is also conducted to demonstrate the robustness to environmental noise. A discussion follows on the use of this new sensor for source type classification.

## 2. GUIDED WAVE MODE DISPLACEMENT

### 2.1 Displacement wave structure

There are two types of guided wave modes that travel in plate structures: Lamb-type and SH-type. Lamb-type modes have displacement along the direction of wave propagation and out-of-plane through the thickness of the plate structure. At relatively low frequencies, the fundamental symmetric Lamb wave mode primary has displacement along the direction of wave propagation, and the fundamental antisymmetric Lamb wave mode primary has displacement out-of-plane through the thickness of the plate. As frequency and/or plate thickness is increased, the displacement characteristics of Lamb-type waves are generally mixed between these two directions. In contrast, SH-type modes have displacement perpendicular to wave propagation, in-plane with the plate structure as shown in Figure 2. Lamb type waves with dominant displacement in the x-z direction are those obtained with the traditional commercially available AE sensors for many years. The SH type waves with dominant displacement in the y direction is obtained with this new horizontal shear wave sensor presented in this paper.

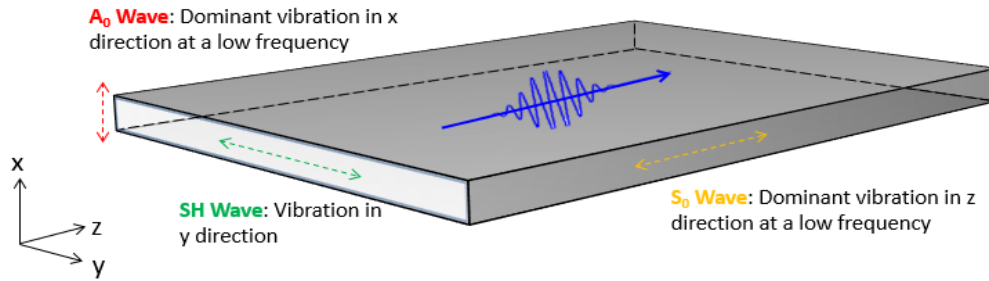


Figure 2. Generalized polarization of guided waves in plates. Lamb-type modes have displacements in the x- and z-directions, while SH-type waves have displacements in the y-direction.

## 2.2 Mode dispersion

It is necessary to view a dispersion curve to understand why the fundamental shear horizontal mode is ideal for AE location analysis. Figure 3 displays phase and group velocities for guided wave modes in an aluminum plate. As is shown, generally all modes are dispersive, i.e., the velocity changes as frequency and/or plate thickness changes. However, the one exception to this is the fundamental shear horizontal (SH0) mode, for which the velocity is independent of frequency or plate thickness. In addition, the velocity of the SH0 mode is equal to the bulk shear wave velocity of the material. Note also that this mode has the highest group velocity of all of the SH modes, meaning that it will always be the first arrival. Sensitivity to this mode is useful for accurate AE location analysis precisely because the velocity will not change for structures of the same material, but have different thicknesses or for which sensors with different frequency ranges are used. This is therefore no need for velocity calibration when setting up AE tests, and also the resultant location error from triggering off of multi-mode content is highly reduced.

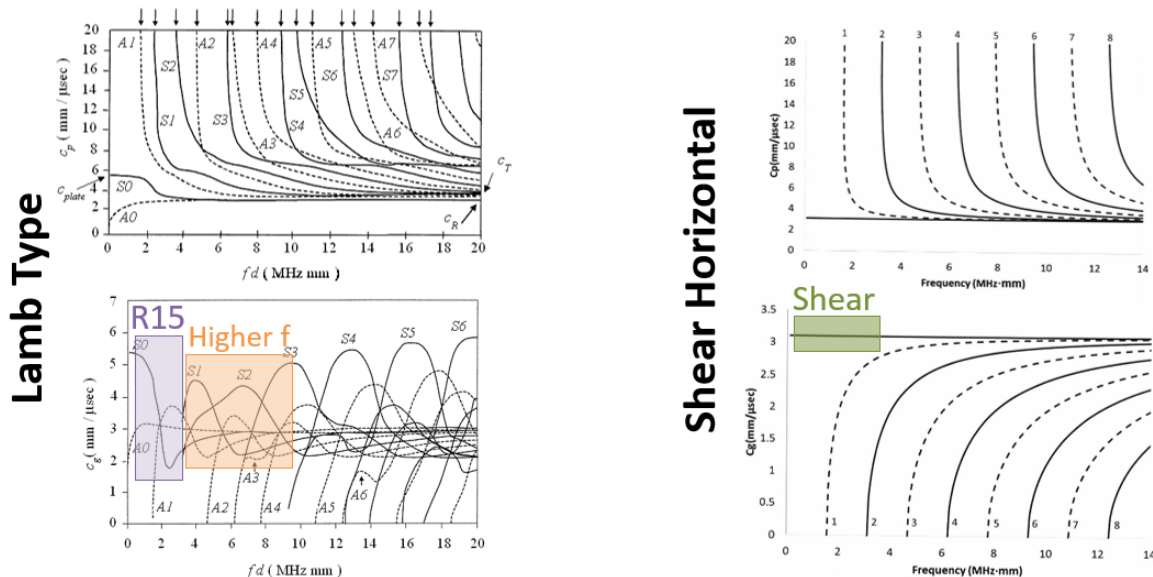


Figure 3. Phase (above) and group (below) velocity dispersion curves for Lamb-type (left) and SH-type (right) guided wave modes in an aluminum plate. Note that the fundamental SH mode (SH0) is the only mode which is nondispersive. After [1].

### 3. SAMPLE LOCATION DATA

#### 3.1 Description of sample location data

In this section, sample location data is presented for two steel pipes which have different thicknesses. The location performance achieved by conventional 150 kHz resonant sensors is compared to the new omnidirectional shear AE sensors. Data is presented for 250 kHz resonant shear AE sensors on an 8-inch diameter pipe and then 100 kHz resonant shear AE sensors on a 12-inch diameter pipe. In both cases, the shear AE sensors show improved location analysis, particularly in the case of simulated noise environment where the triggering threshold was raised from 40 dB to 50 dB. See Figure 4.

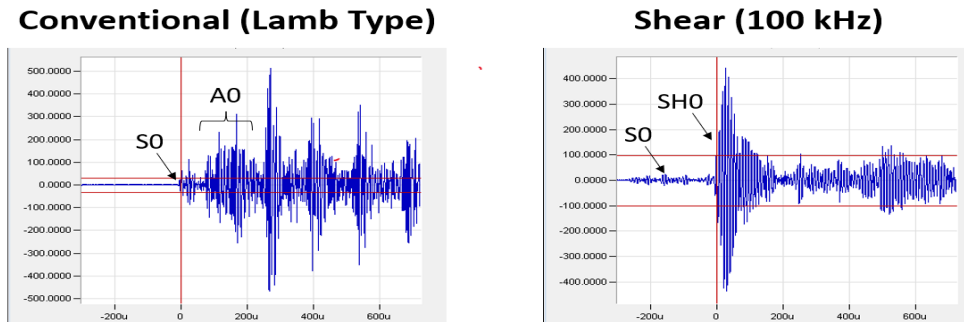


Figure 4. A sample result showing the sharp leading edge SH0 mode for accurate triggering in location analysis.

#### 3.2 Data from 8-inch schedule 40 steel pipe

Two conventional 150 kHz resonant AE sensors (Channels 1 & 2) and two new omnidirectional 250 kHz resonant shear AE sensors (Channels 3 & 4) were placed 10-ft apart on a section of 8-inch schedule 40 steel pipe (0.32-in thickness). Three pencil-lead breaks (PLBs) were conducted at the locations along the length of the pipe shown in Figure 5. The PLBs were conducted in small drilled holes in the pipe, because it is theorized to better simulate true AE events because the event happens within the structure instead of on the surface, and because it gives a more equal excitation of mode content between Lamb-type and SH-type modes than for surface-breaking PLBs.

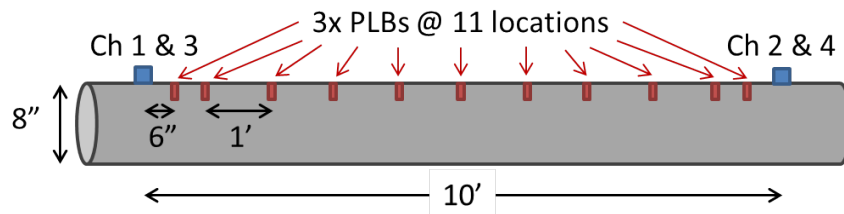


Figure 5. Schematic of location accuracy test setups on an 8-inch diameter steel pipe. Pencil lead breaks (PLBs) were conducted in drilled holes at the locations noted along the pipe length.

These PLBs were repeated with different threshold settings. First, a 50 dB threshold was used with the shear ring sensors, such that the software triggered off of the main arrival of the shear wave packet. This setup gives excellent results. Simultaneously, a 40 dB threshold was used with traditional type R15I sensors, which is the threshold level that would typically be used in low noise environments. This setup gives good to fair results. Finally, a separate set of PLBs was performed with a 50 dB threshold for the R15I sensors. The 50 dB threshold level simulates what might be used in a higher noise environment, such as when vibration noise from running machinery or

minor amounts of noise from environmental sources is present. A higher threshold is typically used to eliminate false damage calls due to noise. This setup results in a poor localization capability for the R15I sensors.

To visualize the amount of error in the location calculated for each PLB, histogram plots were created. Histograms display the number of data points (called counts) within successive fixed ranges (called bins). Figure 6 shows histograms of the error of each PLB for the three different sensor and setting configurations. Data points are plotted for each of the three PLB trials at each location (except in the case of the R15I sensor with a 50 dB threshold, where multiple PLBs failed to localize). The bin width is 0.5 inches, giving bins with the ranges: -0.25 to 0.25", 0.25 to 0.75", 0.75 to 1.25", etc. Bin labels are the value at the center of each bin, which are 0", 0.5", and 1" for the bins listed above.

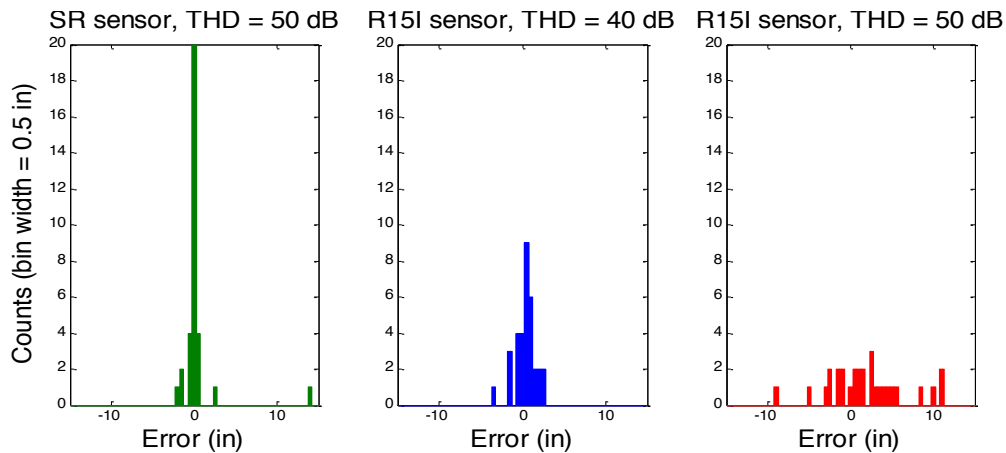


Figure 6. Histogram displaying 1-D location error data from tests on the 8-inch pipe. The number of counts is shown for 0.5 inch bins for the three test configurations: shear ring sensor with 50 dB threshold (left, green), conventional sensor with 40 dB threshold (center, blue), and conventional sensor with 50 dB threshold (right, red). The higher number of counts near 0 inches for the shear ring sensors indicates a more accurate (better) localization result.

### 3.3 Data from 12-inch schedule 40 steel pipe

Two conventional (Lamb-mode sensitive) 150 kHz resonant AE sensors (Channels 1 & 2) and two new omnidirectional 250 kHz resonant shear AE sensors (Channels 3 & 4) were placed 15-ft apart on a section of 8-inch schedule 40 steel pipe (0.41-in thickness). Three pencil-lead breaks (PLBs) were conducted at the locations along the length of the pipe shown in Figure 7. Location error data was processed in the same manner as for the 8-inch pipe, and is shown in Figure 8.

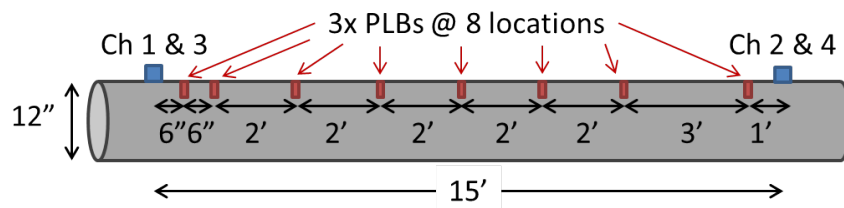


Figure 7. Schematic of location accuracy test setups on a 12-inch diameter steel pipe. Pencil lead breaks (PLBs) were conducted in drilled holes at the locations noted along the pipe length.

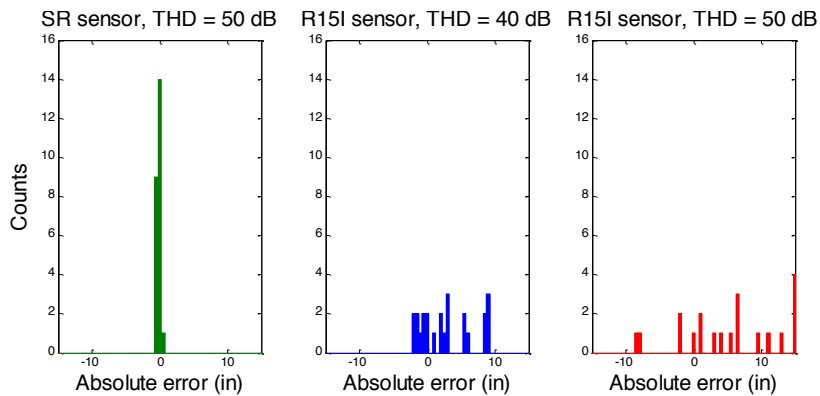


Figure 8. Histogram displaying data from location tests on the 12-inch pipe. The number of counts is shown for 0.5 inch bins for the three test configurations: shear ring sensor with 50 dB threshold (left, green), conventional sensor with 40 dB threshold (center, blue), and conventional sensor with 50 dB threshold (right, red). The higher number of counts near 0 inches for the shear ring sensors indicates a more accurate (better) localization result.

### 3.4 Data Analysis

To interpret the plots, consider two extremes. First, if the localization calculation had nearly zero error, all of the data points would be in the 0" bin and a single bar would be shown. This case is most like the shear ring data, which has the least amount of error, and in fact about two-thirds of the data points are in this bin for both pipe tests. Alternatively, if localization calculations were imperfect, and worked sometimes but were incorrect at other times, we would expect to have a variety of error values and data would be spread out into many different bins. This case is most like the conventional sensor with a 50 dB threshold, which has the most amount of error and only one data point is in the 0" bin for both pipe tests. The data from the conventional sensor with a 40 dB threshold is in between these two cases, with data packed generally closer to the 0" bin as opposed to being dispersed.

The data shown in the histograms in Figure 8 can be expressed numerically as well. The average (mean) absolute localization error for the shear ring sensor, 40 dB threshold traditional sensors, and 50 dB threshold traditional sensors in the 12 inch pipe test above are 0.26", 3.6", and 10.5", respectively. This metric succinctly describes the large amount of error that occurs for the conventional sensor.

It is clear that shear ring sensors show a distinct increase in localization accuracy when compared with conventional sensors, especially in a simulated noise environment, as represented by the 50 dB threshold example. Additionally, the shear ring sensors locate the PLBs very well on both pipe sizes, which have different thicknesses (0.32" and 0.41"). The conventional R15 sensors don't perform equally on both pipe sizes because the guided wave modes detected have velocities that change with the thickness of the pipe. In fact, velocities of modes detected using conventional AE sensors can range from 120,000 in/sec to 240,000 in/sec for carbon steel. PLBs must be performed by the user on each test structure in order to correctly pick the velocity to use with the conventional R15 sensor for a given detection threshold on that structure. This is in contrast with the shear ring sensors, which detect the shear horizontal guided wave mode; this mode always travels at the shear wave velocity (128,000 in/sec for carbon steel).

The advantage of using a constant velocity for location algorithms cannot be overstated. User definition of the wave velocity experimentally is a common cause of error and confusion in the setup and analysis of conventional AE sensors. This error would add additional error to the data

collected above and was not considered in the error comparison in this experiment. Additionally, in structures where the thickness changes from one point to another, conventional AE sensor source location will have difficulties while the shear ring sensors will not. Use of the shear-type mode was a key to commercial success in other guided wave applications, for example in long range pipeline inspection and phased array plate inspection, and its benefits are being realized for this application as well.

#### **4. ENVIRONMENTAL NOISE**

An experiment with simulated rain was also conducted to demonstrate the robustness to environmental noise. The sensor setup illustrated in Figure 5 was used and a garden hose was used to spray water onto the pipe in the region between the sensors to simulate moderate rain. The thresholds used were those that corresponded with highest location accuracy, which were 50 dB for the shear sensors and 40 dB for the conventional sensors. After 3 seconds of spray, 1328 hits were recorded by the conventional sensors and 0 hits were recorded by the shear sensors. This demonstrates the ability of the shear sensors to continue accurate location analysis for cases where noise from environmental or mechanical sources may be present. It can also be noted that the shear sensors did detect the water drop signals when the threshold was lowered considerably. The water drop signals detected by the shear sensors had amplitudes approximately 20 dB lower than for conventional sensors.

#### **5. SOURCE TYPE CLASSIFICATION**

The shear sensor also opens new opportunities for use in source classification and direct experimental measurement to further develop theoretical wave models. When used in conjunction with conventional sensors, all guided wave modes existing within the structure can be detected. This can allow for improved source classification, if information is known about the relative mode content generated by different types of sources (cracks of different orientations and severities, corrosion, fretting, etc.). Additionally, since the mode content from both Lamb-type and SH-type waves can be detected, validation of new theoretical models and finite element modeling results can be achieved.

#### **6. CONCLUDING REMARKS**

The new omnidirectional shear wave sensor has great potential for enhanced acoustic emission data collection and analysis. It is proposed to use this sensor in combination with the traditional Lamb-type sensor to achieve a number of possible strong benefits. A brief list of benefits follows. See Table 1.

Table 1. Potential benefits of using the Omnidirectional Horizontal Shear Wave Sensor for Improved Acoustic Emission data collection and analysis.

<ul style="list-style-type: none"><li>• Simple calibration and setup.</li></ul>
<ul style="list-style-type: none"><li>• Improved location analysis.</li></ul>
<ul style="list-style-type: none"><li>• Significant reduction in sensitivity to water loading and other environmental conditions.</li></ul>
<ul style="list-style-type: none"><li>• May find defects earlier or possible those not even seen by conventional Lamb-type AE probes.</li></ul>
<ul style="list-style-type: none"><li>• Source identification may be possible when used with conventional Lamb-type sensors (utilizing pattern recognition, machine learning, AI, in providing a substantially rich physically based feature vector).</li></ul>
<ul style="list-style-type: none"><li>• Sensor can be used in passive, then active mode for improved defect characterization.</li></ul>
<ul style="list-style-type: none"><li>• Greater possibility of using a variety of different and efficient multi-element, multi-mode, and frequency transducers.</li></ul>

## 7. REFERENCES

1. J.L. Rose, *Ultrasonic Guided Waves in Solid Media*, Cambridge University Press, Cambridge, UK, 2014.

# Characterization of Fiber Break by Quantitative Acoustic Emission in a Model Carbon/Epoxy Composite

Zeina Hamam<sup>a)</sup>, Nathalie Godin<sup>a)</sup>, Claudio Fusco<sup>a)</sup>, Thomas Monnier<sup>b)</sup>

a) Univ Lyon, INSA de Lyon, MATEIS UMR 5510, F-69621 Villeurbanne, France.

b) Univ Lyon, INSA-Lyon, LVA EA677, F-69621, Villeurbanne, France.

## ABSTRACT

In this work, a modelling approach in order to predict the characteristics of the AE signal due to fiber break is developed. For this purpose, we model AE using the Finite Element Method and we compare the simulation with experimental results of Single Fiber Fragmentation Test (SFFT). The SFFT enables to preferentially produce fiber break. It is carried out on dogbone-shaped specimens made from a long carbon fiber T700 embedded in an epoxy resin. In order to gather information on a wider frequency bandwidth, we use two different types of transducer. The analysis of the detected signals shows a strong dependency of the distance between transducer and source on the frequency content of the signals. In this case, the high frequency content of the signal associated to fiber breakage is not validated for every AE signature. For the numerical simulations, the entire geometry of the specimen is considered. We model the fiber breakage by separating the nodes belonging to the faces of the fracture. The numerical out-of-plane velocities are collected on the specimen surface. We consider six type of sensors, a point-contact sensor and five resonant sensors, whose transfer function were experimentally determined by the reciprocity method. After being validated, the FE model is used to investigate the effects of different parameters on the signal, such as the thickness of the specimen, the position of the fiber, the position of the failure, the nature of the matrix and the sensors response. The results of this contribution highlight the limitations of the conventional source identification procedures. Furthermore, the parametric study allows generating training data for machine learning algorithms. With the numerical approach, it may be possible to enlarge the training set with numerical signals.

**Keywords:** AE modelling, Fiber break, FE model, descriptors, sensors effect.

## 1. INTRODUCTION

The Acoustic Emission (AE) technique is widely used to detect failures in composite material. The different types of failures such as fiber breakage, interface debonding, matrix cracking and delamination are identified thanks to their AE signature [1-4]. In most of the studies dealing with failures in polymer matrix composites, higher frequency and higher amplitude are assigned to fiber breaks as mode of failure and lower frequency and amplitude are assigned to matrix cracking. Despite their effectiveness, these methods of analysis are still considered as qualitative methods. Besides, in many cases, the results of the analysis cannot be generalized to other studies of composite failure [5-7]. In fact, the AE signals depend not only on the type of failure but also on parameters like the type of sensor, geometry of the sample and the distance between source and sensor. All these parameters affect the signal recorded by AE system [8-10]. In this context, in various works, AE signals are calculated by analytical approaches or by finite element simulations [11-20] in order to understand the effects of transformations due to

propagation medium and the recording system. In this study, we focus on the identification of the features of fiber break from AE signals using Finite Element Method. For this purpose we use a model material consisting of an epoxy matrix containing a single brittle carbon fiber for our experimental tests and numerical simulations. The modeling of fiber breaks as AE source in polymer matrix composite material is the main objective of this work. In the experimental part, a Single Fiber Fragmentation Test (SFFT) is carried out on a carbon fiber embedded in the epoxy, in order to produce preferential fiber break. Two types of resonant sensors are used. Concerning the modeling part, the entire geometry of the specimen is modelled using Finite Elements Method (FEM) by means of Abaqus software and a dynamic calculation is performed. The fiber breaks are created in different positions on the specimen. The model has been validated by comparison with experimental data. Three type of sensors are considered (point-contact and resonant sensors) in order to understand and to quantify the sensor effects on the signal waveform.

## **2. EXPEREMENTAL PROCEDURE AND NUMERICAL MODEL**

### **2.1 Experimental procedure**

The specimen is made of a single long carbon fiber T700 embedded in epoxy/amine matrix. The dimensions of the specimen are shown in Figure 1. The SFFT is a tensile test applied on single fiber composite in the axial direction, in order to create fiber breakage. Usually the debonding occurs at the same time as the fiber breaks, but in our case, because of a high interfacial strength, debonding does not occur. The SFFT is carried out using the tensile test machine (type: MTS, capacity 5 kN), at room temperature and with a deformation rate of 0.5 mm/min.

The AE monitoring is carried out by means of multiple sensors using a PCI-2 data acquisition system. Tensile tests are performed with two kinds of sensors (nano 30 and PicoHF sensors) located at the same position on each face of the specimen 40 mm apart. These two sensors display a good sensitivity in different frequency ranges, 200 to 900 kHz for nano 30 sensor and 500-1850 kHz for Pico HF sensor (MISTRAS Group data). In all cases, medium viscosity vacuum grease is used as coupling agent. Each sensor is connected to a preamplifier (gain 40 dB, type 20 H) and AE signals are recorded by a PCI-2 acquisition system (MISTRAS Group). Each AE signal waveform is digitized and recorded, with a sampling rate of 2 MSPS or 5 MSPS. The acquisition threshold is set to 35 dB and the acquisition parameters are equal to 25  $\mu$ s, 50  $\mu$ s and 1000  $\mu$ s for the peak definition time (PDT), the hit definition time (HDT) and the hit lockout time (HLT). All recorded signals are filtered in the bandwidth [20 - 1200] kHz.

The analysis of the experimental results is based on the calculation of descriptors as defined in [1, 21]. In our work, the main descriptors analyzed are amplitude, energy, frequency centroid (FC) and peak frequency (PF). Moreover, the time frequency graphs are obtained according to smoothed pseudo Wigner-Ville distribution.

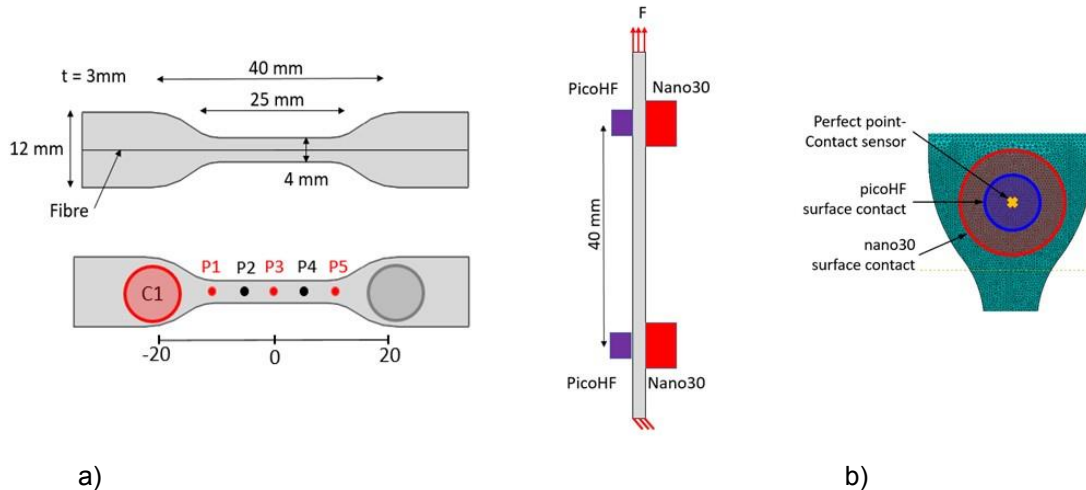


Figure 1: a) Specimen with sensors positions and fiber break positions ( $P_i$ ) for the simulation and b) surface of the sensors.

## 2.2 AE model

The single fiber fragmentation is modeled using FEM by means of Abaqus® software (6.14-5) with dynamic calculation. We modeled the entire geometry of the specimen. The geometry is meshed using tetrahedral elements (C3D4) mainly, the element size varies between 0.01 mm and 0.2 mm and the calculation step time is 0.1  $\mu$ s. The fiber is located in the middle of the specimen. Epoxy is modelled as an elastoplastic material with damping properties. The viscoelasticity of the matrix is taken into account by the Rayleigh parameters ( $\alpha = 50$  and  $\beta = 10^{-6}$ ). The fiber breakage is modelled by instantaneously separating the nodes forming fracture faces and creating a wave. During the modelling of AE signals, it was assumed that the failure process occurs without change in its rate. The numerical signals are collected on the specimen surface, at sensor positions. Three types of sensor are considered in the modeling part: one point-contact sensor and two resonant sensors. The first one is considered as perfect sensor, which accurately preserves the detected signal, namely the out-of-plane velocity calculated on the node corresponding to the sensor position (figure 1b). The resonant sensors are taken into account by their transfer function, which was experimentally determined in our laboratory by the reciprocity method [21-24]. First, we calculate the out-of-plane velocity corresponding to the sensor surface contact and then we convolute it with the sensor transfer function. Simulated signals are then filtered between 1 kHz and 1 MHz by a Butterworth bandpass filter, which is the frequency range of interest in AE.

## 3. RESULTS AND DISCUSSION

In this section, first we compare the experimental and numerical results in order to validate the FEM model. Five fiber breaks are modeled at five different positions (denoted  $P_i$ ) shown in the figure 1. Each break is simulated for 150  $\mu$ s, which is sufficient to attenuate the signal. We calculated signals with sensor effects for the two types of sensors (nano30 and picoHF). Then, the simulated and experimental signals are compared. This comparison is carried out for signals of five fiber breaks at different positions, collected at sensor C1 position (figure 2). A good agreement is observed between the simulation and the experiment results, allowing us to validate the FEM model.

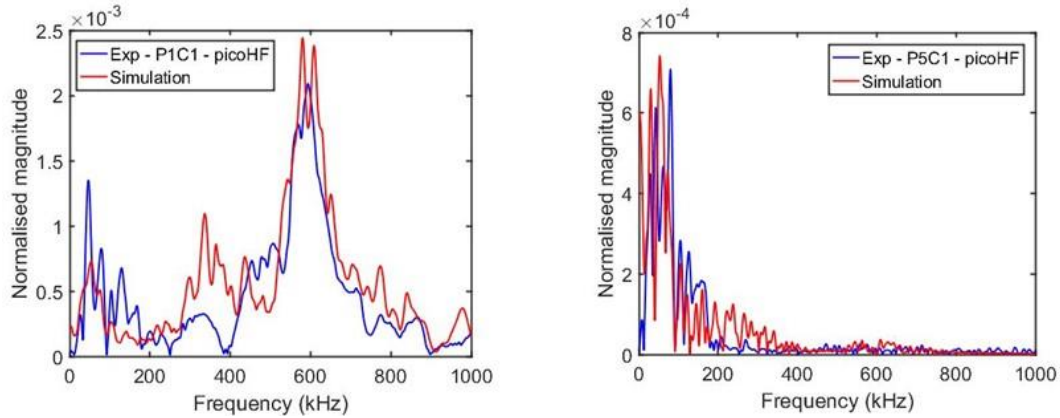


Figure 2 : Comparison between the simulated signal and the experimental signal due to a fiber break at two positions denoted P1 and P5 (P1 is the nearest position and P5 the farthest position from the sensor).

In the model, the signal detected by perfect point-contact sensor, is the out of plane velocity of the node at sensor position (Figure 1-b). The advantage of studying this kind of sensor is that the signal is not altered by the sensitivity of the sensor or its aperture effect of the surface contact. Figure 3 shows the time-frequency transforms for the several fiber breaks (P1 to P5). The frequency content of the signals is dominated by high frequency but it decreases farther away from the source.

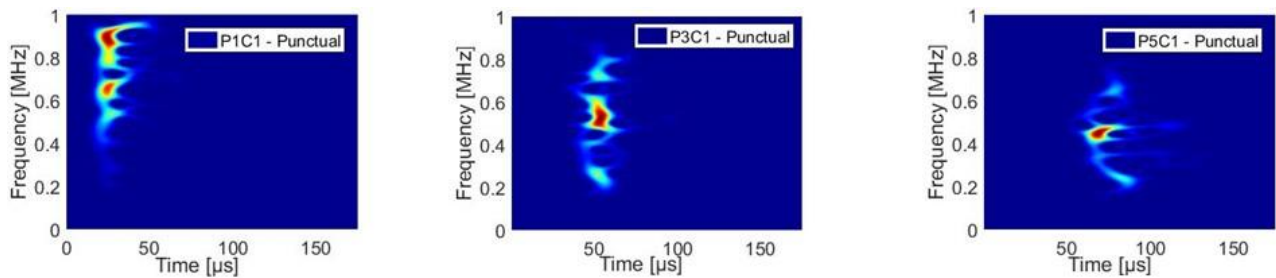


Figure 3 : Time-frequency results obtained with the pseudo Wigner-Ville distribution for three source positions for signals recorded by perfect point-contact sensor denoted punctual (P1 is the nearest position and P5 the farthest position from the sensor).

For one fiber break, signals are calculated at nodes on the line from the position P1 to the end of the specimen along the gauge length. It is equivalent to different sensor positions, therefore, different distance source / sensor. The use of 2D Fourier Transform (Figure 4) allows to visualize the modal content of propagating waves in the sample (figure 4a) and to visualize the effect of the sensors (figure 4b). For point-contact sensor, the frequency content is significantly higher comparing to signals detected by resonant sensors.

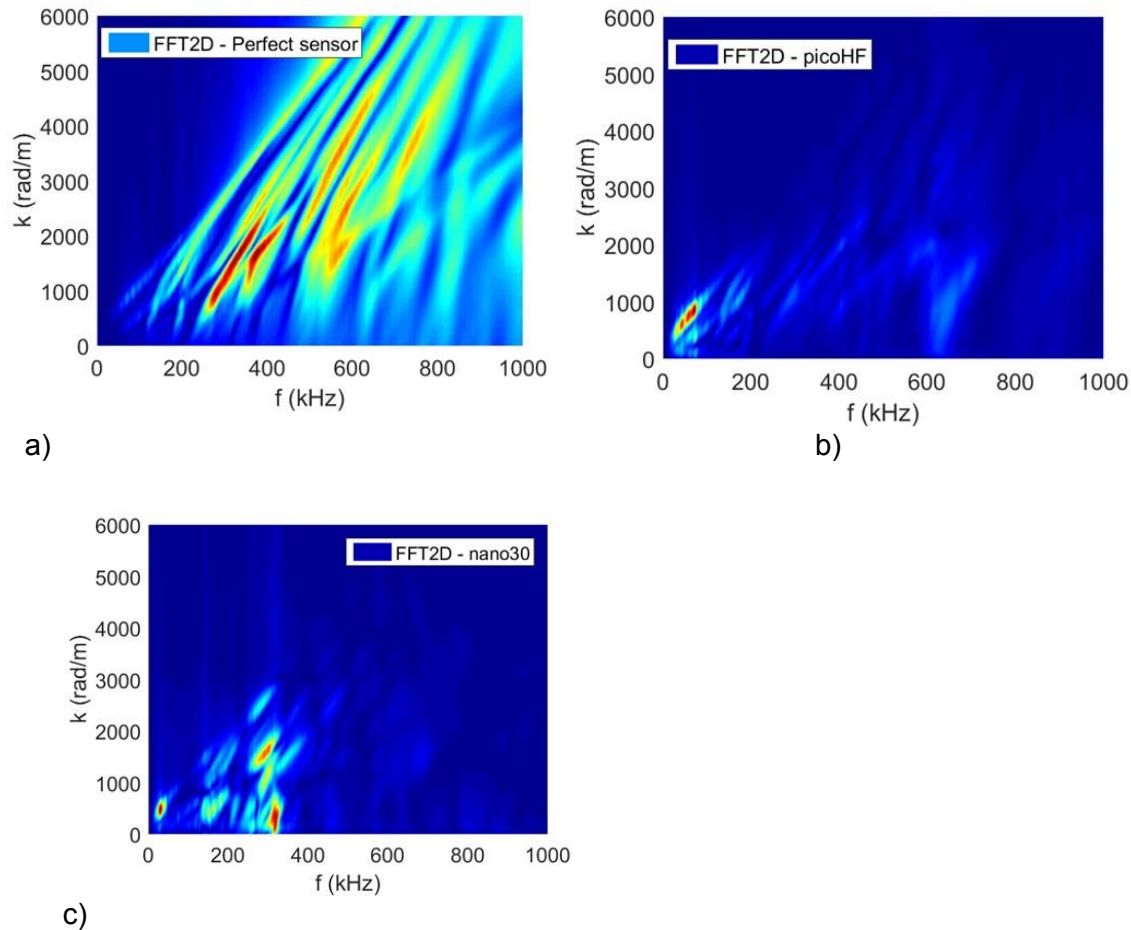


Figure 4 : 2DFFT (wavenumber  $k$  versus frequency  $f$ ) of the numerical signals obtained for the fiber break at position P1, with a perfect sensor (a) with a picoHF sensor (b) and with a nano30 sensor (c).

#### 4. CONCLUSION

The objective of this work is to build a quantitative relationship between the fiber break as source of Acoustic Emission and the detected signal by unravelling the effect of the different stages of the AE acquisition chain. The advantage of simulating perfect point-contact sensor is to get signals not altered by the sensor effects. Therefore, the frequency content proves that the fiber breaks release waves with very high frequency content in single fiber composite specimen. Contrary to signals recorded by cylindrical sensor, the frequency reached with this type of sensor, for remotes sources, is still considered as high frequency. The results of this contribution highlight the limitations of the conventional source identification procedures. Modeling approaches that simulate “primitive” AE sources can be useful for (1) optimizing sensor selection and placement, (2) quantifying the wave propagation effects (3) generate training data for machine learning algorithms. With the numerical approach, it may be possible to enlarge a training set.

#### 5. REFERENCES

[1] Godin N., Reynaud P. and Fantozzi G., Acoustic Emission and Durability of Composite Materials, John Wiley & Sons, 2018.

- [2] Anastassopoulos A. and Philippidis T., Clustering methodology for the evaluation of acoustic emission from composites, *Journal of Acoustic Emission*, vol. 13, pp. 11-12, 1995.
- [3] Sause M., In situ monitoring of fiber-reinforced composites: Theory, basic concepts, methods, and applications. Springer series in materials science 242, 2016.
- [4] Gutkin R., Green C., Vangrattanachai S., Pinho S., Robinson P. and Curtis P., on acoustic emission for failure investigation in CFRP: Pattern recognition and peak frequency analyses, *Mechanical Systems and Signal Processing*, vol. 25, n° 14, pp. 1393-1407, 2011.
- [5] Oz F. E., Ersoy N. and Lomov S. V., Do high frequency acoustic emission events always represent fibre failure in CFRP laminates?, *Composites Part A: Applied Science and Manufacturing*, vol. 103, pp. 230-235, 2017.
- [6] Maillat E., Morscher G. N., Pujar V. V. and Lemanski J. R., Feasibility and limitations of damage identification in composite materials using acoustic emission, *Composites Part A: Applied Science and Manufacturing*, vol. 75, pp. 77-83, 2015.
- [7] Godin N., Reynaud P., Fantozzi G., Challenges and limitations in the identification of acoustic emission signature of damage mechanisms in composites materials. *Appl. Sci.*, 8(8), 1267, 2018
- [8] Aggelis D., Shiotani T., Papacharalampopoulos A. and Polyzos D., The influence of propagation path on elastic waves as measured by acoustic emission parameters, *Structural Health Monitoring*, vol. 11, no. 3, pp. 359-366, 2011.
- [9] Carpinteri A., Lacidogna G., Accornero F., Mpalaskas A., Matikas T. and Aggelis D., Influence of damage in the acoustic emission parameters, *Cement and Concrete Composites*, vol. 44, pp. 9-16, 2013.
- [10] Kharrat M., Placet V., Ramasso E., and Boubakar L., Influence of damage accumulation under fatigue loading on the AE-based health assessment of composite material: Wave distortion and AE-features evolution as a function of damage level. *Composites Part A: Applied Science and Manufacturing*, 109, pp. 615-627, 2018
- [11] Scruby C., Wadley H. and Hill J., Dynamic elastic displacements at the surface of an elastic half-space due to defect sources, *Journal of Physics D-Applied Physics*, vol. 16, pp. 1069-1083, 1983.
- [12] Ohtsu M., Ono K, A generalized theory of acoustic emission and source representations of acoustic emission. *J. acoustic Emission* 1986; 5:124-133, 1986
- [13] Giordano M., Condelli L., Nicolais L., Acoustic emission wave propagation in a viscoelastic plate, *Composites Science and Technology* 59, 1735-1743, 1999.
- [14] Sause M.G.R. and Horn S., Simulation of acoustic emission in planar carbon fiber reinforced plastic specimens, *Journal of Nondestructive Evaluation*, 29 (2), 123-142, 2010.
- [15] Hamstad M., O'Gallagher A. and Gary J., Effects of lateral plate dimensions on acoustic emission signals from dipole sources, *Journal of Acoustic Emission*, vol. 19, pp. 258-274, 2001.
- [16] Wilcox P., Lee C., Scholey J., Friswell M. I., Wisnom M. and Drinkwater B., Progress Towards a Forward Model of the Complete Acoustic Emission Process, *Advanced Materials Research* , Vols. 13-14, pp. 69-76, 2006.
- [17] Cuadra J., Vanniamparambil P., Servansky D., Bartoli I. and Kontsos A., Acoustic emission source modeling using a data-driven approach, *Journal of Sound and Vibration*, vol. 341, pp. 222-236, 2015.
- [18] Prosser W.H., Hamstad M.A., Gary J. and O'Gallagher A., Finite Element and Plate Theory Modeling of Acoustic Emission Waveforms, *Journal of Nondestructive Evaluation*, 18 (3), 83-90, 1999.
- [19] Sause M. G. and Richler S., Finite element modelling of cracks as acoustic emission sources, *Journal of nondestructive evaluation*, vol. 34, no. 1, p. 4, 2015.
- [20] Le Gall T., Monnier T., Fusco C., Godin N. and Hebaz S.E. , Towards quantitative acoustic emission by finite element modelling : contribution of modal analysis and identification of pertinent descriptors, *Appl. Sci.*, 8(12), 2557; 2018
- [21] Morizet N., Godin N., Tang J., Maillat E., Fregonese M. and Normand B., Classification of acoustic emission signals using wavelets and Random Forests: Application to localized corrosion, *Mechanical Systems and Signal Processing*, vol. 70, pp. 1026-1037, 2016.
- [22] Ono K., Through-Transmission Characteristics of AE Sensor Couplants, *Journal of Acoustic Emission*, vol. 34, 2017.
- [23] Goujon L. and Baboux J.-C., Behaviour of acoustic emission sensors using broadband calibration techniques, *Measurement Science and Technology*, vol. 14, no. 7, p. 903, 2003.
- [24] Monnier T., Seydou D., Godin N. and Zhang F., Primary calibration of acoustic emission sensors by the method of reciprocity, theoretical and experimental considerations, *Journal of Acoustic Emission*, vol. 30, pp. 152-166, 2012.

# Damage Identification in Composites through Acoustic Emission Monitoring

Neha Chandarana<sup>a</sup>, Emmanuel Ramasso<sup>b</sup>, Constantinos Soutis<sup>c</sup>, Matthieu Gresil<sup>a</sup>

<sup>a</sup>i-Composites Lab, School of Materials, The University of Manchester, Manchester, UK;

<sup>b</sup>Department of Applied Mechanics, FEMTO-ST, Université Bourgogne Franche-Comté, Besançon, France; <sup>c</sup>Aerospace Research Institute, The University of Manchester, Manchester, UK.

## ABSTRACT

In this work, three carbon/glass hybrid composite tubes are instrumented with eight piezoelectric wafer active sensors (PWAS), used as passive receivers of acoustic emission (AE) signals. A three point bending quasi-static loading is conducted, either in a single cycle until failure or incrementally through multiple loading/unloading cycles. In the first instance, AE signal features such as maximum amplitude, peak frequency, signal duration, and energy are used to distinguish between different damage mechanisms such as matrix cracks, delamination, and fibre breakage. The group velocity of the longitudinal modes –  $L(0,1)$  and  $L(0,2)$  – is obtained experimentally in a pitch-catch configuration between the PWAS network using the time of flight (ToF). The time of arrival (ToA) method is then used to calculate damage source locations from the received AE signals. To involve more signal features for data classification, an unsupervised clustering algorithm is applied to the datasets. Optimisation of the number of clusters is completed by maximising the robustness and minimising the uncertainty of the final result. It is found that the temporal evolution of clusters indicate the ability to distinguish between the initiation and growth of damage, as well as identifying non-damage related signals caused by extraneous noise or related to the test set-up.

**Keywords:** Composites, normalised mutual information, pattern recognition, piezoelectric sensors, unsupervised clustering

## 1. INTRODUCTION

Composite materials have become attractive for use in structural applications over recent years, since their properties can be tailored according to needs, but assessment of damage remains a challenge. Periodic non-destructive inspections (NDI) of components can give an insight into their performance but the complexity of these techniques often results in significant down-time and increased labour costs. The cost of inspection in aerospace composites, for example, can represent up to a third of the lifecycle costs [1]. Since composite materials allow for the integration of sensors, with negligible effect on their mechanical properties, permanent structural health monitoring (SHM) systems have sparked a great deal of interest [1]. Piezoelectric transducers are particularly used for their low cost, small size, durability, and low power consumption [2].

In this work, quasi-static three point bending of carbon/glass hybrid composite tubes has been completed. By monitoring acoustic emission (AE) signals during loading, it is possible to estimate damage source locations and speculate about different damage modes [3], [4] via signal analysis. The effort is in distinguishing between matrix cracking, delamination, and fibre breakage. An

unsupervised pattern recognition algorithm – an extension of [5] – has been applied to AE data to understand the initiation and progression of damage when the data is separated into clusters.

## 2. MATERIALS AND METHODS

### 2.1 Instrumentation of composite tubes

The composite tubes (60.3 mm internal diameter and 1.6 mm thick) presented in this work are a hybrid of unidirectional (UD) carbon fibres oriented in the axial ( $0^\circ$ ) direction and UD glass fibres in the hoop ( $90^\circ$ ) direction (supplied by Easy Composites Ltd.). The lay-up order of fibers is [0, 90, 0, 90, 0]. Each specimen was cut to a length of 1 meter prior to instrumentation with sensors.

Three specimens were tested, each instrumented with piezoelectric wafer active sensors (PWAS) [6] supplied by PI ceramic – PIC255 with 10 mm diameter and 0.5 mm thickness [7]. Eight PWAS were surface mounted on each specimen for AE monitoring during loading. On specimen 1, 32 PWAS were also bonded for pitch-catch excitation of guided waves. The arrangement of PWAS is shown in Figure 1.

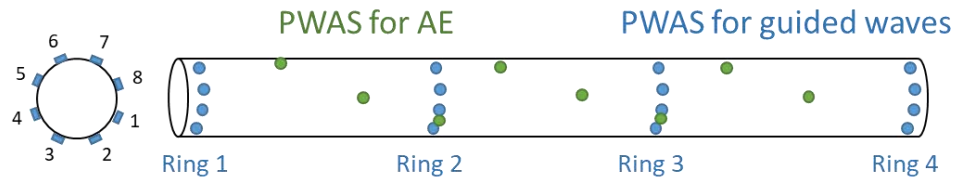


**Figure 1.** Schematic showing the approximate positions of PWAS used for AE (green) and guided waves (blue) on specimen 3.

### 2.2 Experimental set-up

The experimental set-up for flexural three point bending is shown in Figure 2. Three specimens were tested in total: specimen 1 was first subjected to a low velocity impact with approximately 5 J (resulting in an axial crack of approximately 7 cm length [8]), followed by three point bending over five cycles of loading/unloading; specimens 2 and 3 were subjected to bending until failure. The low frequency cycling of specimen 1 was introduced to encourage the progression of damage through repeated loading. The load vs. time curves are shown in Figure 3.

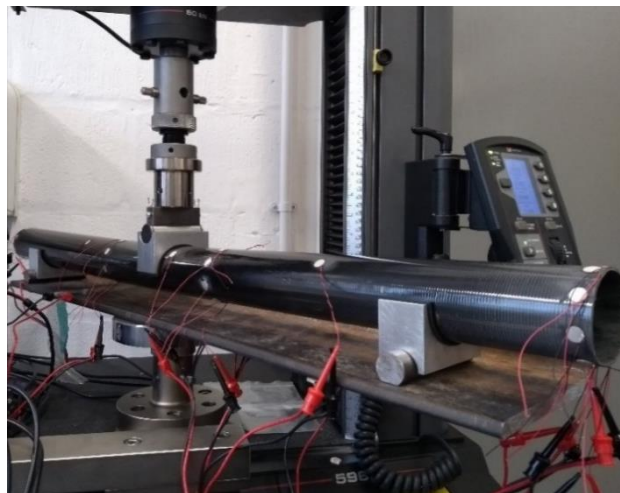


**Figure 2.** Experimental set-up for three point loading of specimen 1.

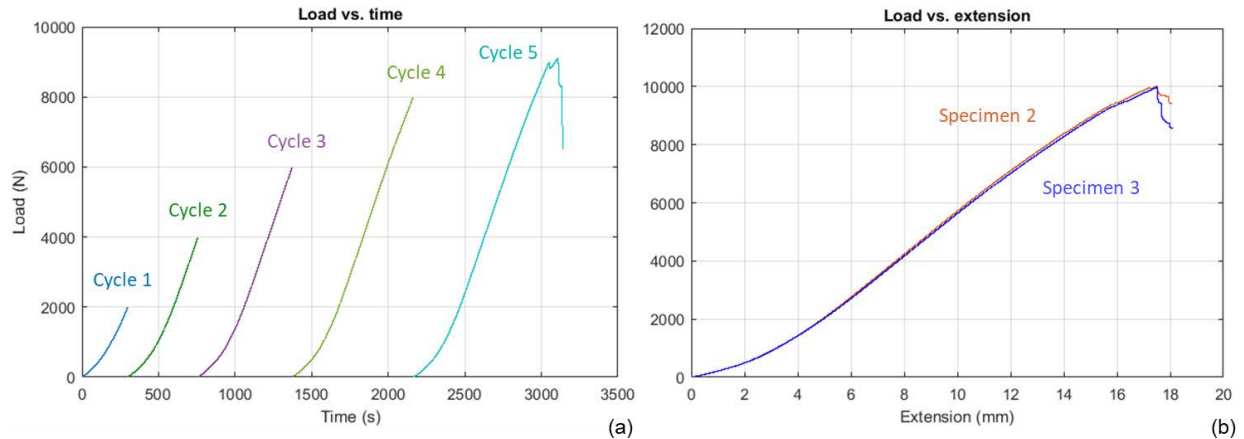


**Figure 3.** (a) Load vs. time for all cycles on specimen 3; (b) Load vs. extension for specimens 2 and 3.

### 2.3 AE data acquisition and processing

During loading, AE activity was recorded via eight channels on a PCI-2 based acquisition system supplied by Mistras. Discrete AE waveforms (hits) were recorded using the 'AEwin' software package. The threshold amplitude was set to 55 dB to eliminate sources of extraneous noise, and to account for the 20 dB of pre-amplifier gain per channel. The sampling rate was set at 10 MHz (5 MHz on 2 channels due to hardware limitation) and AE timing parameters set to: peak definition time (PDT) = 200  $\mu$ s, hit definition time (HDT) = 800  $\mu$ s, hit lockout time (HLT) = 1 ms, maximum signal duration = 100 ms. Using subsets of 4 from a total of 17 features (as extracted through 'AEwin') per AE hit an unsupervised pattern recognition algorithm (based on the Gustafson-Kessel algorithm [9]) was applied to the full dataset for each specimen. For specimen 1, the five cycles are concatenated in time to form one large dataset. The optimal number of clusters for each dataset is found by maximizing the normalized mutual information criterion (NMI) [10].

## 3. RESULTS AND DISCUSSION

The time of arrival (ToA) method available within 'AEwin' is used to calculate AE source locations in order to track the growth of damage in the specimens during each loading cycle of specimen 1 (Figure 4). The presence of signals during earlier cycles of loading correlates well with the damage locations observed in the final cycle of loading, suggesting that it may be possible to estimate the failure location before reaching 70% of the breaking strength of the specimen.

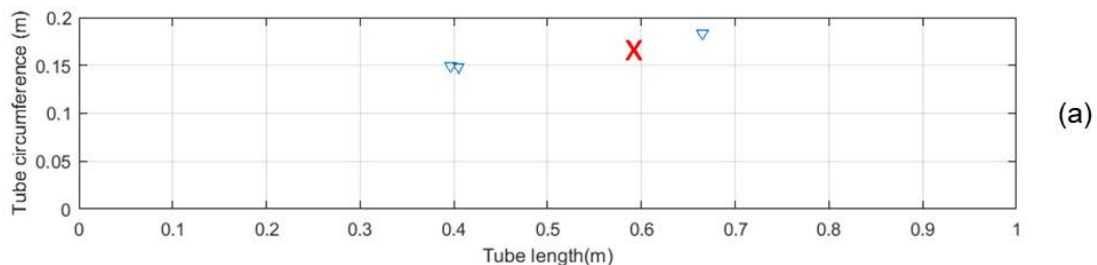


**Figure 4 (to be continued).** Calculated damage locations during each loading of specimen 1: (a) cycle 1 (blue  $\nabla$ ), (b) cycle 2 (green  $\wedge$ ), (c) cycle 3 (purple  $>$ ), (d) cycle 4 (lime green  $<$ ), (e) cycle 5 (turquoise  $\square$ ).

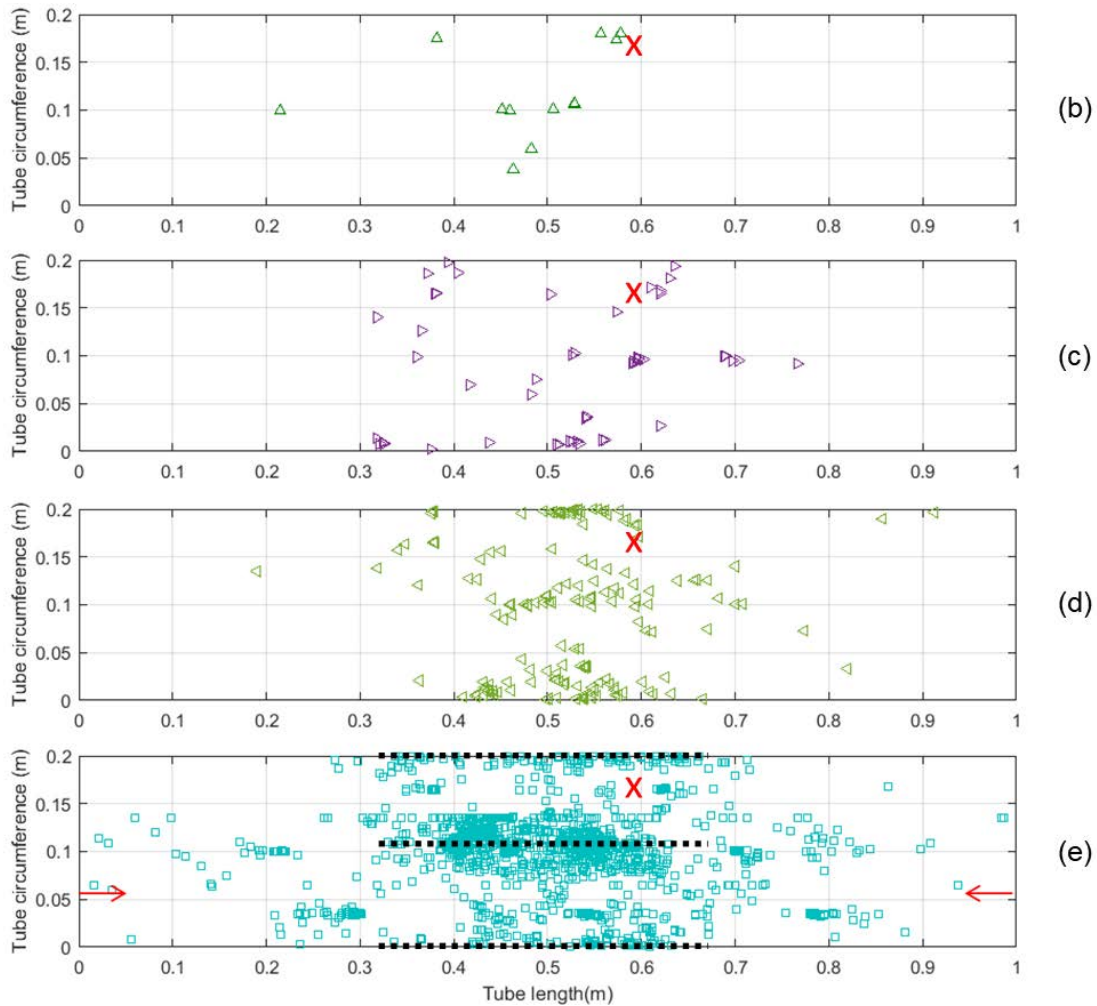


**Figure 4.** Estimated damage locations during loading of specimen 1: (a) cycle 1 (blue v), (b) cycle 2 (green ^), (c) cycle 3 (purple >), (d) cycle 4 (lime green <), (e) cycle 5 (turquoise □). Dashed lines indicate locations of the through-thickness final failure cracks. Red arrows indicate the top of the specimen.

Application of the unsupervised clustering algorithm on AE hits from specimen 1 results in separation of the data into 9 clusters. The initiation and evolution of signals within each cluster, over the five cycles of loading are shown in Figure 5. A noteworthy observation is that, though the data are separated into these 9 clusters, all clusters do not initiate at the beginning. In the present work, a criterion related to the onset time of different clusters ensures that they are always spread out in time. The reasoning being that damage in composites tends to be decomposed into different phases with cascades during loading. Based on this, it is possible to develop a classification of damage types, for each cluster. It is argued that AE data belonging to cluster 1 are likely to arise due to friction between the specimen and test equipment: this cluster represents the largest group of data points, and data are acquired almost continuously during loading. Similarly, the data in clusters 2 and 3 does not result in a significant change in cumulated energy. AE data belonging to clusters 8 and 9 are more likely related to the final failure of the specimen: an abrupt increase in energy is observed, indicating high energy, catastrophic damage events during these last few seconds of loading. The final failure of the specimen took the form of two longitudinal cracks on either side of the tube – a compression-type failure rather than true bending. This is due to the high proportion of axial fibres greatly enhancing the flexural stiffness of the tube. Clusters 4-7,

therefore, likely represent damage signals arising from a combination of mechanisms such as delamination, axial matrix cracking, and breakage of the hoop-oriented glass fibrils and/or fibres.

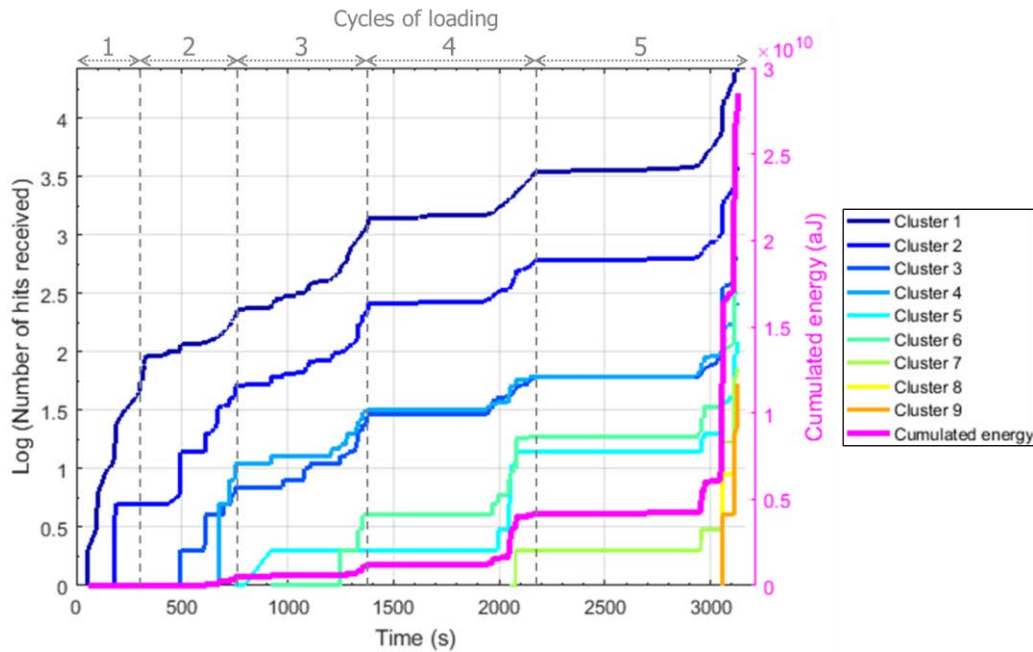


**Figure 5.** Number of AE hits recorded by all channels, separated into clusters, for specimen 3.

When the clustering algorithm is applied to specimens 2 and 3, both tested in a single cycle until failure, the data is separated into 8 and 15 clusters, respectively. The behaviour of clusters in these two specimens is shown in Figure 6. Although the specimens are assumed to be almost identical, the AE signals recorded during loading can be affected by small variations in: material properties, specimen geometry, sensor placement, sensor bonding, positioning with respect to the machine, and noise in the environment. Number of clusters aside, the most obvious difference when comparing the plots is the behaviour of clusters 2 and 4 on specimen 2. The exponential increase in signals at around 400 s likely result from extraneous noise since the change in cumulated energy is negligible. The envelope of each damage profile provides an assessment of uncertainty related to the final clustering result.

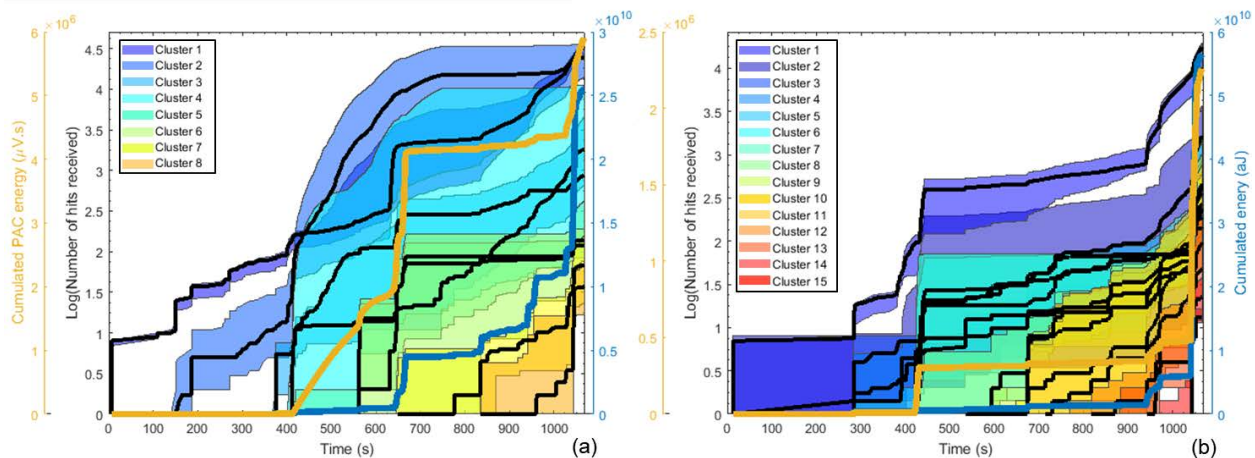


**Figure 6.** AE hits from all channels separated into clusters for (a) specimen 2 and (b) specimen 3.

#### 4. CONCLUDING REMARKS

In the present work, the potential for the use of acoustic emission is demonstrated as a tool for detecting, localising, and classifying damage mechanisms arising during quasi-static loading. The use of an unsupervised clustering algorithm eliminates any operator bias and reduces the time taken to obtain a final result. Further work is required to develop a means of linking data clusters to individual damage modes in the composite, by means of destructive and non-destructive validation via, for example, x-ray computed tomography. Identifying the location, size and type of damage is of great importance in the effort to estimate residual life and long term performance of the composite tube [11].

#### 5. ACKNOWLEDGEMENTS

The authors acknowledge the funding and technical support from BP through the BP International Centre for Advanced Materials (BP-ICAM) and financial support from EPSRC (EP/L01680X) through the Materials for Demanding Environments Centre for Doctoral Training which made this research possible. The authors also acknowledge the EIPHI Graduate School (contract "ANR-17-EURE-0002" and FEMTO-ST Institute for both funding and technical input to support the collaboration with The University of Manchester.

#### 6. REFERENCES

- [1] K. Diamanti and C. Soutis, "Structural health monitoring techniques for aircraft composite structures," *Prog. Aerosp. Sci.*, vol. 46, no. 8, pp. 342–352, 2010.
- [2] N. Chandarana, D. M. Sanchez, C. Soutis, and M. Gresil, "Early damage detection in composites during fabrication and mechanical testing," *Materials (Basel)*, vol. 10, no. 7, 2017.
- [3] N. Godin, S. Huguet, and R. Gaertner, "Integration of the Kohonen's self-organising map and k-means algorithm for the segmentation of the AE data collected during tensile tests on cross-ply composites," *NDT E Int.*, vol. 38, no. 4, pp. 299–309, 2005.
- [4] G. Kotsikos, J. T. Evans, A. G. Gibson, and J. Hale, "Use of acoustic emission to characterize corrosion fatigue damage accumulation in glass fiber reinforced polyester laminates," *Polym. Compos.*, vol. 20, no. 5, pp. 689–696, 1999.
- [5] E. Ramasso, V. Placet, and M. L. Boubakar, "Unsupervised Consensus Clustering of Acoustic Emission Time-Series for Robust Damage Sequence Estimation in Composites," *IEEE Trans. Instrum. Meas.*, vol. 64, no. 12, pp. 3297–3307, 2015.
- [6] V. Giurgiutiu, *Structural Health Monitoring with Piezoelectric Wafer Active Sensors*, 1st ed. Academic Press, 2008.
- [7] PI Ceramic, "Piezoelectric Ceramic Products." [Online]. Available: [http://www.piceramic.com/download/PI\\_Piezoelectric\\_Ceramic\\_Products\\_CAT125E.pdf](http://www.piceramic.com/download/PI_Piezoelectric_Ceramic_Products_CAT125E.pdf).
- [8] N. Chandarana, H. Lansiaux, and M. Gresil, "Characterisation of Damaged Tubular Composites by Acoustic Emission, Thermal Diffusivity Mapping and TSR-RGB Projection Technique," *Appl. Compos. Mater.*, vol. 24, no. 2, pp. 525–551, 2017.
- [9] D. E. Gustafson and W. C. Kessel, "Fuzzy clustering with a fuzzy covariance matrix," *Proc. IEEE Conf. Decis. Control*, pp. 761–766, 1979.
- [10] A. L. N. Fred and A. K. Jain, "Combining multiple clusterings using evidence accumulation," *IEEE Trans. Pattern Anal. Mach. Intell.*, vol. 27, no. 6, pp. 835–850, 2005.
- [11] C. Soutis and P. W. R. Beaumont, Eds., *Multi-scale modelling of composite materials: the art of predictive damage modelling*, 1st ed. Cambridge: Elsevier, 2005.

# Overview of Acoustic Emission in Monitoring Powder Technology

Eric Serris, Ana Cameirao, Frédéric Gruy, Jean-Michel Herri, Gérard Thomas  
Mines Saint-Etienne, SPIN EMSE, CNRS UMR 5307, LGF, CS 62362,  
F-42023 St Etienne, France

## ABSTRACT

Acoustic emission has been successfully applied for monitoring a large variety of industrial processes. In this overview of several studies of application of acoustic emission in powder technology, we try to develop this non-destructive technique in some processes with powder. Acoustic emission during powder compaction allows us to understand the behavior of brittle materials and quantify the fragmentation of such powders. With viscoelastic powder, the compaction is different and we recorded weak acoustic emission. For crystallization processes, we have an information of the beginning of nucleation of crystals before all other experimental on-line techniques. We can have also other information of crystal growth, crystal size and if we have re-dissolution of the product. Another process with powder is a slurry transport in a flow loop. The first experiments show also the first moments of crystallization but we can have also information of flow pattern of the slurry and the former emulsion state. To finish, we will discuss on a beginning fundamental work on acoustic emission of particle impact on several surfaces. This work will help us to better characterize all these processes with powders.

**Keywords:** monitoring, flow loop, crystallization, powder, compaction

## 1. INTRODUCTION

We show that acoustic emission (AE) is a very attractive non-intrusive technique for monitoring crystallization processes. AE has been successfully applied in many fields of material sciences [1] and it was also used in the pharmaceutical industry for monitoring various chemical engineering processes [2] including fluidized bed granulation [3], fluidized bed coating [4], powder compaction [5-6], etc. However, few studies deal with the use of AE to monitoring crystallization processes [7-11]. In this paper, we will give an overview of acoustic emission use in several processes in powder technology.

## 2. EXPERIMENTAL RESULTS

### 2.1 Compaction of powders

All acoustic emission is recorded with a  $\mu 30$  sensor from Mistras group with no filter in frequency. The sensor is fixed with coupling grease on the wall of the die. Aspirin AC 360 is a crystallized aspirin provided by Rhône Poulenc Rorer. The granulometry of grains is  $360 \mu\text{m}$  and the grains look like sticks. AE tests are realized following the same compaction procedure. The pressure rising up to  $300 \text{ MPa}$  is achieved with a punch velocity of  $1 \text{ mm min}^{-1}$ . This pressure is held for  $1 \text{ min}$ , then a pressure-drop followed with a punch velocity of  $10 \text{ mm min}^{-1}$ . The results are represented in Figure 1 with the curve of cumulative event counts as a function of axial stress. Two sections are evident on the curve variations: before and after an axial stress of  $100 \text{ MPa}$  [6].

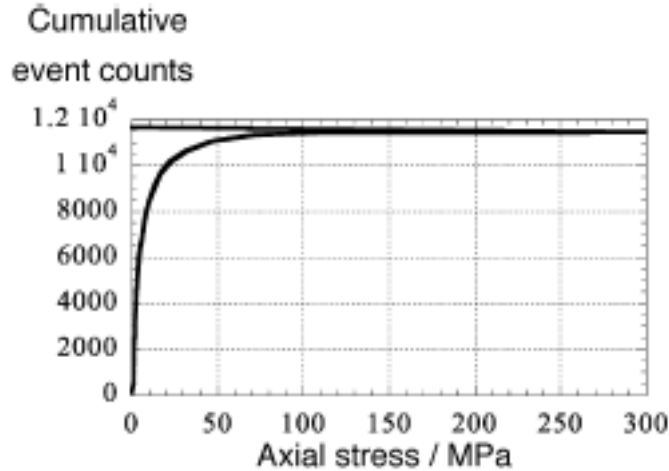


Figure 1 : Cumulative event counts vs. axial stress for aspirin AC 360.

Before 100 MPa, high AE rates were recorded, and a lot of bursts can be observed on the oscilloscope screen. After 100 up to 300 MPa, no AE is recorded. AE is also undetectable during the isobaric stage duration of 1 min, but not during pressure drop.

Specific surface area and porosity have been determined on tablet obtained for various values of maximal axial stress (punch velocity of 1 mm min<sup>-1</sup> up to maximum stress, 1-min duration isobaric step and 10 mm min<sup>-1</sup> pressure drop). Figure 2 presents the results obtained concerning specific surface area.

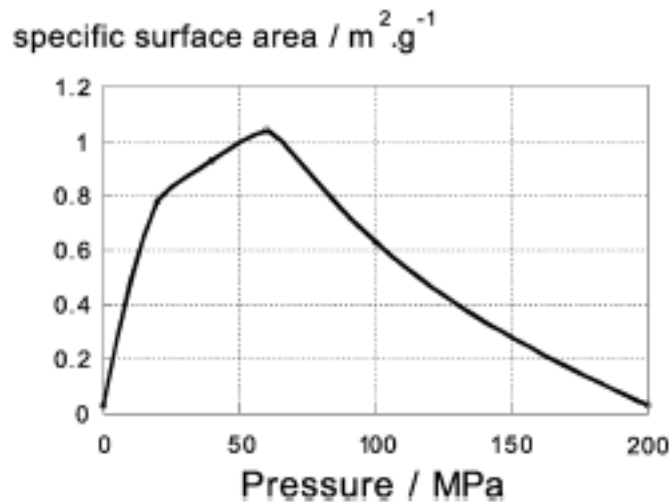


Figure 2 : Specific surface area of aspirin AC 360 vs. compaction pressure.

The specific area first increases up to 60 MPa, then it decreases. The only phenomenon that may lead to a specific area increase is grain fragmentation. Thus, we can relate this fact to the AE registered during the same time. We have to keep in mind that intergranular or intragranular cracking may occur during compact ejection and, as a consequence, may induce errors in specific area measurements. Nevertheless, we assume that these phenomena do not occur for the pharmaceutical products used in this work, as suggested by direct observations. Figure 3 presents the results obtained concerning relaxed porosity. The porosity decreases continuously during the rise of compaction pressure, but very strongly during the first stage up to 100 MPa. We

consider that plastic and viscoplastic deformations are responsible for this porosity drop. This deformation is also responsible for the specific area diminution after a compaction pressure of 60 MPa by the way of an interface grain cling. Thus, for the studied aspirin, this deformation may occur, but it is not detected by AE.

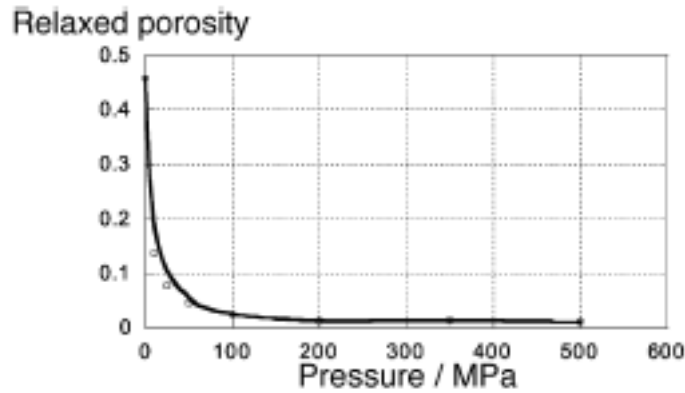


Figure 3: Relaxed porosity of aspirin AC 360 vs. compaction pressure.

As for the aspirin AC 360, we can conclude that grain fragmentation and rearrangement are characterized by AE emitted during compaction. This AE is represented by several bursts on the oscilloscope screen and by increasing rates of cumulative event counts. Furthermore, viscoplastic deformation of aspirin grains is not followed by any noticeable AE.

### 2.2 Crystallization of powders

Two sensors: a WD and a F15 provided by Mistras whose center frequency are respectively of 450 kHz and 150 kHz are used in this work [12]. They are fixed directly on the vessel with coupling grease.

The first experiment on citric acid is recorded after dissolving a large amount of powder (2 kg) in 1 L of pure water. We show the evolution of AE amplitude during three hours after the introduction of 500 g of citric acid in order to reach a supersaturated state. This evolution is plotted in Figure 4. Two periods (from 0 to 1000 s and from 5000 to 6000 s) of acoustic activity is observed. The first one is the dissolution and the particles impacts of the powders. The other one is not obvious. Normally nothing changes during this period of dissolution.

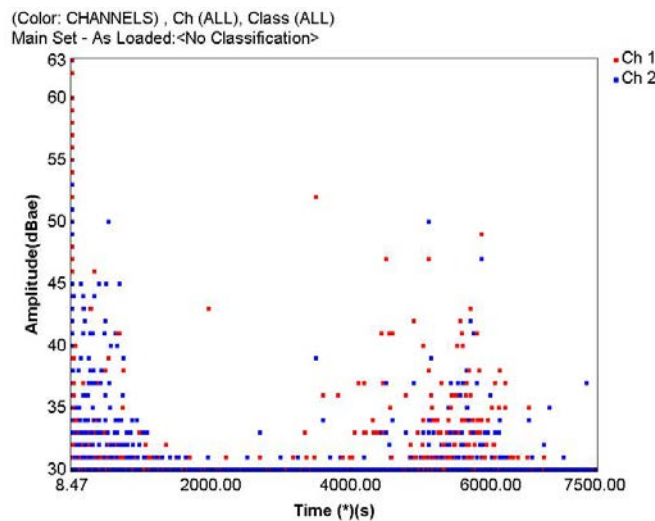


Figure 4 : Amplitude of AE (dB) versus time(s).

In order to have an idea of what may happen during this period, let's have a look on the evolution of centroid frequency versus time.

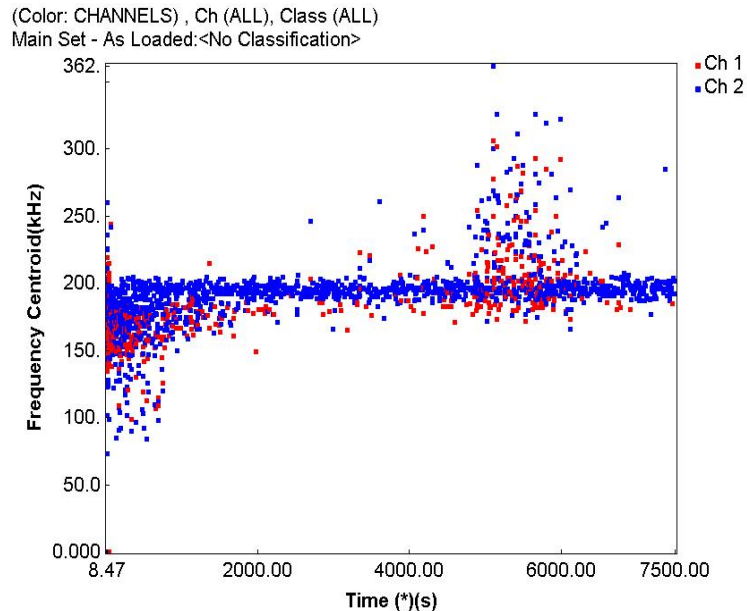


Figure 5 : Centroid frequency (kHz) versus time (s).

The centroid frequency of dissolution phenomena is generally under 200 kHz but for the second part of AE activity the frequency is above 200 kHz. In oxalate ammonium crystallization in Gherras work [11], it is generally near 250 kHz for nucleation and/or growth of particles. Considering that we are above the supersaturation stage, we have a crystallization of citric acid during this period.

### 2.3 Monitoring flow loop during hydrates formation

The acoustic emission sensor (Mistras, R15) was located at the beginning of the flow loop horizontal section. Coupling grease was used between the loop wall and the sensor for improving the transmitting efficiency of acoustic signals. The main experimental results are the acoustic energy together with the pressure drop and the cumulated chord length for droplets, crystallized droplets and agglomerates. Results are given in Figure 6.

Before the formation of hydrates, experiments show a regular oscillation in the absolute energy characteristic of the state of the dispersion of the droplets in the continuous phase, corresponding to a polydispersity population of droplets around 10  $\mu\text{m}$ . When methane was injected, the absolute energy increased and return to the initial level before the beginning of crystallization. The high transfer of gas into the oil phase seems to affect the attenuation of the signal in case of continuous oil phase. The R15 sensor detected the beginning of crystallization by a steep AE event increase. Even if some oscillations are observed, the tendency of the results is to increase and remain approximately constant until the end of the experiment. The absolute energy seems mainly correlated with the amount of hydrates and the size of the particles/agglomerates, and lesser but still correlated with the continuous phase.

The AE sensor proved to be envisaged to measure the hydrates fraction along the pipe and also to detect changes in the state of the liquid-liquid dispersion together with the solid, during emulsification and crystallization and even plug and rheological study.

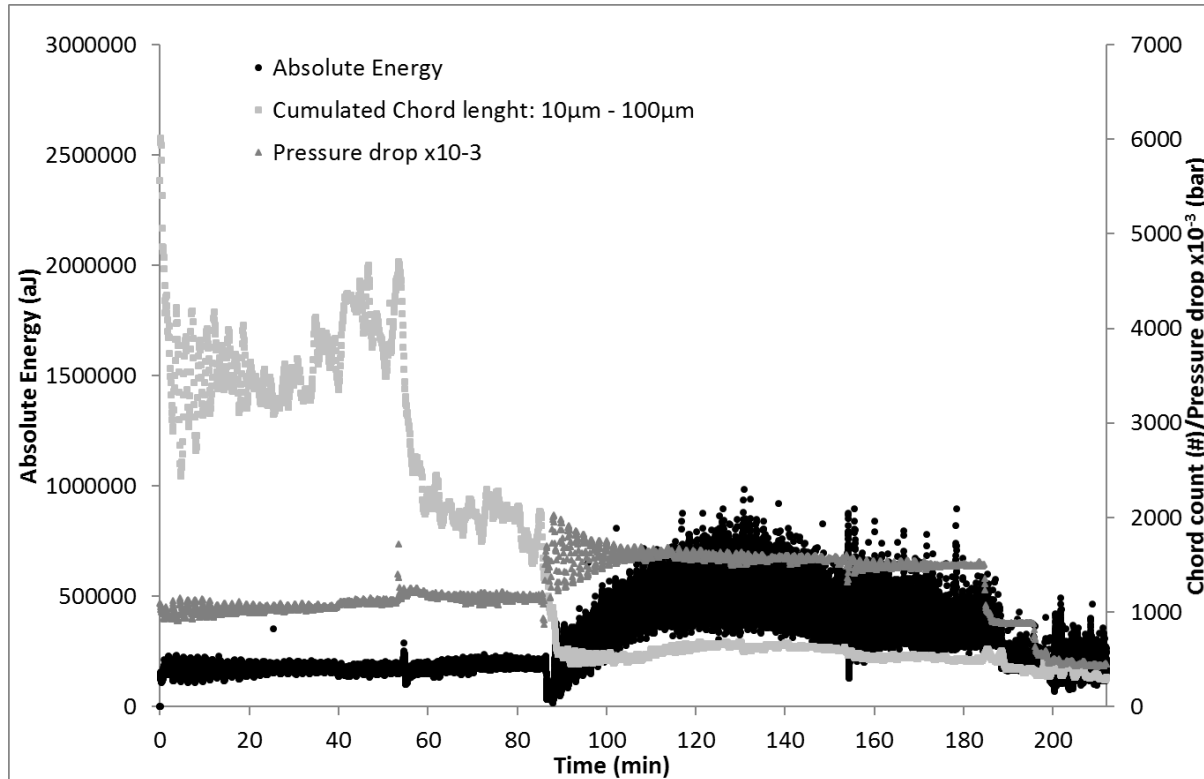


Figure 6 : Energy, chord length and pressure drop during time for experiment at 40 % water cut with oil phase at 400 L.h<sup>-1</sup>.

### 3. CONCLUSIONS

Acoustic emission can be useful to monitor industrial processes with powder. The laboratory experiments have provided interesting results. In order to generalize acoustic emission in these processes, we must go further in understanding particle impacts. Interesting works has been done recently [14-16], but we need to have different modelling, taking into account all kind of powders and all kind of surfaces. The use of a DEM (Discrete Element Method) approach coupled with computational fluid dynamics must be useful and help us characterize the velocities and the impacts of particles with different flow regimes.

### 4. REFERENCE

1. A. Marec, J. Thomas, R. El Guerjouma, Damage characterization of polymer based composite materials: Multivariable analysis and wavelet transform for clustering acoustic emission data, *Mech. Syst. & Signal Process.*, vol 22, 2008, 1441-64.
2. J.W.R. Boyd, J. Varley, The uses of passive measurement of acoustic emissions from chemical engineering processes, *Chemical Engineering Science*, vol. 56, 2001, 1749-1767.
3. E.M. Hansuld, L. Briens, J.A. McCann, A. Sayani, Audible acoustics in highshear wet granulation: Application of frequency filtering, *International Journal of Pharmaceutics*, vol. 378, 2009, 37-44.

4. K. Naelapää, P. Veski, J.G. Pedersen, D. Anov, P. Jørgensen, H.G. Kristensen, P. Bertelsen, Acoustic monitoring of a fluidized bed coating process, *International Journal of Pharmaceutics*, vol. 332, 2007, 90-97.
5. J. Salonen, K. Salmi, A. Hakanen, E. Laine, et K. Linsaari, "Monitoring the acoustic activity of a pharmaceutical powder during roller compaction," *International Journal of Pharmaceutics*, vol. 153, 1997, 257-261.
6. E. Serris, L. Perier-Camby, G. Thomas, M. Desfontaines, G. Fantozzi, Acoustic emission of pharmaceutical powders during compaction, *Powder Technology*, vol 128(2-3), 2002, 296-299.
7. E.L. Lube, A.T. Zlatkin, In-process monitoring of crystal perfection during melt growth, *Journal of Crystal Growth*, vol. 98, 1989, 817-826.
8. T.Sawada, Y.Gohshi, C.Abe, K.Furuya, Acoustics Emission from Phase Transition of Some Chemicals. *Analytical Chemistry* , vol 57, 1985, 1743-1745.
9. T. Chotard, A. Smith, N. Codet, M. De Baillencourt, D. Fargeot and C. Gault, Effect of malic and citric acid on the crystallisation of gypsum investigated by coupled acoustic emission and electrical conductivity techniques, *J. of Materials Science*, vol 41(21), 2005, 7210-7217.
10. D. Betteridge, M.T. Joslin, T. Lilley, Acoustic Emissions from Chemical Reactions, *Analytical Chemistry*. Vol 53, 1981, 1064-1073.
11. N. Gherras, E. Serris, G. Fevotte, Monitoring Industrial Pharmaceutical Crystallization Processes Using Acoustic Emission in Pure and Impure Media, *International Journal of pharmaceutics* vol 439(1-2), 2012, 109-119.
12. E. Serris, A. Cameirao, F. Gruy, Monitoring industrial crystallization using acoustic emission. In *Proceedings of the 32nd European Conference on Acoustic Emission Testing Prague, Prague, Czech Republic, 7–9 September 2016*.
13. A. Cameirao, E. Serris, A. Melchuna, J.M. Herri, P. Glenat, Monitoring gas hydrate formation and transport in a flow loop with acoustic emission, *Journal of Natural Gas Science and Engineering* vol 55, 2018, 331-336
14. C. Ruiz-Carcel, A. Starr, E. Nsugbe, Estimation of powder mass flow rate in screw feeder using acoustic emission, *Powder technology*, 336, 2018, 122-130
15. M.G. Droubi, R.L. Reuben, J.I. Steel, Flow noise identification using acoustic emission energy decomposition for sand monitoring in flow pipeline, *Applied acoustics*, 131, 2018, 5-15
16. Y. Hu, L. Wang, X. Huang, X. Qian, L. Gao, Y. Yan, On-line sizing of pneumatically conveyed particles through acoustic emission detection and signal analysis, *IEEE transactions on instrumentation and measurement*, 64(5), 2015,1100-1109

# AE Measurement during Friction Stir Welding of Flame-resistant Magnesium Alloy with Simulated Inclusions

Kazuki Takahashi<sup>a</sup>, Takayuki Shiraiwa<sup>a</sup>, Manabu Enoki<sup>a</sup>, Kaita Ito<sup>b</sup>, Eitaro Yukutake<sup>c</sup>

<sup>a</sup>The University of Tokyo; <sup>b</sup>National Institute for Materials Science;

<sup>c</sup>Industrial Technology Innovation center of Ibaraki Prefecture

## ABSTRACT

Friction stir welding (FSW) is a solid state joining process. By inserting the tool with the pin at the tip into the material, friction heat is generated and it softens the material. The material plastically flows around the tool and the specimens are joined. Due to low heat input during FSW, the grain coarsening is suppressed. It was shown that higher strength at joints can be obtained compared with the conventional welding process in Al alloy and conventional Mg alloy. Recently, in order to reduce the environmental impact and improve the transportation efficiency of train body, flame-resistant Mg alloy was developed. In order to make railway vehicles, FSW is applicable to the joining of long plate of flame-resistant Mg alloy. To monitor the FSW process of flame-resistant Mg alloy, wireless AE streaming system was developed in our group. Although AE signals during FSW process was considered to be related to the defects in the welding zone, the relationship between the AE events and the defects is not clear. In this study, we introduced the defects by mixing the simulated inclusions and measured the AE signals by wireless AE streaming system. In the case of specimens with the simulated inclusions, higher AE RMS voltage was obtained compared with that without the simulated inclusions.

**Keywords:** Friction Stir Welding; Acoustic Emission; Flame-resistant Mg Alloy; Joining Technology; Process Monitoring

## 1. INTRODUCTION

Friction stir welding (FSW) is a solid-state joining process [1]. This process takes place below the melting temperature of the material, and the grain coarsening and tensile strength reduction of the joint can be suppressed as compared with the conventional welding process. However, defect formation depends on the welding parameters such as rotation speed, traverse speed, tool geometry and so on. It is expected to apply FSW to the calcium-added flame-resistant magnesium alloy in order to reduce weight of railway vehicles, but it is more difficult to join the flame-resistant magnesium alloy by FSW than aluminum alloys and conventional magnesium alloys [2]. In order to evaluate the reliability of the joint and to obtain the appropriate welding parameters, it is necessary to detect the defect formation during FSW of the flame-resistant magnesium alloy. About 25 m FSW is needed to assemble railway vehicles but conventional wired AE monitoring needs dozens of AE sensors for this process. It is not practical way to use many AE sensors with complicated wire. Moreover, it is not allowed to attach the AE sensors directly on the material. In our previous studies, we developed the wireless continuous AE measurement device moving with the FSW tool in order to measure the AE signals generated during FSW of the flame-resistant magnesium alloy [3]. This device made it possible to measure the AE signals during FSW of long plate samples with a small number of AE sensors as compared with conventional AE measurement method. In addition to this, AE signals during FSW of flame-resistant Mg alloy were measured by wireless CWM and tensile

test and defects observation were conducted [4]. However, the relationship between AE signals and defects in the welding zone were not clear. In this study, simulated inclusions were introduced in the AZ31 Mg alloy and FSW experiment was conducted.

## 2. EXPERIMENTAL PROCEDURE

### 2.1 FSW experiment

The material used in this study was AZ31 (Al 3 %, Zn 1 %) magnesium alloy sheets. As shown in Figure 1(a), the dimensions of the plates were 70 mm width, 200 mm length and 2 mm thickness. The center on the long side of two plates was welded along the butt line. The tool had a 20 mm diameter shoulder and screwed pin. The tool pin had 1.9 mm height and 6 mm diameter. During joining, the tool rotated clockwise with tilt angle of 3° to promote material flow.

Alumina having an average particle size of 500 μm (JIS R6001, F36) was used as simulated inclusions in order to investigate the relationship between the inclusions in the material and AE signals during FSW process. It was introduced in the butt line of the plates with changing the amount and the area. Figure 1(b) shows the simulated inclusions and the cross section of plate.

In this FSW experiment, the tool rotation rate was set at 1000 rpm and the welding speed was set at 10 mm/s.

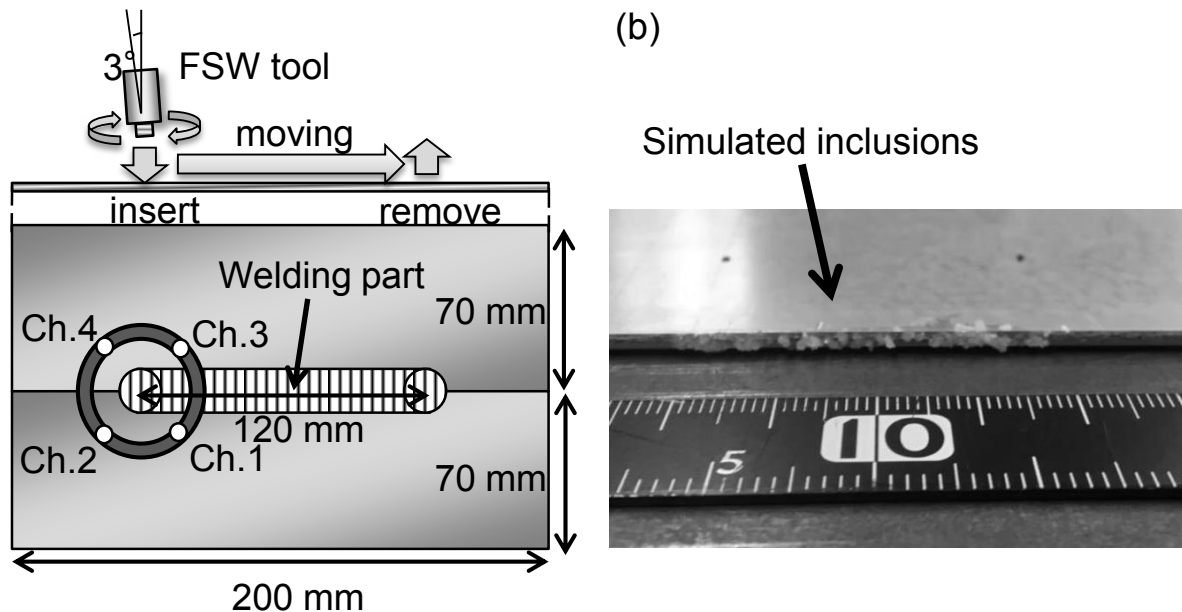


Figure 1: (a)The dimensions of the specimen and the position of AE sensors, (b)AZ31 plate with simulated inclusions

### 2.2 AE measurement

The position of AE sensors is shown in Figure 1(a). Four of AE sensors (type AE-254SMH177, Fuji Ceramics Corporation, Japan) were attached on the jig moving with tool. Movable AE sensor jig had a mechanism for canceling the advance angle of tool and the pistons making the contact between AE sensors and specimen surface stronger. The neodymium magnets were attached on the AE sensors and back plate in order to strengthen adhesion. Figure 2 shows the wireless CWM (Continuous Wave Memory) system. STEMLab125-14 (Red Pitaya) was used as a wireless CWM device [4]. STEMLab125-14 was

powered by Li-ion mobile battery in order to isolate the wireless CWM system electrically and to decrease the influence of electrical noise.

The waveforms were recorded to hard disc drives by the wireless CWM with about 4 MHz (divide 125 MHz by 32) of sampling frequency, 14-bit resolution and  $\pm 1$  V range. A high pass filter with 50 kHz of cut-off frequency was applied by internal software of CWM system to reduce noise caused by vibration. AE events were detected with 10 mV threshold voltage.

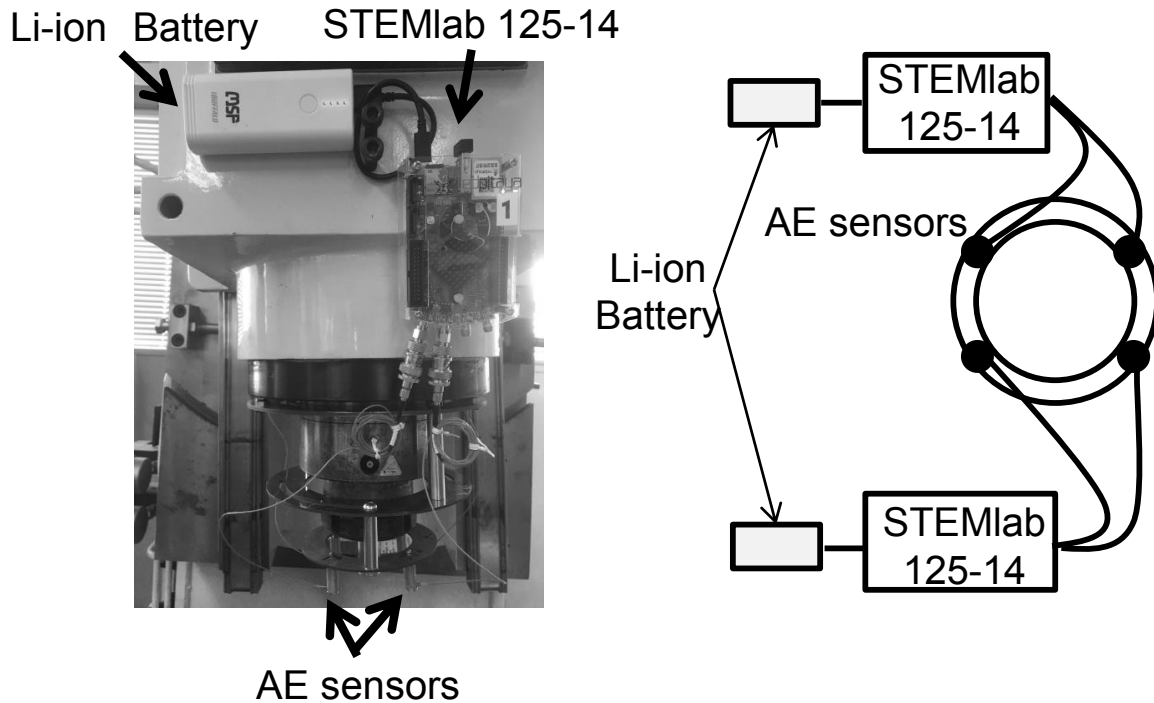


Figure 2: Wireless CWM system

### 3. RESULTS

Figure 3 shows RMS voltage during FSW process. Since FSW process is not considered to be a steady state immediately after start and just before termination, RMS voltage of this part was ignored. In the case that simulated inclusions were introduced at the position from 0 to 60 mm of joining line, high RMS voltage was obtained in the first half of FSW (Figure 3(a)). In the case that simulated inclusions were introduced at the position from 60 to 120 mm, high RMS voltage was obtained in the latter half of FSW (Figure 3(b)). On the other hand, lower RMS voltage was obtained in the case that simulated inclusions were not introduced (Figure 3(c)).

As shown in Figure 3, RMS voltage increased while joining the area where simulated inclusions were introduced. Therefore, it is supposed that inclusions in the material are one of the causes of AE during FSW of flame-resistant magnesium alloy.

### 4. CONCLUSIONS

In this study, simulated inclusions were introduced in AZ31. AE signals were measured with wireless CWM during FSW process. The relationship between AE signals and simulated inclusions were studied. It is considered that simulated inclusions introduced in the material induced higher RMS voltage.

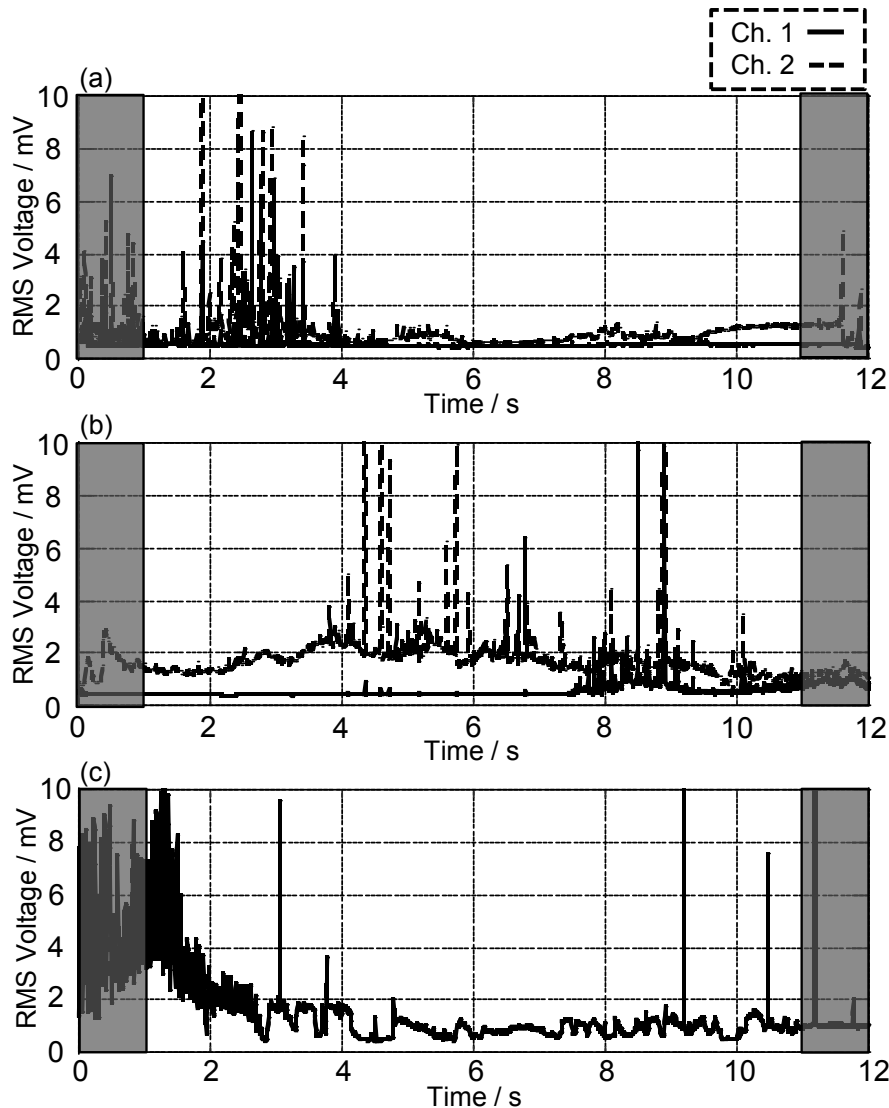


Figure 3: RMS voltage during FSW process (a) simulated inclusions introduced from 0 to 60 mm, (b) simulated inclusions introduced from 60 to 120 mm (c) no simulated inclusions

## 5. REFERENCE LINKING

- [1] W. M. Thomas *et al.*, (1991). "Investigate of weld defects in similar and dissimilar friction stir welded joints of aluminum alloys of AA7075 and AA6061 by X-ray CT radiography", International Patent Application PCT/GB92/02203 and GB Patent Application 9125978.8, UK Patent Office, London, December 6.
- [2] Akiyama *et al.*, (2000). "Development of flame-resistant magnesium alloy" *Materia*, Vol.39, pp.72-74.
- [3] M. Katayama, K. Ito, H. Fujii and M. Enoki, (2017). "Wireless AE measurement for FSW of long size steel plate", *CAMP-ISIJ*, Vol.30, pp.306.
- [4] K. Ito and M. Enoki, (2017). "Development of independently operated sensor node with continuous wireless transmission of AE waveform", *Proceedings of the 21<sup>st</sup> Acoustic Emission Conference*, pp.113-116.

# Structural Health Monitoring of Crack Initiation and Growth in Mooring Chains using FEA Methods for Acoustic Emission Characterisation

Ángela Angulo<sup>a,b</sup>, Han Yang<sup>a,b</sup>, Jialin Tang<sup>a,b</sup>, Ali Khadimallah<sup>a</sup> and Slim Soua<sup>a</sup>,

<sup>a</sup> TWI Ltd, Condition and Structural Health Monitoring, Integrity Management Group.  
Granta Park, Great Abington, Cambridge, CB21 6AL, United Kingdom;

<sup>b</sup> Brunel University London, Kingston Lane, Uxbridge, Middlesex, UB8 3PH, United Kingdom;

## ABSTRACT

Mooring chains for floating offshore installations, typically designed for a 25 year service life, are loaded in fatigue in seawater environments. It is crucial that the life of such structures is extended by regularly replacing old components and performing periodic in-service inspections. Although traditional methods can be successful at detecting and assessing fatigue cracks, the hazardous nature of operation calls for remote techniques that can be applied continuously to identify damage initiation and progress. Appropriate replacement plans must enhance current strategies by implementing real-time data retrofit.

Acoustic Emission (AE) has been shown to be a promising technique to detect cracks and fatigue damage in mooring chains. The present paper describes an AE-based methodology combined with Finite Element Analysis (FEA) for crack initiation and growth for Structural Health Monitoring (SHM) of mooring chains.

**Keywords:** acoustic emission, mooring chains, structural health monitoring, cracking, finite element analysis.

## 1. INTRODUCTION

One of the major problems in the design of offshore equipment is fatigue damage accumulation. Although this topic has been extensively studied in the literature, theoretically, numerically and experimentally [1] [2] [3] [4] [5] [6] [7], the available inspection and monitoring technologies developed to date have not been able to fully overcome the severe environmental challenges associated with offshore service activities. Furthermore, in addition to the structural challenges that onshore structures experience, offshore assets withstand harsh marine environments as a result of severe storms, highly corroding sea water, sea quakes and cyclic wave loading [8] [9]. Due to the increasing demand for structural retrofit into conventional inspection strategies, Structural Health Monitoring (SHM) is of interest to a wide range of industries. AE is a non-destructive monitoring technique that is widely used. One of the benefits of its application is the real-time assessment of the structural condition of industrial assets. The primary goal of this study is to investigate the applicability of AE approach for crack initiation and propagation detection and localization on a mooring chain [10]. The Finite Element Analysis (FEA) main objective is to simulate the dynamic response from an incremental crack growth. This is achieved by developing a FEA method for the implementation in a non-symmetric geometry.

Previous modelling work [10] has shown indication of the active damage regions in loaded mooring chains. Because of the inherent uncertainties present in any SHM technique, any monitoring technology should be used as part of a full mooring chain structural integrity

assessment. In addition to the continuous data output, a risk-based integrity management strategy may also be included based on data from periodic inspections, numerical modelling showing stress distributions or crack propagation and historic and current operational conditions.

### **Research background**

Previous research by the authors [10] [11], show the results of a FEA model that simulates instantaneous crack growth in a mooring chain link. The method used was successfully implemented in 2D in a long plate for a range of crack depths, all growing instantaneously from the un-cracked state. It was also successfully implemented in a 3D mooring chain link.

Additional work presented in [12], showed a new method to simulate incremental crack growth using cohesive zones. For such model, many parameters are required which are not readily available for materials. The method is complex and presents a more suitable approach to predicting crack growth. The generation of realistic AE signals was achieved, whereas the prediction of realistic crack growth was not possible. As a result, the method was not recommended for this application due its complexity. It was therefore recommended to implement a pre-defined incremental crack growth approach and to analyze the dynamic response of the AE generated.

### **Preliminary methods**

Preliminary methods [10] [12] consisted of simulating the crack growth using known and incremental changes in crack length. This is a straightforward method to apply for symmetric geometry as boundary conditions can be removed. However, this method can be complex for non-symmetric geometries, as the seam used to define the crack for the instantaneous crack growth cannot be altered over time for incremental crack propagation. Similarly, ties cannot be adjusted over time.

Preliminary method one: defines the contact between un-cracked surfaces and incrementally deletes the contact to grow the crack. The results were not satisfactory as the contact definition in Explicit (using ABAQUS) returned numerical errors generating undesired waves.

Preliminary method two: defines a blunt crack that is two elements wide (symmetric) and deletes elements to grow the crack. The results proved the approach can be very complex to implement in Explicit, involving VUMAT subroutine. It was therefore implemented using the Standard method.

## **2. APPROACH**

### **Method description**

The selected approach corresponds to the incremental crack growth method. The methodology artificially deletes elements by reducing their stiffness (Young's Modulus) to  $\sim 0$ . This method simulates the crack growth and is controlled by defining temperature-dependent material properties. The crack grows by assigning an instantaneous temperature change with each crack growth increment (i.e. the temperature is used as an arbitrary variable to change the stiffness with time).

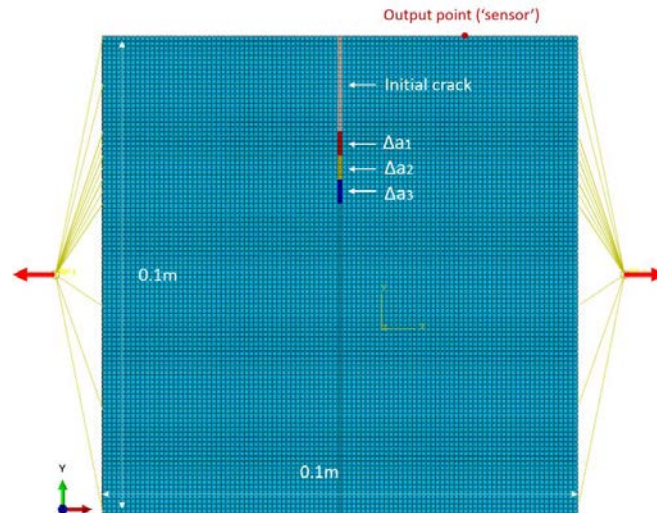
### **Model description**

2D and 3D Finite Element (FE) linear elastic modelling have been implemented using ABAQUS software. Both studies are carried out on a carbon steel material (see Table 1).

**Table 1 Material properties**

Temperature (°C)	Young's Modulus (GPa)	Poisson's Ratio	Density (Kg/m <sup>3</sup> )
0	~0	0.3	7830
20	207	0.3	7830

For the 2D model, where 2D linear elements are used, the dimensions of the plate are 0.1m × 0.1m. A 500N tensile force is applied to both ends through reference point coupling in the U1 direction (indicated by the red arrow, Figure 1)

**Figure 1 Model description of the 2D Square plate**

The reference points are fixed in U2, U3 (displacements along y and z, respectively), UR1, UR2 and UR3 (rotations about x, y and z, respectively). The central-base point is fixed in U2 to prevent rigid body motion of the model. The mesh size of 1 mm and a time step of 80 ns were used. The output node is situated halfway between the crack and the end face.

The crack growth method can be described as follows: four steps are set up to simulate the crack opening, the load is applied in the 'initial crack' step smoothly and then held constantly during growth. Such procedure avoids generating waves. The load function according to the smooth step method defined in ABAQUS software is as follows.

$$a = 6 \times 10^6 \times t^5 - 1.5 \times 10^9 \times t^4 + 10^7 \times t^3 \quad 0 \leq t \leq 0.01 \text{ s};$$

Where a is the crack length and t is time. In the initial step, the temperature of the whole model was 20 °C. During the initial crack step, the temperature of the elements which belong to the 'initial crack' region was changed to 0 °C. This resulted in a Young's modulus value of ~0, therefore simulating the crack opening. Elastic waves (acoustic emissions) are generated as the result of this sudden release of energy.

In order to study the influence of different crack sizes on the generated acoustic emissions, three more steps after the 'initial crack' step were added. The sizes of the three cracks are:

$$\Delta a_1 = 22.5 \text{ mm}; \Delta a_2 = 25 \text{ mm}; \Delta a_3 = 27.5 \text{ mm};$$

To further validate the modelling method, a 3D model is implemented. The 3D and 2D models were based on the same crack length and width (3D model thickness was 5mm), as well as the same crack propagation method and parameters. Linear hexahedron elements were used.

### 3. RESULTS

The manifestation of AE is represented by vertical displacements. The recorded waveform at the output point is shown in Figure 2. The top-left and top-right plots of Figure 2 are the displacements from the output points of the 2D and 3D models, respectively. From 0s to 0.01s, the load is applied smoothly during the ‘initial crack’ step. The crack growth step 1 ( $\Delta a_1$ ), crack growth step 2 ( $\Delta a_2$ ) and crack growth step 3 ( $\Delta a_3$ ) occur from 0.01s to 0.02s, 0.02s to 0.03s and 0.03s to 0.04s, respectively.

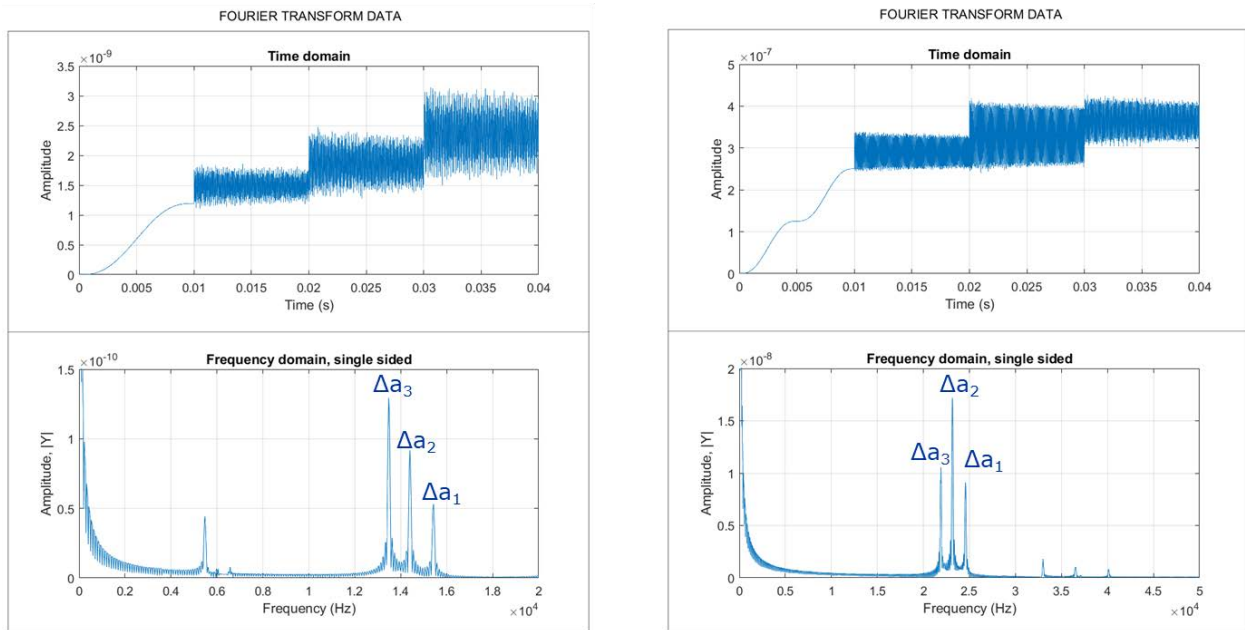


**Figure 2 Time and frequency domain of displacements in the 2D model (left) in 3D model (right)**

In the time domain, similarities can be observed between the 2D and 3D models. The average amplitudes of the waves increased with the crack length increase for both models in the time domain. However, during crack growth, the wave amplitude obtained from the 2D model was two orders of magnitude lower than the corresponding wave of the 3D model, situated between  $2 \times 10^{-7}$  and  $4 \times 10^{-7}$ .

In order to investigate the signatures of the crack growth in its frequency domain, Fourier transform was used during data processing. For both 2D and 3D models, three distinct peaks for each crack release can be seen (increasing with growing crack in the 2D model) and the frequency decreased as the crack length increased. For the 3D model, the largest peak amplitude corresponds to the second crack step.

### 4. SUMMARY

The current method consisted of reducing the elements stiffness at the crack tip region to simulate the crack growth. The results show that the average amplitude of the AE waves

increased with the crack growth. It can also be seen that the frequency of the AE signals generated from the crack propagation decreased as the crack length increased.

Additional development and sensitivity analysis are required for the current method. The influence of different parameters used in the modelling such as crack growth release time, crack growth size and initial crack size will be further investigated. Cyclic loading response will also be modelled. Furthermore, it is very important to validate the FE model with experiment results. AE monitoring of crack opening experiments which are similar to the numerical modelling cases will be conducted to get more convinced data for the application of the current method.

## 5. REFERENCES

- [1]. H. Agerskov and N. Pedersen, "Fatigue life of offshore steel structures under stochastic loading," *Journal of Structural Engineering*, vol. 118, no. 8, pp. 2101-2117, 1992.
- [2]. H. Alawi, A. Ragab and M. Shaban, "Corrosion fatigue crack growth of steels in various environments," *Journal of Engineering Materials and Technology (ASME)*, vol. 111, no. 1, pp. 40-45, 1989.
- [3]. K. Komai, M. Noguchi and H. Okamoto, "Growth characteristics of surface fatigue cracks of high-tensile strength steel in synthetic seawater," *JSME International Journal*, vol. 31, no. 3, pp. 613-618, 1988.
- [4]. K. Komai, K. Minoshima, S. Kinoshita and G. Kim, "Corrosion fatigue crack initiation of high-tensile-strength steels in synthetic seawater," *JSME International Journal*, vol. 31, no. 3, pp. 606-612, 1988.
- [5]. J. S. Monsalve-Giraldo, C. M. S. Dantas and L. V. S. Sagrilo, "Probabilistic fatigue analysis of marine structures using the univariate dimension-reduction method," *Marine Structures*, vol. 50, pp. 189-204, 2016.
- [6]. Y. Low, "A variance reduction technique for long-term fatigue analysis of offshore structures using Monte Carlo simulation," *Engineering Structures*, vol. 128, pp. 283-295, 2016.
- [7]. Y.-H. Zhang and M. Dore, "Fatigue crack growth assessment using BS 7910:2013 - Background and recommended developments," *International Journal of Pressure Vessels and Piping*, vol. 168, pp. 79-86, 2018.
- [8]. T. Moan, "Life cycle structural integrity management of offshore structures," *Structure and Infrastructure Engineering*, vol. 14, no. 7, pp. 911-927, 2018.
- [9]. T. Thorpe, P. Scott, A. Rance and D. Silverster, "Corrosion fatigue of BS 4360:50D structural steel in seawater," *International Journal of Fatigue*, vol. 5, no. 3, pp. 123-133, 1983.
- [10]. A. Angulo, C. Mares, T. Gan and S. Souza, "Finite element analysis of crack growth for structural health monitoring of mooring chains using ultrasonic guided waves and acoustic emission," *J. Procedia Structural Integrity*, pp. 5, 217-224, 2017.
- [11]. Angulo, G. Edwards, T. Gan and S. Souza, "Mooring integrity management: novel approaches towards in situ monitoring," in *In Structural Health Monitoring-Measurement Methods and Practical Applications*, London, Intechopen, 2017, p. Chap. 5.
- [12]. Angulo, C. Mares, T. Gan and S. Souza, "Crack Initiation and Growth Acoustic Emission Analysis with Finite Element Analysis for Structural Health Monitoring of Mooring Chains," in *Proceedings of the Eleventh International Workshop on Structural Health Monitoring*, Stanford, 2017.

# Characterization of Microdamage of Flexible Solar Cell under Fatigue Load using AE and LT Techniques

Takahiro MATSUEDA<sup>a\*</sup>, Shuichi WAKAYAMA<sup>a</sup>, Kosuke NAKAHARA<sup>b</sup>,  
Akihiro TAKANO<sup>b</sup>

<sup>a</sup>Tokyo Metropolitan University; <sup>b</sup>F-WAVE Company, Limited

## ABSTRACT

Flexible solar cells in service are subjected to external load such as thermal expansion mismatch between solar cells and the base. It is considered that microdamages are initiated and accumulated due to those external loads. Some mode of microdamages causing shunt results in the electrical degradation of flexible solar cells. In our previous study, it was revealed that electrical degradation of solar cell is caused by microdamage parallel to the loading direction due to the buckling around through-hole under static tensile loading. The purpose of the present study is to reveal the mechanisms of microdamage initiation and accumulation, and their contribution to the electrical degradation during fatigue fracture. In the present study, cyclic tensile tests performed with the 0.8% and 1.2% maximum strains. Microdamages initiation were detected by the acoustic emission (AE) techniques. The electrical degradation of solar cell was evaluated by monitoring electrical power calculated from Current-Voltage (I-V) curve. Furthermore, microdamages contributing to the electrical degradation were identified by the Lock-in thermography (LT). For the cyclic tensile tests, the first AE signal was detected at the through-holes. Temperature around through-holes increased and electrical power decreased in low cycles. Then AE signals resulted by microdamage initiation were detected each cycles and electrical power was gradually decrease with the increase in the number of cycles until the test stop. It was then indicated that microdamage both of initiating extremely low cycle and high cycle contributed to the electrical degradation. Consequently, it was suggested that the AE, LT and I-V curve monitoring enable to characterize the electrical degradation during fatigue fracture.

**Keywords:** Flexible solar cell, Fatigue, Microdamage, Lock-in thermography

## 1. INTRODUCTION

Since flexible solar cells have excellent flexibility and lightness, they have been widely used as one of the sustainable energy systems. Flexible solar cells in service are subjected to external load such as thermal expansion mismatch between solar cells and the base. It is considered that microdamages are initiated and accumulated by those external loads. Some mode of microdamages leads the electrical degradation of flexible solar cells [1-5]. In order to understand the mechanism of electrical performance degradation of flexible solar cell, these two processes should be clarified.

In our previous study, it was revealed that electrical degradation of solar cell is caused by microdamage parallel to the loading direction due to the buckling around through-hole under static tensile loading [6]. On the other hand, the electrical degradation behavior under cyclic loading has been unclear yet and there are only a few studies [7] in spite of flexible solar cell in-service may be subjected to fatigue load due to mismatch of thermal expansion. The purpose of the present study is to detect the microdamages, sensitively and identify the microdamages contributing to the electrical performance degradation during fatigue fracture. Cyclic tensile tests were carried out for this purpose. Microdamage during the cyclic tensile tests were detected and

characterized using acoustic emission (AE), lock-in thermography (LT) technique [8-10] and monitoring electrical performance.

## 2. SPECIMEN AND EXPERIMENTAL PROCEDURE

### 2.1 SPECIMEN PREPARATION

In the present study, the commercially available a-Si/a-SiGe flexible solar cell modules, F-WAVE were employed as specimens. Figure 1 shows the illustration of the flexible solar module. Specimen in this study has laminated structure which consists of 7 layers of thin films; PE/ITO/a-Si/a-SiGe/metal electrode/film substrate/back electrode. The flexible solar modules are separated by patterning lines. There are two types of through-holes in this flexible solar module. The one provides the electrical connections between back electrode and ITO and the other provides the electrical connections between metal electrode and back electrode to connect unit cells in series [11]. The flexible solar module was cut into the specimen of one unit cell with the dimension of  $207 \times 35 \times 0.17$  mm. The two conductive tapes were attached on the back electrode in order to monitor electrical power generation of a unit cell.

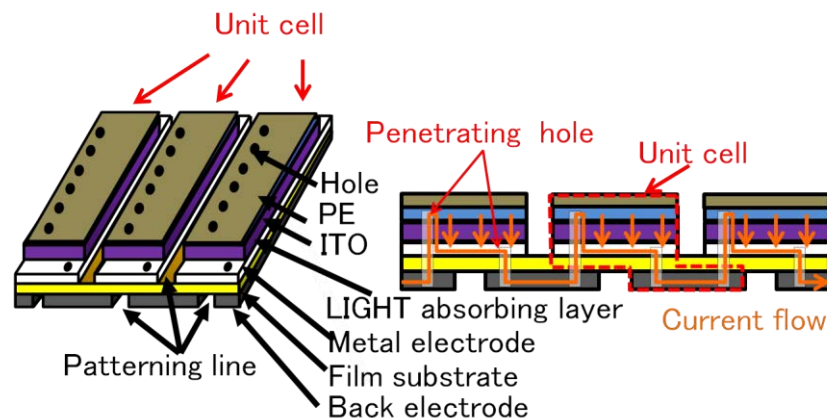


Figure 1: Schematic illustration of the flexible solar cell used in present study.

### 2.2 Experimental Procedure

#### 2.2.1 Test Condition of Cyclic Tensile Fatigue Test

Figure 2 shows the schematic illustration of tensile fatigue testing system. The tensile fatigue tests of the flexible solar cells were performed with the gage length of 200mm. The mechanical cyclic load was applied by fatigue testing machine (SAGINOMIYA SEISAKUSHO, INC, FT-10-1600). Maximum strains were 0.8% and 1.2%. The stress ratio was 0.1.

#### 2.2.2 Measurement Conditions of AE Signals and electrical performance

In order to detect microdamage caused by fatigue load, AE technique was used during test. Four resonance model AE sensors (PAC, PICO; resonant frequency 400kHz) were attached on a through-hole, a patterning line, a smooth surface and an edge of specimen by elastic bond and these sensors were called as Ch.1 ~ Ch.4, respectively. The AE signal was amplified by 40dB and the threshold level was 20  $\mu$ V. The band pass filter was selected at a range from 20 to 1200 kHz. The AE signals were recorded and proceeded by the AE analyzer (Vallen System GmbH, AMSYS-5).

For monitoring electrical performance, the specimen was irradiated by solar simulator (Pecell technology, PEC-L01) during the test. Current and voltage generated by flexible solar cell were measured by the source meter (Keithley Instruments Inc., 2400).

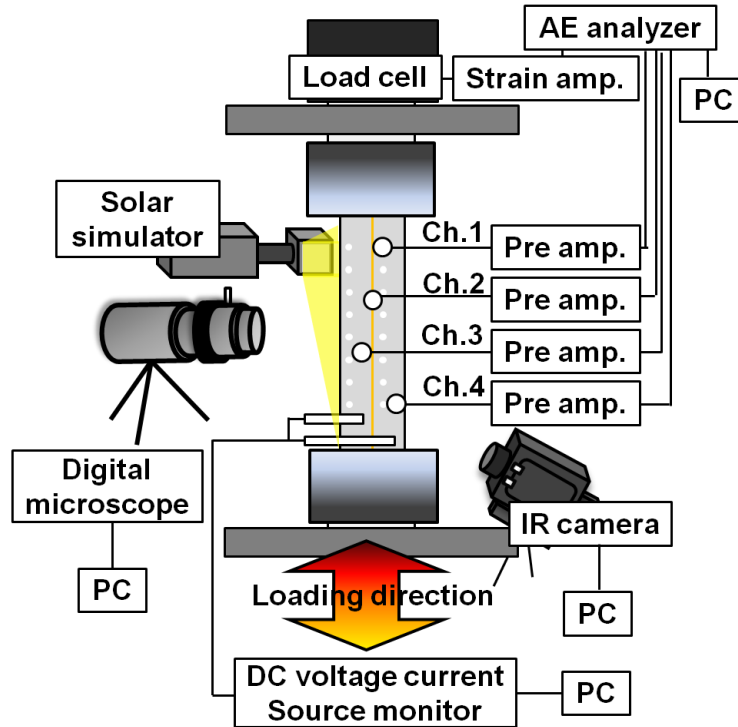


Figure.2: Schematic illustration of cyclic tensile fatigue test system.

### 2.2.3 Measurement Conditions of LT

For the detection of the shunts which contributed electrical performance degradation in a specimen, fatigue test was suspended and the increase in temperature modulation resulted from shunt was detected using LT technique. IR thermal images were recorded during the monotonic tensile tests of the flexible solar cells. The damage contributing to the electrical performance degradation was excited by the periodical input bias. The temperature at the local area around damage was increased due to the shunt. The excited signals were discriminated from back ground signals by the digital lock-in processing. For the temperature history at each pixel, the frequency component synchronized with the input bias was extracted through the fast Fourier transform (FFT). The LT image was obtained by repeating the same processes for all pixels. It is worth noting that the damage contributing to the electrical performance degradation can be distinguished from the others by LT technique in principle. The sinusoidal voltage with the amplitude of 2 V and the frequency 1 Hz was applied to the unit cell, and then current and voltage were measured by the source meter.

## 3. RESULTS AND DISCUSSION

### 3.1 Fatigue test with the 0.8% maximum strain

For identification of microdamage contributing to electrical performance degradation of the flexible solar cell under fatigue load, it is necessary to detect and characterize microdamages. Figure 3 shows the Load, cumulative AE energy, the maximum electrical power normalized by one before test,  $P_{max}$  is plotted as a function of the cycle and LT images resulted from 0.8% maximum strain fatigue test.

As described Fig. 3, the first AE signal was detected at the through-hole. And then the cumulative AE energies at the other sensors were increased in order of patterning line, the edge of specimen and the smooth surface. Increase of AE energy was temporary stopped until 1700 cycles. And then AE energy at through-hole and smooth surface were rapidly increased. AE energy at through-hole and smooth surface were increased each cycle until test stop.

$P_{max}$  had been decreasing from 2000 cycles to test stop. It is indicated that the flexible solar cell should be used to consider the electrical performance degradation in high cycle fatigue under 0.8% cyclic strain.

As shown in LT images, until 1000 cycles, the increase in temperature was not observed. The temperature around several through-holes increased continuously from 2000 cycles and then the region of temperature increasing had been expanding as the increase in cycles until test stop.

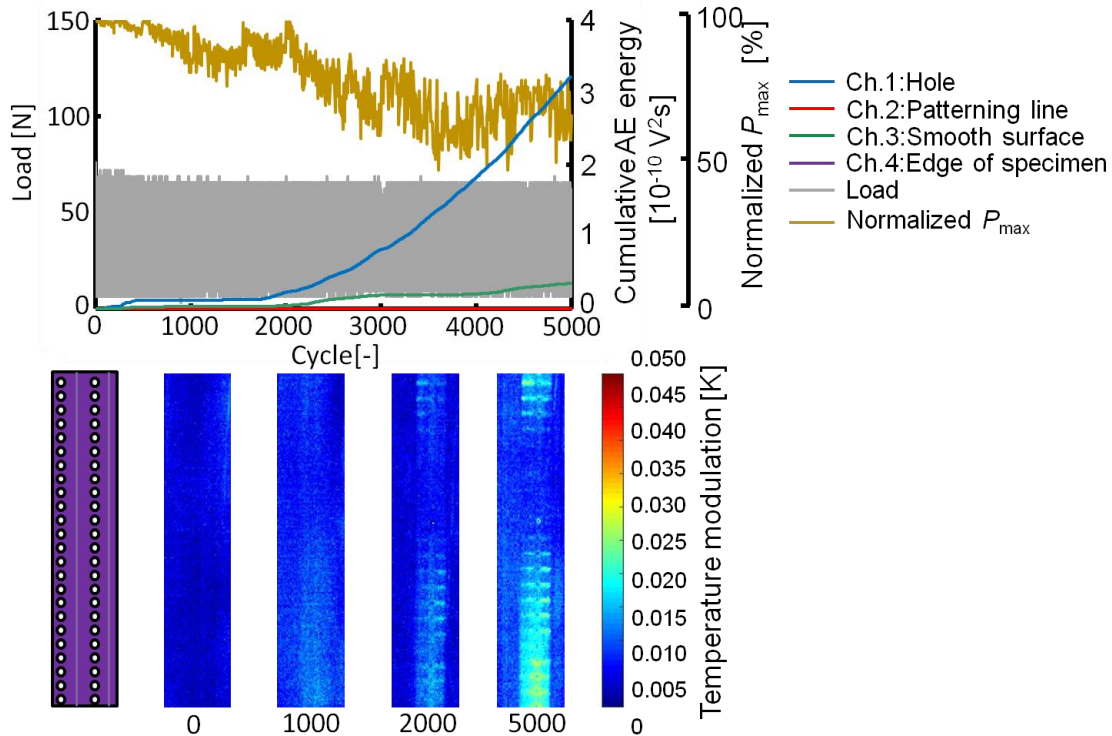


Figure 3: Cumulative AE energy,  $P_{max}$  and LT images of 0.8% strain fatigue test.

### 3.2 Fatigue test with the 1.2% maximum strain

Figure 4 shows the Load, cumulative AE energy,  $P_{max}$  is plotted as a function of the cycle and LT images resulted from 1.2% maximum strain fatigue test. As described in the figure, the first AE signal was detected at the through-hole and the cumulative AE energy at through-hole was rapidly increased immediately similarly to 0.8 % maximum strain fatigue test. And then the cumulative AE energy at the other sensors were also rapidly increased in order of the smooth surface, patterning line and the edge of specimen, but AE generation around the through-hole was significantly active compared to 0.8 % maximum strain fatigue test. It was indicated that microdamages initiated around through-holes, intensively. Cumulative AE energies at each channel were rapidly increasing at extremely low cycles and then generally continue to be the constant value.

$P_{max}$  had been decreasing until 200 cycles and  $P_{max}$  at 200 cycles was reduced to 30% before test. And then  $P_{max}$  was remaining flat to the end of this test. It is indicated that the performance degradation of the flexible solar cell under 1.2% cyclic strains was rapidly proceeding in extremely low cycles.

As shown in LT images, the temperature around several through-holes increased continuously from 100 cycles.

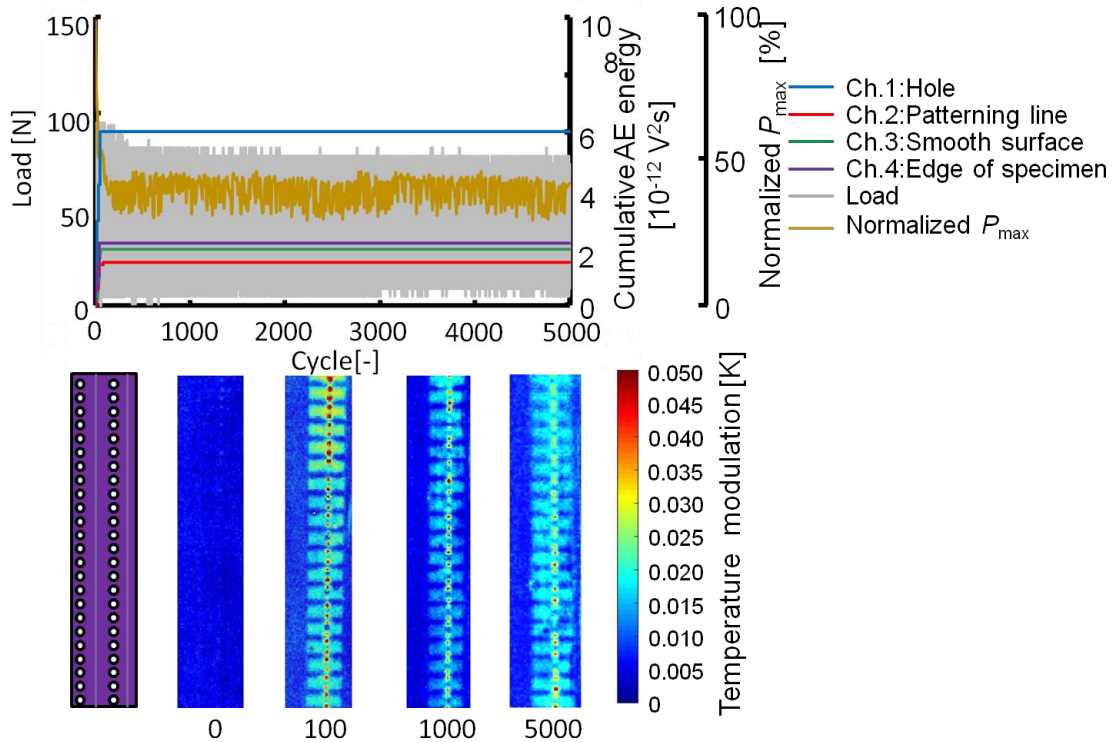


Figure 4: Cumulative AE energy,  $P_{\max}$  and LT images of 1.2% strain fatigue test.

### 3.3 Contribution of crack closure to performance degradation process

Increase in temperature under fatigue load was observed in bands. On the other hand, the increase in the temperature around a through-hole was only observed under monotonic tensile load [6]. Crack tip under fatigue load was subjected crack closure. This crack closure initiated AE signals and shunts which contributing the increase in temperature of specimen surface under fatigue load.

## 4. Conclusions

In present study, the cyclic tensile fatigue test of the flexible solar cell was carried out in order to identify the microdamage contributing to the electrical degradation during fatigue fracture and following conclusions were obtained.

1. The microdamages initiated under cyclic tensile load were well detected using AE technique. In the both 0.8 % and 1.2 % maximum strain fatigue tests, the first microdamage initiated around the through-hole was earlier than the others.
2. It was revealed that the increase in temperature around the through-hole was earlier than the others under cyclic tensile load using LT technique. This tendency was coincided on that of AE detection.
3. Crack closure at crack tip under fatigue load contributed to performance degradation.

## 5. References

- [1] IEC 61215, (2005). "Crystalline Silicon Terrestrial Photovoltaic Modules – Design Qualification and Type Approval: Edition 2", IEC.
- [2] Wohlgemuth, J. H., (2008). "The effect of cell thickness on module reliability", *Proceeding of 33rd IEEE Photovoltaic Specialists Conference*, doi: 10.1109/PVSC.2008.4922770.
- [3] Pingel, S., Zemen, Y., Geipel, T. and Berghold, J., (2009). "Mechanical stability of solar cells within solar panels" *Proceeding 24<sup>th</sup> European Photovoltaic Solar Energy Conference and Exhibition*, pp.3459-3463.
- [4] Köntges, M., Kunze, I., Kajari-Schröder, S., Breitenmoser, X. and Bjørneklett, B., (2011). "The risk of power loss in crystalline silicon based photovoltaic modules due to micro-cracks", *Solar Energy Materials & Solar Cells*. Vol. 95, issue 4, pp. 1131–1137.
- [5] Jones, R., Johnson, R., Jordan, W., Wagner, S., Yang, J., and Guha, S., (2002). "Effects of mechanical strain on the performance of amorphous silicon triple-junction solar cells", *Conference record of 29<sup>th</sup> IEEE photovoltaic conference*, pp.1214-1217.
- [6] Tazawa, H., Sakai, T., and Wakayama, S., (2013). "Characterization of damage in a-Si/a-SiGe flexible solar cells under mechanical strain by AE technique and lock-in thermography", *Proceeding 28<sup>th</sup> European Photovoltaic Solar Energy Conference and Exhibition*, 3CV.1.33, CD-ROM, 4 pages.
- [7] Jason Maung, K., Thomas Hahn, H., Ju, Y.S., (2010). "Multifunctional integration of thin-film silicon solar cells on carbon-fiber-reinforced epoxy composites", *Solar Energy*, Vol. 84, pp. 450–458.
- [8] Huth, S., Breitenstein, O., Huber, A., Dantz, D., Lambert, U. and Altmann, F., (2002). "Lock-in IR-thermography - A novel tool for material and device characterization", *Solid State Phenomena*, Vol. 82-84, pp.741-746.
- [9] Straube, H. J., Wagner, M., Schneider, J., and Breitenstein, O., (2011), "Quantitative evaluation of loss mechanisms in thin film solar cells using lock-in thermography", *Journal of Applied Physics*, Vol. 110, doi:10.1063/1.3651397.
- [10] Breitenstein, O., Rakotoniaina, J. P., Al Rifai, M. H. and Werner, M., (2004). "Shunt Types in Crystalline Silicon Solar Cells", *Progress in Photovoltaic: Research and Applications*, Vol. 12, pp. 529-538.
- [11] Takano, A., Kamoshita, T., (2004), "Light-Weight and Large-Area Solar Cell Production Technology", *Japanese Journal of Applied Physics*, Vol. 43, Part 1, No. 12.

# Application of Non-Contact Laser Impact with Acoustic Emission Analysis and Tomography Technique for Damage Detection in Concrete

Tomoki Shiotani<sup>1</sup>, Katsufumi Hashimoto<sup>1</sup>, Masaharu Nishikino<sup>2</sup>  
and Katsuhiko Mikami<sup>2</sup>

<sup>1</sup> Dept. Civil & Earth Resources Engineering, Kyoto University, Kyoto, 615-8540, Japan

<sup>2</sup> National Institutes for Quantum and Radiological Science and Technology, Kansai  
Photon Science Institute, Kyoto, 619-0215, Japan

## ABSTRACT

Tomography techniques have been developed based on acoustic emission and elastic-wave propagation to visualize the internal defects in concrete. For instance, the tomography results can reasonably estimate the wave velocity distribution in consideration of P-wave propagation detours, which are supposed to be altered by the disturbance such as internal defects. As for the excitation of elastic waves on the surface of targeted structure, it is generally known that contact time of a steel sphere ball drop depends on the diameter of the ball, and the frequency component generated by the ball impact is derived by the contact time. In this study, to realize remote inspection works, the elastic wave is induced onto the concrete surface by the impact laser system employing high-power pulse, followed by investigating the influence of laser intensity and spot size. To implement the prompt and reasonable laser remote sensing system to damage detection in concrete, high speed scanning of laser pulse irradiation is introduced on the surface of concrete. Amplitude and frequency dependence are analyzed between the ray paths of the propagated elastic waves, calculating P-wave and surface wave propagation time with amplitude attenuation. The applicability of laser-induced elastic wave for the technique is thus investigated when internal defects of concrete is visualized by means of tomography technique.

**Keywords:** acoustic emission, laser impact, concrete, p-wave, surface wave, tomography

## 1. INTRODUCTION

To induce the elastic wave and the vibration into concrete, the impact laser system is employed for high-power pulse, which irradiates the concrete surface to generate vibrations that can excite elastic waves on the structural surface of interest. Amplitude and frequency dependence are analyzed among the ray paths of the propagated elastic waves, calculating P-wave and surface wave travel time with amplitude attenuation. According to visualization of internal defect in concrete by means of tomography technique, the applicability of laser-induced elastic wave for the technique is consequently investigated.

In order to determine the velocity distributions by tomography, the following analytical steps are taken. The arrival time at each sensor was determined with an Akaike Information Criterion (AIC) picker [2,3]. For the digitized wave record  $x_k$  of length  $N$ , the AIC value is defined as

$$\begin{aligned} \text{AIC}(k) = & k \times \log \{ \text{var}(x[1, k]) \} \\ & + (N - k - 1) * \log \{ \text{var}(x[k + 1, N]) \} \end{aligned} \quad (1)$$

where  $\text{var}(x[1, k])$  indicates the variance between  $x_1$  and  $x_k$ , and  $\text{var}(x[k, M])$  is the variance between  $x_k$  and  $x_M$ .

The point where the AIC value is minimized with the least-square method corresponds to the optimal separation point of two stationary time series, and thus the arrival time is reasonably determined as the phase onset by the AIC picker. This is because noise could be represented by lower AIC values, whereas wave signals generally show higher AIC values. From the determined arrival time, the velocity of the elastic wave is calculated. The observed propagation time  $T_{obs}$  is obtained by Eq. (2).

$$T_{obs} = T_o - T_s \quad (2)$$

where  $T_s$  is the time of excitation and  $T_o$  is the arrival time [4].

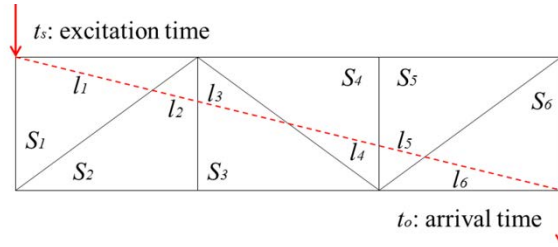


**Figure 1 Slowness for calculation of propagation time**

In the elastic-wave tomography algorithm, the reciprocal of the velocity is referred to as the “slowness,” which is given as an initial parameter into each element as shown in Fig. 1. The theoretical propagation time  $T_{cal}$  is derived from the total of the propagation time calculated by the slowness and the distance in each element (refer to Eq. (3)). The difference between the observed propagation time ( $T_{obs}$ ) and the theoretical propagation time ( $T_{cal}$ ) is obtained by Eq. (4).

$$T_{cal} = \sum_j s_j * l_j \quad (3)$$

$$\Delta T = T_{obs} - T_{cal} \quad (4)$$

where  $l_j$  is the length crossing each element and  $s_j$  is the slowness of each element.

Then, the slowness in each element is revised in order to reduce the difference between the observed propagation time and the theoretical propagation time. The amount of the slowness correction is calculated by Eq. (5). Consequently, the revised slowness is obtained by Eq. (6).

$$\begin{bmatrix} \Delta s_1 \\ \Delta s_2 \\ \vdots \\ \Delta s_j \end{bmatrix} = \begin{bmatrix} \sum_i \frac{\Delta T_i * l_{i1}}{L_i} / \sum_i l_{i1} \\ \sum_i \frac{\Delta T_i * l_{i2}}{L_i} / \sum_i l_{i2} \\ \vdots \\ \sum_i \frac{\Delta T_i * l_{ij}}{L_i} / \sum_i l_{ij} \end{bmatrix} \quad (5)$$

$$s'_j = s_j + \Delta s_j \quad (6)$$

where  $L_i$  is the total distance of wave propagation through the  $i$ -element.

The iteration procedure based on Eq. (5) and Eq. (6) is used to determine the optimal slowness and eventually the velocity in each element corresponding to the observed propagation times of multiple paths over the structure. Thus, the velocity distribution is determined.

In order to determine the ray path more accurately, the ray-trace algorithm is applied, taking detours of elastic waves due to reflection and diffraction into account. In particular, the arrival time of each wave is obtained by using a 3D ray-trace algorithm extended from a 2D ray-trace, which was proposed in the past research [5]. The slowness of each element is corrected from the difference between the first travel time observed and that computed in the 3D element, because the algorithm enables the use of 3D finite elements for meshing the target space.

## 2. EXPERIMENTAL SETUP

High-speed laser system has been employed as a remote sensing technique to detect defects inside a concrete specimen [6]. In the proposed measurement setup, irradiated laser pulses enable to generate vibration and detected by the system, which is compatible to that obtained by using the conventional hammering method. In this study the laser system is thus introduced to generate elastic waves which propagate in concrete for the aforementioned tomography computation in order to visualize defect in concrete.

Beam focus and energy density were controlled from 2.79 J/cm<sup>2</sup> to 82.5 J/cm<sup>2</sup> at laser irradiated location on the surface of specimen. Impact energy can be altered by 50/ 150/ 250 mJ and frequency was set at 0.2 Hz. Laser beam was irradiated on the surface of specimen with focused and de-focused condition as shown in Fig. 2.

A simply supported concrete specimen was targeted, 300 mm height x 300 mm width x 100 mm thickness with 10 mm thickness styrofoam simulating a defect, embedded at 5 mm (85 mm) depth. In Fig. 3 the specimen and experimental overview are depicted, where sensor of #1 to #4 are placed on other side of laser irradiation surface to detect through-the-thickness wave, namely P-wave and surface wave is detected by the sensor #5 set on the same surface of the irradiation. Two types of 30 kHz and 60 kHz resonant frequencies' AE sensors were arrayed at almost same positions on the both side of the concrete surfaces. Each distance between the sensors from #1- #4 was 60 mm. A sampling rate of waveform record was set at 10 MHz.

## 3. RESULTS AND DISCUSSION

Fig. 4 shows typical waveforms detected by AE sensor #2 and #4 respectively. The laser excitations were made by focused and defocused laser impact of 250 mJ irradiated at A and B. As shown in Fig. 3, the propagation path from A to #2 is through the concrete with defect and that from B to #4 is through the intact concrete. P-wave arrival times determined with AIC are

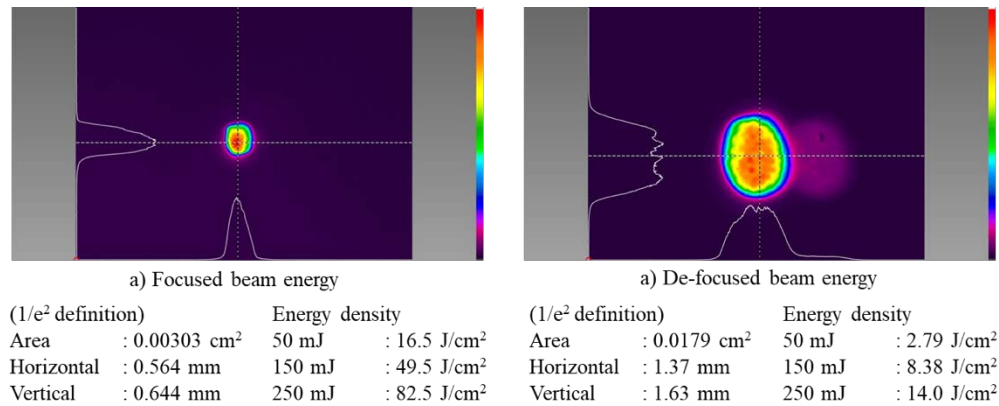


**Figure 2 Impact laser irradiation condition**

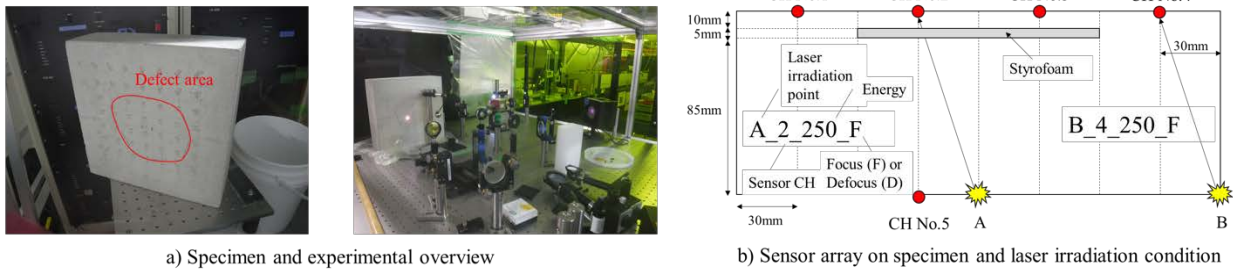


**Figure 3 Experimental overview and condition**

noted on each graph in Fig. 4. As the waveforms are very similar and the arrival time is almost compatible for both cases, the beam focusing condition such as  $14 \text{ J/cm}^2$  in the case of defocused and  $82.5 \text{ J/cm}^2$  in the case of focused (as found in Fig. 2), appears not influence on the arrival time neither do source identification. Accordingly, attenuation of amplitude and P-wave arrival time delay are confirmed when the defect disturbs the propagation-path, compared the results with A to #2 path and those with B to #4 path. In addition to the previous excitation points A and B, another point C is added and P-wave arrival time differences between paths among A-C and sensor #1-4 are picked up and the velocity distribution is finally obtained as shown in Fig. 5. Note, laser impact of irradiation of 250 mJ energy and focused beam condition are used for the measurement to implement the tomography analysis.

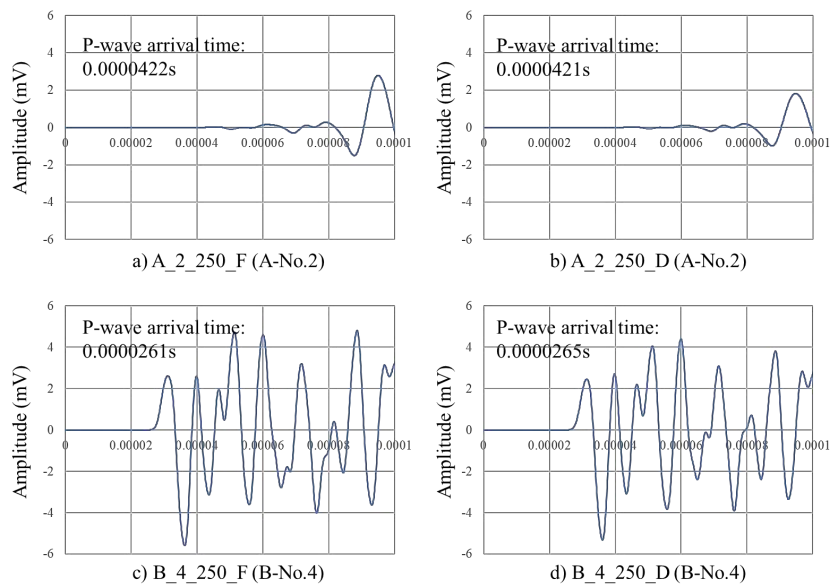


**Figure 4 Detected waveforms with 250mJ laser energy**

In the result of wave velocity tomography, it is generally recognized that the lower elastic-wave velocity appears the more serious deterioration, and styrofoam (simulated defect) embedded location is thus assumed. As in Fig. 5, the tomography result clearly indicates the width of defect; however, as for the depth, the result does not provide the required graphic resolution. In addition, the bottom area gives low velocity (2500 to 3000 m/sec), instead of intact condition. Those errors might be obtained due to poor ray path density than of other areas, resulting in less information of propagation paths into the computation process such as P-wave arrival time and so for the velocity. As for the surface wave, Fig. 6 shows the waveforms and FFT spectrums at sensor #5 when the excitation is generated at B with 250mJ energy. The results of 30kHz and 60kHz resonant frequency detected at almost the same location are demonstrated

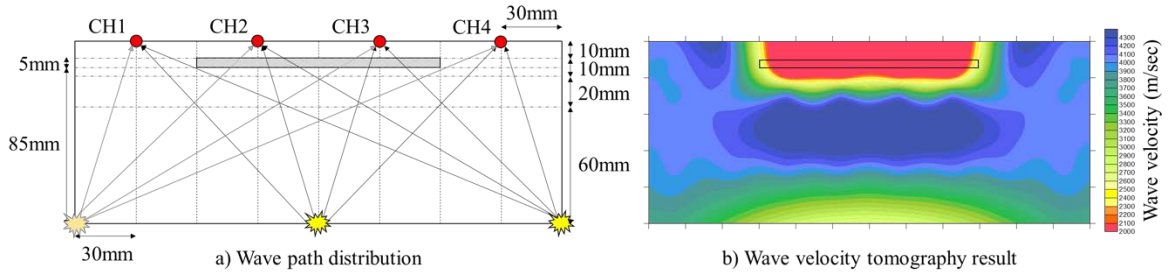


**Figure 5 Wave path and velocity distribution**

as in Fig 6a and b, respectively. Although the prominent peak frequencies are different depending on the sensors' frequency response, arrival times for the both cases appear compatible. The time-frequency spectrums with wavelet transform are shown in Fig. 7. It is obvious that times showing frequency peak are different in the specific frequency adapted. The arrival time of the peak for about 25 kHz, e.g., is about 160-170  $\mu$ s resulting in 900 m/s of wave velocity having wavelength of 3.6 cm. It is reported that the peculiar frequencies' dispersion i.e., the frequency providing different wave velocity to others suggests the existence of anomaly inside of materials of interest, and therefore the internal damage might be characterized by the surface wave dispersion. [7][8].

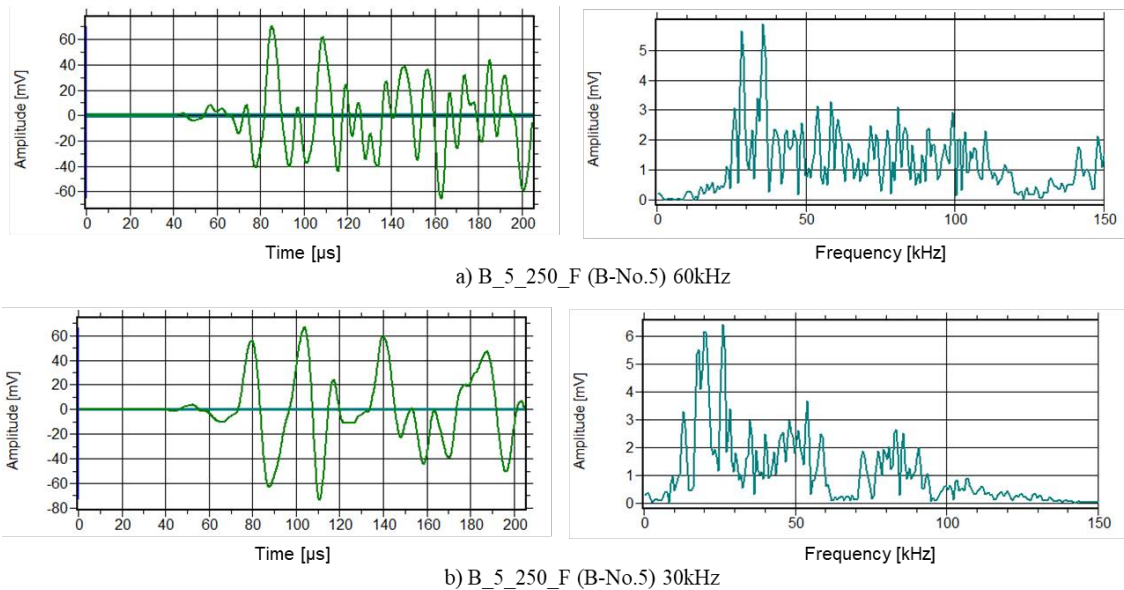


**Figure 6 Waveforms and FFT spectrum at No.5 when irradiated at B**

#### 4. CONCLUSION

Impact laser system was introduced for high-power pulse, which irradiates the concrete surface to generate vibrations. Non-contact elastic wave excitations by acoustic emission due to the laser impact was induced and wave velocity tomography was applied for detecting defects in concrete. Amplitude and P-wave arrival time were analyzed between the ray paths of the propagated elastic waves through concrete w/o simulated defect. Since laser-induced elastic wave for the technique was sufficiently applicable to AE excitation, leading to induce elastic waves in concrete, visualization of internal defect by means of tomography technique was successfully conducted. In addition, it was inferred that internal damage might be suggested by the dispersive behavior of surface wave, implying the potential of surface wave tomography

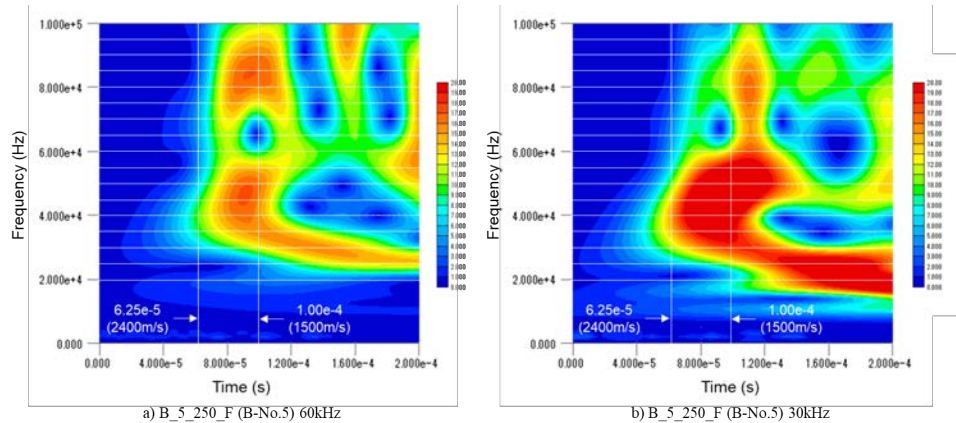


**Figure 7 Time-Frequency spectrum with wavelet transform**

enabling visualization of the internal damage based on one-side access monitoring using laser measurement techniques.

## REFERENCES

- [1] Y. Kobayashi, T. Shiotani, D. G. Aggelis, H. Shiojiri. (2007). "Three-Dimensional Seismic Tomography for Existing Concrete Structures", *Proceedings of Second International Operational Analysis Conference, Vol. 2*, pp. 595-600.
- [2] H. Akaike, (1974). "Markovian representation of stochastic processes and its application to the analysis of autoregressive moving average processes", *Annals of the Institute of Statistical Mathematics Vol.26, No.1*, pp.363-387.
- [3] H. Zhang, C. Thurber, C. Rowe, (2003). "Automatic P-Wave Arrival Detection and Picking with Multiscale Wavelet Analysis for Single-Component Recordings", *Bulletin of the Seismological Society of America, Vol. 93, No. 5*, pp. 1904-1912.
- [4] S. Osawa, T. Shiotani, H. Kitora, Y. Momiyama, (2014). "Damage Visualization of Imperfectly-Grouted Sheath in PC Structures", *31st Conference of the European Working Group on Acoustic Emission*, DGZfP, Berlin, Germany, <http://www.ewgae2014.com/portals/131/bb/fr1b3.pdf>.
- [5] K. Sassa, Y. Ashida, T. Kozawa M. Yamada, (1989). "Improvement in the Accuracy of Seismic Tomography by use of an Effective Ray-Tracing Algorithm", *MMIJ/IMM Joint Symposium Volume Papers*, pp.129-136.
- [6] S. Kurahashi, K. Mikami, T. Kitamura, N. Hasegawa, H. Okada, S. Kondo, M. Nishikino, T. Kawachi, Y. Shimada, (2018). "Demonstration of 25-Hz-inspectionspeed laser remote sensing for internal concrete defects", *Journal of Applied Remote Sensing, Vol. 12, No. 1*, doi: 10.1117/1.JRS.12.015009.
- [7] Wen-Hsiang Tsai, Yu-Ting Liu, Yiching Lin, Yu-Feng Lin (2014), "Detecting the Depth of Concrete Deterioration Using Rayleigh Wave Dispersion Based on Time-Frequency Analysis", *Proceeding of 11<sup>th</sup> European Conference on Non-Destructive Testing (ECNDT2014)*, [https://www.ndt.net/events/ECNDT2014/app/content/Paper/411\\_Lin\\_Rev1.pdf](https://www.ndt.net/events/ECNDT2014/app/content/Paper/411_Lin_Rev1.pdf)
- [8] N. Okude, T. Nishida, T. Shiotani, (2016). "A Basic Study of Elastic-Wave Based Inspection technique for Evaluating Rebar-Concrete Interface Conditions", *Proceedings of IAES-23, IIIAE2016 Kyoto and ICAE-8*, pp. 551-554.

# Damage Quantification of RC decks by Means of Rain-Induced AE Excitations and Source Location Bias

Tomoki Shiotani<sup>1</sup>, Katsufumi Hashimoto<sup>1</sup>, Kazuo Watabe<sup>2, 3</sup>  
and Hidefumi Takamine<sup>2, 3</sup>

<sup>1</sup> Dept. Civil & Earth Resources Engineering, Kyoto University, Kyoto, 615-8540, Japan

<sup>2</sup> Research & Development Center, Toshiba Corp., Kawasaki, 212-8582, Japan

<sup>3</sup> NMEMS Technology Research Organization, Chiyoda-ku, Tokyo, 101-0026, Japan

## ABSTRACT

It is very important nowadays to establish economic and appropriate management systems for ageing concrete infrastructures, in order to guarantee the performance and safety with identifying severe deterioration through their service life. As it is imperative for the damage evaluation of infrastructures to establish an efficient non-destructive testing (NDT), an acoustic emission (AE) tomography technique has been developed. The AE tomography estimates wave velocity distribution, which is supposed to be decreased as the damage progresses, inside the reinforced concrete. The AE tomography combines an iterative AE source location algorithm with travel-time tomography to produce a visualization of the elastic wave velocity. However, since the computation for the elastic wave ray-trace algorithm considering all potential detours of elastic waves takes up much time, and in case that only a few AE signals are detected, AE tomography technique does not always work efficiently. In this paper, AE signals induced by rain droplets on surface of reinforced concrete (RC) deck are utilized as elastic waves' excitations, and wave velocity and attenuation tomography assuming linear ray paths are performed in conjunction with AE source locations. Accordingly, in consideration of AE source location bias caused by sensor array such as sensor distance and coordination, rain-induced elastic waves lead to thousands of AE events after in-situ measurement for a few minutes. Consequently, the tomography results show accurate and time-saving analysis to detect the cracked area and quantify the damage in the RC deck.

**Keywords:** acoustic emission, rain, RC deck, crack, tomography, source location

## 1. INTRODUCTION

Utilizing AE monitoring, an efficient method for inspection of RC bridge decks is developed by using rain-induced AE signals, although the rain signals are considered as noise and removed in terms of AE signal detections from RC structures in service. When raindrops hit the road, elastic waves are generated on the surface and travel through the deck to AE sensors attached on the undersurface of the deck. Since it is assumed that raindrops fall uniformly over the entire road top surface, the AE source locations should show a uniform distribution where the deck is not damaged. On the other hand, the source distribution in cracked areas appears to be sparse or vacant and estimated density of the elastic wave sources by location analysis is expected to reveal the existence of cracks inside. Also, the computation technique of source location is introduced in order to provide an appropriate diagnosis system for damage quantification of RC decks by means of the rain-induced AE excitations.

The present authors have studied AE tomography techniques based on elastic-waves to visualize the internal defects in concrete. With AE tomography, it can reasonably be assumed that lower elastic-wave velocity and higher attenuation rate correspond to heavier deterioration.

The AE tomography estimates wave velocity and attenuation rate distribution which is supposed to be decreased as the damage progresses in the targeted structure. It combines an iterative AE source location algorithm with travel-time tomography to produce a visualization of the damage property. However, AE source location results based on the conventional AE source location algorithm are biased for most events, because of the sensor arrangements. The source location bias gives a certain error to the tomography results as a function of AE source numbers, locations and elastic wave ray-path density. This study investigates and provides an appropriate diagnosis system for damage quantification of RC decks by means of the rain-induced AE excitations and the tomography technique.

## 2. ATTENUATION AND WAVE VELOCITY TOMOGRAPHY PROCEDURE

Assuming that the propagation path of P-wave is a straight line, the tomography analysis via the attenuation-rate and the wave-velocity distribution was carried out in order to identify the horizontal cracks in RC slab. The source locations of all AE events are used as input, where a constant wave velocity (m/s) and attenuation-rate (dB/m) across the tested member is assumed for calculation. The amplitude and the excitation time at the source of the considered AE event is estimated on the basis of the arrival times and the amplitudes recorded by the sensors. The attenuation rates and wave velocities along all straight ray-paths between the source and the receiving sensors are computed.

The algorithm for AE source location is based on the Inglada's method, which is used in seismic engineering for locating the epicenter of earthquakes [1,2]. By assuming a constant wave velocity inside the tested specimen, the source location of an AE event is determined from the arrival times of their associated elastic waves at the locations of several sensors. In this paper, 3000 m/sec was set as the constant value in consideration of averaged speed in intact and deteriorated concrete.

For each AE event, the peak amplitude of the elastic wave at the source is unknown. Consequently, it can be approximated to calculate wave velocity and attenuation rate along the considered wave paths. In the tomography algorithm, the arrival time and the peak amplitude of the signal recorded by each sensor is plotted as a function of the distance between the source and the sensors. The linear regression between the arrival time and the peak amplitude of the elastic wave and the distance from the source is computed. The AE dispatched time and the peak amplitude at the source is referred to as equal to the value for the case that the distance is equal to zero.

Tomography computation is carried out based on elastic wave parameters with the velocity and the attenuation rate in this paper. In the tomography based on the attenuation, the analyzed area of interest must be divided into mesh elements characterized by their own wave velocities and attenuation rates. Then, a first estimate on distribution of the wave velocities and the attenuation rates is to be provided as input. By comparing those values along each wave path to its calculated value of the assumed distribution, the SIRT algorithm can lead to proper distribution of the wave velocities and the attenuation rates. The measured travel time and attenuation rate along each ray path is estimated from Eq. (1).

$$AR_{measured,i} = \frac{A_{source} - A_{sensor,i}}{\sum_j^{N_i} d_{i,j}} \quad (1)$$

where,  $AR_{measured,i}$ : measured average attenuation rate along the wave path from the source to the  $i^{th}$  sensor,  $A_{source}$ : estimated peak amplitude of the elastic wave associated to the considered AE event at its source,  $A_{receiver,i}$ : peak amplitude of the elastic wave measured at the  $i^{th}$  sensor,  $N_i$ : mesh number of elements crossed by the wave path from the source to the  $i^{th}$  sensor and  $d_{i,j}$ : length of the wave path from the source to the  $i^{th}$  sensor in the  $j^{th}$  element.

Second, the attenuation rate along each wave path based on distribution of the attenuation rates in the mesh elements is computed by Eq. (2).

$$AR_{calculated,i} = \frac{\sum_j^M AR_j \cdot d_{i,j}}{\sum_j^M d_{i,j}} \quad (2)$$

where,  $AR_{calculated,i}$ : calculated average attenuation rate along the wave path from the source to the  $i^{\text{th}}$  sensor (dB/m),  $AR_j$ : attenuation rate in the  $j^{\text{th}}$  element (dB/m) and  $M$ : mesh number of elements crossed by the ray path from the source to the  $i^{\text{th}}$  sensor.

Afterwards, the difference between the measured and the calculated attenuation rates is calculated for each wave path by using Eq. (3).

$$\Delta AR_i = AR_{measured,i} - AR_{estimated,i} \quad (3)$$

In a similar manner to Eq. (1), the differences of the attenuation rates on all the wave paths are estimated by Eq. (4).

$$\Delta AR_j = \frac{\sum_{i=1}^N \Delta AR_i \cdot d_{i,j}}{\sum_{i=1}^N d_{i,j}} \quad (4)$$

where  $N$ : the number of wave paths crossing the  $j^{\text{th}}$  element. The attenuation rate in each element is then updated with Eq. (5).

$$AR_{j,updated} = AR_j + \Delta AR_j \quad (5)$$

The procedure from Eq. (2) through Eq. (5) is repeated until the convergence is reached. As for wave velocity as the parameter of SIRT algorithm, the same manner as attenuation rate is applied for computing wave velocity distribution in the area of interest and analyzed.

### 3. RAIN-INDUCED AE DETECTION AT EXISTING RC BRIDGE DECK

A real RC bridge deck was selected as study targets which has deterioration such as rebar corrosion, breaking by salt damage, and deck fatigue. AE measurement was carried out in the RC bridge deck. 15 AE sensors are set on the bottom side of RC bridge decks. Resonance frequency of AE sensor is 30 kHz. AE sensors arrangement on the RC deck is shown in Fig. 1. Thickness of both RC bridge decks is 235 mm. Large crack with water leakage trace was confirmed. Threshold value of LUCY (location uncertainty) is set on 300 mm as half spacing of two adjacent sensors in this study. LUCY means source location accuracy and is the root-mean-square of the difference between calculated and observed distances between source and sensor [3].

The data was extracted during the rain peak and analyzed the source locations. Fig. 2 shows the AE source location results of the measured panel and the horizontal cracks located at 150 mm or less from the surface of the deck (mostly in the top layer) by visual inspection of the cored samples. Source locations considered to have low reliability has been filtered. The extracted data for only 700 seconds indicated enough amounts of AE sources for analysis are identified. In the figures, relatively low-density areas surrounded by dashed lines can be seen in the panel. Red line shows the sensor arrayed area. This low-density area is suspected to be heavily deteriorated, since AE is generated on the road surface and it travels through the deck and detected by the AE sensors attached on the bottom surface of the deck. Since raindrops hit all over the road surface uniformly, the AE source locations should show uniform distribution in the case of a sound deck. On the other hand, if severe damage like large horizontal crack is

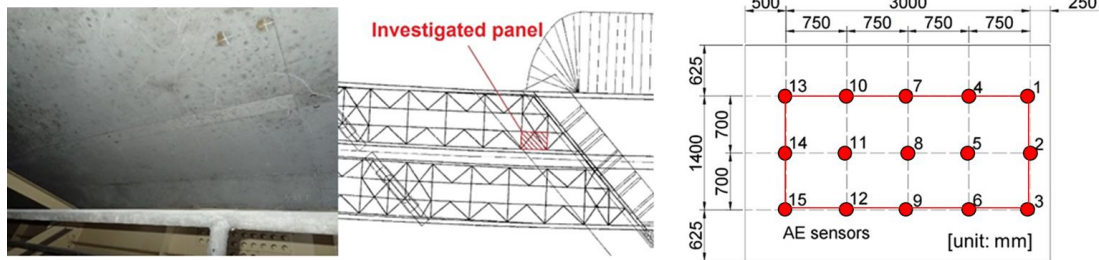


**Figure 1 Sensor arrangements for AE measurement on the real RC bridge decks**

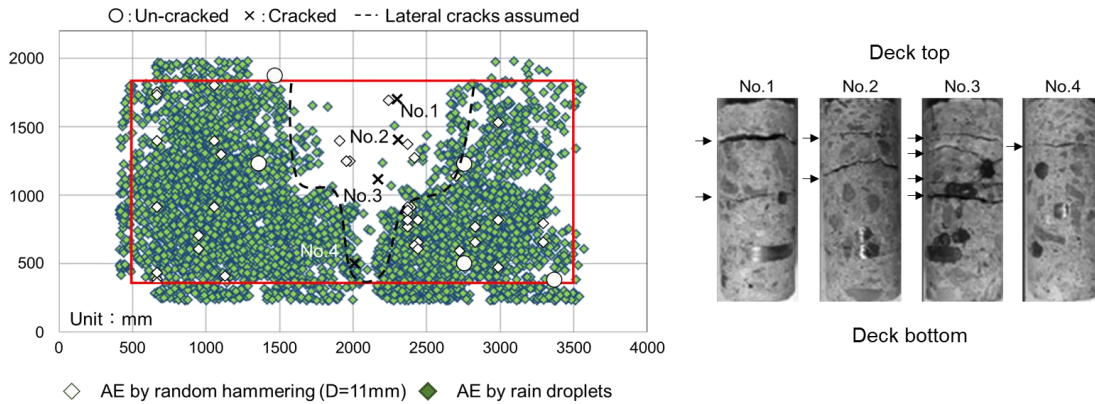


**Figure 2 Result of AE source location analysis**

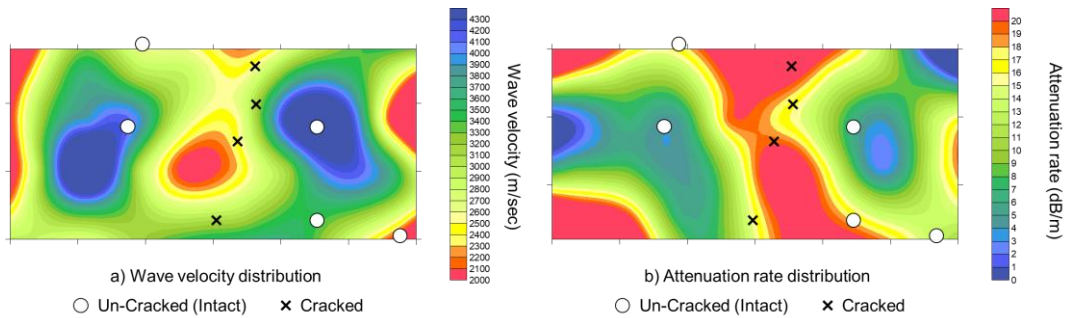


**Figure 3 Wave velocity and attenuation rate distribution**

inside the deck, as depicted in the figure, the AE generated at the road surface is attenuated, diffracted, or blocked by the crack. Consequently, AE sensors right under the crack receive fewer AE or don't receive rain-induced AE at all, and the source distribution under the crack would be sparse or vacant. Therefore, by calculating the AE source locations, the density of the AE sources would reveal the existence of the crack inside the deck. Since all AE sources generated by raindrops are in the plane of the road surface, the source locations can be estimated easily. Additionally, heavy rain generates large amount of hits on the road in a short time, and it realize the inspections with great efficiency.

#### 4. RAIN-INDUCED AE TOMOGRAPHY WITH WAVE VELOCITY AND ATTENUATION RATE

As expected, a sufficient number of rain-induced AE events respecting the quality criteria has been found as shown in Fig. 2. The wave velocity distribution by means of AE tomography, as explained above, in this panel has been successfully computed from these data and the results

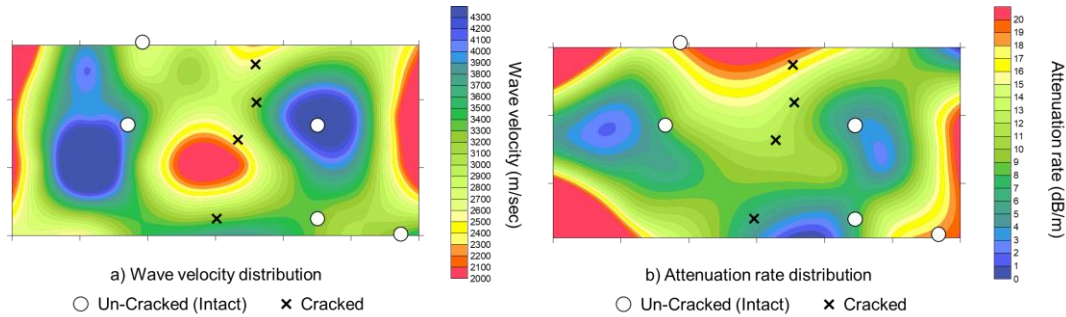


**Figure 4 Wave velocity and attenuation rate distribution ( $d=\sqrt{2}$ )**

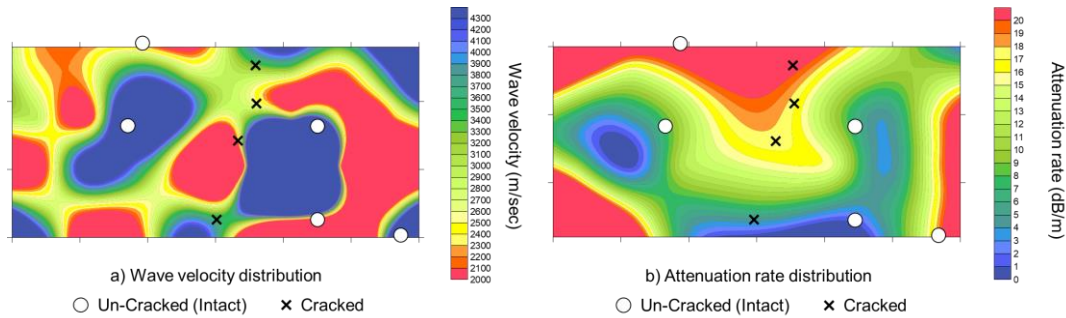


**Figure 5 Wave velocity and attenuation rate distribution ( $d=2$ )**

for the top layer of the deck, where the cracks were located, are presented in Fig. 3 for wave velocity tomography and attenuation rate tomography respectively.

The relatively low-density areas in the panel surrounded by dashed lines in Fig. 2 is supposed to be an extended horizontal crack [4]. The horizontal cracks were located at 150 mm or less from the surface of the deck (mostly in the top layer) by visual inspection of the cored samples. Therefore, it is reasonably understood that wave velocities and attenuation rate in top layer are lower than bottom layer. After all, in the tomography results, the soundness of concrete and the presence of horizontal crack roughly correspond to the wave velocity and the attenuation rate distribution. The wave velocity and attenuation rate inside the core samples presenting large horizontal cracks are generally lower than 2700 m/s and more than 20 dB/m at least over a certain part of their depth and the wave velocity inside the un-cracked core samples is generally higher than 2700m/s over their entire depth. The tomography computation was re-executed in consideration of sensor array coordination with different sensor distance. Longer sensor distance causes more source location bias, since AE hits are missed due to attenuation in the travel path.

While setting the sensor distance ratio at  $d=1$  as shown in Fig. 1, tomography results obtained by the sensor arrangements with  $d=\sqrt{2}$  and  $d=2$  are displayed in Fig. 4 and Fig. 5 with source location results. As the result, source locations are biased only in the enclosed central area with the 4 nearest sensors as shown in Fig. 6 ( $d=\sqrt{2}$ ) and Fig. 7 ( $d=2$ ). It is quantitatively indicated that longer sensor distance (less sensors) gives less ray path density, which directly means less data amount in the tomography computation, changing sensor distance from  $d=1$  to  $d=2$ , they are not exactly corresponding with the original result ( $d=1$ ). The threshold values for wave velocity of 2700 m/s and attenuation rate of 20 dB/m might lead to misjudge the presence of horizontal crack, however, it can be assumed in the tomograms that the middle part of targeted area is damaged. On the other hand, those findings and accuracy on damage detection in the results cannot be achieved when  $d=2$  for velocity distribution. Consequently, it is concluded in this paper that a limitation to perform an adequate resolution of tomography results followed by AE measurement depends on the sensor array.

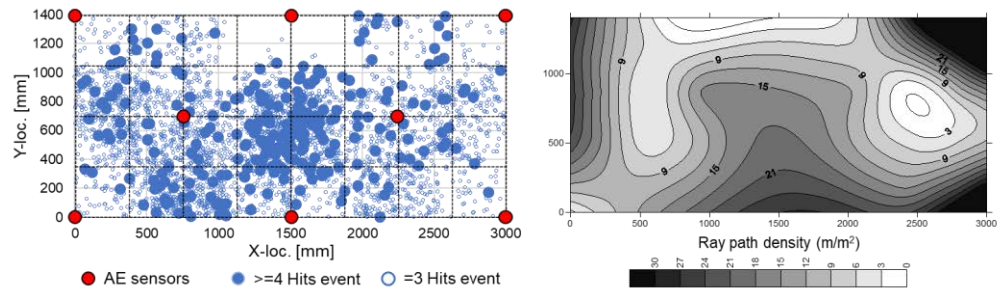


**Figure 6 Source location result and ray-path density distribution ( $d=\sqrt{2}$ )**

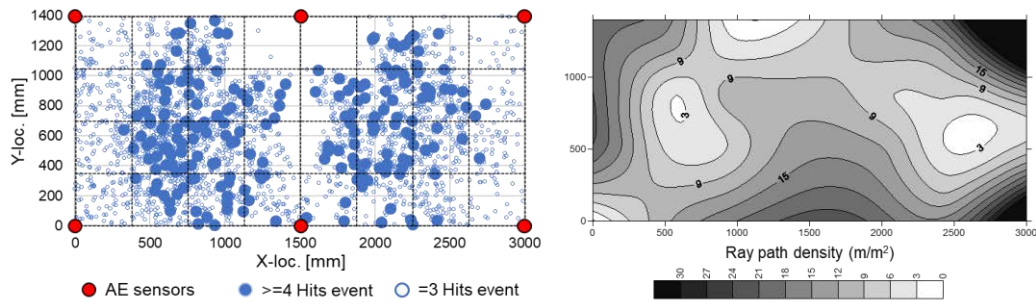


**Figure 7 Source location result and ray-path density distribution ( $d=\sqrt{2}$ )**

## 5. CONCLUSION

The elastic waves generated by the rain hitting the pavement surface can be recorded and used for reconstructing the wave velocity and the attenuation rate distribution inside RC slab. This method presents the advantage that a large number of AE events can be recorded in a very short period of time. Also, the computation technique assuming linear ray-paths enables to make the computation time drastically shorter than conventional ray-trace algorithm since the calculation process is undoubtedly simpler based on linear ray-paths without the detours. It is additionally believed that wave velocity and attenuation rate distribution can be calculated with hundreds or thousands of the rain-induced AE events more precisely than those results with using a few internal AE events such as secondary AE induced by traffic loading. Further investigation is needed to identify the appropriate sensor array in consideration of source location bias and the threshold value of elastic wave parameters, wave velocity and attenuation rate, to judge the damage in targeted structure when the proposed tomography technique is applied.

## REFERENCES

- [1] Salinas, V., Vargas, Y., Ruzzante, J. And Gaete, L., *Localization algorithm for acoustic emission*, *Physics Procedia*, Vol. 3, pp 863-871, 2010.
- [2] Ge, M., *Analysis of source location algorithms*, *J. Acoustic Emission*, Vol. 21, pp 14-28, 2003.
- [3] Hamstad, M.A., *Acoustic emission source location in a thick steel plate using Lamb modes*, *J. Acoustic Emission*, Vol. 25, pp. 194-214, 2007.
- [4] Takamine, H., Watabe, K., Miyata, H., Asaue, H., Nishida, T., Shiotani, T., *Efficient Damage Inspection of Deteriorated RC Bridge Deck with rain-induced AE Activity*, *Proceedings of IAES-23, IIIAE2016  $\beta$ Kyoto and ICAE-8*, pp.231-236, 2016.

# Development of Prestressed Concrete Bridge Tendon Damage Diagnosis System using Acoustic Emission Technique

Dong-Woo Seo<sup>a</sup>, Ga-Young Kim<sup>b</sup>, Ki-Tae Park<sup>b</sup>, Dong-Hyun Kim<sup>b</sup>, Yoon-Gi Hong<sup>b</sup>

<sup>a</sup>Korea Institute of Civil Engineering and Building Technology; <sup>b</sup>Rectuson Co., Ltd.

## ABSTRACT

In 2016, the prestressed cable (tendon) of the overpass bridge in Seoul was ruptured due to corrosion, resulting in severe traffic congestion, inconvenience and massive economic loss. It is estimated that the prestressed concrete type bridges will reach 1.8 billion USD, which is 50% of the annual budget in whole new bridge construction market in South Korea. Therefore, the efficient and economical inspection and monitoring technology to manage the tendon of the prestressed concrete bridge. The collapse of such structures can be prevented in advance, it is considered that the structural health can be greatly improved. The purpose of this study is to design the acoustic emission monitoring system and to determine optimal sensor type, quantity and installation location. In order to construct a low-cost acoustic emission monitoring system for tendon safety management of aging prestressed concrete bridges, both indoor and outdoor experiments were conducted to collect acoustic emission signals and to analyze its characteristics with several tendon damage scenarios. The final goal was to establish a low-cost system that installs the minimum sensor and detect the tendon damage remotely to the maintenance manager.

**Keywords:** Prestressed concrete bridge, tendon damage, non-destructive test, inspection, monitoring.

## 1. INTRODUCTION

In Korea, since the introduction of prestressed concrete (hereafter called "PSC") bridges, in the 1960s, 38% of the total bridge construction are PSC types. In particular, the number of old PSC structures over 30 years since the 1970 's "compression construction" is increasing rapidly [1].

In 2016, the tendon of a PSC type bridge, Jungungcheon overpass bridge, in the inner ring road of the Seoul Metropolitan City was damaged by corrosion, resulting in sever traffic congestion, civil unrest, inconvenience, and huge economic loss. It is estimated that the prestressed concrete type bridges such as the Jungungcheon overpass bridges will reach 2 trillion won (Korean currency), which is 50% of the 4 trillion won per year in the entire bridge construction market in Korea [2-3]. Therefore, the efficient and economical inspection and monitoring technology to manage the PCS bridge tendons are necessary. The collapse of the structure can be prevented in advance and the integrity of the structure can be greatly improved.

Currently, various non-destructive methods for detecting PSC bridge tendon damage are in research and development, but the field utilization is low due to low reliability and high cost. Acoustic Emission (AE) technique, which is a kind of nondestructive testing method, detects sound waves generated by artificial impact or steel material breakage with AE sensor and detects the sound source [4-5]. The AE technique is applicable to evaluate the degree of corrosion and fracture of stranded wire for the purpose of evaluating the safety condition of

bridges. The Korea Concrete Institute [6] conducted a study using the AE technique for the investigation of tendon failure of PSC bridges and the safety evaluation of bridges. This report describes the progression of tendon failure and corrosion, tracking the location of fracture of tensions due to the speed of sound waves, and establishing long-term monitoring system technology. Currently, it is evaluated as the most effective method applicable to PSC bridges worldwide. Therefore, in this study, the feasibility of applying the acoustic emission technique for the bridge cable safety management was experimentally examined.

## 2. EXPERIMENTS AND RESULTS

### 2.1 Laboratory test: signals from a strand

In this study, to determine the optimum type of AE sensor, tensile tests were carried out to measure the AE signal characteristics against the physical behavior until the moment of ultimate failure by applying a tensile force to the strand specimens (corrosion and mechanical damage) used in actual bridges. Tensile tests were carried out using a 100 ton UTM (Universal Testing Machine) of Korea Institute of Civil Engineering and Building Technology (KICT).

Two types of AE sensor are applied with 60 kHz and 150 kHz resonant type. The test specimens were carried out in two levels of corrosion condition and mechanical damage. The mechanical damage was applied to one wire of strand by using a grinder.

Table 1. Specimen description

Case	Note
Corrosion 1	Mass loss rate approximately 7.0%
Corrosion 2	Mass loss rate approximately 1.5%
Mechanical damage	Cross section loss on a wire by grinder

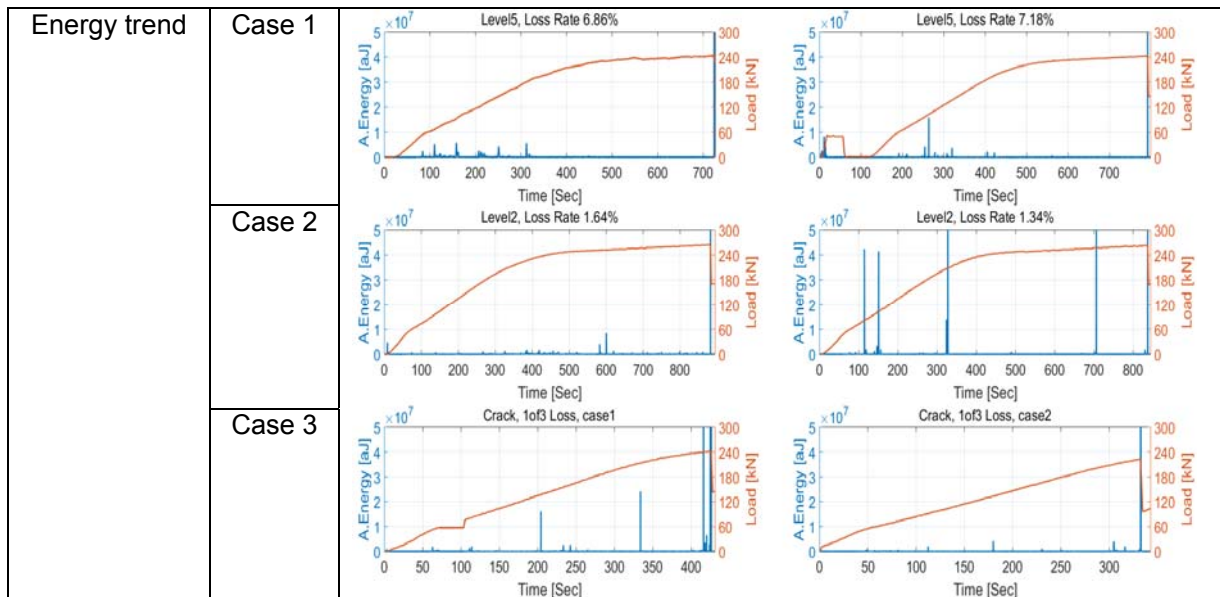
Table 2. Sensor types

Channel	Resonant frequency
1	60 kHz
2	150 kHz

Table 3. Specimen description: RMS trend

Specification	Result			
	Resonance frequency	60 kHz	Amplification ratio	40 dB
RMS trend	Case 1			
	Case 2			
	Case 3			

Table 4. Specimen description: energy trend



Experimental results show that the 60 kHz resonance sensor has superior sensitivity characteristics than the 150 kHz resonance sensor. In cases of corrosion (case 1 and 2), signal generation was confirmed at the loading point, but the signal was stabilized as tensile progressed and no special signal was detected until just before fracture. This is because the stranded wire with severe progress of corrosion is not separated from the cross section (inadequate signal generation from the AE point of view) and is only increased to just before the break. In the case of mechanical damage, the first specimen, which had a relatively large number of strand breaks, showed a significant signal in the tensile load applied just before fracture.

## 2.2 Field test: signals through concrete surface from tendon

Field test was conducted to PSC girder type Hongjecheon bridge in Seoul to confirm installation condition of on-site sensors, and installed AE test equipment to confirm signal response characteristics under real conditions. The Hongjecheon bridge is a PSC girder bridge of internal tension type. Since it is impossible to access to the actual tendon, the sensor is installed at the position close to the location of the tendon on the inner concrete surface.



Fig. 1 Field measurement and sensor installation

The AE system is based on a portable PC that can be moved as shown in the figure above, making it easy to access the site. The AE sensor was installed on a concrete surface with a metal plate and then mounted on a magnetic holder.

Table 5. Specimen description

Channel	Amplification ratio	Resonant frequency
1, 4	40 dB	60 kHz
2, 5	40 dB	150 kHz
3, 6	40 dB	Wideband(100~900 kHz)

The sensor was installed at a distance of 10 m to the left and right from the AE system, and the signal was generated by hitting the concrete surface with a hammer while changing the distance from the sensor by 1 m. The sensor was installed with six 60 kHz resonance type, 150 kHz resonance type, and wide band type (100 ~ 900 kHz) one by one on the right and left sides, respectively.

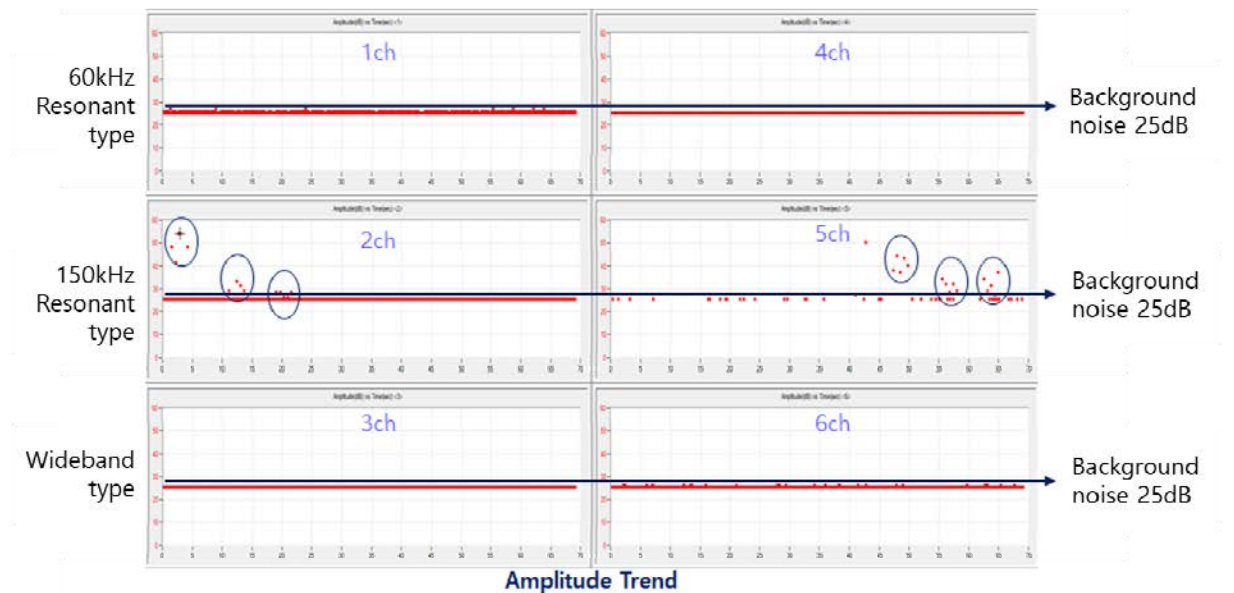


Fig. 2 Test results

It has been confirmed that there is no additional environmental noise other than 25 dB. It was confirmed that the signal difference between the AE sensor and the background noise was 150 kHz resonant type and the signal attenuation was considerably large because the signal was not detected at the position apart from 3 m or more. Further tests will be carried out by diversifying the collection conditions and test methods based on the 150 kHz resonance sensor.

### 3. CONCLUSIONS

Considering both concrete and internal tendons, which constitute the prestressed concrete bridge, the acoustic emission sensors were selected considering the characteristics of concrete

and tensile members (i.e., tendons). The results show that the 150 kHz resonance type sensor is the best for the concrete, and the 60 kHz resonance type sensor is the most sensitive for the direct measurement to the tendon system.

The sensor installation location was selected based on the on-site survey results, and it was planned that the monitoring would be 12 channels for the inner tension type and 12 channels for the outer tension type based on one box girder. However, there is a need for additional research as to how to arrange and install the sensors to check the condition of the tendon system.

Table 6. AE Sensor Specifications for direct measurement from a strand

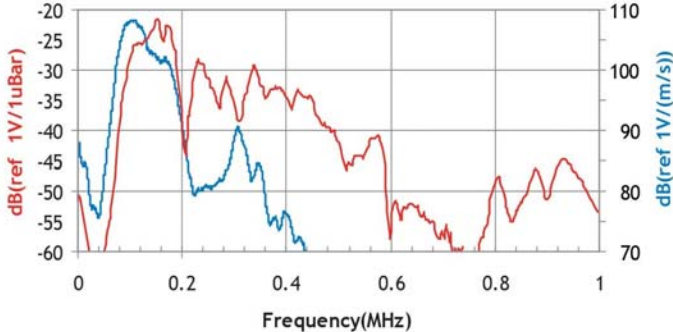
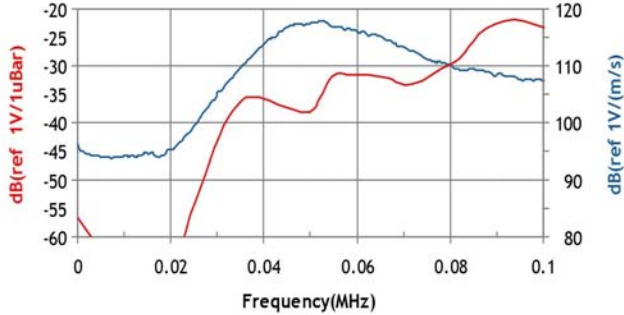
Physical specification	Case Material : Stainless Steel Face Material : Ceramic Shock Limit : 500g Connector Locations : Side	
Resonant frequency	150 kHz	
Pre-amplifier	Integral Pre-Amplifier 40dB	
Calibration sheet		

Table 7. AE Sensor Specifications for measurements through concrete surface

Physical specification	Case Material : Stainless Steel Face Material : Ceramic Shock Limit : 500g Connector Locations : Side	
Resonant frequency	60 kHz	
Pre-amplifier	Integral Pre-Amplifier 40dB	
Calibration sheet		

#### **4. ACKNOWLEDGEMENTS**

This research was supported by the internal projects (20190115-001) supported by the Korea Institute of Civil Engineering and Building Technology.

#### **5. REFERENCE LINKING**

1. Korea Infrastructure Safety and Technology Corporation, "Cable inspection and damage cases of cable supporting bridges", 2016.
2. Fallis, G. and Peeler, M., "Non destructive detection of fractures in prestressed and post-tensioned cables," PTI Journal, 2009.
3. DaSilva, M., Javidi, S., Yakel, A. and Azizinami, A., "Nondestructive method to detect corrosion of steel element in concrete, The Nebraska Department of Roads", USA, 2009.
4. Federal Highway Administration, "Corrosion monitoring research of New York City bridge," FHWA Publication No.: FHWA-HRT-14-024, December, 2013.
5. Colony, C., Rogers, D., Nims, D. and Bradley, J., "Investigation, Proposed Rehabilitation and Application of a Corrosion Sensor to the Anthony Wayne Bridge Suspension Cables," International Cable Supported Bridge Operator's Conference, Halifax, Canada, 2016.
6. Korea Concrete Institute, "Development of acoustic emission techniques for preventing sudden collapse of prestressed concrete bridges," Final report, pp.14-43, 2006.

# Development of Structural Health Monitoring Technology for Internal Tendon of PSC Bridge Using Acoustic Emission Technology

Dong-Hyun Kim<sup>a</sup>, Yoon-Gi Hong<sup>a</sup>, Dong-Woo Seo<sup>b</sup>, Ki-Tae Park<sup>b</sup>

<sup>a</sup>RECTUSON. Co., LTD., 51756 12-1, Gaposinhangnam-ro, Masanhappo-gu, Changwon-si, Gyeongsangnam-do, Korea.

<sup>b</sup>Korea Institute of Civil Engineering and Building Technology, 283, Goyangdae-ro, Ilsanseo-gu, Goyang-si, Gyeonggi-do, 10223, Korea.

## ABSTRACT

The necessity of safety diagnosis of structures has recently been emphasized due to the aging of public PSC bridges over 20 years. Tendons consist of external tendon and internal tendon type. External tendon types are already undergoing inspection and repair through visual inspection and general non-destructive methods in case of problems. However, internal tendon-type PSC bridges are buried in the concrete filled with grout to prevent corrosion of stranded strand, and after the severe damage caused by corrosion, there is no inspection method that can be confirmed. Acoustic emission technology has attracted attention recently as a technology capable of diagnosing defects of large structures and locating defects. The acoustic emission technique was used to detect the failure state of the internal tendon of the PSC bridge and to analyze the defect signal transmitted through the tendon to find the degree of damage and the location of the defect. The purpose of this study is to evaluate the integrity of the tendon by distinguishing the general signal from the concrete and the defect signal from the internal tendon. Average frequency and RA value were used as parameters for fault diagnosis and analysis. In addition, RTRI and Ib Value were applied for the evaluation of defectiveness and Integrity. Finally, in this study, it was confirmed that diagnosis of internal tendon of PSC structure is possible by analyzing the acoustic emission characteristic signal generated in the PSC structure at the time of load application.

**Keywords:** Acoustic emission, PSC bridge, internal tendon, Structural Health Monitoring.

## 1. INTRODUCTION

Prestressed concrete (PSC) has been widely applied to the construction of structures such as overpasses in the form of supporting the upper structure by pre-stressing the concrete using the stranded material. Since the late 1960s, corrosion and rupture of tensional materials have occurred in many European and North American countries and have been continuously maintained for structures constructed using the PSC method. [1-2]

Recently, there have been many researches on the detection of early defects to secure diagnosis technology and to prevent the breakage of tensions due to the social issue of securing the safety of these structures. [3]

The purpose of this study is to propose the health monitoring method of the tendon by applying acoustic emission technology to determine whether the PSC girder bridge is damaged. The following researches were carried out to achieve this research objective. First, the correlation analysis between the average frequency and the RA value is proposed as the acoustic emission

parameter for the PSC structure diagnosis. [4-6] Second, In order to determine the presence or absence of defects, RTRI [7] and Ib Value [8-9] were used to evaluate the acoustic emission parameters for PSC structure diagnosis. Finally, it was confirmed that the integrity evaluation of the internal tendon is possible by analyzing the acoustic emission characteristic signal issued at the time of load application by preparing the normal and defect samples of the tendon for the health monitoring of the PSC structure.

## 2. EXPERIMENTAL SETUP

### 2.1 Experiment of PSC structure defect detection

Load test was carried out for PSC structural specimens. PSC structural test specimens are shown to have internal PSC type, and a total of three specimens were tested for two damaged PSC beams and one normal PSC beams. This confirmed the possibility of detection of already damaged tendons. The left side of Fig. 1 is a photograph of the site at the time of the experiment.



Fig.1 PSC structure defect detection experiment (left) and on site installed PSC structure (right)

Detailed specifications of the PSC structural specimen are as follows. Experiments were carried out on PSC beams 1 and 2. Table 1 shows the specifications of the PSC structure test specimen.

Table.1 Specification of PSC Structure

Name	Specification			Placement of tendons			Type of damage
	Length	Width	Hight	Normal	Damage	Total	
PSC-1	6,350	300	600	2	0	2	-
PSC-2	6,350	300	600	0	2	2	Mechanical damage
PSC-3	6,350	300	600	0	2	2	Corrosion

The right side of Fig. 1 shows the on-site condition of the PSC structure test specimens. The PSC beam that performed the experiment is the left two. The AE sensor uses a total of 8 channels, the 60 kHz resonance type for the four channels installed in the anchorage, and the 150 kHz resonance type for the four channels attached to the concrete surface. Table 2 shows the sensor information used in the experiment.

Table.2 Specification of AE sensor

Channel	Amplification Ratio	Resonance Frequency	Installation Location
1ch, 3ch, 5ch, 7ch	40dB	60kHz	Anchorage
2ch, 4ch, 6ch, 8ch	40dB	150kHz	Concrete Surfaces

As shown in left side of Fig. 2, the AE signal was measured while gradually increasing the load on the PSC beam. The reference weight of 1Ton was stacked on the PSC beam one by one, and the reference weight was stacked up to 4 for one PSC beam. AE Activity observation and signal acquisition during maintenance time were performed with a load holding time of about 10 minutes for each reference weight increase. The left side of Fig. 2 shows the installation of a reference weight on the specimen for load application.

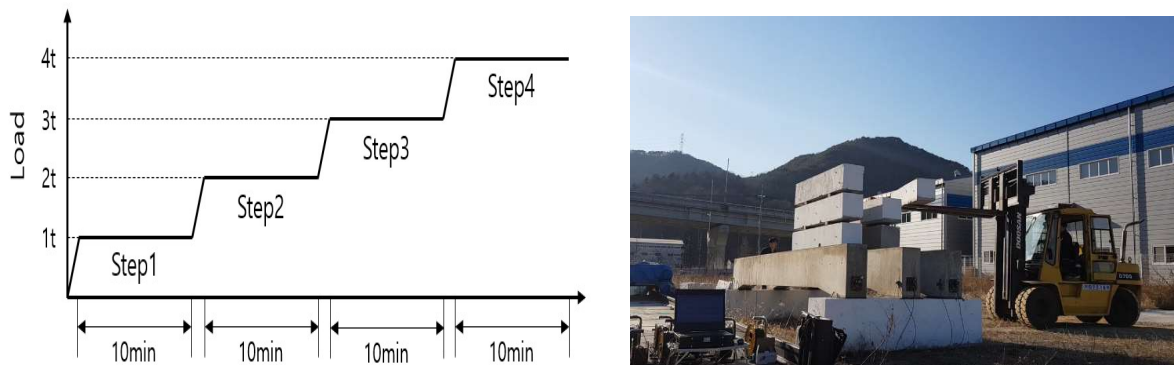


Fig.2 Load cycle for experiment (left) and Installation of reference weight for load application (right)

## 2.2 AE Activity

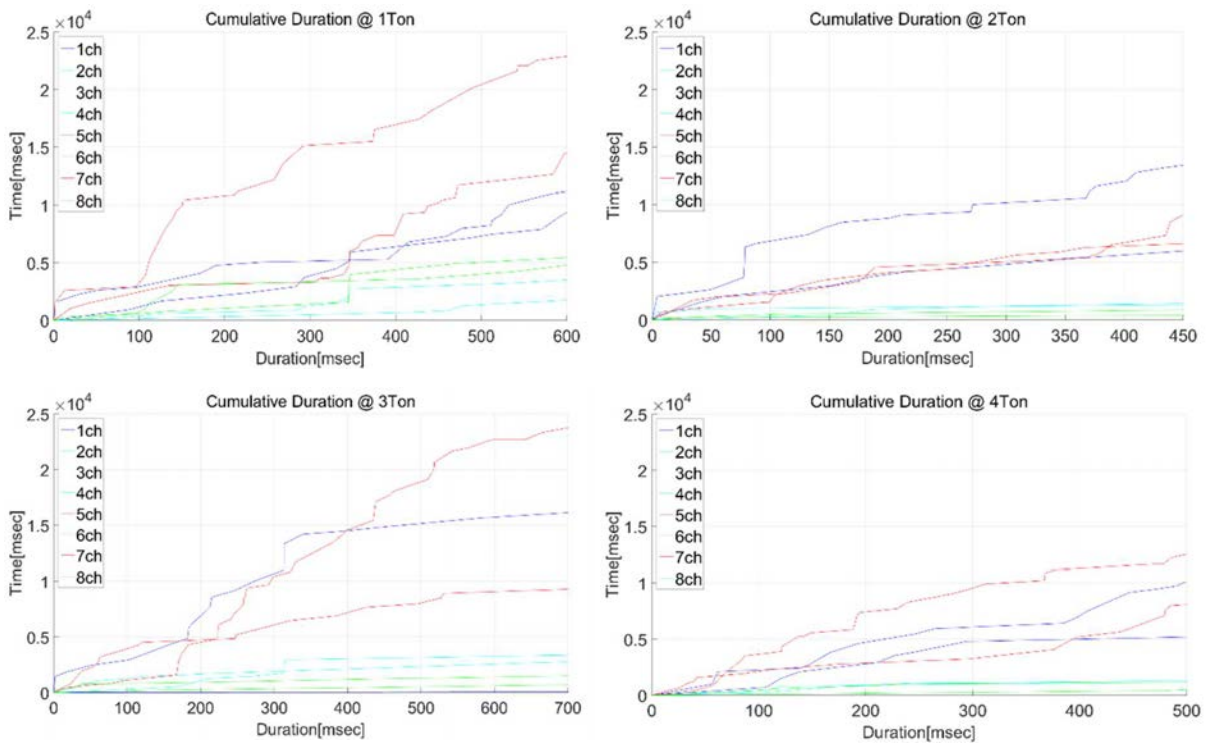


Fig.3 Cumulative Duration (from 1 ton to 4 ton)

Fig. 3 is a graph showing cumulative durations measured during each holding time (1 ton to 4 ton). It can be seen that the signal persistence of the sensor channel installed in the relatively defect PSC test specimen is larger. Exceptionally, the signal persistence of channel 3 tends to be noticeably large among the sensors installed in the normal PSC test specimen, but the same signal does not tend to appear in channel 1 installed on the opposite side.

### 2.3 Average Frequency vs RA Value

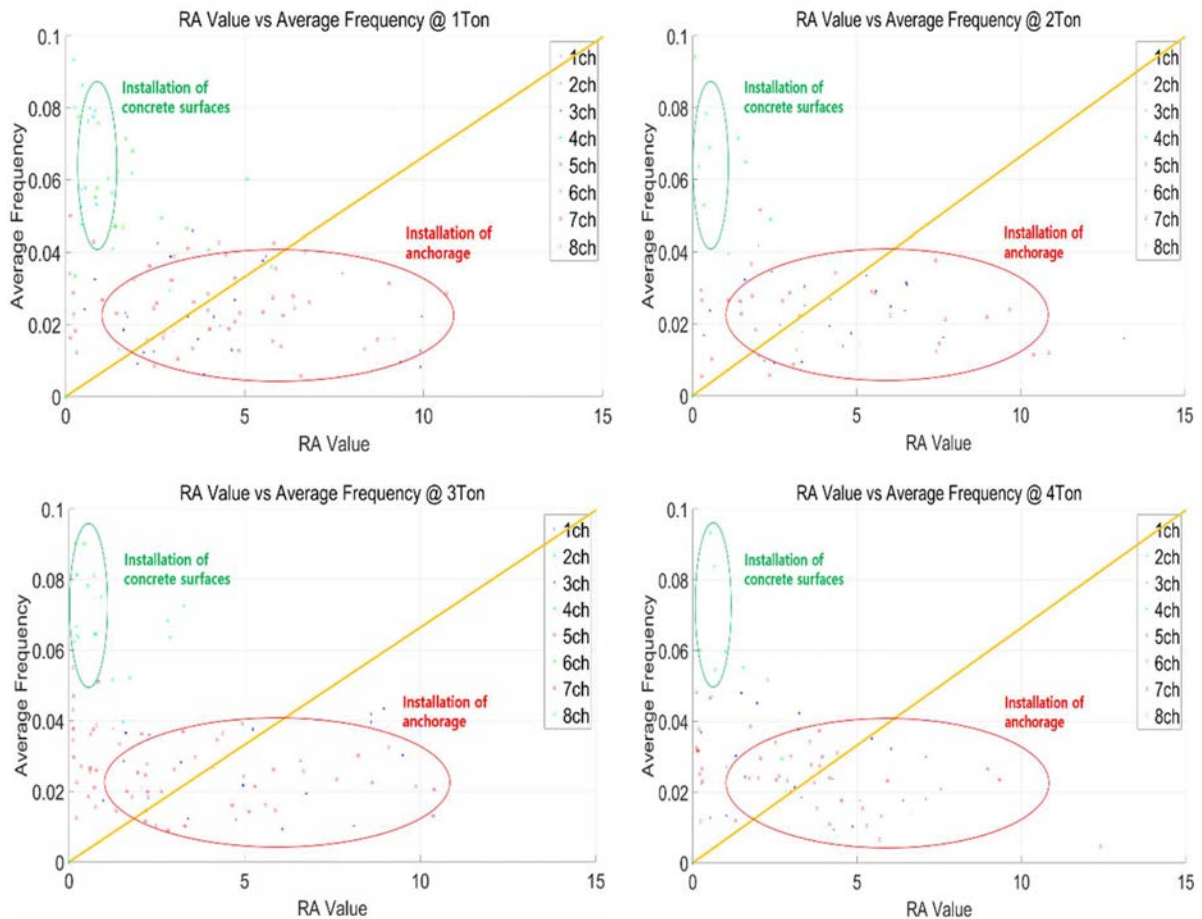


Fig.4 Average Frequency vs RA Value

Fig. 4 shows the correlation between the average frequency and the RA value of the measured signal. The results of the sensor installed on the tendon anchorage - 1ch & 3ch (normal), 5ch & 7ch (defective) - and the sensor installed on the concrete surface - 2ch & 4ch (normal), 6ch & 8ch (defective) - are distinguished from each other. This tendency is judged by the secondary AE activity [10] that occurs when the load is applied to the strand where the fracture occurs, which is prominent in the defective PSC specimen. Secondary AE activities are mainly characterized by shear cracks.

## 2.4 RTRI Value

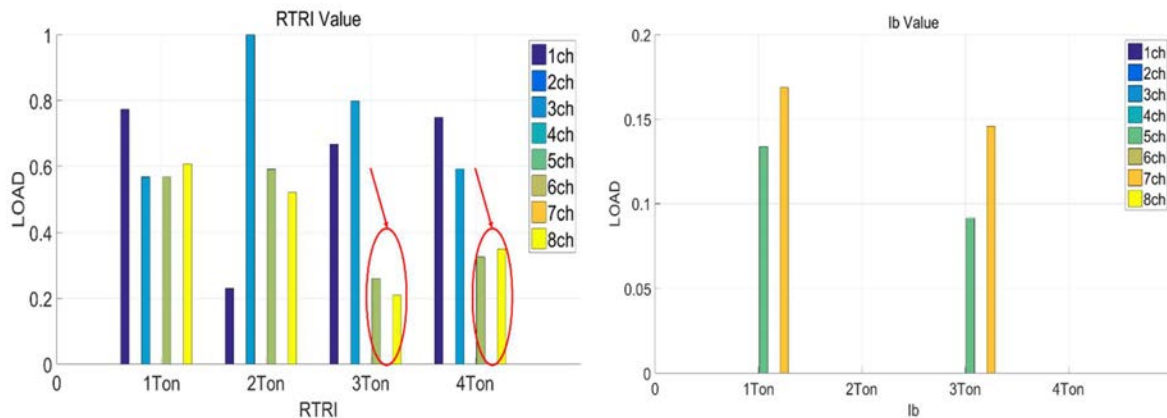


Fig.5 RTRI (left) and Ib Value (right) analysis

The left side of Fig. 5 shows the result of analyzing only the RTRI of the sensor installed on the tendon anchorage separately. When the defective PSC specimen was compared with the normal PSC specimen, it was confirmed that the RTRI was smaller and the tendency was decreased as the load increased. However, in the case of a 2-Ton load, exceptions such as 1 channel, which are smaller than those of normal specimens, were also confirmed.

## 2.5 Ib Value

Ib Value was confirmed only in 5ch and 7ch installed on the defective PSC anchorage for 1Ton load and 3Ton load as shown in the right side of Fig.5. This is because the strand in the tendon is partially destroyed and it is judged as a signal that the instability of the structure is proactively displayed. Further experiments are needed to determine if there is reproducibility on the same a1, a2 constant criteria.

## 3. RESULTS

In this study, the integrity evaluation using the acoustic emission technology was performed for the safety diagnosis of the internal tendon of the PSC structure, and the following conclusions were drawn. Acoustic emission activity analysis showed that cumulative duration signals were measured largely in defective PSC specimens. However, the channel (3ch) in which the larger signal was generated in the normal PSC specimen appeared, and it was judged that it is difficult to distinguish the normal and defective only by the simple signal amplitude. RA value and average frequency shows the difference in the signal characteristics between the channel installed in the anchorage and concrete. RTRI Value As a result, RTRI of defective PSC test specimen was low only for the channel installed on the anchorage area. However, since there is an exceptional signal channel (1ch), it is necessary to establish a standard for repeated testing. Ib Value analysis, signals were observed in some load sections (1, 3Ton) only for the channels installed on the anchorage, which is considered to be a preceding signal for the structural anomaly. Since the results of this study are analyzed by one experiment, it is necessary to confirm the reproducibility of the same phenomenon through repeated experiments and to conduct a follow - up study on establishment of clear criteria through data accumulation.

#### 4. REFERENCES

- [1] Laura Anania, Antonio Badala, Giuseppe D'Agata, Damage and collapse mode of existing post tensioned precast concrete bridge: The case of Petrulla viaduct, *Engineering Structure*, Vol.162, pp.226-244 (2018)
- [2] Wei-Hua Hu, De-Hui Tang, Jun Teng, Samir Said, Rolf. G. Rohrmann, Structural Health Monitoring of a Prestressed Concrete Bridge Based on Statistical Pattern Recognition of Continuous Dynamic Measurements over 14 years, *MDPI/Sensors*, Vol.18, 4117 (2018)
- [3] Pablo M. Paez, Beradi Sensale, Improved prediction of long-term prestress loss in unbonded prestressed concrete members, *Engineering Structure*, Vol.174, pp.111-125 (2018)
- [4] Arash Behnia, Hwa Kian Chai, Tomoki Shiotani, Advanced structural health monitoring of concrete structures with the aid of acoustic emission, *Construction and Building Material*, Vol.65, pp.282-302 (2014)
- [5] Hisham A. Elfergani, Rhys Pullin, Karen M. Holford, Damage assessment of corrosion in prestressed concrete by acoustic emission, *Construction and Building Material*, Vol.40, pp.925-933 (2013)
- [6] Christian U. Grosse, Masayasu Ohtsu, *Acoustic Emission Testing, Part B Application*, Springer, Dordrecht, pp. 211-238 (2008)
- [7] Xiu Luoa, Hiroshi Hayaa, Tomoaki Inabaa, Tomoki Shiotanib, Yasuhiro Nakanishib, Damage evaluation of railway structures by using train-induced AE, *Construction and Building Material*, Vol.18, pp.215-223 (2004)
- [8] Mohamed K. ElBatanouny, Paul H. Ziehl, Aaron Larosche, Jesé Mangual, Fabio Matta, Antonio Nanni, Acoustic emission monitoring for assessment of prestressed concrete beams, *Construction and Building Material*, Vol.58, pp.46-53 (2014)
- [9] T.Shiotani, Z.Li, S.Yuyama, M.Ohtsu, Application of the AE improved b-value to quantitative evaluation of fracture process in concrete-materials, *Acoustic Emission Group, Journal of Acoustic Emission*, Vol.19, No.5~6, pp.235-246 (2001)
- [10] Xiu Luoa, Hiroshi Hayaa, Tomoaki Inabab, Tomoki Shiotanic, Seismic diagnosis of railway substructures by using secondary acoustic emission, *Soil Dynamics and Earthquake Engineering*, Vol.26, pp.1101-1110 (2006)

# Use of Acoustic Emission in Combination with Machine Learning for Monitoring of Gas-liquid Mixing in Stirred Tanks

G. Forte<sup>1,2</sup>, F. Alberini<sup>2</sup>, M.J.H. Simmons<sup>2</sup>, E.H. Stitt<sup>1</sup>

<sup>1</sup> Johnson Matthey Technology Centre, Billingham, TS23 4LB, UK

<sup>2</sup> School of Chemical Engineering, University of Birmingham, Edgbaston, B15 2TT, UK

## ABSTRACT

Operations involving gas-liquid agitated vessels are common in the biochemical and chemical industry where ensuring good interphase contact is essential. In this work, acoustic emission (AE), using a piezoelectric sensor, was applied to evaluate gas-liquid mixing regime within two-phase (gas-liquid) and three-phase (gas-solid-liquid) mixtures in a 3 L stirred tank equipped with a Rushton Turbine and a ring sparger. As gas bubbles move upward through the vessel, they collapse, break or coalesce generating sound waves transmitted to the wall and to the acoustic transmitter. By varying impeller speed and gas flow rate, the acoustic spectrum was obtained for each flow regime (ungassed condition, loaded and complete dispersion) and analysed using machine learning to assess predictive capability. A logistic regression algorithm was applied to the acquired dataset which was divided into a training set, used to train the machine in recognising features in the spectrum corresponding to each condition, and a testing set, unseen by the machine, used to evaluate the accuracy of regime prediction. The obtained results show that the system successfully recognises acoustic spectrum corresponding to the different regimes with an accuracy higher than 90% both in the presence and absence of suspended particles.

The conducted study demonstrates the capability of AE to identify (as long as accurate training is provided) the flow regime within a two or three-phase vessel, with potential to be applied at large scale for process monitoring.

**Keywords:** Acoustic Emission; Gas-liquid mixing; stirred tank; machine learning.

## 1. INTRODUCTION

Improving process monitoring is a common need within the process industry, including chemical, food, biochemical and pharmaceuticals [1]. Desirable features for any in-process measurement are for it to be non-invasive, suitable for on-line installation and with sufficient temporal resolution to give a “real time” response, in order to avoid delays in intervening with control measures. Among several techniques responding to such identikit, Acoustic Emission (AE) is a data-rich technique with high potential for on-line monitoring.

The AE in a process will often be a combination of numerous acoustic events all propagating to the sensor via different paths. Although most AE research has focused on fault detection (leakage, failure,..) [1], more recent studies have also investigated AE as a means of monitoring physico-chemical changes within processes involving powder and fluids [2-4]. Applications in multiphase mixing are also reported in the literature. While the first known reference on gas-liquid

flow dates from the 1920s [5], more recently Addali et al. [6] have used AE energy information to predict gas void fraction in a two-phase (air-water) slug flow.

Gas-liquid reactors are very common operating units in biochemical and chemical industry, where ensuring appropriate interphase contact and gas dispersion is critical. Different regimes can be achieved when gas is sparged into stirred tanks: namely as flooded, loaded, completely dispersed, and gas recirculation [7] depending on gas flow rate, tank design and fluids properties. In this work AE data is acquired for loaded and completely dispersed regimes as well as in ungasged condition (to simulate accidental shut down of air feed) in a 3 L stirred tank equipped with a Rushton Disc Turbine. A machine learning supervised algorithm, logistic regression, is applied to identify features in the acoustic spectrum that can be used to recognise the different conditions, having already shown its potential in other applications [9]. Machine learning (ML) has recently seen increasing interest and application in chemical and manufacturing industry as the techniques are able to deal with large data sets and provide reliable statistical analysis which are both essential as industry embraces the challenges of smart manufacturing and Industry 4.0.

## 2. MATERIAL AND METHODS

### 2.1 Stirred tank configuration

A schematic of the stirred vessel is shown in Figure 1. The diameter of the 3 L tank ( $T$ ) was 0.14 m, and it was equipped with four baffles with width,  $B = T/10$  and a ring-shape gas sparger with eight 0.5 mm orifices placed equally around the ring, located at the bottom of the tank. A stainless steel six blade Rushton Disc Turbine (RDT6) with diameter 0.056 m ( $D/T = 2/5$ ) was used for stirring. The used liquid was an aqueous solution of Nickel nitrate hexahydrate (99,99% Sigma Aldrich®) and its level was set to 0.21 m ( $H/T = 3/2$ ).

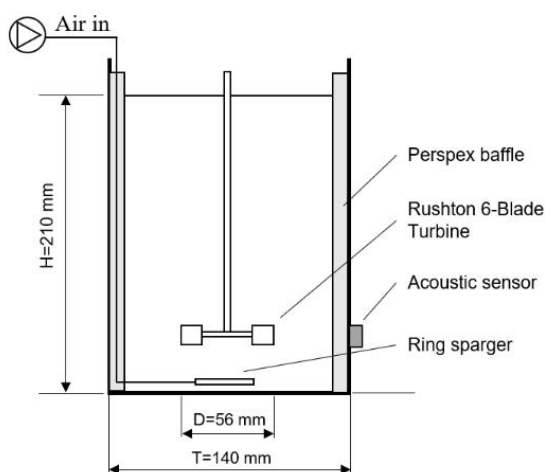


**Figure 1. Schematic of the stirred vessel**

The airflow (ranging between  $5\text{-}10\text{ L min}^{-1}$ , equivalent to 1.5 and 3 vvm respectively) was fed via the ring sparger. During the different experiments the Reynolds number was kept between 15,000 and 60,000 (turbulent regime). The impeller speed (300-1300 rpm) and the gas flow rate were

changed in order to set the required operating regime (loading or recirculation) and then the same conditions of impeller speed were recorded with no air fed to the system (to mimic failure of gas feed unit).

Stainless steel particles were used for the three-phase experiments. The particles, used at concentrations of 3, 4 and 5 % w/w had a density  $\rho_s = 8000 \text{ kg m}^{-3}$  and size between 0.177 and 0.420 mm.

## 2.2 Acoustic emission

The approach taken for design of the apparatus follows existing practice in the literature [10]. A piezoelectric sensor (Vallen Systeme GmbH, Icking, Germany), with resonance frequency of 375 kHz and diameter of 20.3 mm, was attached to the tank in Figure 1 using a silicone based vacuum grease. The sensor was attached to a preamplifier (40 dB gain, Vallen Systeme) and an oscilloscope (5243A Pico® Technology Limited) connected to a laptop (PicoScope® 6 software) was used to record data. Measurements at each condition were taken for 0.2 s with a sampling rate of 750 kHz, ensuring coverage of the resonance frequency of the sensor in the spectrum (Nyquist rule). The sensor was placed on the vessel outside wall at a height  $C$  corresponding to the impeller region,  $C = 0.046 \text{ m}$  ( $T/3$ ).

## 2.3 Data processing and machine learning

The time-domain signals were processed using the Fast Fourier Transform (FFT) function; the spectrum was filtered removing signal below 5 kHz and the 1000 most variable frequency peaks were selected as features characterising each condition before being fed to the machine learning algorithm (logistic regression). A schematic of the data processing is reported in Figure 2.

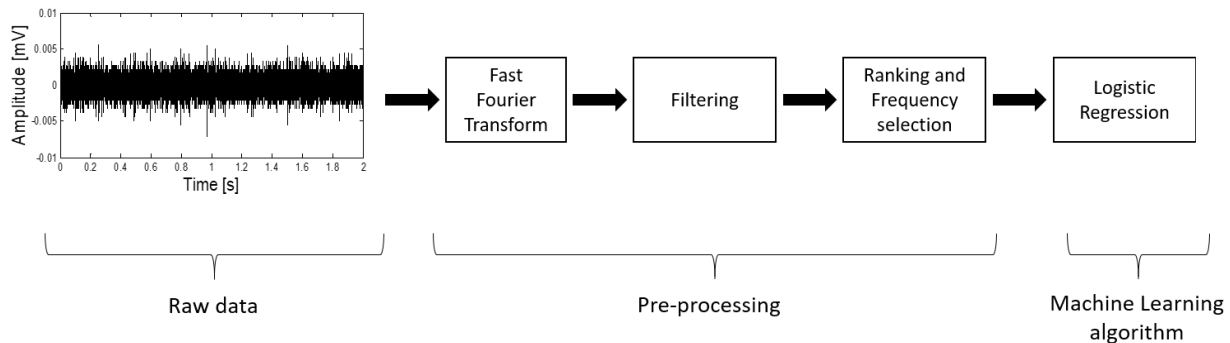


**Figure 2. Scheme of the data processing**

The logistic regression algorithm can be defined as a binomial regression, where the output is a probability,  $h_{\theta}$ , of a condition being verified, in the specific case the belonging of the signal to one of the three conditions. Logistic regression makes use of a logistic function, also known as sigmoid function:

$$h_{\theta^i}^i(x) = 1/(1 + e^{-\theta^i T x}) \quad (1)$$

where  $h_{\theta}^i(x)$  is the obtained probability, that the spectrum  $x$  belongs to a given condition  $i$  based on the parameter  $\theta^i$ . For each condition,  $i$ , a parameter  $\theta^i$  is obtained in the learning process, consisting of an optimisation run on the parameter using the gradient descent strategy. The training dataset consisted of 210 spectra (70 for each regime).

Two test datasets are acquired, one at the three different regime conditions with the bi-phasic mixture, and a second one in which solids are added to the mixture. The presence of solids at such concentration does not alter the gas-liquid mixing regime [11], but can represent a disturbance on the acoustic signal due to impacts between particles and the wall and interparticle contact.

The task is addressed as a classification problem: once the training process is finalised, the machine is challenged: the system is given an unseen spectrum and it evaluates whether it corresponds to loading, recirculation or ungasged condition.

### 3. RESULTS

A dataset composed of 100 spectra was fed to the trained algorithm to be classified. To each of them, a predicted class (ungassed, loading or recirculation) is assigned. In Figure 3, the results of the test are reported in a prediction map for the biphasic case.

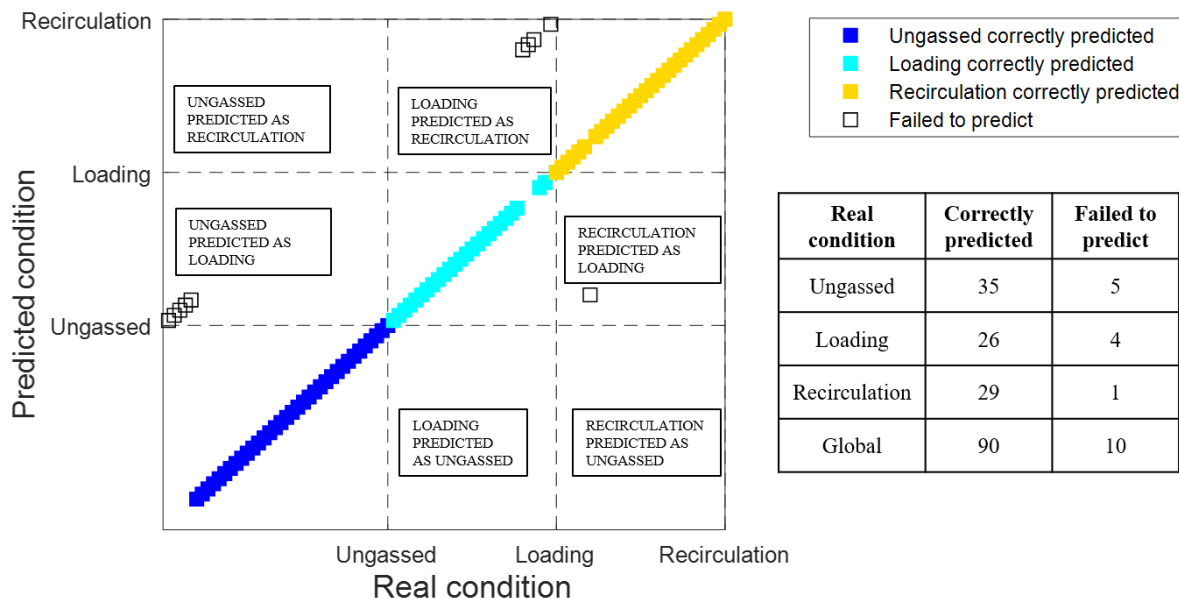


**Figure 3. Prediction map for gas-liquid case**

In Figure 3, all the coloured points represent cases correctly predicted by the system, while the white squares are the cases predicted in error. The first five spectra are wrongly classified as loading instead of ungasged and therefore are contained in the loading prediction region on the map. A few others are not classified correctly by the algorithm; however, the overall accuracy of prediction is 90%.

In the second part of the study, stainless-steel particles are added at different concentrations and the acoustic signal is acquired for each of the three regimes. The obtained results are summarised in Figure 4.

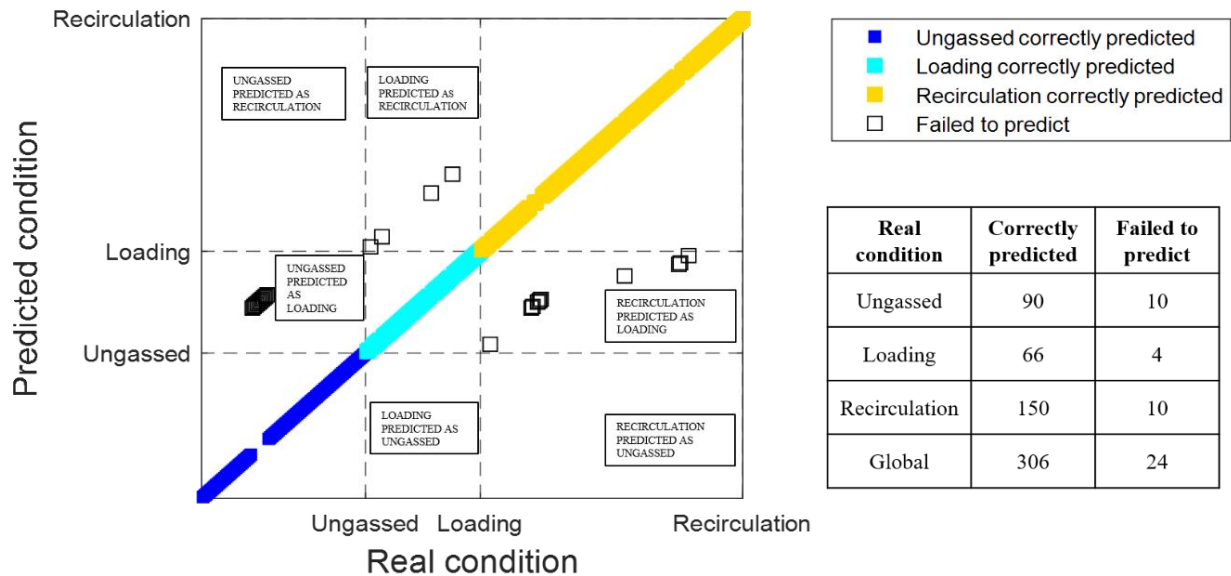


**Figure 4. Prediction map for gas-liquid-solid case**

In this case, the dataset comprised of 330 spectra and the accuracy increases to 92.3%, with an even distribution of errors across the different conditions. The presence of the solids does not affect the classification algorithms despite the fact that the training was carried out solely for two-phase gas-liquid flow conditions. The reason for this can be found in the influence of the solids on different frequencies from the ones characterising the air bubble disruption and impacts.

This finding allows extension of the methodology used for two-phase to applications where solids are critical to the process, as in cases of heterogeneous reaction. It is indeed possible to monitor dispersion of gas regardless of suspension of solids with high accuracy.

#### 4. CONCLUSIONS

In this work, Acoustic Emission was used in combination with a logistic regression machine learning algorithm to identify gas-liquid mixing regimes in a stirred tank. The machine was trained to recognise ungassed, loading and recirculation regimes using a training dataset, consisting of the acoustic spectrum acquired under gas-liquid flow conditions. The system was then challenged to recognise such regimes under both two-phase and three-phase conditions (obtained adding stainless steel particles), achieving an accuracy equal to and above 90% respectively. The conducted study aims to propose AE as a potential diagnostic and condition monitoring technique for fluid mixing applications in combination with the use of machine learning algorithms.

## REFERENCES

- [1] J. W.R. Boyd and J. Varley, 'The uses of passive measurement of acoustic emissions from chemical engineering processes', *Chemical Engineering Science*, vol. 56, no. 5, pp. 1749–1767, 2001.
- [2] C. Aldrich and D. A. Theron, 'Acoustic estimation of the particle size distributions of sulphide ores in a laboratory ball mill', *J. S. Afr. Inst. Min. Metall.*, vol. 100, no. 4, pp. 243–248, 2000.
- [3] K. H. Esbensen *et al.*, 'Acoustic chemometrics—from noise to information', *Chemometrics and Intelligent Laboratory Systems*, vol. 44, no. 1–2, pp. 61–76, 1998.
- [4] A. Crouter and L. Briens, 'Passive acoustic emissions from particulates in a V-blender', *Drug Dev. Ind. Pharm.*, vol. 41, no. 11, pp. 1809–1818, 2015.
- [5] W. H. Bragg, 'The world of sound', (Bell, London), pp 69-74, 1921
- [6] A. Addali, S. Al-lababidi, H. Yeung, D. Mba, and F. Khan, 'Acoustic Emission and Gas-Phase Measurements in Two-Phase Flow', *Proceedings of the Institution of Mechanical Engineers, Part E: Journal of Process Mechanical Engineering*, vol. 224, no. 4, pp. 281–290, Nov. 2010.
- [7] A.W Nienow. M.M.C.G. Warmoeskerken, J. M. Smith, and M. Konno, 'On the flooding/loading transition and the complete dispersal condition in aerated vessels agitated by a Rushton-turbine', in 5th European Conference on Mixing, Wurtsburg, West Germany, pp. 143–154, 1985.
- [8] J.M. Hilbe, 'Logistic Regression Models' *Chapman & Hall/CRC Press*, 2009.
- [9] T. Wuest, D. Weimer, C. Irgens, K. Thoben, 'Machine learning in manufacturing: advantages, challenges and applications', *Production & Manufacturing Research*, vol. 4, no. 1, pp. 23–45, 2016.
- [10] A. Nordon, R. J. H. Waddell, L. J. Bellamy, A. Gachagan, D. McNab, D. Littlejohn G. Hayward, 'Monitoring of a heterogeneous reaction by acoustic emission', *The Royal Society of Chemistry: the Analyst*, vol.129, pp.463-467, 2004.
- [11] C.M. Chapman, A. W. Nienow, M. Cooke, J. C.Middleton, J. C., 'Particle-gas-liquid mixing in stirred vessels. Part IV: Mass transfer and final conclusions', *Chem Eng Res Des*, vol. 61, no. 3, pp. 182–185, 1983b.

# Acoustic Emission in Process of Thermal Decomposition of Potassium Hydrogen Carbonate Crystals

Shavkat Azimov, Vladislav Petukhov and Abdukholik Lakaev  
Umarov Physical-technical Institute, Academy of Sciences of Tajikistan, Dushanbe,  
Tajikistan

## ABSTRACT

Acoustic emission was investigated in process of potassium hydrogen carbonate (PHC) thermal decomposition. Different literature sources indicate very wide range of temperatures for its thermal destruction start (from 100 to 400°C). Study of AE generated at this process has found to be helpful for more exact determination the temperature of its beginning.

Heated transparent PHC crystals without losing their shape turn into opaque potassium carbonate (PC), while carbon dioxide (CO<sub>2</sub>) and water evaporate. Temperature of the thermal degradation onset ~ 130-150°C was determined in result of various samples tests: single PHC crystals, monolayer of dozen loosed crystals and tablets pressed from thousands of crystals.

Data of PHC powder thermal decomposition obtained by thermogravimetric and differential thermal analyses found out a good compliance with AE data concerning the temperature range of the process. An X-ray diffraction analysis used to identify the initial substance and products of PHC thermal decomposition.

Tests with tablets of PHC revealed two separate temperature regions of AE activity that do not intersect. 1st region of 60-90°C determined as an “elastic unloading range”. AE caused by mechanical relaxation of crystals releasing the elastic energy stored in the process of tablet pressing. 2nd region of 130-200°C related directly to the thermal decomposition of PHC.

Kaiser effect was detected at the process of mechanical relaxation during the cyclic heating/cooling of PHC tablets in the temperature range of 60-90°C.

In result of the study, the AE technique can be recommended to control the regeneration process of CO<sub>2</sub> absorbers based on a composite from PC precipitated on an aluminum oxide  $\gamma$ -Al<sub>2</sub>O<sub>3</sub> porous matrix, which is converted to PHC during the sorption of CO<sub>2</sub>. The temperature limits of the regeneration process, which results in the reverse transformation of PHC into PC, can be monitored by the AE activity accompanying this process.

**Keywords:** acoustic emission; thermal decomposition; potassium hydrogen carbonate; potassium carbonate, carbon dioxide, crystals.

## INTRODUCTION

Potassium hydrogen carbonate also named as potassium bicarbonate or carbonic acid monopotassium salt (KHCO<sub>3</sub>) is an inorganic compound, colorless monoclinic crystals. It is widely used in various fields, e.g. as a food additive, corrosion inhibitor, and an ingredient of fire extinguishers. It is used as well as a fertilizer in agriculture, and having fungicidal properties, is used in organic farming for the control of powdery mildew and apple scab [1]. PHC appears as a component of the regeneration cycle of an absorber of atmospheric carbon dioxide based on a potassium carbonate (K<sub>2</sub>CO<sub>3</sub>) composite deposited on the porous  $\gamma$ -Al<sub>2</sub>O<sub>3</sub> matrix [2]. Thermal destruction of PHC proceeds according to the formula:  $2\text{KHCO}_3 \rightarrow \text{K}_2\text{CO}_3 + \text{CO}_2 + \text{H}_2\text{O}$  (1)

The literature indicates different temperature limits of the process at that: from 100°C to 400°C. The purpose of this work was using the AE method to clarify the temperature of the onset of thermal decomposition of PHC. As well to compare the obtained data with the data of used thermogravimetric method (TG) with differential thermal analysis (DTA). An X-ray diffraction analysis (XRD) identified the initial substance and products of PHC thermal decomposition.

## 2. EXPERIMENTAL

Reagent grade samples of PHC were placed on an upper surface of quartz waveguard inside the electrical furnace. Thin layer of vacuum pump oil was used as an acoustical contact. Acoustic emission (AE) signals were received by transducer R-151-AST (PAC) fixed on a bottom surface of waveguard outside of furnace and connected to PCI-2 system. Sample temperature was controlled by the differential Cu-constantan thermocouple fed via the F136 nanovoltamperimeter and the R111 amplifier into the parametric input of the PCI-2. Three types of PHC samples, shown in Fig. 1, were heated from room temperature up to 250°C through the series of 3X20 tests. For comparison, a thermogravimetric analysis (TG) was also carried out in combination with the differential thermal analysis (DTA) of PHC powder by the F. Paulik, J. Paulik system. The analyzed sample was previously kept at a temperature of 100°C for 2 hours to remove crystallization water, and then cooled to room temperature without ambient air access. To identify the substances, before and after the thermal decomposition tests X-ray diffraction analysis was carried out on by Dron-3 diffractometer.

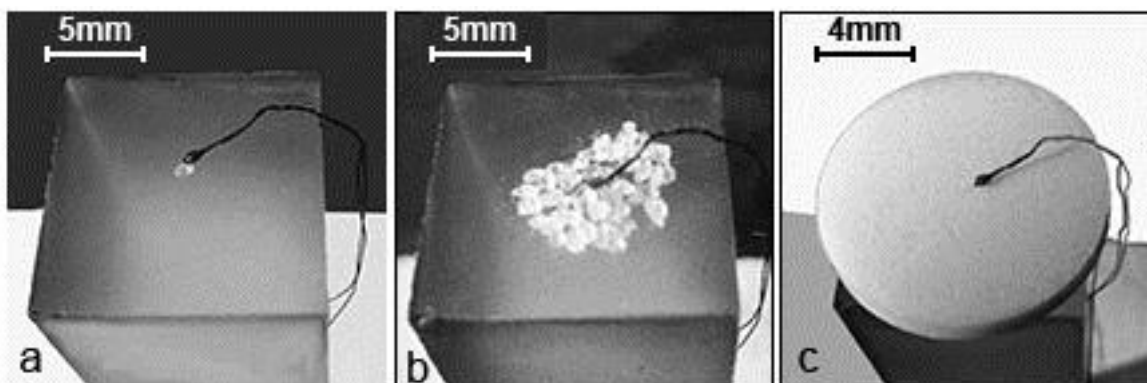


Fig.1. Test samples of PHC: a) - single crystal; b) - monolayer of freely laying several crystals; c) - tablet of 1.5 g, compressed from thousands of crystals.

## 3. RESULTS AND DISCUSSION

By heating the samples with varied amount of substance, i.e. beginning from PHC single crystals, then by tests monolayers of dozens of loosed crystals and at last, up to thousands of crystals pressed into the tablet, the boards of thermal decomposition of PHC were defined more accurately. The onset of the process has been found about 130-150°C, which corresponds to an average 5 times less scatter than the mentioned one in the existing literature.

In tests with PHC crystals pressed into the tablet, the interval of AE activity was detected in the temperature range of 40-80°C. Certainly, in this area AE caused by the process of release of elastic energy stored in PHC crystals under the pressure, i.e. caused by the crystals' relaxation, as the sample gets hot. Fig. 2 shows the AE Amplitude spectrum and the Cumulated AE Signal

Strength vs. Temperature for the heated PHC tablet weighing 1g and pressed at 200 kg/sm<sup>2</sup>. It is important that relaxation ends before the substance thermolysis beginning, and these processes can be separated by AE. The 2nd interval of AE activity with T° = 130-200°C is directly related to the thermal decomposition of PHC. The absence of the 1st interval of AE activity within 40°C < T° < 80°C at the tests with single crystals and monolayers of loosed PHC dozens of crystals can serve as negative evidence to relaxation process as a reason of AE activity in tablets' tests.

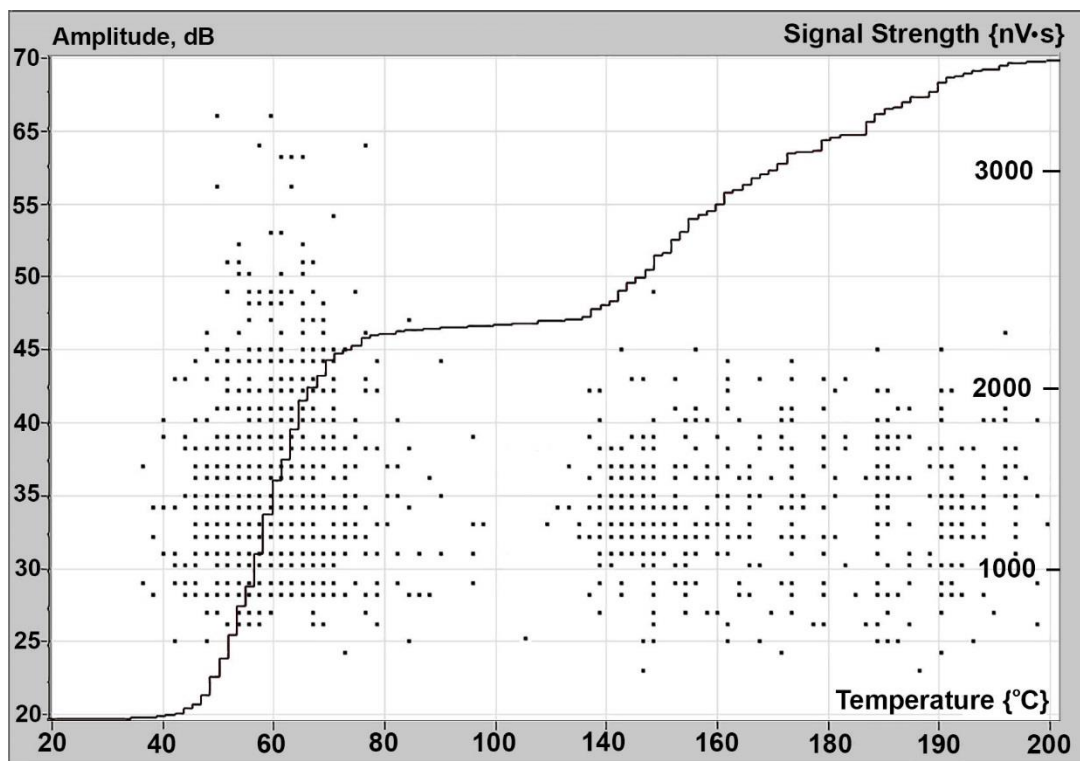


Fig.2. AE amplitude spectrum for the heated PHC tablet (·);  
Cumulated AE Signal Strength vs. Temperature (—).

There are shown in Fig. 3 time dependences of temperature, TG - mass changes, DTG - differential thermogravimetric and DTA - differential thermographic for hinge of 1g PHC powder. The thermogravimetric test began at room temperature after pre-holding the sample at T° = 100°C for 2 hours, followed by cooling without air to avoid water adsorption by the powder. The area of PHC thermal destruction is highlighted in gray. The beginning of the process can be tracked by accelerated mass loss, and its completion - when the mass loss stops. An additional feature to indicate the process of thermal destruction is to find out the boundaries of the sample temperature dependence failure, as far as the reaction of the PHC decomposition is endothermic. According to the thermogravimetry data, the thermal decomposition process of the PHC starts at ~ 130°C and finishes at ~ 180°C, which gives a good agreement with the data obtained by the AE method.

Tests with PHC compressed in tablet shape revealed Kaiser Effect. Fig. 4 shows the total AE Hits account; Amplitude-time spectrum and the temperature curve for the sample subjected to cyclic heating within the temperature range where PHC pressed crystals' mechanical relaxation occurs. In this case the temperature is changing cyclically, to act as a cyclically varying mechanical load in a classic test that detects the Kaiser Effect. It is clearly seen that at the first thermal loading of the sample the relaxation process, which generates AE, begins at 30°C and stops at the subsequent cooling. At the sample repeated heating the relaxation, followed by AE,

starts only when the specified temperature level is exceeded. This is evidence of the presence of the Kaiser Effect.

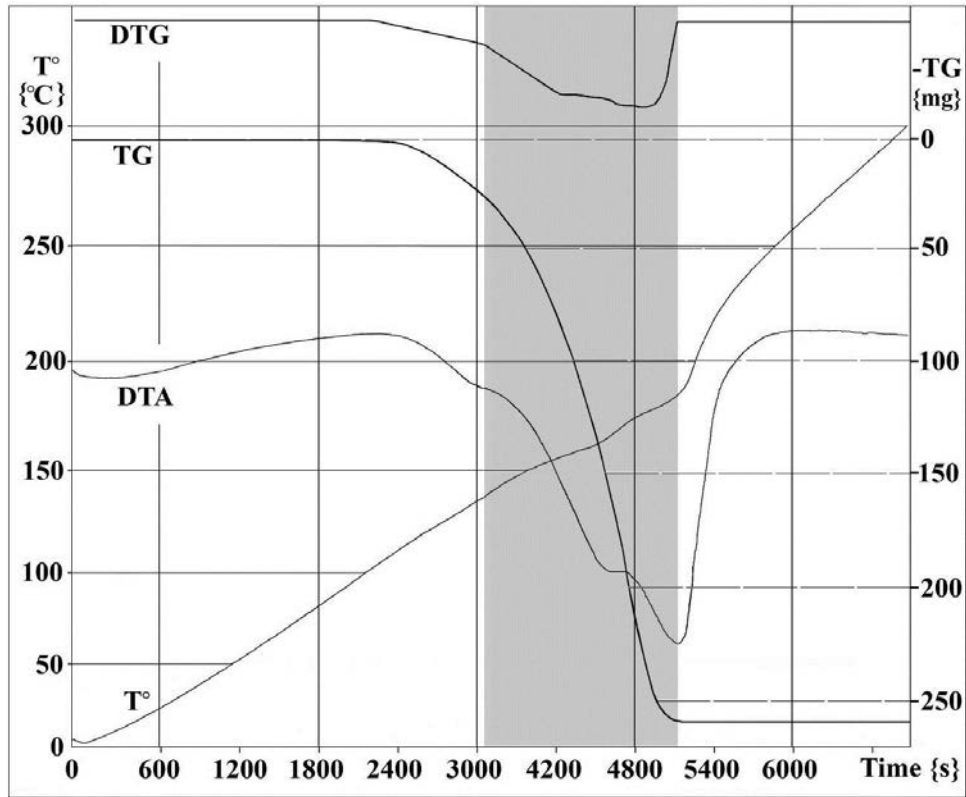


Fig.3. Thermogravimetric characteristics of PHC:  $T^\circ$ , TG, DTG and DTA.

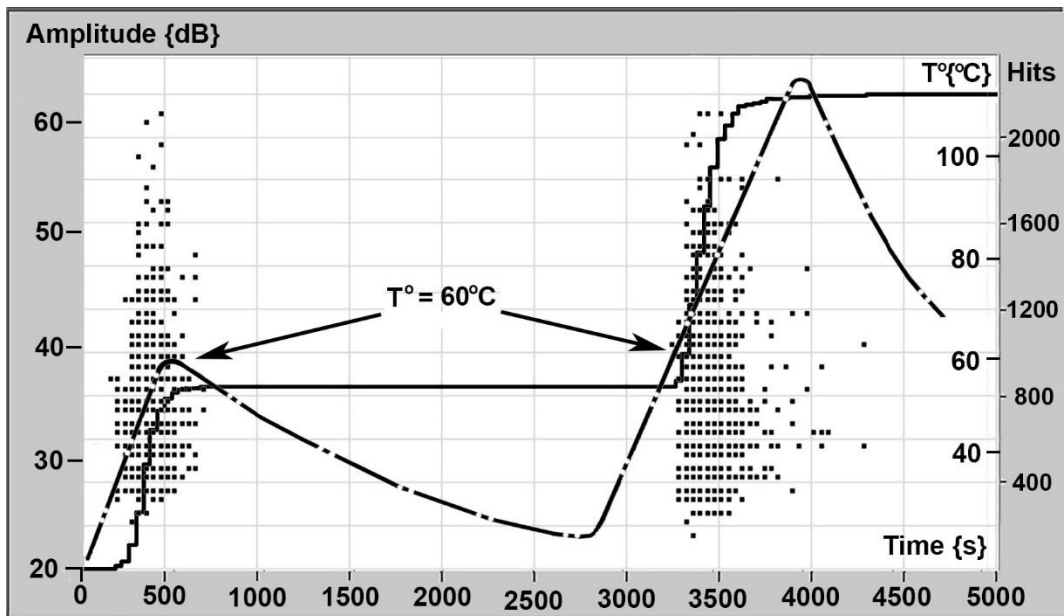


Fig.4. Total AE Hits account; Amplitude-time spectrum and Temperature-time dependence of PHC tablet cyclic heating.

In [2] a composite sorbent  $K_2CO_3/\gamma-Al_2O_3$  was synthesized and tested for direct carbon dioxide capture from ambient air. As a result of  $CO_2$  sorption, potassium carbonate is converted to potassium hydrogen carbonate and by heating at  $T^\circ = 250-300^\circ C$  the sorbent is regenerated. In the same paper, it was shown that effective release of  $CO_2$  occurs already at  $T^\circ \sim 200^\circ C$ . At the same temperature, the XRD spectrum shows a complete recovery of  $K_2CO_3$  from  $KHCO_3$  after heating. Increasing the temperature to  $250-300^\circ C$  in general slightly increases the output of  $CO_2$ . The results of our research show that the upper temperature of regeneration can be limited by  $200^\circ C$ . This will lead to reduction of power inputs for regeneration and utilization of carbon dioxide. The AE method can reliably control the dynamics of the regeneration process.

## CONCLUSIONS

1. Potassium hydrogen carbonate thermal decomposition has been studied by means of AE technique, supplemented by differential thermal analysis, thermogravimetric analysis and X-ray diffraction analysis.
2. There are detected two not intersecting temperature ranges of AE activity at the heating of potassium hydrogen carbonate crystals and powder pressed in form of tablets. It's supposed that AE within the 1st range of  $60-90^\circ C$  caused by mechanical relaxation of crystals releasing the elastic energy accumulated in the process of tablet pressing. AE within the 2nd range of  $130-200^\circ C$  has been related directly to the thermal decomposition of potassium hydrogen carbonate.
3. Kaiser effect was detected at the process of crystals' mechanical relaxation during the cyclic heating/cooling potassium hydrogen carbonate tablets in the temperature range of  $60-90^\circ C$ .
4. AE method can be recommend to control the regeneration process of carbon dioxide absorbers based on a composite from potassium carbonate, deposited on a porous matrix of  $\gamma$ -aluminum oxide, which is converted into potassium hydrogen carbonate during sorption of carbon dioxide. The dynamics of the regeneration resulting in the reverse transformation of potassium hydrogen carbonate into potassium carbonate can be monitored by the AE activity accompanying this process.

## REFERENCES

1. Potassium Bicarbonate Handbook. Armand Products Company, 469 North Harrison Street Princeton, NJ 08543-5297, <http://www.armandproducts.com>.
2. J.V. Veselovskaya, V.S. Derevschikov, T.Yu. Kardash, O.A. Stonkus, T.A. Trubitsina, A.G. Okunev. "Direct  $CO_2$  capture from ambient air using  $K_2CO_3/Al_2O_3$  composite sorbent". International Journal of Greenhouse Gas Control. Vol. 17, p. 332–340, 2013.
3. I.T. Goronovskii, J.P. Nazarenko, E.F. Nekriach. "Kratkiy spravochnik po khimiyi" (Concise handbook of chemistry), p. 144, 1974.
4. J.A. Dean. "Lange's handbook of chemistry", p.3.43, 1972.
5. B.E Poling, G.H. Thomson, D.G. Friend, R.L. Rowley, W.V. Wilding. "Perry's chemical engineers' handbook book", 8<sup>th</sup> edition, section 2: Physical and Chemical Data, p.2-21, 2009.

# Acoustic Emission based Crack Tracking for Concrete Structures

Fengqiao Zhang, Yuguang Yang  
Delft University of Technology, the Netherlands

## ABSTRACT

Acoustic Emission (AE) monitoring is one of the possibilities to detect the crack distribution in existing concrete structures. However, the conventional method requires further destruction like opening of new cracks or propagation of the existing cracks. In this paper, a new strategy of using local cumulative AE activities during unloading to track the crack trajectory is proposed. With this strategy, a relatively low load level which does not cause further destruction to the structure is needed. The possibility of this strategy is experimentally examined using a real-scale beam of 10-ton damaged under cyclic loading. For calibration, the crack opening is measured by Digital Image Correlation (DIC). The crack patterns detected by the new strategy and DIC show good agreement.

**Keywords:** concrete beam, cyclic loading, Acoustic Emission, source localization, crack tracking.

## 1. INTRODUCTION

The safety of the large stock of aging existing concrete structures is important to the society. As a key link in the maintenance of these structures, the present conditions including the crack distribution have to be evaluated accurately. At the moment, effectively evaluating the crack distribution inside the structures remains challenging. One of the available possibilities is to use Acoustic Emission (AE) technique [1,2]. In the conventional method, application of AE requires opening of new cracks or further propagation of the existing cracks, which is linked to heavier loading of the structures towards its ultimate limit state. Usually this is recognized as proof loading test of the structures [3], which requires heavy loading equipment with high cost. In this paper, a different strategy on crack tracking is proposed. In the proposed approach, a relatively low magnitude of load is applied to open the existing cracks. The AE activities during the crack closure is used to track the trajectories of the cracks.

The new strategy is validated by a large scale lab test of a 10-ton reinforced concrete beam. For calibration, the crack development is analyzed by Digital Image Correlation (DIC) measurement. The result of this paper provides the possibility of AE based crack tracking in the assessment of the present conditions of the existing concrete structures.

## 2. AE BASED CRACK TRACKING

### 2.1 AE activity during unloading

For concrete structures with cracks, it was shown that during unloading, the closure of the existing cracks or the friction between rebar and concrete, etc. may lead to the AE activities [4,5]. In order to make use of the AE activities during unloading, the expression Calm Ratio was proposed by Ohtsu et al. in [5,6], which was defined as the ratio of the cumulative AE activities

during unloading to that of the whole cycle. In a later study reported by Yang et al. [4] on beams from an existing concrete bridge, it was found that the calm ratio is proportionally linked to the crack opening. The observations suggest that the AE activities during unloading can be used as an indication of the presence of existing cracks.

## **2.2 AE source localization and error estimation**

As a widely applied algorithm, grid search method is employed in the study to determine the location of the AE signal source [1]. The basic principle of the algorithm is to compare the calculated arrival time difference from the estimated location and the observed arrival time difference from the measurement [7].

Factors involved in the algorithm such as the choice of arrival time picking methods and the presence of cracks influence on the travel times of the signal, thus induce an offset between the estimated source location and the real source location, which is defined as source localization error in [8]. According to Zhang, considering an arrival time picking error within 5  $\mu$ s and a crack with an opening in range of [0.05 3] mm between the source and the receiver, the source localization error was around 15 cm in a target area of 1m  $\times$  1m. This amount of source localization error should be taken into account in the AE based crack tracking in concrete structures.

## **2.3 Local cumulative AE activities**

In the study of Ohtsu et al. [5,6] and Yang et al. [4], the relationship between AE activities and the crack opening were studied at global level across the height of the whole specimen. Similar relationship is expected at the level of the crack trajectory locally. In this paper, a term local cumulative AE activities is proposed. The AE activities during unloading located in each cell are counted as the local cumulative AE activities during unloading. Here, cells are discretized measuring area. The size of the cell determines the accuracy of the crack tracking but is limited by the AE source localization error. This approach of using local cumulative AE activities during unloading to track the crack pattern is referred to as AE based crack tracking. It cannot only locate the existing cracks, but also indicate the local crack opening along its trajectory.

# **3. EXPERIMENT**

To explore the AE source localization on real-size structural members, a test on a 10-ton reinforced concrete beam with length of 10 m, height of 1.2 m, and width of 0.3 m was conducted. The concrete had a nominal compressive strength of 65 MPa. The maximum aggregate size was 16 mm. Reinforcing bars in the beams were 6 $\phi$ 25, with concrete cover of 25 mm. The beam was simply supported with a span of 9 m and loaded by a point load at 3 m from one support (Figure 1).

The beam was loaded cyclically shown in Figure 2. The first seven load cycles are marked as L1-L7. After the beam was loaded to 250 kN in L5, two smaller magnitudes of load (L6 and L7) were applied on the beam to reproduce the practical condition that structures in service can be deteriorated due to heavier loads before the assessment.

Fourteen AE sensors of R6I-AST with a central frequency of around 60 kHz were installed on the south side of the beam to record the AE hits (Figure 1). The hits with the peak amplitude over 60 dB were selected to do the source localization. In the source localization, the arrival times were based on the threshold crossing method where the threshold was set to be 45 dB in the data acquisition system.

On the north side of the beam, a sprinkle pattern was painted to do the DIC displacement measurement. Since the boundary conditions of the beam is plain stress, the crack distribution at the two side surfaces can be assumed as constant in the width direction of the specimen. Therefore, the measured crack development from DIC can be used to calibrate the AE source localization results.

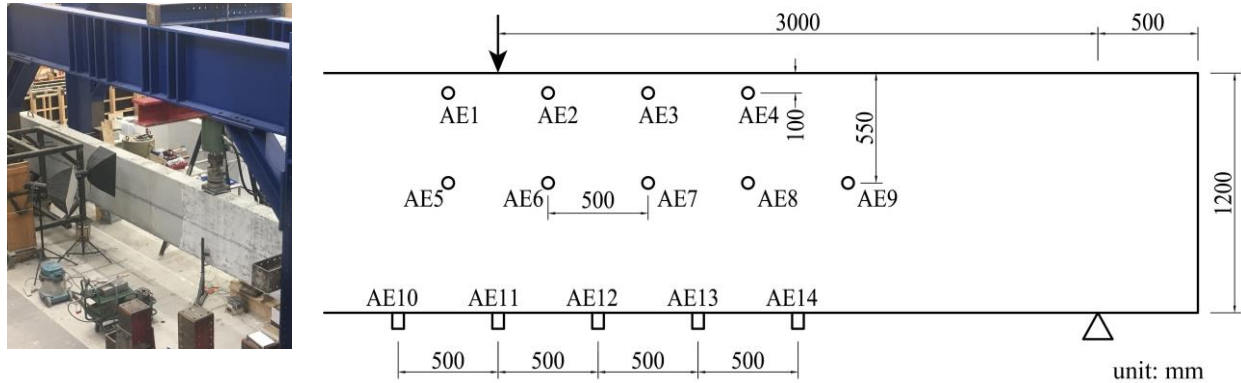


Figure 1: (left) test setup and (right) AE sensor layout on the back side

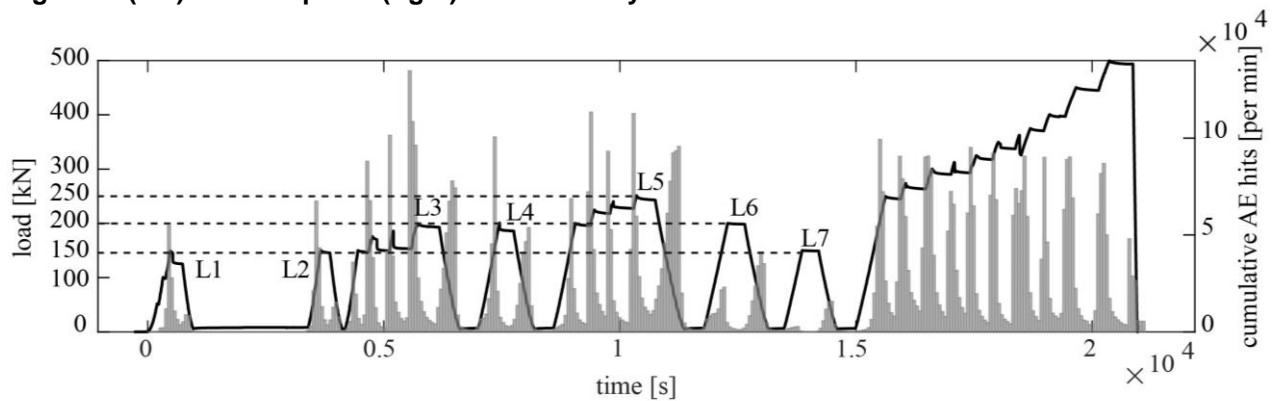


Figure 2: loading history combined with the cumulative AE hits per minute; the load cycles of interest are marked as L1-L7

## 4. RESULTS

### 4.1 Crack development

In the three-point bending test, the gradient of the bending moment resulted in a gradual propagation of the bending cracks with the increase of the load level. Crack patterns at different load levels have been obtained by DIC. The crack pattern at 250 kN in L5 is shown in Figure 3 (left) as an example in which the five cracks reaching the neutral axis of the specimen were studied further and marked as C2-C6. The crack C1 was marked because it was the first initiated crack (in L1). Consequently, C2, C3, C4, and C5 occurred in L3, and C6 occurred in L5. During the load cycles L6 and L7, no new cracks were observed.

The crack opening along its trajectory was determined using DIC output. Measuring points were selected on the profile of the crack (C4 shown in Figure 3, right, as an example). The short line

at each point indicates the local normal direction. The crack opening was calculated by checking the displacement difference between the two points in the normal direction of the crack locally.

The opening of the cracks C3 and C4 at 200 kN (L6) and 150 kN (L7) from the previous unloaded condition is shown in Figure 4. It can be found that the re-opening of the existing crack was proportionally linked to the applied load. For the crack opening along its trajectory, in general, the crack opening was wider in the bottom part than that at the crack tip. While, due to the opening of the secondary cracks near the crack C4 in the bottom, the crack opening of C4 below 0.3 m is limited. In this study, the lower bound of the DIC measurement is assumed to be 0.05 mm due to the resolution limitation. Therefore, according to the DIC measurement, C3 hardly opened in L6 and opened towards a height of around 0.3 m in L7; C4 opened towards a height of around 1 m and 0.9 m in L6 and L7, respectively.

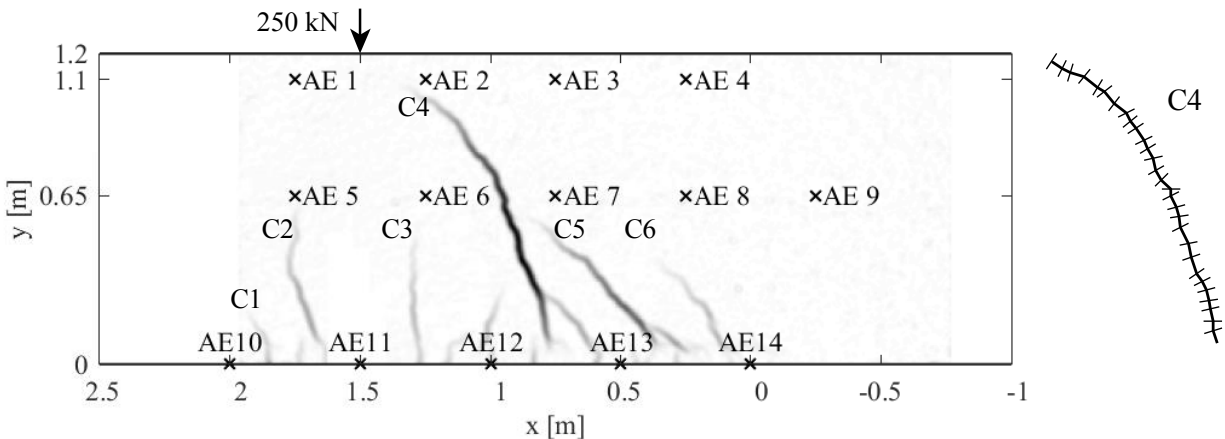


**Figure 3: DIC measurement: (left) crack pattern at 250 kN, and (right) measuring points for the opening of C4 (the short line at each point shows the normal opening direction.)**

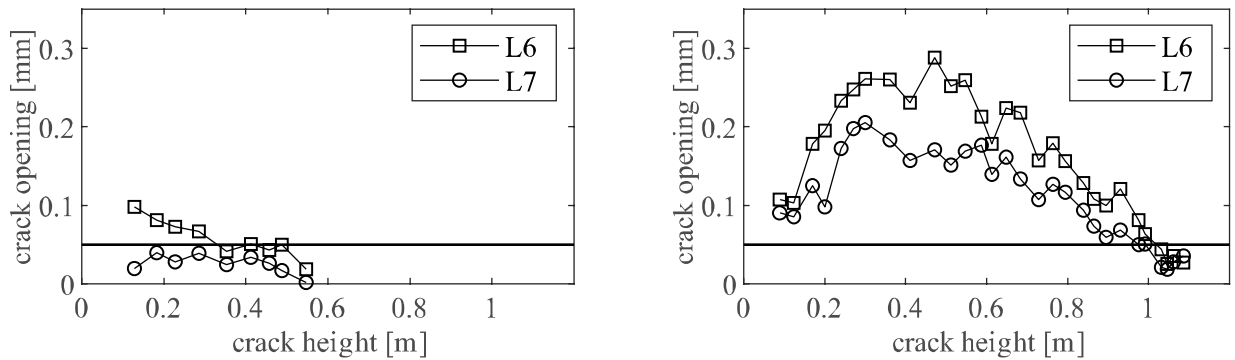


**Figure 4: opening of existing cracks C3 (left) and C4 (right) in the loading process of L6 and L7**

#### 4.2 AE source localization in the unloading

The AE activity during unloading was observed to be more active than that during loading in L6 and L7 (shown in Figure 2). This meets with the expectation that for the damaged beam with a higher previous load (in this case, 250 kN in L5), in the cyclic loading of a smaller load level, more AE activities were generated due to the closure of the cracks during unloading.

Grid search method was applied to do the source localization, with the target area (i.e. 2500 mm × 1200 mm) divided by a mesh with a size of 5 mm. Sources located outside the sensor enclosed area had less localization accuracy [8] and were neglected in this work.

The AE source localization results during unloading in L6 and L7 are shown in Figure 5. Each point represents one localized AE activity. It can be seen that AE activities were mostly localized around the cracks C2, C4 and C5, while the cracks C3 and C6 could not be traced back. This may be due to the fact that C3 and C6 were opened limitedly in L6 and L7, observed from DIC measurements (the maximum opening of C3 is shown to be less than 0.1 mm in Figure 4, C6 not shown). The closure of these narrow cracks may generate weak signals which could not be received by the AE sensors after attenuation in the propagation. Other cracks which were not reaching the neutral axis could not be detected due to the same reason. It can also be found that the crack C4 was traced back with a higher crack height in L6 than in L7, which met with the DIC measurements.

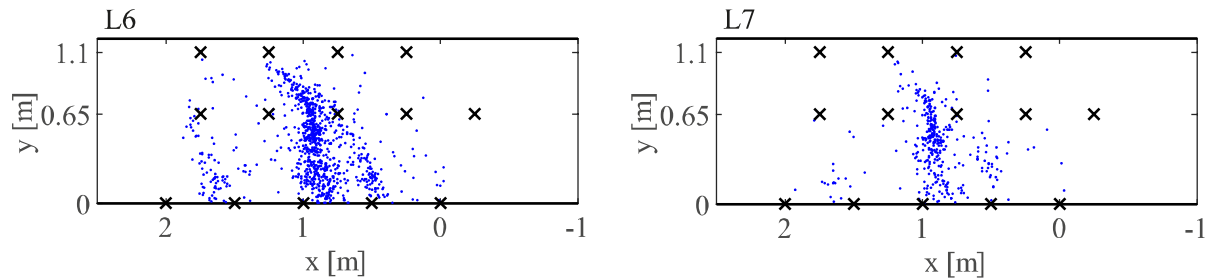


**Figure 5: AE source localization in the unloading process: (left) L6 and (right) L7**

In order to indicate the crack opening along its trajectory, the local AE activities during unloading was calculated. The target area was discretized by cells of size of 80 mm × 80 mm and the number of AE activities located in each cell was counted. The results are illustrated in Figure 6. The cumulative AE activities ranged from 0 to 40 in each cell. The crack opening measured by DIC is shown on the same graph with a scale of 250 times for comparison.

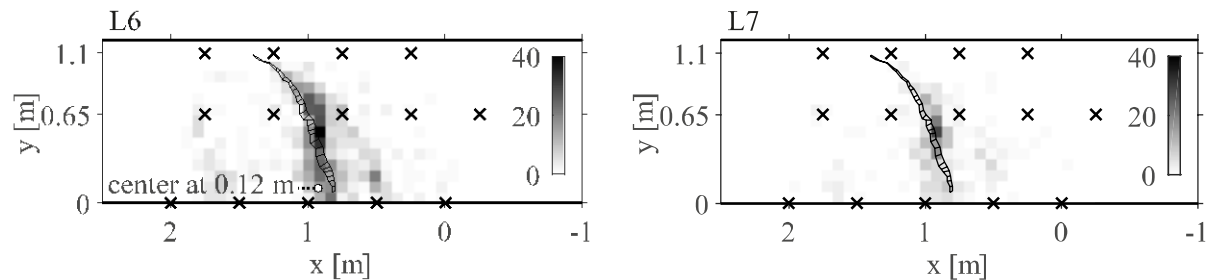


**Figure 6: local cumulative AE activities during unloading in: (left) L6 and (right) L7, compared with the crack opening of C4 from DIC; the center of AE clustering around C4 at 0.12- m height is marked in L6**

By comparing the local cumulative AE activities with the crack opening along the trajectory of the crack C4, it can be found that cells at heights in range of [0.3 0.65] m had more AE activities, where larger crack openings were observed. An initial conclusion can be drawn that in the cyclic loading, the local cumulative AE activities during unloading proportionally corresponded with the crack opening in the previous loading. It can therefore be used as a local indicator of the crack opening along its trajectory. A further quantitative relationship will be reported in another paper with test data from more specimens.

Regarding to the accuracy of AE based crack tracking, the crack tip of C4 can be tracked with a higher accuracy than the bottom part of the crack. If assuming the center of AE clustering as the

crack center, the bottom part of the crack C4 was located with an error of around 16 cm (two cells) to the left of DIC result, shown in Figure 6, left. This error came from the influence of the secondary crack between the source and the receiver, combined with the influence of arrival time picking error from the threshold crossing method. More cracks between the source and the receiver can result in larger crack tracking errors. Additional considerations need to be taken.

## 5. CONCLUSIONS

This paper explores the possibility of using local cumulative AE activities during unloading to track the crack pattern in reinforced concrete beams with no further destruction. By comparing with the physical damage in terms of crack opening measured by DIC, several conclusions can be drawn:

- In the performed test in this paper, the local cumulative AE activities during unloading is able to track the trajectory of the cracks with the maximum normal opening larger than 0.1 mm. The closure of narrow cracks less than 0.1 mm may not be detected by the sensors within 0.5 m.
- With an existing crack between the source and the receiver, the accuracy of the AE based cracking tracking has a reduction of around 16 cm. With multiple cracks, additional considerations have to be taken when applying this method.
- The local cumulative AE activities during unloading turns out to be proportionally related to the local normal crack opening from previous loading. The relationship between the cumulative AE activities and the crack opening in a local scale will be quantified in another paper with more test data from various beams.

## 6. REFERENCE LINKING

1. Grosse, C.; Ohtsu, M. *Acoustic emission testing: Basics for research-applications in civil engineering*. 2008; p 1-404, 3540698957.
2. Schechinger, B.; Vogel, T. Acoustic emission for monitoring a reinforced concrete beam subject to four-point-bending. *Construction and Building Materials* 2007, 21, 483-490.
3. Yang, Y.; Hordijk, D.A.; de Boer, A. Acoustic emission measurement in the proof loading of an existing bridge affected by asr. In *5th International Symposium for Life-Cycle Civil Engineering*, Delft, 2016.
4. Yang, Y.; Hordijk, D.A.; de Boer, A. Acoustic emission study on 50 years old reinforced concrete beams under bending and shear tests. In *8th International Conference on Acoustic Emission*, Kyoto, 2016.
5. Ohtsu, M.; Uchida, M.; Okamoto, T.; Yuyama, S. Damage assessment of reinforced concrete beams qualified by acoustic emission. *ACI Structural Journal* 2002, 99, 411-417.
6. Ohtsu, M. Recommendation of rilem tc 212-acd: Acoustic emission and related nde techniques for crack detection and damage evaluation in concrete: Test method for damage qualification of reinforced concrete beams by acoustic emission. *Materials and Structures/Materiaux et Constructions* 2010, 43, 1183-1186.
7. Tobias, A. Acoustic-emission source location in two dimensions by an array of three sensors. *Non-Destructive Testing* 1976, 9, 9-12.
8. Zhang, F. Evaluation of acoustic emission monitoring of existing concrete structures. Master Thesis, Delft University of Technology, the Netherlands, 2017.

# Radar Tower Inspection using Omnidirectional Shear Acoustic Emission Sensors

Jason Philtron<sup>a</sup>, Ronnie K. Miller<sup>b</sup>, Cody Borigo<sup>a</sup>, Steven Owens<sup>a</sup>, and Ward Fong<sup>c</sup>

<sup>a</sup>Guidedwave, 450 Rolling Ridge Dr., Bellefonte, PA, USA;

<sup>b</sup>Independent AE Consultant, Loveland, OH, USA;

<sup>c</sup>United States Air Force, Hill AFB, UT, USA

## ABSTRACT

A new, patent-pending, omnidirectional shear wave Acoustic Emission (AE) sensor has been validated in field trials on steel radar tower structures. This work was conducted under an on-going Phase II SBIR<sup>1</sup> to develop an AE inspection method for radar tower structures. Agencies such as the US Air Force, Federal Aviation Administration (FAA), and National Oceanic and Atmospheric Administration (NOAA) have many such steel tower structures which support rotating radar arrays. Many of these structures have seen continuous use for decades and have received a minimal level of maintenance and inspection. Historically, visual inspection has been relied upon for flaw detection, but this method can be unreliable as small or hidden flaws can easily be missed. AE inspection provides a 100% coverage inspection solution. New omnidirectional shear AE sensors have been used in tandem with conventional sensors. The shear sensors have been validated through detection of cracks confirmed with visual and magnetic particle testing. The shear sensors can also provide an advantage for sensing on exposed structures during environmental noise such as rain which can cause false calls or overwhelm data throughput rates with conventional sensors. Additionally, the sensors provide increased source localization performance with similar sensitivity as conventional sensors, depending on the AE source type. For conventional AE sensors, wave velocity must be determined in the field for each test setup. However, with shear sensors users do not need to calibrate and can rely on handbook values (bulk shear wave velocity for a material) to produce excellent results.

**Keywords:** shear, crack, localization, characterization, sensors

## 1. INTRODUCTION

Reliability of radar tower structures is essential for military and civilian aircraft operation [1]. Agencies such as the US Air Force, Federal Aviation Administration (FAA), and National Oceanic and Atmospheric Administration (NOAA) have many such steel tower structures which support rotating radar arrays. Radar operation is typically continuous, and some tower structures have been in use for 50 years, or longer. Damage (e.g., cracks, corrosion) to steel tower structures leads to decreased structural strength which can eventually result in catastrophic failure. Structural failure will result in radar downtime, as well as loss of expensive equipment. In addition to the need for 100% coverage of the structure, areas with limited access need inspection, which can be challenging for other conventional NDT techniques. AE inspection can provide a fast, reliable, and robust method for tower inspection. Radar rotation

---

<sup>1</sup> The work described in this presentation is part of a Phase II, Small Business Innovating Research program with the U.S. Air Force and Guidedwave. The topic number is AF161-11 and the title of the project is, "Hybrid Acoustic Emission and Guided Wave Inspection System for Radar Towers". Reference CASE NUMBER 75ABW-2019-0030.

with an offset center of mass provides a natural loading function that can be used during inspection, and it has been found that electromagnetic interference (EMI) from radar operation is not of concern for shielded cables and sensors.

Initial field tests of a novel, patent-pending [2,3] omnidirectional shear AE sensor on radar tower structures show promise for increased source location accuracy and insensitivity to environmental noise (rain) when compared to conventional (Lamb-type wave sensitive) sensors, while still maintaining sensitivity to emissions from cracks. Improvements to source location accuracy were achieved using threshold triggering on the main wave packet arrival, as opposed to conventional methods that typically perform complicated waveform analysis in post-processing to achieve improved source location accuracy [4]. Additionally, there is no need to spend time performing a velocity calibration for the shear sensors, since the shear wave velocity is always used. These shear sensors were used in parallel with conventional 150 kHz resonant sensors in several field tests of steel radar tower structures. This paper presents data from multiple tower structures containing real flaws.

## 2. RADAR TOWER GEOMETRY

Radar tower structures are typically constructed of structural steel and have 3, 4, or more support legs connected by a truss structure. The distance between adjacent legs may be as few as 6 feet or as much as 50 feet, depending on the design. Additionally, tower height can range from 25 feet to 50 feet or more. The rotating radar array is housed inside a radome mounted on top of the tower structure. Images of several radar tower designs are shown in Figure 1.



Figure 1. Example radar tower structures, from left to right: Air Force tower, FAA tower [5], and NOAA tower [6].

## 3. RESULTS – CRACK DETECTION

### 3.1 Example location error with conventional sensors

Location calculations using conventional acoustic emission sensors can be prone to error for a variety of reasons. In some cases, the amplitude of emissions from a source may vary during the test period. This can cause significant variation in where along a waveform the software sets the starting point used for delta-t calculations. Due to multi-modal and dispersive mode content, a fixed threshold can easily trigger off of a variety of locations in the signal, from the first wave arrival to near the maximum signal amplitude.

An example of such an error is shown in Figure 2. Data was recorded for 40 minutes during normal radar tower operation by two conventional 150 kHz resonant sensors placed on legs of a steel radar tower structure connected by a horizontal I-beam. This beam was welded to each leg. Software with a floating detection threshold of 40 dB with an FTband of 20 dB was used and a velocity of 90,000 in/sec. Emissions were detected from a visually-confirmed 2-inch long crack in one of the welds. Although the sensor spacing is only 5.5-feet, calculated locations from AE signals were spread over a range of 15 inches, or almost 25% of the sensor spacing. This level of location error can be avoided using shear wave acoustic emission sensors.

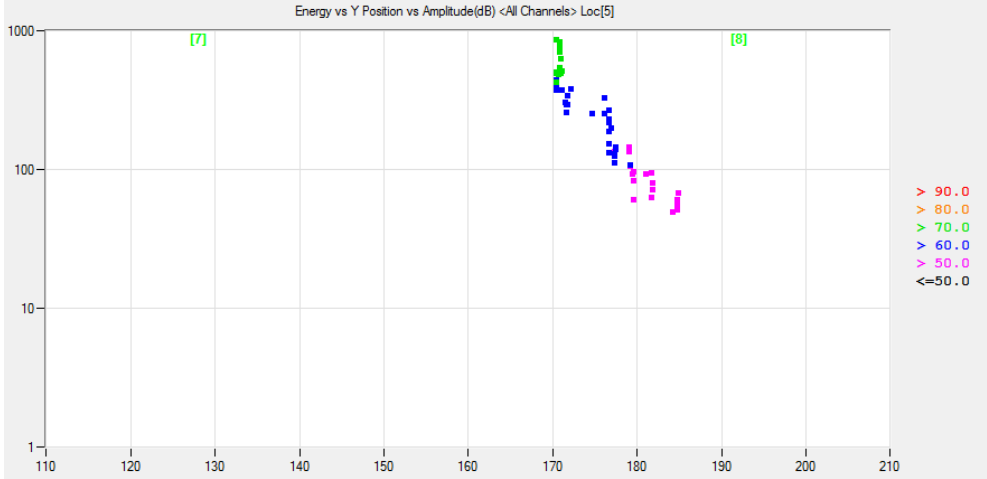


Figure 2. AE data from a 2” crack collected using conventional 150 kHz resonant sensors. Significant variation in calculated location is shown.

**3.2 Example of crack detection with omnidirectional shear sensors**

In order to characterize the crack identified in Figure 2, to determine its precise location, and to assess the capability of the shear sensor to detect emissions from a crack, a set of two shear (200 kHz resonant) and two conventional (150 kHz resonant) sensors were placed on either side of the crack, with a sensor spacing of 28 and 30 inches, respectively. A floating threshold starting at 30 and 40 dB with an FTband of 20 dB was used for the shear and conventional sensors, respectively. Data was collected for 30 minutes during normal radar operation. Results are shown in Figure 3.

The shear and conventional sensors show very similar sensitivity in terms of the energy and amplitude of the recorded waveforms. When comparing the 26 events recorded by the shear sensors to the time-linked events recorded by the conventional sensors, the shear sensors have on average 3 dB greater amplitude. This is a promising result, as it was not known prior to field testing whether the shear sensors would have similar sensitivity to true cracks. It is expected that the relative shear horizontal and Lamb-type guided wave mode energy generated by a crack will be dependent on the type of crack and its relative orientation to the sensors.

The true crack location is close to 171 inches, indicating that the shear sensors provide superior location accuracy. The input velocity for the shear sensors is 123,000 in/sec, which is simply the bulk shear wave velocity of the steel. This velocity can be used because the shear sensors are sensitive to the fundamental shear horizontal guided wave mode, which is non-dispersive and has a phase and group velocity equal to the bulk shear wave velocity that is independent of structure thickness and frequency. Use of the shear wave velocity also saves time and limits confusion, as no calibration procedure is required during sensor array setup to determine the velocity to use for location calculations (unlike for conventional sensors). One of the reasons for

the location error experienced by conventional sensors in this case could be that the wave must travel through multiple thicknesses of the steel structure, for which propagating guided waves will generally have different group velocities. In contrast, the fundamental shear horizontal wave velocity is insensitive to structure thickness.

Additionally, the location data from the shear sensors curiously shows two location clusters, which is believed to be due to the two different paths around the circumference of the tower leg (pipe) between the crack and one of the sensors. The time of arrival data indicates that the groups of hits locating to the two different positions occurred at different relative times during the radar array’s rotation cycle. This suggests that different source mechanisms during the rotation cycle generated ultrasound in different relative directions which resulted in the emissions located from the two wave paths.

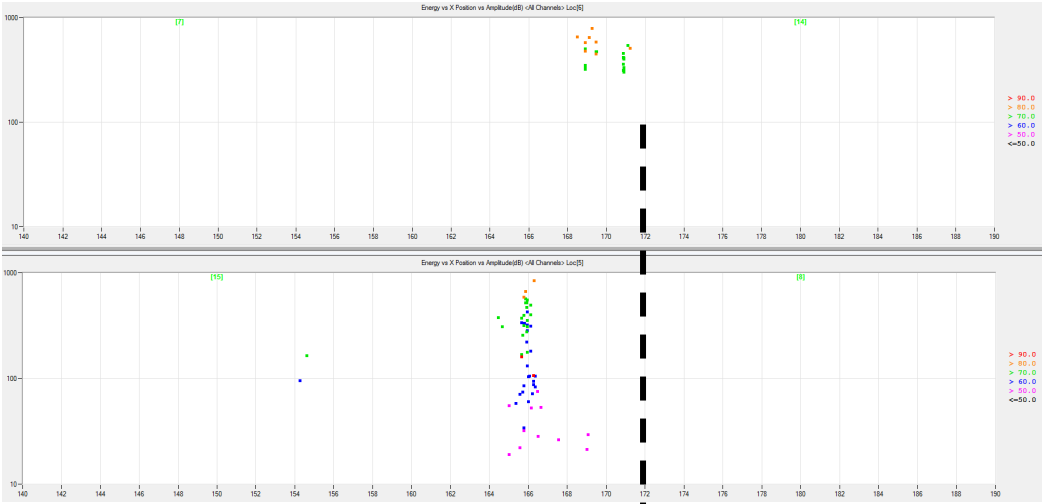


Figure 3. AE data from a 2” crack collected using shear 200 kHz resonant (above) and conventional 150 kHz resonant (below) sensors. The crack location is near 171”, indicated by the vertical dashed line. The amplitude and energy of AE signals recorded by the two sensor types is similar, but the shear sensors provide superior location performance.

**3.3 Example of small flaw detection with omnidirectional shear sensors**

Additional data was collected on a separate section of a steel radar tower. In this case, conventional and shear sensors were placed vertically along a section of pipe which served as a tower leg. This section of pipe had multiple welded cross-beams, and an indication was detected using AE. This indication was not confirmed visually as a crack, but an undercut in a weld area.

The sensor spacing was 30 inches for both the shear (200 kHz resonant) and conventional (150 kHz resonant) sensors, and the two sensor types were offset 4 inches vertically. A floating threshold starting at 30 and 40 dB with an FTband of 20 dB and velocities of 123,000 and 90,000 in/sec were used for the shear and conventional sensors, respectively, and data was collected for 30 minutes during normal radar operation. AE data is shown in Figure 4.

Conventional sensors recorded 123 events during the recording period. These events cluster to an area of ± 2.25 inches, representing ±7.5% of the sensor separation distance. The shear sensors recorded 134 events during this recording period. About 120 of these events were time-linked to the events detected by the conventional sensors, indicating that it is highly likely that the same source was producing all of the detected emission events. The event locations calculated by the shear sensors cluster to an area of ±0.25 inches, representing ± 0.8% of the

sensor separation distance. Additionally, the location of the undercut nearly matches the location calculated by the shear sensors. The shear sensors show improved location accuracy and precision.

In this case the shear sensors show less sensitivity (in terms of recorded signal energy and amplitude) to the detected indication/flaw. However, since the flaw could not be confirmed visually or by another NDT method, no additional characterization of the flaw type is given here, and no further generalizations can be made about the relative sensitivity to flaws by the two sensor types.

It is hypothesized that much of the error in the location calculation when using conventional sensors is due to triggering from different parts of the wave signal. The conventional sensors recorded a more gradual ramp up of signal amplitude, due to the multi-modal and dispersive nature of the wave propagation, where the arrival of multiple wave packets occurs at different times. In contrast, the shear sensors detect the arrival of a single, distinct wave packet. Example waveforms are shown in Figure 5 and Figure 6 for shear and conventional sensors, respectively. The signals shown were generated by an acoustic emission event that was received by both sets of sensors at nearly identical times.



Figure 4. AE data for conventional (left) and shear (right) sensors on a steel tower leg. AE signals indicate damage at a welded cross-beam with a weld undercut, but no visible cracking was identified. The undercut location is near 208-210", indicated by the horizontal dashed box.

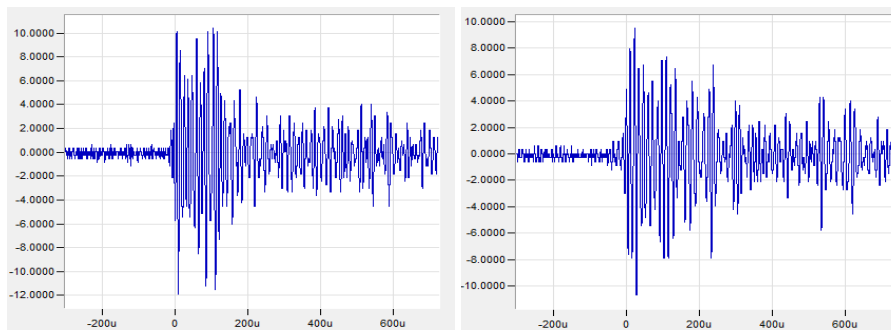


Figure 5. Waveforms recorded by the two shear sensors from a time-linked event also recorded by conventional sensors. The shear sensors show a distinct wave packet arrival. The left and right plots show the arrival at the first and second sensor, respectively.

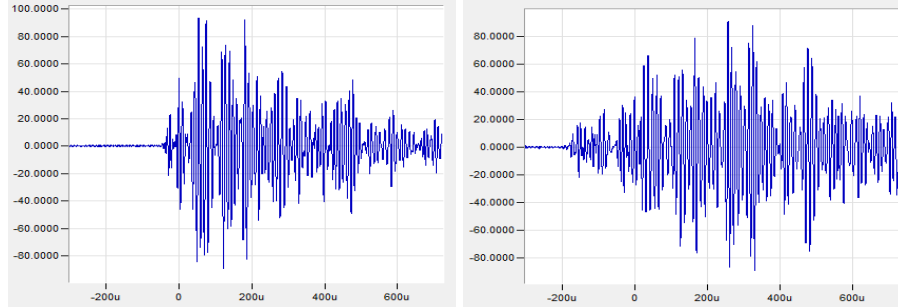


Figure 6. Waveforms recorded by the two conventional sensors from a time-linked event also recorded by shear sensors. The conventional sensors show a more gradual increase in wave amplitude as multiple wave packets arrive at different times. The left and right plots show the arrival at the first and second sensor, respectively.

#### 4. RESULTS – ENVIRONMENTAL NOISE (RAIN)

Data assessing the effect of rain was collected on the Air Force tower shown in Figure 1. The external tower structure was instrumented with 14 conventional 150 kHz resonant sensors which spanned the entire north side of the external tower structure. One 200 kHz resonant shear sensor was collocated on the structure next to a conventional sensor. A fixed threshold of 40 dB was used for all of the conventional sensors and a fixed threshold of 25 dB was used for the shear sensor.

During a 10-minute period of light rain at 39°F, the conventional sensors collectively recorded 51 hits. The shear sensor recorded no hits. The conventional sensor collocated with the shear sensor recorded 11 hits, with a maximum amplitude of 50 dB. The lack of hits recorded by the shear sensor during rain demonstrates a key advantage of using a shear sensor in outdoor environments. Many radar tower structures are external, and data collection during storms, when wind loading is highest, is of particular interest since crack growth is expected during the highest loading events. Beyond tower inspection, other applications such as bridge health monitoring and power transformers could benefit from sensors less sensitive to rain, as typically monitoring is stopped or the data is discarded during periods of rain. When using shear sensors, it may be possible to allow continuous monitoring through storm events.

#### 5. CONCLUSIONS AND RECOMMENDATIONS

Initial field tests of new omnidirectional shear AE sensors show promise for increased localization accuracy and decreased sensitivity to environmental noise. Additional study is needed to further characterize the sensors' benefits and extend field testing onto new structures and into new applications. The shear AE sensors show promise as replacement or companion sensors, depending on the application. In future work, the potential to improve source characterization will be assessed when jointly using conventional and shear AE sensors. Source characterization may be improved through analysis of wave information from all three fundamental guided wave mode types.

## 6. REFERENCES

1. SBIR Solicitation topic number F161-011, "Acoustic Emission of Frangible, Composite, Concrete and Metallic Radar Towers," SBIR / STTR Website, Accessed Jan 15, 2019, <https://www.sbir.gov/sbirsearch/detail/870157>.
2. C. Borigo, S. Owens, and J.L. Rose, "Piezoelectric Shear Rings for Omnidirectional Shear Horizontal Guided Wave Excitation and Sensing," U.S. Patent 20170030848 A1 issued February 2, 2017.
3. J. Philtron, C. Borigo, S. Owens, and R. Love, "Shear Wave Sensors for Acoustic Emission and Hybrid Guided Wave Testing," U.S. Patent Appln. 16/033,911 filed July 12, 2018. (Provisional 62/531,663 filed July 12, 2017.)
4. Acoustic Emission Testing, Volume 6, 3rd Edition, NDT Handbook Series published by ASNT, Ronnie K. Miller and Eric v.K. Hill Technical Editors (2005).
5. *FAA radar (Bennett, Colorado).JPG*, Jeffrey Beall, Creative Commons Attribution 4.0 International license, [https://commons.wikimedia.org/wiki/File:FAA\\_radar\\_\(Bennett,\\_Colorado\).JPG](https://commons.wikimedia.org/wiki/File:FAA_radar_(Bennett,_Colorado).JPG). Accessed January 15, 2019.
6. *Wea01195 - Flickr - NOAA Photo Library.jpg*, Eric Kurth, Creative Commons Attribution 2.0 Generic license, [https://commons.wikimedia.org/wiki/File:Wea01195\\_-\\_Flickr\\_-\\_NOAA\\_Photo\\_Library.jpg](https://commons.wikimedia.org/wiki/File:Wea01195_-_Flickr_-_NOAA_Photo_Library.jpg). Accessed January 15, 2019.

# A new Time-domain Feature called the Really Keen Metric (RKM) for Acoustic Emission Transient Signal Processing<sup>1</sup>

Ronnie K. Miller<sup>a</sup>, Jason Philtron<sup>b</sup>, Cody Borigo<sup>b</sup>, and Steven Owens<sup>b</sup>  
<sup>a</sup>AE Consultant; <sup>b</sup>Guidedwave, Inc., Bellefonte, PA

## Abstract:

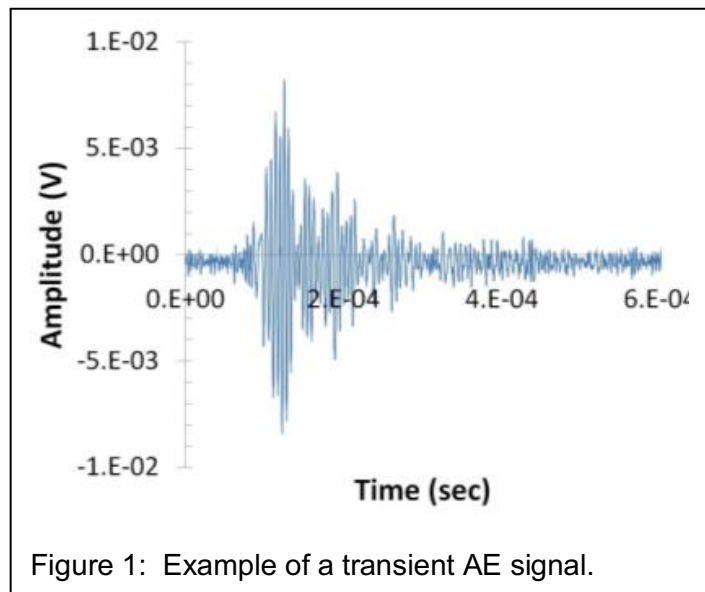
A series of dynamic tests were performed where certain equipment was monitored with Acoustic Emission (AE). Resonant AE sensors were used and coupled to MISTRAS AE instrumentation. The recorded data comprises data files with 8,000 to 10,000 Hits recorded over a very short period of time (<15 seconds). Of interest during these tests were AE signals that are truly indicative of transient signals that have a clear beginning and end and an exponential decay after the peak amplitude is observed. Unfortunately, the data sets were contaminated with considerable amounts of extraneous emission that could only be filtered by manually examining the waveform collected for each Hit. The use of correlation plots to separate these AE signals was helpful to a certain extent but through the process of manual data filtering, it became clear that a well-defined time-domain feature could be very efficient in separating the transient signals from extraneous emissions. This paper presents a concept for a new time-domain feature that is capable of better defining transient-like AE signals as defined above. This feature is called the Really Keen Metric (RKM) and will be presented with actual examples recorded during the above testing.

**Keywords:** Waveforms, Transient-like, Non-transient-like, Data Filtering, Exponential Decay

## 1. Introduction:

In most AE applications, signal processing is based on the assumption that you will be working with a transient shaped signal (volts vs time) that has a clear beginning and end when compared to a detection threshold. In addition, early in the signal, the amplitude rises to a peak and then decays exponentially until the signal reaches the background noise level. A typical signal is shown in Figure 1.

A typical transient signal can be described with a set of time-domain features that can be extracted from a signal like the one shown in Figure 1. These features include: Rise Time, peak Amplitude, Duration, Counts, and



<sup>1</sup> NAVAIR SBIR, Phase II Topic N171-011, Contract # N68335-18-C-0520, "Acoustic Emission and Ultrasonic Inspection System for Advanced Arresting Gear Water Twister".

Energy (or Absolute Energy). In theory, different AE sources create different AE signals when detected by a sensors. The shape of the signal is dictated by the source function, wave propagation, and the characteristics of the sensor that detects the elastic wave that was generated by the AE source. On occasion, correlation plots of these features can be used to differentiate different AE sources. However this is not true in all cases as one sometimes finds signals from extraneous emissions mixed in with the signals of interest.

This paper looks at several cases of signals that were recorded during actual testing of real equipment. Attempts to separate the different signals using the correlation plot approach failed pointing out the need for some other means for separating these signals. The solution was to define a new time-domain feature that could be extracted from the AE signal that provides an indication that the signal is transient in shape by means of a decay measurement. The new feature is called the Really Keen Metric (RKM).

**2. Test Results:**

A series of tests were performed on real equipment as it was being used in the field. A description of the equipment and how it is used is not important in this case. What is important is that conventional resonant transducers were being used and waveforms were being recorded for every Hit detected. The stimulus involved changed dramatically over the course of the test resulting in signals that saturated (around 100 dB) to signals that were barely detectable using a 30 dB detection threshold.

An example of a desirable transient signal is shown in Figure 2. A “good healthy one” is shown on the left with a “low-amplitude questionable one” on the right.

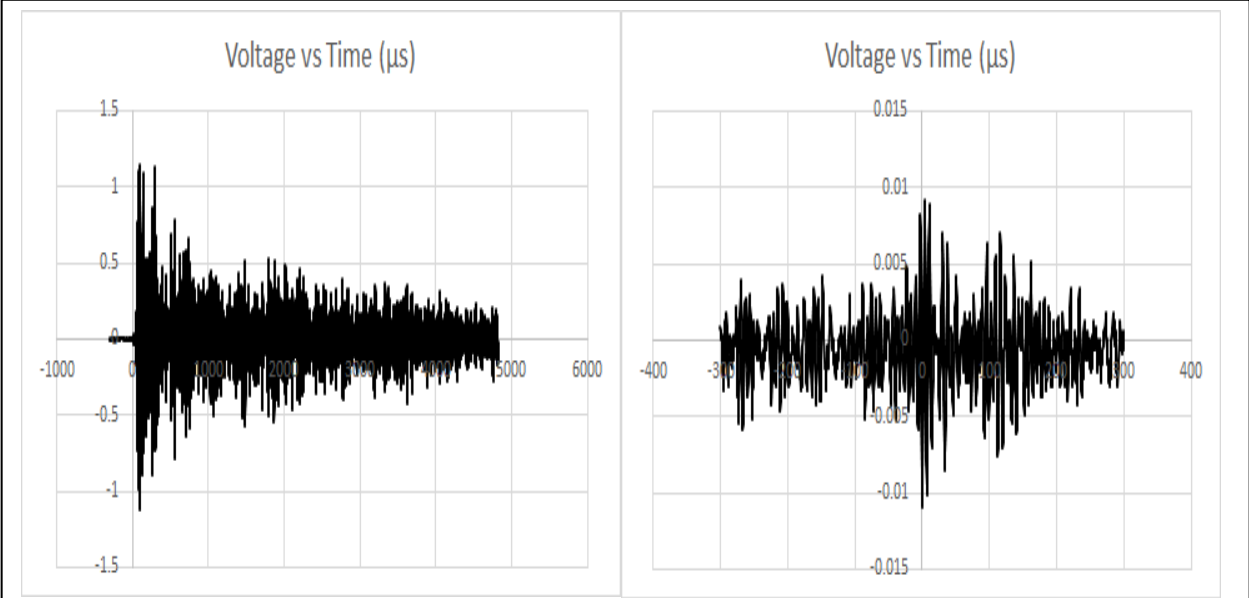


Figure 2: Examples of a “healthy” transient signal (left) and a “low-amplitude questionable” one.

In contrast to the transient-like signals shown in Figure 2, many signals were recorded that appeared quite different as shown in Figure 3. This signal is mostly saturated leading you to believe that the time-domain features extracted from this waveform could easily be used to

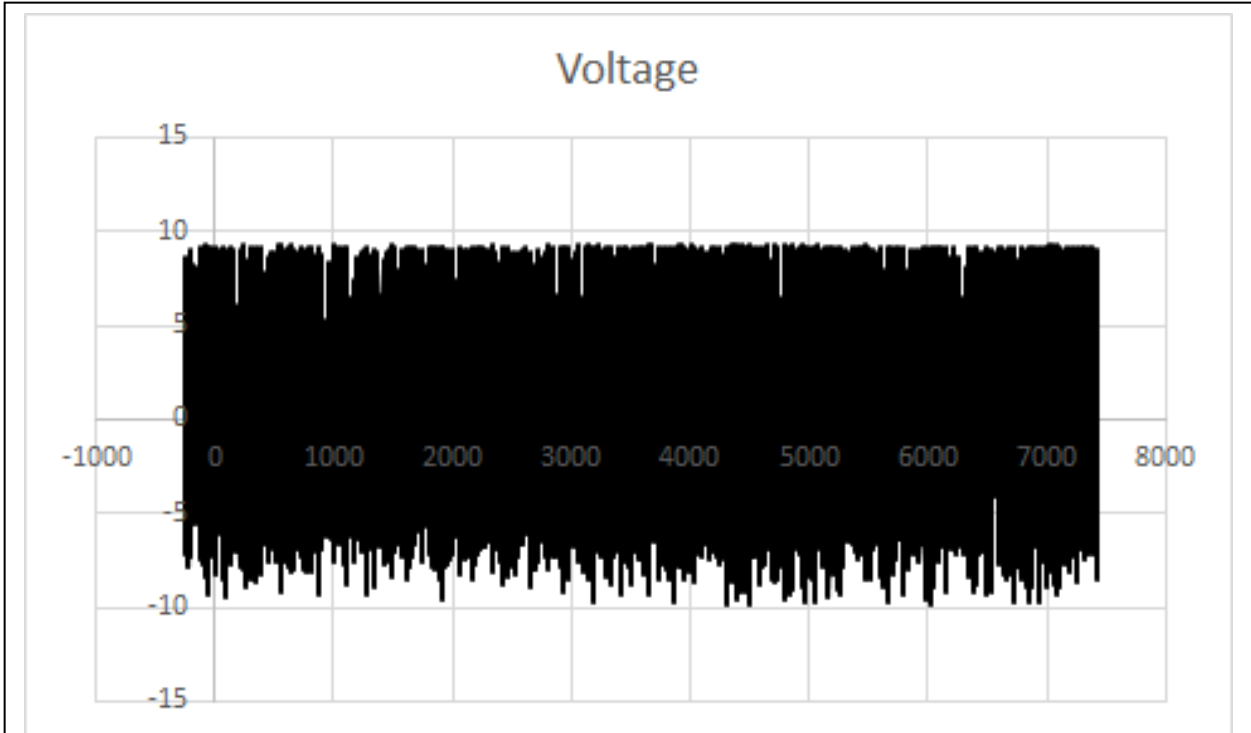


Figure 3: Example of saturated signal recorded during the same test.

differentiate it from the transient signals shown in Figure 2. That's not the case. More examples are shown in Figure 4 where once again, the time-domain features could not be used to easily differentiate these signals from the desirable transient-like features.

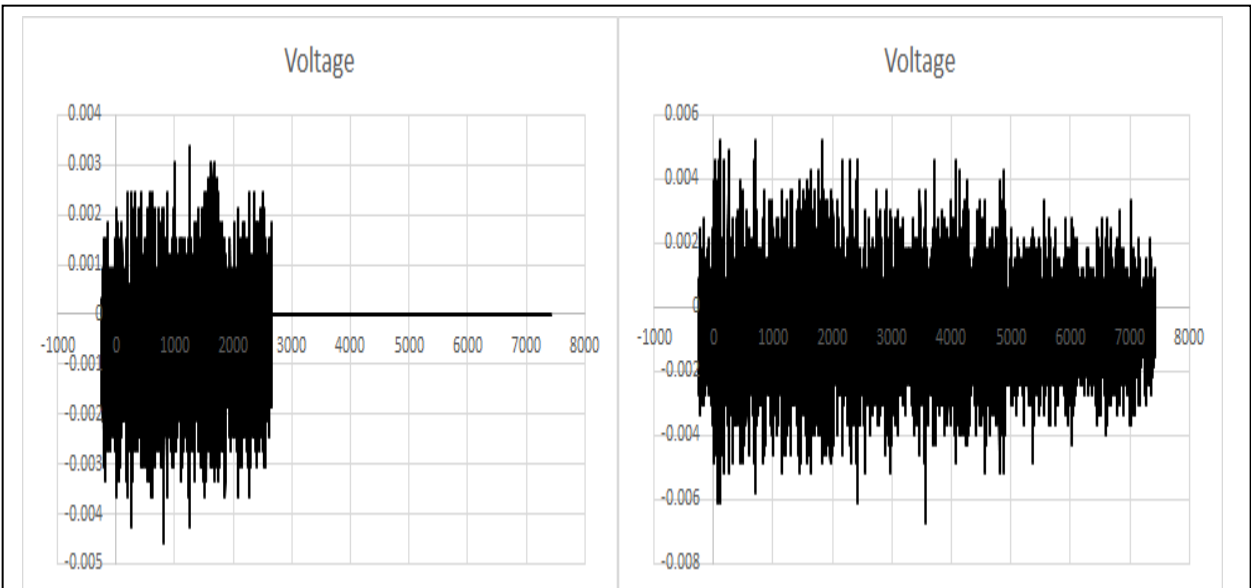


Figure 4: Examples of other extraneous signals recorded during the same test.

In truth, there are no time-domain features defined that focus on the transient shape of the traditional AE signal. Especially the exponential decay that is seen after the peak amplitude is reached. This led to an effort to establish such a feature as described in the following.

The first approach focused on rectifying the signal first. Next, the peak amplitude was identified and then 20 kHz low pass filtering was applied from that point on. The results are shown in Figure 5 for the two transient signals shown in Figure 2. The decay is shown in the graph title in units of  $\mu\text{V}/\mu\text{s}$ . It can be seen that the decay values range from about 1.15 to 164  $\mu\text{V}/\mu\text{s}$ . The same processing was applied to the AE signals shown in Figure 3 and 4 with the results shown in Figure 6. Decay values range from 0.126 to 6,517  $\mu\text{V}/\mu\text{s}$ .

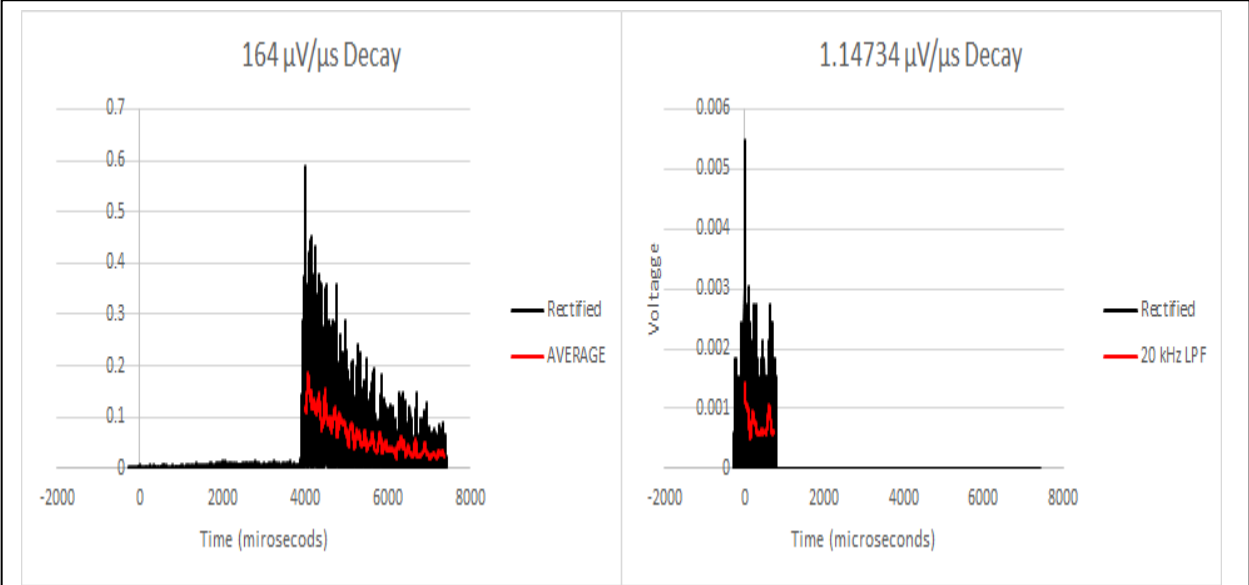


Figure 5: The transient-like signals from Figure 2 after rectification and 20 kHz low pass filtering from the peak amplitude to the end of the waveform.

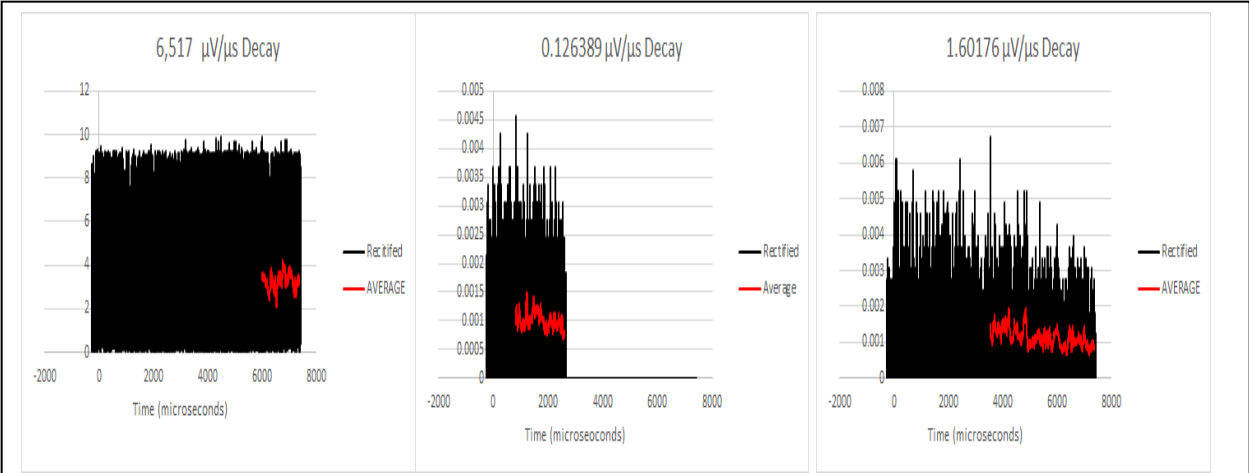


Figure 6: The non-transient-like signals from Figure 3 and 4 after rectification and 20 kHz low pass filtering from the peak amplitude to the end of the waveform.

Based on the results shown above, this method appeared to have too much spread in the values for decay measured in units of  $\mu\text{V}/\mu\text{s}$ . As a result, another approach was investigated where the rectified signal was converted into a logarithmic scale with the same low-pass filtering applied. The results are shown in Figure 7 for the transient-like signals and Figure 8 for the non-transient-like signals. Decay values range from 0.00417 to 0.00872  $\text{dB}/\mu\text{s}$  for the transient-like signals and from -0.00134 to 0.00139  $\text{dB}/\mu\text{s}$  for the non-transient-like signals.

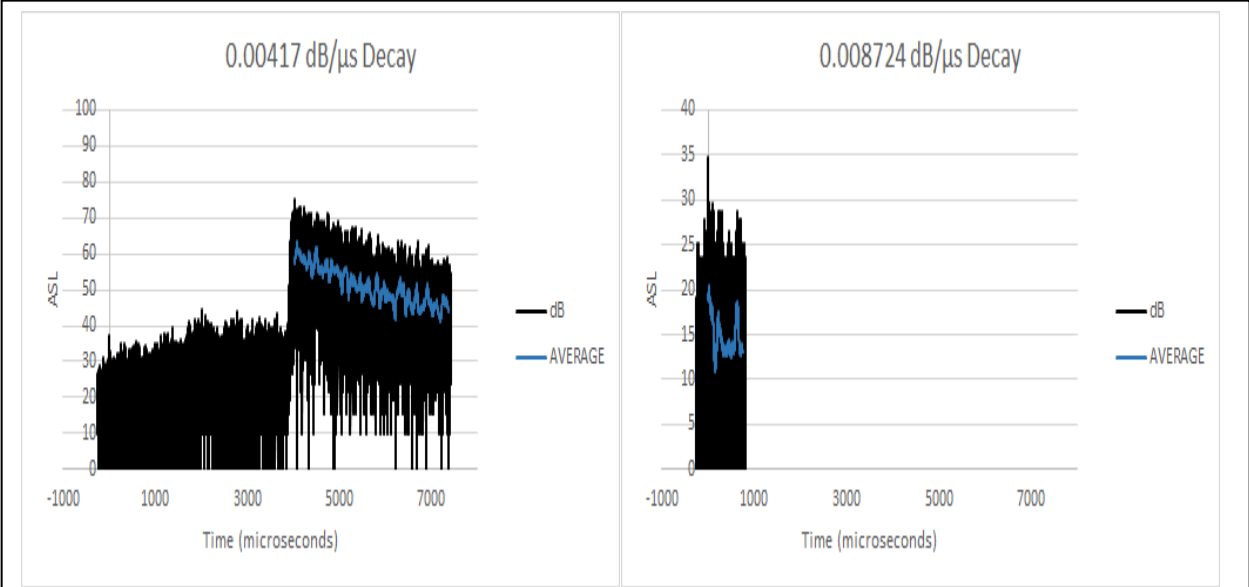


Figure 7: Results after logarithmic conversion, filtering and averaging from the peak amplitude to the end of the waveform for transient-like AE signals.

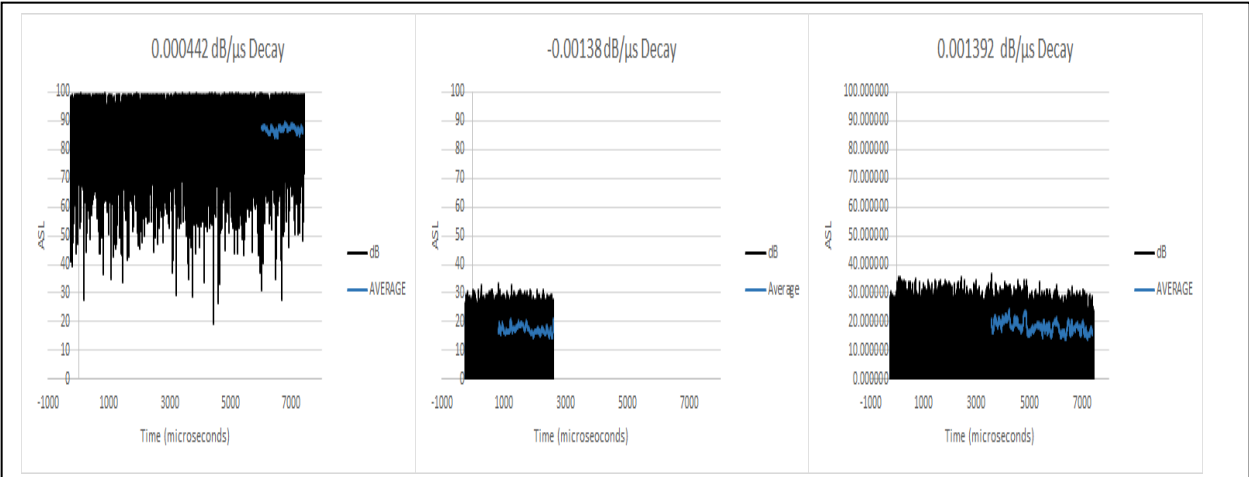


Figure 8: Results after logarithmic conversion, filtering and averaging from the peak amplitude to the end of the waveform for non-transient-like AE signals.

This type of processing was applied to AE signals produced by Electro Magnetic Interference (EMI) as it is expected to produce a much higher decay rate. The results for the signal shown in Figure 9 (left) are shown in Figure 9 (right) where the decay rate is estimated at 1.4896 dB/ $\mu$ s.

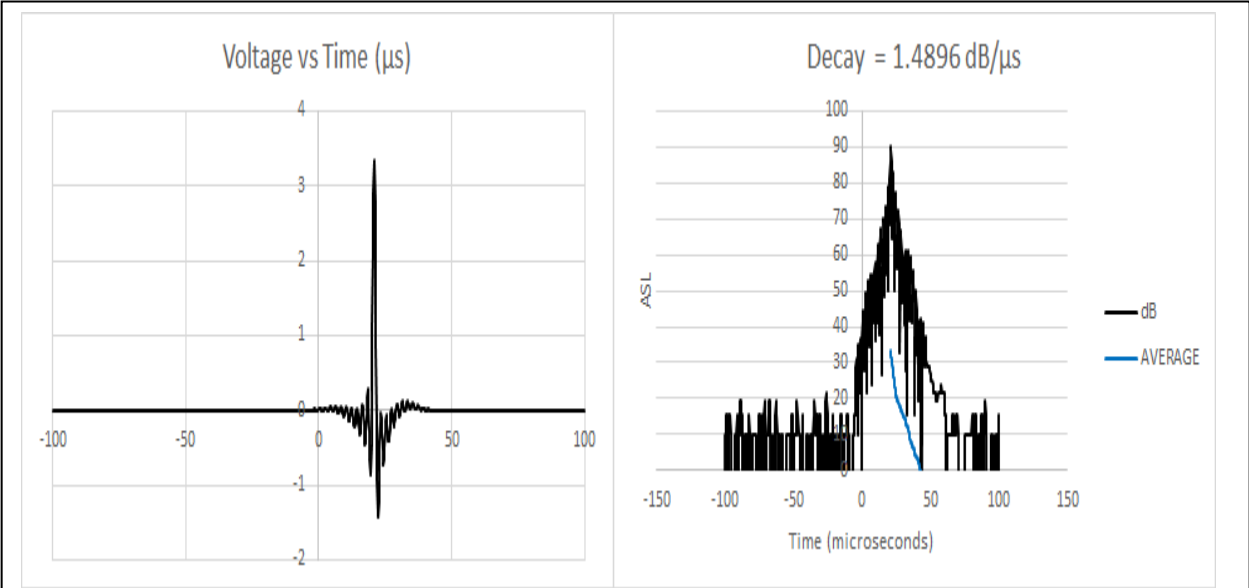


Figure 9: EMI waveforms (left) and results of the proposed signal processing (right).

### 3. Conclusions and Recommendations:

Based on the results of this study, it was determined that transient-like AE signals can be separated from non-transient-like AE signals by virtue of the decay observed in the signal. This was done by processing the portion of the waveform where the peak amplitude is observed to the end of the waveform. The processing first requires rectification of the AE signal and then 20 kHz low pass filtering. Then the rectified and filtered signal is converted into a logarithmic scale so that the decay from the peak amplitude to the end of the waveform can be calculated. This decay feature is called the Really Keen Metric (RKM) and it is recommended that the commercial suppliers of AE instrumentation add this time-domain feature to the list of currently available features that can be extracted from the AE signal.

Ideally, this will lead to faster real time and posttest filtering for separating transient-like and non-transient-like AE signals. In addition, it remains to be seen how useful the RKM feature may be in terms of the mechanical properties of the material being monitored or the performance of the AE sensor used.

# Abstracts of Papers Submitted

## **Burst pressure prediction of composite vessels**

Markus Sause<sup>1</sup>, Stefan Schmitt<sup>1</sup>, Birte Hoeck<sup>2</sup>, Andreas Monden<sup>1</sup>

<sup>1</sup>University of Augsburg, Germany

<sup>2</sup>MT Aerospace AG, Germany

We propose an acoustic emission based method to predict the local stress exposure of a fiber-reinforced material. This approach uses a stepwise increased load profile as common in testing procedures of fiber-reinforced pressure vessels. We apply an artificial neural network to establish a relationship between acoustic emission criteria evaluated for each load cycle and the globally applied load ratio. The acoustic emission training database for this neural network is obtained from lab-scale experiments, such as tensile tests, bending tests, double-cantilever-beam tests, end-notched-flexure tests and lap-shear tests. We present the application of this neural network to burst tests of three small-scale pressure vessels (560 mm length) and two large-scale pressure vessels (2600 mm length) for burst pressure prediction. In all cases, the deviation between predicted and measured burst pressure is less than 3.0 %, with a maximum prediction uncertainty of 9.8 %. In addition, we present a segmentation technique, which allows evaluating the acoustic emission criteria for sub-volumes of the full structure. This is based on precise source localization of the acoustic emission signals using artificial neural networks. The local prediction of load ratios allows evaluating the stress exposure of the structure as function of the applied load cycles. The resulting concentrations of stress exposure are compared to in situ camera analysis during the tests, strain gage measurements and post mortem analysis of the vessels. In all cases, good agreement with the prediction of the local load ratio is found.

**Keywords:** Burst pressure, Failure prediction, Felicity Ratio

## **Using machine learning to predict welding quality from airborne AE sensor data**

Kaiser Asif<sup>1</sup>, Lu Zhang<sup>1</sup>, Sybil Derrible<sup>1</sup>, Ernesto Indacochea<sup>1</sup>, Didem Ozevin<sup>1</sup>, Brian Ziebart<sup>1</sup>

<sup>1</sup>University of Illinois at Chicago, United States

Current weld monitoring and evaluation processes are usually conducted in the post-weld stage. In this way, defects are found after the weld is completed, often resulting in disposal of the expensive material or lengthy repair processes. Simultaneously, weld quality inspections tend to be performed manually by a human, even for an automated weld. Therefore, a proper real-time weld quality monitoring method associated with decision-making strategy is needed to increase the productivity and automaticity in weld. In this study, acoustic emission (AE) as a real-time monitoring method is introduced for gas metal arc weld (GMAW). Several types of AE sensors (R6, WD, R15 and R1.5) are used to cover all possible frequency ranges from 5 kHz to 400 kHz. Additionally, the welding parameters (weld current, voltage, gas flow rate and heat input) are also recorded during the welding process. Different types of weld are artificially created to generate different signals. For the automated decision-making system, machine learning algorithms are used. Several features extracted from the AE and welding parameter monitoring system feed into a machine learning algorithm. For decision-making, we train supervised learning models and evaluate their performances on unseen data. General machine learning models for classification e.g. Logistic Regression predict each data-point separately. In this work, we also show that considering the prediction task as a sequence tagging problem provides better performance. We use our own developed method for sequence tagging in this work. Finally, we compare different feature combinations and models and present the analyses of the automated welding quality prediction system.

**Keywords:** Welding, airborne AE, machine learning

## **Phased Acoustic Emission Sensor Array for Determining Radial and Axial Position of Defects in Pipe-like Structures**

Lu Zhang<sup>1</sup>, Chen Enpei<sup>1</sup>, Gorkem Okudan<sup>1</sup>, Didem Ozevin<sup>1</sup>

<sup>1</sup>University of Illinois at Chicago, United States

The Acoustic Emission (AE) method has been successfully applied to detect and pinpoint horizontal position of defects in pipelines. The AE method relies on propagating elastic waves triggered by the turbulence flow due to the internal pressure release at the leak location or sudden burst due to crack growth or impact. Considering the ratio of length to cross-section in pipe-like structures, the source localization is considered as one-dimensional (1D) problem. In this paper, AE sensor array is positioned around the circumference of pipe. The sensing orientation of each neighbor sensor is designed as longitudinal and transverse directions in order to determine the axial location of defect from the arrival time differences as longitudinal and transverse modes have two distinct wave velocities. Numerical simulations are performed to determine the influence of sensor-source distance in radial coordinate system such that actual coordinate of defect location can be determined. The influence of source-sensor distance is studied by varying the axial and radial position of the simulated source. The numerical results are tested on a laboratory-scale steel pipe. Crack growth and leak are simulated using pencil lead break and orifice, respectively. In conventional AE, each channel detects AE signals independent from each other. The synchronized AE sensing is studied to determine the influence of trigger approach to determine the time of flight.

**Keywords:** Pipe, phase-array AE, localization

## **Development of Optical Fiber AE Sensor by FBG with WDM**

Hisafumi Asaue<sup>1</sup>, Tomoki Shiotani<sup>1</sup>, Katsufumi Hashimoto<sup>1</sup>, Iori Yamamoto<sup>2</sup>, Hidehiro Inaba<sup>2</sup>

<sup>1</sup>Kyoto University, Japan

<sup>2</sup>Fuji Ceramics Corporation, Japan

Electric sensor of AE method have some problem. For example, all weight become heavy if the number of cable connected sensor to equipment increase. It is difficult to embed the sensor based on long-term use due to deterioration or breakdown. The sensor is affected by electrical noise. To solve these problem, AE sensor consisted of FBG was developed by irradiating ultraviolet light to optical fiber. Since the optical fiber has characteristics such as light weight, non-inductivity of electromagnetic interference noise, insulation, explosion resistance, wide band and low loss of signal transmission, the above sensor is resistant to electrical noise, low failure rate, usable even under high or low temperature conditions, and acquisition of high reliability data in long time use. The optical AE sensor can be measured data 800 kHz sampling time using Wavelength Division Multiplexing. As a result of elastic wave waveform with good signal-to-noise ratio could be measured by interrogator capable of high-speed measurement and performing filtering processing.

**Keywords:** Optical fiber, FBG, WDM, Elastic wave, Filtering processing

## **The material condition evaluation of pressure vessels after long-term operation in the oil refining processing using acoustic emission method and structure stress field analysis**

Igor Lyasota<sup>1</sup>, Marek Nowak<sup>2</sup>, Lukasz Sarniak<sup>3</sup>, Pitir Kustru<sup>4</sup>

<sup>1</sup>Cracow University of Technology, Poland

<sup>2</sup>Office of Technical Inspection, Poland

<sup>3</sup>Warsaw University of Technology, Poland

<sup>4</sup>AGH University of Science and Technology, Poland

Different types of pressure equipment are widely used in oil refining and petrochemical processing. A lot of these were made from carbon steels and have been used for a few decades. Long-term operation under extreme conditions causes defect initiation and growth in the microstructure of the equipment materials. The defects, which grow due to work loads, may damage the entire structure and may lead to the failure of the entire industrial unit. Consequently, the development of new non-destructive evaluation methodologies which allow the assessment of the condition of materials comprising the pressure equipment after long-term operation in the refinery industry is very important. The methodologies development is possible as a result of complex destructive laboratory tests combining different experimental techniques. The paper presents results obtained from the complex destructive tests with acoustic emission (AE) recording on real pressure vessel (capacity of 2.6 m<sup>3</sup>) after long-term operation in the refinery industry. The vessel has been operated in crude oil distillation unit for over 40 years. A lot of corrosion damages were present on the inner surface of the vessel shell as a result of long-term operation. The material's microstructure of some shell plates was coarse-grained, which arose from improper heat treatment during plates manufacturing. The hydraulic pressure test with AE recording of the pressure vessel was shown that AE method allowed to detect of local plastic deformation processes and early stage of crack initiation in overheated and corrosion degraded shell's material. The results of the conducted investigations form the basis for the developing of a complex methodology for assessment of the technical condition of pressure equipment in the refinery industry. The investigations, presented in this paper, were realised within the project of LIDER VII Programme financed by the National Centre for Research and Development of Poland.

**Keywords:** Acoustic emission; pressure equipment, material degradation, carbon steel

### **A comparison study of Vibro-Acoustic Modulation technique and Conventional AE**

Behnoush Golchinfar<sup>1</sup>, Majid Ramezani Goldyani<sup>2</sup>, Hossain Saboonchi<sup>1</sup>, Dimitri Donskoy<sup>2</sup>

<sup>1</sup>MISTRAS Group, Inc., United States

<sup>2</sup>Stevens Institute of Technology, United States

The necessity of safety diagnosis of structures has recently been emphasized due to the aging of public PSC bridges over 20 years. Tendons consist of external tendon and internal tendon type. External tendon types are already undergoing inspection and repair through visual inspection and general non-destructive methods in case of problems. However, internal tendon-type PSC bridges are buried in the concrete filled with grout to prevent corrosion of stranded strand, and after the severe damage caused by corrosion, there is no inspection method that can be confirmed. Acoustic emission technology has attracted attention recently as a technology capable of diagnosing defects of large structures and locating defects. The acoustic emission technique was used to detect the failure state of the internal tendon of the PSC bridge and to analyze the defect signal transmitted through the tendon to find the degree of damage and the location of the defect. The purpose of this study is to evaluate the integrity of the tendon by distinguishing the general signal from the concrete and the defect signal from the internal tendon. Average frequency and RA value were used as parameters for fault diagnosis and analysis. In addition, RTRI and Ib Value were applied for the evaluation of defectiveness and Integrity. Finally, in this study, it was confirmed that diagnosis of internal tendon of PSC structure is possible by analyzing the acoustic emission characteristic signal generated in the PSC structure at the time of load application.

**Keywords:** Nonlinear Ultrasonic, Acoustic Emission, Vibro-Acoustic Modulation Technique

### **Far-field wave propagation signals from pencil lead breaks on the open end of a thick-walled layered cylinder: Part 1 Amplitudes and frequency content\***

Marvin Hamstad<sup>1</sup>

<sup>1</sup>University of Denver, United States

Relative to potential use of acoustic emission (AE) to monitor pressure testing of large steel pressure vessels, in-plane pencil lead breaks (PLBs) were carried out on the open end of a remnant of such a vessel. This remnant had an inner diameter of 58 in. (1473 mm), a wall thickness of 3.3 in. (84 mm) and a total cylindrical length of 125 in. (3175 mm) ending in a head welded to the cylindrical section. The cylindrical section did not have a monotonic wall, but instead it was made of 11 layers (10 at about 0.277 in. [7 mm] thick, and the inside one of about 0.47 in. [11.9 mm] thick) to create a layered pressure vessel (LPV). Due to the presence of the multiple interfaces between layers, a question arose as to whether a sensor mounted on the outer layer was relatively less sensitive and had different frequency content for sources on the inner layers compared to sources on the layers? The PLB study used four pairs of different types of AE sensors. The sensor types included: i) strong resonance at a single frequency region; ii) multiple resonance frequencies; iii) and iv) broadband response with different frequency responses. Each sensor pair was acoustically coupled, one on the outside surface and one directly below on the inside surface. The sensor pairs were located at 66 in. (1676 mm) (20 times the wall thickness) from the PLB points. This distance was considerably less than the helical path of about 214 in. (5436 mm). Considering PLBs on the ends of the different layers, part 1 focused on changes in the character of the AE signals from the four sensor types. Comparisons for each sensor type were made of the amplitudes of the outside sensor relative to those of the inside one. In addition, as the PLB was moved to different layers, the changes in the signals and frequency content of the different sensor signals were studied. Except for one sensor type, the outer sensor peak signal amplitudes relative to the inner sensor peak signal amplitudes changed significantly as the PLB layer moved from the outer layers to the inner layers. In addition, the signals and frequency content also varied with changes in the PLB layer. The results represent a lower bound due to the potential for some increased transmission between layers when a LPV is pressurized to significant levels.

\* The author is grateful for the funding, purchase of equipment, facilities and excellent experimental support provided by NASA Marshall Space Flight Center, Huntsville, AL, USA.

**Keywords:** Thick-walled layered cylinder, pencil lead breaks, four sensor types, inside and outside sensors, wave propagation, amplitudes, frequency content.

## **Far-field wave propagation signals from pencil lead breaks on the open end of a thick-walled layered cylinder: Part 2 Modes of wave propagation\***

Marvin Hamstad<sup>1</sup>

<sup>1</sup>University of Denver, United States

Relative to potential use of acoustic emission (AE) to monitor pressure testing of large steel pressure vessels, in-plane pencil lead breaks (PLBs) were carried out on the open end of a remnant of such a vessel. This remnant had an inner diameter of 58 in. (1473 mm), a wall thickness of 3.3 in. (84 mm) and a total cylindrical length of 125 in. (3175 mm) ending in a head welded to the cylindrical section. The cylindrical section did not have a monotonic wall, but instead it was made of 11 layers (10 at about 0.277 in. [7 mm] thick, and the inside one of about 0.47 in. [11.9 mm] thick) to create a layered pressure vessel (LPV). Due to the presence of the multiple interfaces between layers, a question arose as to whether a sensor mounted on the outer layer was relatively less sensitive and had different frequency content for sources on the inner layers in comparison to sources on the outer layers? The PLB study used four pairs of different types of AE sensors. The sensor types included: i) strong resonance at a single frequency region; ii) multiple resonance frequencies; iii) and iv) broadband response with different frequency responses. Each sensor pair was acoustically coupled, one on the outside surface and one directly below on the inside surface. The sensors were located at 66 in. (1676 mm) (20 times the wall thickness) from the PLB points. This distance was considerably less than the helical path of about 214 in. (5436 mm). Considering PLBs on the ends of the different layers, part 2 focused on identification of Lamb modes of wave propagation in the AE signals from the four sensor types. In addition, by use of superimposed group velocity curves on frequency versus time results, the peak intensity in the frequency versus time domain for the outside sensor types was studied relative to determination of the presence of dominant full thickness propagation or dominant single layer propagation. For PLBs on the outer

most layers, both single layer propagation and full thickness propagation were present in some of the outer sensor signals.

\* The author is grateful for the funding, purchase of equipment, facilities and excellent experimental support provided by NASA Marshall Space Flight Center, Huntsville, AL, USA

**Keywords:** Thick-walled layered cylinder, pencil lead breaks, four sensor types, inside and outside sensors, wave propagation, Lamb modes

### **Self-Healing Degradation of Asphalt Concrete Materials due to Cooling Cycle:**

Behzad Behnia<sup>1</sup>, Henrique Reis<sup>2</sup>

<sup>1</sup>Department of Civil and Environmental Engineering, 106 William Rowley  
Laboratories, Clarkson University, United States

<sup>2</sup>University of Illinois at Urbana-Champaign, United States

Asphalt concrete is one of the most widely used materials in transportation infrastructure, covering the surface of approximately 94% of more than 4 million miles of highways in United States. Asphalt pavements located in cold regions or in milder climate areas with large daily temperature fluctuations encounter thermal cracking manifesting itself in the form of several transversely oriented surface-initiated top-down cracks of various lengths and widths. Self-healing as an intrinsic property of asphalt materials mitigates the thermal cracking process in asphalt pavements and extends pavements' service life. However, self-healing properties of asphalt pavement gradually diminishes with aging. The present study utilizes the Acoustic Emission (AE) technique and the fracture-based Disk-shaped Compact Tension (DCT) test to provide quantitative assessment of self-healing of thermally-induced damage in asphalt concrete materials at the micro (AE test) as well as macro (DCT test) levels. Asphalt concrete specimens were subjected to eight controlled cooling cycles and effects of resting, i.e., dwell time, between cooling cycles on self-healing were investigated. The Felicity effect phenomenon was observed in this study indicating occurrence of self-healing in the material. The AE test results showed gradual degradation in self-healing capability of asphalt mixtures as the material was exposed to cooling cycles. However, it was observed that the rate of self-healing degradation was not constant as it was higher at the beginning and then gradually reduced until it reached almost zero after the fourth cooling cycle. Moreover, AE results also indicated that the 12 hours dwell time between cooling cycles significantly increased the self-healing by more than 30% and allowed the material to regain most of its self-healing capabilities. DC(T) fracture energy results were consistent with the findings from AE test. Results also demonstrated that, on the average, 12 hours resting time increased fracture energies of asphalt mixtures by about 13%.

**Keywords:** Asphalt concrete; thermal cracking; self-healing; Acoustic Emission; disk-shaped compact tension; cooling cycles; Felicity effect; Kaiser effect

### **Application of Surface-Wave Tomography to Sealed Conditions of Repaired Cracks in Concrete**

Nobuhiro Okude<sup>1</sup>, Tomoki Shiotani<sup>2</sup>

<sup>1</sup>Tokai Technology Center, Kyoto University, Japan

<sup>2</sup>Kyoto University, Japan

NDT method to confirm sealed conditions of repaired cracks in concrete has not been yet established. As a promising technique, the surface-wave tomography is applied to evaluate the conditions. In a concrete abutment for water pipelines located at a cold region, surface cracks are visually identified. Since these cracks are repaired with sealing, the tomography measurement is applied before and after sealing in concrete. As a result, it is confirmed that the repaired conditions are successfully evaluated by the surface-wave tomography. In this regard, it is found that the effects of wave-lengths of the surface-waves and material properties of sealing agent are to be further clarified for practical applications.

**Keywords:** Surface wave, injected depth, crack injection method

### **Modeling the acoustic emissions produced by the dynamic fracture of a glass beam**

Valentin van Gemmeren<sup>1</sup>, Jurg Dual<sup>1</sup>

<sup>1</sup>Institute for Mechanical Systems, ETH Zurich, Switzerland

In structural health monitoring, a wide variety of parameters are employed to characterize acoustic emissions (AE) belonging to specific failure modes. To better understand acoustic emissions and the corresponding parameters, researchers aim to model the fracture process and the resulting elastic waves. In previous work, we have developed a method to induce precisely controlled dynamic fracture in a glass beam by focusing flexural waves at an arbitrarily chosen location in space and time. During the fracture event, a single AE occurs, propagates through the glass beam and is measured with a laser Doppler vibrometer. The AE from this experiment is reproducible as the loading conditions during fracture are highly controlled. We model the fracture process as the instantaneous splitting of the beam into two parts and the subsequent unloading of the fracture surfaces. Then, we simulate the propagation of the resulting elastic waves through the glass beam with a spectral element model. The AE obtained in the simulation show good quantitative agreement with the measured AE from the experiment.

**Keywords:** AE modeling, dynamic fracture

### **Infrastructure monitoring: solutions and examples**

Horst Trattnig<sup>1</sup>, Michael Hauserer<sup>1</sup>

<sup>1</sup>Vallen Systeme GmbH, Germany

The tragic collapse of the Morandi Bridge in Genoa in August 2018 is another indication that the massive worldwide investment backlog for long living infrastructures is not yet solved. On the one hand huge investments are required to replace the dilapidated structures and on the other hand lots of time is required for planning the reconstructions. During the years of required planning time, the critical structures are still in operation and the risk has to be minimized. The owner of the infrastructures, like cities and municipalities, use monitoring solutions as backup. Among other methods such as temperature measurement, strain gauges ect., the demand for Acoustic Emission is strongly increasing and moves more and more in focus to solve the task. The method is suitable for permanent monitoring and its flexibility makes it adaptable to a variety of test objects. Vallen System GmbH is involved in many monitoring projects as equipment provider together with service providers, engineering firms and the infrastructure owners. The measuring systems have been adapted to the new requirements throughout the entire measuring chain, from the sensors, their mounting devices and cables, via the data recording to the software. A plurality of external sensors e.g. for temperature or strain gauges etc. can be recorded in a standardized way via data loggers and processed together with the Acoustic Emission data in the Vallen software. In the future, decision relevant information will be accessible via cloud based dashboard.

**Keywords:** Infrastructure monitoring bridge

### **Multichannel fiber laser acoustic emission sensor system**

Caitlin Williams<sup>1</sup>, Meredith Hutchinson<sup>2</sup>, Marriner Merrill<sup>2</sup>, William Pogue<sup>2</sup>, Peter Finkel<sup>2</sup>, Geoffrey Cranch<sup>2</sup>

<sup>1</sup>KeyW Corporation, United States

<sup>2</sup> US Naval Research Laboratory, United States

We demonstrate a multichannel fiber laser acoustic emission (AE) sensor system comprising four fiber laser sensors on a single optical fiber in an accelerated fatigue experiment. Specifically,

experiments are reported using fiber laser sensors to detect cracking in aluminum plates (multiple sensors) and riveted lap joints (single sensor). The multichannel data acquisition system is event driven and capable of sampling sensor signals at a rate of up to 25 MS/s per channel. The laser sensors are shown to provide comparable signal-to-noise ratio to industry standard piezo-electric sensors (MISTRAS S9225). We also present AE event and location-finding data from these experiments, along with data from piezo-electric sensors co-located with the fiber laser sensors.

**Keywords:** Fiber laser sensors, crack detection, accelerated fatigue

### **Acoustic Emission Information Discovery at the University of Illinois**

Mary C Schlembach<sup>1</sup>, William H Mischo<sup>1</sup>

<sup>1</sup>University of Illinois at Urbana-Champaign, United States

In the late 1990s, Allen T. Green, president of Acoustic Technology Group, donated his personal collection of acoustic emission publications to the Grainger Engineering Library at the University of Illinois at Urbana-Champaign. This collection is comprised of around 4,500 articles, technical reports and conference papers. The collection is particularly strong in government and corporate technical reports and has been utilized by researchers for many years. While many of the papers are available electronically, we are reviewing the more unique items in preparation for digitization. Some of these digitized documents will be placed in the Library's document repository, IDEALS. The Library has also developed an expanded information discovery and delivery service, called Easy Search, which provides access and full-text linking capabilities to journal, book, and report literature of acoustic emission. The full-text links in Easy Search resolve to publisher sites, government agency document sites, and to open access versions of the papers. Open access versions are available to anyone using the system. Our presentation includes information about digitization, copyright issues, and a demonstration of the Easy Search discovery software.

**Keywords:** Information discovery, publications, full text, open access

### **On the Use of Acoustic Emission in Vibrations Testing or Progressive Failure Monitoring and Modeling**

Brian Wisner<sup>1</sup>, Mira Shehu<sup>1</sup>, Johnathon Kordell<sup>2</sup>, Abhijit Dasgupta<sup>2</sup>, Harsh Baid<sup>3</sup>,  
Antonios Kontsos<sup>1</sup>

<sup>1</sup>Drexel University, United States

<sup>2</sup>University of Maryland, United States

<sup>3</sup>AlphaStar, United States

Damage in material systems is a stochastic, multiscale process which bridges incubation, nucleation, and growth. As the level of damage in a system progressively increases, changes in material response to external loads occur. In the case of rotor blades, shifts in the natural frequency during vibrational testing have been proposed and used as a means to identify damage as well as to replace components. Significant shifts, though, that can reliably identify damage during component use typically do not occur until near the end of component life and therefore provide minimal warning of impending failure. In this context, Acoustic Emission (AE) monitoring is proposed as a scale bridging method used in conjunction with frequency shifts for detection of early damage starting at the microscale, as well as for significant damage as end of life approaches. This work demonstrates the feasibility of this concept for two aerospace material systems, a precipitate-hardened aluminum alloy (Al 2024-T3) and a carbon fiber reinforced composite (IM7/8552). The specimens were damaged by application of a resonant frequency in a single degree of freedom shaker while the vibration response was measured by an accelerometer attached to the tip of the specimen. Additionally, strain and AE activity was monitored via sensors placed near the root of the specimen where damage is most significant. The monitored AE was first compared to results obtained for these material systems in monotonic and cyclic loading experiments where particular damage mechanisms were identified. The ensemble of recorded AE

data was then used in a post processing-scheme based on outlier analysis to form damage progression curves. The use of such progressive failure estimates produced by AE monitoring into a virtual testing framework is also presented.

**Keywords:** Vibrations, Resonant Frequency, Acoustic Emission, Progressive Failure Analysis, Virtual Testing

### **Acoustic Emission Monitoring for Additively Manufactured Materials**

Brian Wisner<sup>1</sup>, Emine Tekerek<sup>1</sup>, Mir Shehu<sup>1</sup>, Antonios Kotsos<sup>1</sup>

<sup>1</sup>Drexel University, United States

Acoustic Emission (AE), among other Nondestructive Evaluation (NDE) techniques, has been demonstrated to be particularly useful in the characterization of material behavior and the monitoring of their failure processes. Such NDE information, has been used to infer on material design choices mostly by connecting AE with microstructure and failure information to make both design and manufacturing changes. For example, in metallic alloys the role of defects such as voids, twins and inclusions has been investigated using AE during mechanical testing and resulted in insights related to recommendations of the appropriate use of metallurgical procedures to manufacture them. In this context, the increasing use of advanced manufacturing methods has resulted in an unprecedented number of new materials which although they are produced using the same base material (e.g. aluminum) they are now made using novel methods (e.g. selective laser melting, SLM) and consequently their quality and performance needs to be evaluated to allow their adoption in engineering applications. In this talk, the potential of AE monitoring to assess the manufacturing quality of a particle-reinforced Aluminum system is investigated. Specifically, AE monitoring coupled with microscopy is used to create a link between the level of the laser power used in SLM, the produced microstructure, and the resulting mechanical properties of this additively manufactured material. Extensions related to the use of AE in advanced manufacturing are also provided.

**Keywords:** Additive Manufacturing, Metals, Acoustic Emission, Mechanical Behavior, Characterization

### **Detection of Contaminants in Unidirectional Carbon Fiber Lay-ups**

Fady Barsoum<sup>1</sup>, Isabel McBrayer<sup>1</sup>

<sup>1</sup>Embry-Riddle Aeronautical University, United States

Composite manufacturing facilities work hard to ensure that the presence of contaminants in their lay-ups are minimized. Eradicating all potential contaminants is, however, not possible in a standard manufacturing environment as it is a costly and time-consuming exercise. Composite repairs performed “on the fly” are also at an increased risk for potential contaminants from microparticles in the air and from various oils and solvents.

The purpose of this paper is to investigate the presence of contaminants in composite lay-ups, using interrogation of an acoustic emission signal. The test specimens for the investigation are four ply unidirectional carbon fiber flat panels with a contaminant introduced between the second and third ply. A Hsu Nielsen source is utilized to produce the acoustic signal, and the resulting data for virgin and contaminated test specimens is then collected and compared using hardware from MISTRAS, and software program AEWIn to interrogate the signals. Tensile testing to failure is then conducted to assess the effects of the contaminants on the failure progression of the test specimens. This is part of a larger study into the use of Acoustic Emission testing to study the effects of different variables on composite repairs.

**Keywords:** Composites, Repairs, Contaminants

## **Investigating the Structural Response of Composite Repairs under Cyclic Loading**

Fady Barsoum<sup>1</sup>, Isabel McBrayer<sup>1</sup>

<sup>1</sup>Embry-Riddle Aeronautical University, United States

Composite repairs are a useful tool in industries such as Aerospace, Automotive and Naval. Particularly when extended downtime is undesirable. Different repair techniques exist in industry and each repair technique is subject to multiple variables, to include ply orientation, overlap length, grade of epoxy, double sided vs. single sided and scarf angle. As such it can be difficult to ascertain the integrity of a repair, specifically with respect to life under cyclic loading.

The purpose of this study is to investigate the effects of different repair variables under cyclic loading, using interrogation of an acoustic emission signal. This report focusses on external patch type repairs on thin laminates, and the effects of overlap length and ply orientation on the failure progression under cyclic bending loads. The test specimens for the investigation are four ply unidirectional carbon fiber flat panels that are damaged with a small perforation prior to repair. Both virgin and repaired test specimens are then subjected to cyclic three-point bending at 5Hz for a fixed number of cycles before being subjected to a tensile to failure test. The tensile testing is accompanied by Acoustic Emission monitoring in order to assess the failure modes of the test specimens, initiated by cyclic loading. Resulting data for virgin and contaminated test specimens is then collected and compared using hardware from MISTRAS, and software program AEWIn to interrogate the signals. This is part of a wider study to assess structural composite repairs to thin laminates under various cyclic type loading conditions.

**Keywords:** Composites, Repairs, Cyclic Loading

## **An Acoustic Emission IoT Framework for Monitoring, Data Management, Diagnostics and Prognostics**

Krzysztof Mazur<sup>1</sup>, Brian Wisner<sup>1</sup>, Antonios Kotsos<sup>1</sup>

<sup>1</sup>Drexel University, United States

Monitoring of complex structures subject to loading, data management and mining, as well as efficient signal processing of Acoustic Emission (AE) data for diagnostics and prognostics are crucial parameters for the successful implementation of AE in asset management applications. Recorded AE signals contain a variety of intrinsic (hardware) and extrinsic (noise) factors that make the damage assessment process both complex and computationally expensive. In addition, the use of a constantly growing amount of statistical/machine learning tools to analyze AE data, would benefit from efficient data workflows and processing procedures. In this context, this talk presents a novel Internet of Things (IoT) framework for AE that can be implemented to perform online predictions of remaining useful life (RUL) during material and structural behavior assessment. The framework consists of two parts: the hardware/software integration that allows the establishment of an IoT framework and the computational approach to perform RUL predictions. The IoT framework comprises three components: the Edge, the Fog and the Cloud. The Edge is the bottom level hardware that interfaces with the sensors used and is capable of filtering and transmitting data. The Fog is the hardware that provides an environment where computational algorithms for both diagnostics and prognostics can be implemented leveraging cloud-like properties. The Cloud is used to store data as well as to perform demanding computations such that required large databases and training sets. The computational approach is based on the use of an outlier analysis combined with custom information quality metrics used to identify a given set of degradation states. Predictions of RUL are made by extracting and processing AE features and then using Gaussian mixture modeling to identify different signal types by clustering. Such information is then used to train a linear support vector machine and adaptive neuro-fuzzy network that can be implemented to make RUL predictions. An application of the proposed approach in fatigue experiments of an aerospace-grade composite material is

presented. Extensions that can make this approach applicable to industrial applications are discussed.

**Keywords:** Acoustic emission, Prognostics, Diagnostics, Remaining Useful Life, Internet of Things, Data Mining, Machine Learning

### **Acoustic Modes in Optical Fibers for Lamb Wave and Acoustic Emission Detection**

Kara Peters<sup>1</sup>, Junghyun Wee<sup>1</sup>

<sup>1</sup>North Carolina State University, United States

Fiber Bragg grating sensors are traditionally used as both quasi-static strain sensors and ultrasound acoustic structures when bonded to structures. In the latter case, the optical fiber is constrained at the bond location and therefore displaces locally with the propagating ultrasonic wave in the structure. In addition, traveling ultrasound waves (fundamental longitudinal mode) are also generated in the optical fiber through force transmission. The amplitude and direction of the resulting traveling ultrasound waves strongly depends on the form of the bond between the optical fiber and the substrate. In this presentation we investigate the directionality and amplitude of the resulting traveling wave as a function of the different bond interfaces. For example, we start with a simple adhesive bonds and then add the presence of a protective coating or tubing between the structure and the optical fiber, creating additional adhesive layers. The experimental results demonstrate the presence of multiple traveling modes and their reflections off the multiple interfaces. We also compare the results to a theoretical representation using coupled mode theory. The implications of these results on the detection of Lamb waves and acoustic emission in structures will be discussed.

**Keywords:** fiber Bragg grating, Lamb waves, structural health monitoring

### **Monitoring of fatigue cracking and damage of metallic materials through Acoustic Emission and Digital Image Correlation**

Stephanie Deschanel<sup>1</sup>, Julien Rethore<sup>2</sup>, Jerome Weiss<sup>3</sup>

<sup>1</sup>Mateis - INSA Lyon, France

<sup>2</sup>Gem - Centrales Nantes, France

<sup>3</sup>Institut des Sciences de la Terre, Université Grenoble Alpes, France

The failure of mechanical structures under cycling loading, remains a considerable technological challenge as it occurs unexpectedly when the structure is operating apparently in a safe and steady state regime, without external signs of mechanical deterioration. It is therefore important to find new ways to identify early precursors of fatigue. The acoustic emission (AE) technique has received growing interests to detect and monitor fatigue cracks.

Here we report for the first time, in different metallic materials, the detection of acoustic emissions specific of fatigue crack growth. These so-called acoustic multiplets are characterized by nearly identical waveforms, signature of a unique source, are repeatedly triggered over many successive loading cycles at the same stress level, and originate from a single location. They mark the slow, incremental propagation of a fatigue crack at each cycle, or the rubbing along its faces.

In addition, experiments have been performed to specifically monitor the fatigue crack growth with AE and digital image correlation (DIC), simultaneously. DIC allows displacement field measurements at the surface of the specimen from the images. This measurement can be analyzed to detect the presence of cracks and follow their propagation. The goal is thus to answer the fundamental question about the exact origin of these multiplets through the interpretation of AE signals coupled with DIC and to ensure the physical processes involving the appearance of these signals. To our knowledge, such signals have never been reported in the case of metal fatigue, and no study combined the two methods.

In fine, being specific to fatigue cracking, these groups could be used as early warnings of crack propagation, which will ultimately lead to structural failure. Their detection and characterization thus open the way towards a new, reliable monitoring of the onset of fatigue cracking during mechanical tests or within structures in service.

**Keywords:** AE, fatigue cracking, multiplets

### **Study of dislocation dynamics of copper single crystals under cycling loading through acoustic emission and microstructural characterizations**

Gabriel L'Hote<sup>1</sup>, Stephanie Deschanel<sup>1</sup>, Sophie Cazottes<sup>1</sup>, Maurine Montagnat<sup>2</sup>

<sup>1</sup>Mateis, INSA Lyon, France

<sup>2</sup>IGE, Université Grenoble Alpes, France

Acoustic Emission (AE) is an appropriate tool to study crystalline plasticity. Two kinds of plasticity may be identified: one linked to numerous, small and uncorrelated dislocation motions (mild plasticity) and another linked to dislocation avalanches (wild plasticity).

Here, we study pure Cu single crystal, with different orientations favoring multiple glide, the AE sources being reduced to dislocations motion and micro cracking only. Uniaxial stress-controlled low-cycle fatigue tests are performed through different stress steps are imposed. Two types of AE are considered: continuous (background noise associated with the mild plasticity) and discrete AE (above a given threshold, associated with avalanches). Dislocation structure is characterized before, during and after cyclic test using ECC-imaging, in a Supra-55VP SEM.

The first results show that the amount of continuous AE energy increases with the imposed stress level. Almost no discrete AE is recorded before the macroscopic yield strength. Above the yield, discrete AE is observed, especially during the first cycles. Meanwhile, the continuous AE is observed at each cycle, but decreasing in intensity with the number of cycles. The plastic intermittency and dislocation avalanches rapidly decay over very few cycles, meaning that the dislocation structure evolves rapidly during the first cycles, through avalanches and single dislocation motion. After few cycles, as a structure is formed, the movement of single dislocation is made harder by the formation of dislocation junction. Consequently, the dislocation mean free path decreases and the elastic energy generated by their motions falls off simultaneously. Thus, continuous AE decreases until it becomes stationary, sign that the dislocation structure evolves less rapidly than at the beginning of the cycles. Also, the evolution of the wildness degree of plasticity (fraction of plastic deformation accommodated through dislocation avalanches) is studied in correlation with AE energy distributions along the cycles and according to the force applied and the dislocation structure formed.

**Keywords:** AE, dislocation, microstructure, cyclic loading, pure Cu single crystals

### **Off-the-Shelf Tools for Generalized, Automated Large-Scale Location Accuracy Refinement**

Horst Trattnig<sup>1</sup>, David Kosnik<sup>2</sup>, Richard Nordstrom<sup>3</sup>

<sup>1</sup>Vallen Systeme, Germany

<sup>2</sup>CTLGroup, United States

<sup>3</sup>Nordstrom Consulting, United States

Location analysis of AE data has been a powerful tool, but location accuracy can be limited by a variety of physical and signal-processing factors. Working groups such as AEWG, EWAGAE, and JCAE have been a good forum to discuss these limits, and understanding of these issues has increased steadily; however, practical means to apply the resulting refinements to large amounts of data have been limited.

Several developments in recent years have made approaching such scalability issues with AE location refinements more manageable. Implementation of open database (SQL) formats as a

replacement to proprietary binary data formats is perhaps the most significant. Along with SQL queries, external scripting tools can be built to facilitate large-scale analyses.

This talk focuses on a scalable, automated approach to location refinements through SQL queries and scripting. A generalized arrival-time-picking algorithm approach is described which can (1) be employed with at least one off-the-shelf commercial system and (2) compare the data with thousands or millions of events without reprogramming. Examples of how the two routines - the arrival time picking routine and the automated data refinement - are applied are given from examples.

**Keywords:** Location analysis, automation

### **Applying Location Accuracy Refinement to Simulated Location Testing Results**

David Kosnik<sup>1</sup>, Richard Nordstrom<sup>2</sup>

<sup>1</sup>CTLGroup, United States

<sup>2</sup>Nordstrom Consulting, United States

In the last two AEWG meetings, we have presented simulated location results using automated arbitrary waveform pulses over relatively large-scale data results (typically 10,000 distinct location results) and generated some errors that arise in AE location results. Simulating errors was just a step toward scaled testing refinement, in this year's talk, we start to address not just simulating the errors, but how the errors can be limited and mitigated. Part 1 of this talk was the off-the-shelf routines which give us a means to apply corrections across large amounts of data. This was necessary to facilitate a scalable approach to the results. The next step was means to record data in such a manner that we could compare original results versus proposed correction mechanisms side by side. The final step was to apply correction mechanisms. Over the years, many, many error corrections that could be applied to waveforms one at a time have been published. Here we show how some of these can be adapted through the scalable approach and how they perform en masse against simulated errors.

**Keywords:** Location analysis, automation

### **Fiber-optic acoustic emission sensor systems using fiber Bragg gratings**

Ming Han<sup>1</sup>, Guigen Liu<sup>2</sup>, Yupeng Zhu<sup>2</sup>

<sup>1</sup>University of Nebraska-Lincoln, United States

<sup>2</sup>Michigan State University, United States

Compared to traditional piezoelectric acoustic emission (AE) sensors, fiber-optic AE sensors have many advantages such as small size, light weight, immunity to electromagnetic interference, multiplexing capability, and remote sensing capability. However, the development of practical fiber-optic AE sensor systems has many challenges in terms of detection sensitivity, system cost, and robust operation when subject to environmental perturbations. We present our recent work on fiber-optic AE sensor systems based on fiber-Bragg gratings (FBGs) aimed for overcoming these challenges. Specifically, 1) we perform noise analysis of the sensor system and the results show that the AE detection sensitivity is mostly limited by the frequency noise of the laser source. 2) We will discuss the use of low-cost distributed feedback (DFB) semiconductor laser with self-injection locking for high-sensitivity AE detection. 3) We will introduce a new multiplexing/demultiplexing method of FBG AE sensors based on laser intensity modulation. 4) We will present several sensor designs and demodulation methods that are adaptable to large-background strains.

**Keywords:** AE sensors; Optical fiber sensors; Fiber Bragg gratings; Lasers

## **AE and X-Ray study of Microstructure Damage to Cr-Mo-V Rotor Steel as a Consequence of Extremely Long Operation**

Albert Leksovskii<sup>1</sup>, Boris Baskin<sup>1</sup>, Shavkat Azimov<sup>2</sup>

<sup>1</sup>Ioffe Physical Technical Institute, Russian Academy of Sciences, St. Petersburg, Russia

<sup>2</sup>Physical-technical Institute, Academy of Sciences of Tajikistan, Dushanbe, Tajikistan

Long-term forecast of stability of complex-alloyed materials of electric equipment requires knowledge of micro-destruction mechanics, deformation kinetics and permissible value of accumulated deformation. Acoustic emission (AE) studied to characterize Cr-Mo-V rotor steel damage in the initial structural state and as a result of operation for more than 20 years at 300°C and 510°C. AE data acquisition system used developed in Kurchatov's IAE. Samples of 100×10×3 mm deformed at 0.22 mm/min at 20°C by 1958U-10-1 test machine. X-ray study covered: residual stresses (type I)  $\sigma_{residual}$ , MPa; micro-deformation  $\langle \epsilon \rangle$ ; internal structural stresses (type II)  $\sigma < \epsilon >$ , MPa; average size of mosaic blocks  $D$ , nm and dislocation density  $\rho_{total}$ , cm<sup>-2</sup>. AE was caused by local explosive plastic deformation, having rate of change about 2-3 orders of magnitude higher than "background" creep rate. This leads to a nonlinear redistribution of local stresses and causes "mesostructural" changes. Degradation of Cr-Mo-V heat-resistant steel plasticity as consequence of more than 20 years operation at 510°C and 300°C observed. This is caused by an increase in microdistortions of crystal lattice, dislocation density, sizes of mosaic blocks and accompanied by AE intensity  $\dot{N}$  and average amplitude  $\bar{A}$  increase. According to AE linear location data, formation of clusters - areas of local explosive plastic deformation - is accelerated by increasing stresses of type II. Clustering leads to equilibrium mesocrack generation of millimeter range probability increase.

**Keywords:** Acoustic emission; alloyed steel; explosive plastic deformation; cluster; equilibrium mesocrack; internal structure stresses

## **Acoustic Emission Characterization of a Composite Overwrapped Pressure Vessel as a Structural Health Monitoring Method**

Behnoush Golchinfar<sup>1</sup>, Miguel Gonzalez Nunez<sup>1</sup>, Patsi Francis<sup>1</sup>

<sup>1</sup>MISTRAS Group, Inc., United States

Composite Overwrapped Pressure Vessels (COPVs) are substituting the conventional metal pressure vessels that were previously used for storage and containment of compressed gases at above atmospheric pressure due to its higher storage capacity and properties, such as being lightweight. Monitoring of these vessels plays an important role in the Compressed Gases industry. It is vital to detect structural damage that could later lead to compromised burst pressure strength in a composite cylinder. Acoustic Emission monitoring technique has been proven to be an acceptable testing method applied during periodic inspection.

In this study, characterization of one of the most recent manufactured COPVs was conducted by Acoustic Emission sensors. Attenuation tests at 0, 45, and 90 degrees angles were performed on the cylinder of a pressure vessel by implementing four various sensors including both broadband and resonant sensors. The wave propagation velocity in the material was also measured on the cylinder in various directions for comparison purposes. These tests resulted in different velocities being obtained in different directions. The characterization of the head of the pressure vessel was also conducted via the same sensors.

The achieved results would help us through better understanding the structure in terms of acoustic waves and figuring out the superior method for monitoring the brand-new composite overwrapped pressure vessels. In addition to that the acquired data is vital for the next steps toward generating a procedure for the test setup, data collection and data analysis using Acoustic Emission.

**Keywords:** Acoustic emission, composite overwrapped pressure vessel

## **Experimental Characterization of PKBBI Sensor: the Low Power Flat Frequency Response, Broadband Acoustic Emission Sensor**

Hossain Saboonchi<sup>1</sup>, Gonzalez Nunez Miguel<sup>1</sup>

<sup>1</sup>MISTRAS Group, Inc., United States

Application of Modal Acoustic Emission (MAE) method to evaluate the health of the pressure vessels has been established in standards and procedures. Most of these standards ask for broadband transducers with certain level of flatness in the frequency response of the sensor in a specific frequency range with certain level of sensitivity so that the captured traveling waves' energy gets a fair representation from all the different modes present in that frequency range. In this paper the PKBBI sensor, developed by MISTRAS Group Inc, as required by these standards, is characterized. The results of some example real applications have been presented and analyzed to further evaluate the capabilities of this sensor. The PKBBI sensor shows superior performance in the MAE analysis versus the conventional sensors. Spectrograms of the waves have been overlaid to the group velocity curves to evaluate and analyze the acoustic emission modes and how they can be utilized to extract valuable information on the traveling path, medium, and source classification of acoustic event.

**Keywords:** Acoustic Emission, Experimental Characterization, sensor, Modal AE

## **AE Measurements and Analysis on a Layered Pressure Vessel**

Adrian Pollock<sup>1</sup>, Miguel Gonzalez<sup>1</sup>, Hossain Saboonchi<sup>1</sup>

<sup>1</sup>MISTRAS Group, Inc., United States

Acoustic emission (AE) testing on a layered steel vessel was performed during a pressure test. A comparison of both conventional feature-based AE and Modal Acoustic Emission (MAE) was carried out. Most of this paper deals with the results obtained with this latest-generation transducer, especially some applications of MAE technology.

On site, high priority was assigned to source location to provide maximum support to the Radiographic Testing measurements that were scheduled to begin immediately after the AE pressurization activities were completed. Acoustic Emission technique was capable of determining the location of the source cluster. In addition to that by using the Modal AE, the waveforms were further analyzed for additional characterization and location refinement.

MAE results described in this paper include source location refinements, source-sensor distance measurements used to validate the linear nature of the discovered source cluster, and the demonstration that wave propagation characteristics (at least for the discovered cluster) were like those of an unrestrained plate having the same thickness as a single layer of the layered vessel.

**Keywords:** Modal Acoustic Emission, Layered Vessels. Wave Propagation

## **Power Transformers Monitoring**

Caricia Martinez<sup>1</sup>, Arturo Nunez<sup>1</sup>

<sup>1</sup>MISTRAS Group, Inc., United States

Power Transformers represent the largest portion of capital investment in transmission and distribution substations. Owners face several challenges:

- Their assets are reaching or have already reached the end of their operating life
- Delivery times for a new transformer are very long (18 – 24 months)
- Ever increasing demand prohibits the transformers to be taken out of service for routine electrical testing. There only a few techniques that can be applied with the transformer energized, these are Dissolved Gas Analysis, Oil quality, Infrared Inspection, Vibration and Acoustic

Emission. Acoustic Emission (AE) is a powerful tool used to "listen" and register acoustic signals of different frequencies generated within a power transformer. An acoustic emission monitoring might be implemented to detect, locate and assess faults on power transformers.

The main advantages of this technique are:

- No transformer outage is required to perform the inspection
  - Non invasive
  - Global monitoring of the asset
  - Use of multiple Acoustic Emission sensors provide location of the fault (s)
  - Offers real time information of when the fault is active
  - Indicates under what operating conditions the fault is active
  - Severity of the fault can be determined
  - Continuous monitoring to ensure safe operation and prevent a catastrophic failure
- This paper presents the latest developments on this technology and cases studies are presented.

**Keywords:** Power Transformers, Online monitoring

### **3D-printed anisotropic structure for switching elastic wave propagation**

Yoshihiro Mizutani<sup>1</sup>, Ryuichiro Otonari<sup>1</sup>, Takeshi Ashizawa<sup>1</sup>, Akira Todoroki<sup>1</sup>

<sup>1</sup>Tokyo Institute of Technology, Japan

Several anisotropic structures made of CFRP and PLA are prepared by using 3D-printer. The structures consisting "switch" which can control propagation direction of elastic wave. One of the structures consists of hundreds of narrow columns that act as wave guides. When an external force is applied to the structure, the columns buckle, and its buckling direction instantaneously reverts according to the direction of external force. We use this phenomenon to make the switch. The other structure consists of CFRP with curved fibers. As elastic wave propagates along the fibers, the structure which can control direction of curved fibers is prepared to realize the switch. In order to discuss feasibility of the structures for switching wave propagation direction, wave propagation in the structures are visualized by scanning ultrasonic receiver on the structure's surfaces.

**Keywords:** Elastic wave, anisotropic material, 3D-printed material

### **The Qualification / Certification Dilemma - An Innovated Approach for the Development of Advanced Nondestructive Testing Technicians**

Donald Blanchette<sup>1</sup>

<sup>1</sup>MISTRAS Group, Inc., United States

Organizations and companies will gain the competitive edge only through the integration of strategies that bring together the power of technology and an engaged and well-trained workforce. The pace of change of the marketplace and customer expectations demand a continuous improvement to how individuals are being trained and certified for advance nondestructive testing applications such as Acoustic Emission. Dr. Adrian Pollock believed that a solution to this challenge is not to "force-fit" individuals into positions that are mismatched with their responsibilities and duties that don't fit their technological and certification profiles.

This paper will provide Dr. Pollock's conceptual and practical approach to the training and certification of individuals that will be conducting Acoustic Emission as Level 1 and 2s.

**Keywords:** AE Training Certification, Advanced NDE

### **AE as a Vehicle for High School STEM Outreach**

David Kosnik<sup>1</sup>

<sup>1</sup>CTLGroup, United States

The multidisciplinary nature of the practice of acoustic emission (AE) monitoring makes AE a useful vehicle for engaging high school (i.e. US secondary school, typically ages 14-18) students in courses under the science-technology-engineering-mathematics (STEM) umbrella. Specifically, aspects of theory and analysis techniques familiar to AE practitioners, such as attenuation, frequency considerations, and location analysis, may be adapted to demonstrate real-world applications of concepts presented in high school courses such as geometry, advanced algebra, trigonometry, calculus, and physics, as well as the introductory engineering, electronics, and computer science courses now offered in more and more school districts. In addition, hypothesis-driven investigative and problem-solving approaches presented within AE case studies give students a look into broad applications of the scientific method in general. This paper will summarize my experience in making presentations to various high school mathematics and introductory engineering classes over the past few years. All class presentations were based on the same AE case study involving diagnosis of anomalous noises on a movable bridge, but the presentation to each class was specifically tailored to the concepts studied in that class in coordination with the classroom teacher.

**Keywords:** K12 outreach, STEM, case study

### **Increase uptime and plant reliability deploying asset monitoring solutions**

Arturo Nunez<sup>1</sup>

<sup>1</sup>MISTRAS Group Inc., United States

Traditionally, periodical testing of assets has been the method of choice to evaluate its integrity. This approach can have some disadvantages such as erroneous measurements, unavailability of the asset for testing or testing using different instrumentation settings/techniques. The development of instrumentation for continuous monitoring allows the inspection intervals to be reduced significantly as well as to be able to monitor the asset during the very different operating conditions it experiences, hence allowing to identify correlation between fault mechanisms (cracks, leaks, corrosion, arcing, etcetera) and the operation of the asset.

This paper presents different applications where asset monitoring is used for detecting active faults in power transformers, tube leaks in boilers, cracks on combustion turbines, thickness measurements. Case studies where the benefits for monitoring are presented.

**Keywords:** Monitoring, acoustic emission, remote

### **Identifying The Presence and Position of Wheelflat via Acoustic Emission**

Okan Topcu<sup>1</sup>

<sup>1</sup>Turkish State Railways, Republic of Turkey

Intensive usage of railways brings structural problems together for both track and rolling stocks. Wheelflat is one of the most important problems faced in trains and detecting the wheel flat in real time without interrupting train operation is important for all infrastructure managers and railway operators. While there are studies to detect the wheelflat up to 40 km/h, there is no literature to identify the position of wheel with wheelflat real time. In one of the recent research projects of the State Railways of the Republic of Turkey, acoustic emission measurements were carried out to detect the presence and position of wheel flat. The aim of this study is to identify the presence of wheel flat and the position of the wheel flat at the wheels of trains passing through at different speeds up to 65 km/h. A linear array of acoustic emission sensors array was mounted on the rail with the spacing of 3 m or 5 m. Three different types of acoustic emission sensors (F15I, R6I, WD) were mounted on the web of the rail to understand the influence of AE frequency to the wheelflat measurement while trains at different speeds were passing through. The presence of wheel flat was detected by repetitive impact signal with the periodicity proportional to wheel diameter and train velocity. The periodic impact was observed in the time driven absolute energy per average

signal level or streamed waveform signals. The expected impact frequency was determined by the inverse of impact period. The position of wheel with wheel flat was measured by relative time of flight of the peak signal by the sensor array. According to the results of the study acoustic emission amplitude energy increases exponentially with increasing train speed, and the presence and position of wheel flat can be determined real time using AE.

**Keywords:** Wheel flat, rail wheels, acoustic emission, train wheels inspection

### **History and Development of Acoustic Emission Personnel Qualification and Certification**

Miguel A. Gonzalez Nunez<sup>1</sup>, Adrian A. Pollock<sup>1</sup>

<sup>1</sup>MISTRAS Group, Inc., United States

The need for widespread AE technician certification came to be recognized at Physical Acoustics Corporation in 1986. Prior to that time, education in AE was readily available to engineers and scientists at short courses offered by the equipment manufacturers, at the meetings of dedicated groups such as AEWG and EWGAE, and at conference series such as the International AE Symposia held biennially in Japan. Physical Acoustics Corporation made a first public offering of technician-oriented AE training based on the recommended training course outline already available in the American Society for Nondestructive Testing's publication SNT-TC-1A. Since then, Physical Acoustics Corporation (now MISTRAS Group Inc.) has offered AE Level I, Level II and Level III courses over 150 times. Trainings have been delivered to over 2000 technicians and other attendees, in the curriculum of SNT-TC-1A, ISO 9712 and in numerous specialized AE certification schemes. This presentation will focus upon the qualification and certifications processes, and the challenges for new and emerging AE applications.

**Keywords:** Personal Qualification and Certification

### **APPLICATION OF ACOUSTIC EMISSION DURING PRESSURE TEST OF AUSTENITIC STEEL VESSEL**

Václav Svoboda<sup>1</sup>, František Žemlička<sup>1</sup>

<sup>1</sup>*Preditest Ltd., Pod Višňovkou 1662/23, 14000 Praha 4, Czech Republic*

The paper describes a method of pressure testing of a vessel made from austenitic steel type AISI 304. The method of acoustic emission was used as a non-destructive inspection tool. On the outer surface of the vessel was placed a network of AE sensors comprising the entire volume of the vessel. In normal operation, this pressure vessel operates under cryogenic conditions (-160 ° C). During the pressure test with nitrogen, increased emission activity was registered, especially in the cylindrical part of the vessel. The individual emission events were not located in sub-sources (clusters), but were distributed throughout the shell volume. This caused a complication in evaluation of the pressure vessel according to the current valid standards for the evaluation of the AE signals. By further analysis has been found that the registered AE signals were induced by phase transformation of austenite to deformation-induced martensite, including the reverse process at local sites.

**Keywords:** Pressure test, austenitic steel vessel

ICAE-9 & AEWG-61 SPONSORS



## KRN Services



AE Specialists since 1992

[www.KRNServices.com](http://www.KRNServices.com)

